DTU Library

NOx reduction in grate-fired Waste-to-Energy plants

Jepsen, Morten Søe

Publication date:
2018

Document Version
Publisher's PDF, also known as Version of record

[Link back to DTU Orbit](#)

NO$_X$ reduction in
grate-fired Waste-to-Energy plants

Morten Søe Jepsen
PhD Thesis
2018

Preface

This thesis describes the work carried out at the Combustion and Harmful Emission Control (CHEC) Research Centre, Department of Chemical and Biochemical Engineering, Technical University of Denmark. The thesis was written in partial fulfillment of the requirements for a Ph.D. degree in Engineering. The work conducted and presented in this thesis was performed in the period from December 2014 to February 2018, and was supervised by Professor Peter Glarborg, Associate Professor Peter Arendt Jensen and Thomas Norman, R&D Department Manager at B&W Vølund.

Kgs. Lyngby, February 23th, 2018

Morten Søe Jepsen

NO$_x$ reduction in grate-fired Waste-to-Energy plants

Abstract

Due to the great environmental problems related to emission of NO$_x$ from combustion processes a large emphasis has been put on minimising the emission over the last decades. Furthermore, in order to accommodate the strict NO$_x$ emission levels, which is projected to be tightened even more in the coming years in many countries, new measures must be taken. It is important to develop models to predict the NO$_x$ formation and degradation at varying furnace operating conditions to allow for an optimization of furnace design and operating conditions. Chemical models predicting the NO$_x$ formation and degradation in a grate-fired combustor have been developed. However, these models do not take fluid dynamics into account and are typically too complex to be implementing in computational fluid dynamics (CFD) codes. CFD codes are required to take fluid dynamics into account, thereby predicting NO$_x$ formation and degradation more accurately. These modelling short-comings presently limit the industry from obtaining better process control and improved design of combustion facilities.

Initially in this thesis numerous chemical models that describes the NO$_x$ formation and reduction are identified. One of these models was selected for further work.

The identified detailed chemical kinetic model was reduced using the Simulation Error Minimization Connectivity Method (SEM-CM) and the Path Flux Analysis (PFA) method to yielding a number of skeletal mechanisms with varying size. It was identified that a skeletal model consisting of 38 species and 251 reactions, developed using the SEM-CM algorithm, offered the best compromise between model size and accuracy.

Full scale Waste-to-Energy (W-t-E) plant measurements were conducted identifying the concentration profile of major combustion products and combustibles close to the fuel bed. Furthermore, the speciation and concentration profile of the NO$_x$ precursors were measured close to the bed, and it was shown that accurate predictions of the NO$_x$ precursor speciation is essential for accurate NO$_x$ predictions.

The formation of NO$_x$ at the W-t-E plant (Affald+) used for data collection was modelled post process the modelling of the combustion process. This was done using B&W Vølunds in-house CFD model and the skeletal model developed in this study. The modelling was performed based on process conditions obtained from the plant control system and data collected during measurements at the plant. Results from the mod-

elling showed large differences between the predicted and measured NO_x emissions. It is believed the difference is caused by errors in the predictions of the temperature field in the furnace. The process is very dependent on temperature. Consequently a precise prediction of the temperatures is a precondition for precise results with respect to NO_x.

A skeletal model for the SNCR process was developed through reduction of the detailed chemical kinetic model using the SEM-CM algorithm. A skeletal model consisting of 21 species and 50 reaction was identified as the most suitable for CFD modelling as it offered a good compromise between accuracy and size.

The efficiency of NO_x reduction by injection of NH_3 (SNCR) into the flue gas was determined through full scale measurements. Furthermore, the flue gas composition in the SNCR zone was measured. Besides normal combustions products (CO_2 and H_2O), high CO concentrations of up to 6000ppm was measured in the lower part of the SNCR zone.

The SNCR process was modelled post process the combustion using the skeletal model developed in this study. The modelling was performed based on process conditions obtained from the plant control system. Large differences between predictions by the CFD model and measurements were found. The large differences is believed to be due to inaccuracies in the prediction of the CO concentration field, which the SNCR process is highly dependent on, and a predicted recirculation of flue gases in the SNCR zone.

NO$_x$-reduktion i ristefyrede affaldsforbrændingsanlæg

Resumé

Grundet store miljømæssige konsekvenser knyttet til udledning af store mængder af NO$_x$, er stor fokus blevet rettet mod minimering af NO$_x$ emissioner fra forbrændings-processer gennem de seneste årtier. Ydermere, for at overholde de strenge emissonskrav på NO$_x$-udledning, emissionskrav som forventes strammet yderligere i mange lande indenfor den nærmeste fremtid, er nye tiltag er nødvendige. Det er af stor nødvendighed, at udvikle modeller som kan bruges til beskrives af NO$_x$-dannelse og reduktion i af-faldskedler ved forskellige driftsindstillinger. Disse modeller kan efterfølgende bruges til optimering af kedeldesign og optimering af driftsindstillinger. Modeller til beskrivelse af NO$_x$-dannelse og reduktion er før blevet udviklet. Disse modeller tager dog ikke hen-syn til fluiddynamik og er typisk alt for komplekse til at kunne blive implementeret i "computational fluid dynamics" (CFD) koder. Til nøjagtig beskrivelse af NO$_x$-dannelse og reduktion i industrielle systemer, er brugen af CFD en nødvendighed. De førnævnte komplikationer afholder i given stund industrien fra at opnå en bedre proceskontrol og et optimeret design af forbændingsfaciliteter.

Indledningsvis i afhandlingen blev en række kemiske modeller til beskrivelse af NO$_x$-dannelse og reduktion identificeret, og af disse blev én udvalgt.

Ved brug af "Simulation Error Minimization Connectivity Method" (SEM-CM) algorit-men og "Path Flux Analysis" (PFA) metoden blev den identificerede detaljerede kemiske model reduceret. Dette resulterede i en række skeletmodeller med varierende størrelse. På baggrund af analyser af modellernes nøjagtighed og modellernes størrelse viste det sig, at det bedste kompromis mellem modelstørrelse og nøjagtighed blev opnået for den udviklede skeletmodel bestående af 38 specier og 251 reaktioner.

Målinger af koncentrationsprofiler for forbrændingsprodukterne, CO$_2$ og H$_2$O, samt brandbare gasser fra pyrolyse af affald lige over affaldslaget, blev målt på et affaldsfor-brændingsanlæg. Ydermere blev koncentrationsprofilerne for NH$_3$ og HCN fra pyrolyse af affaldet målt, og forholdet mellem disse produkter bestemt. Det blev vist, gennem modellering af NO$_x$-dannelse, at en nøjagtig bestemmelse af forholdet mellem NH$_3$ og HCN frigivet fra brændselslaget, er essentiel for nøjagtigt modellering af NO$_x$-dannelse i affaldsforbrændingsanlæg.

NO$_x$-dannelse i et affaldsforbrændingsanlæg blev modelleret i CFD. Dette blev gjort,

ved brug af den udviklede skeletmodel til beskrivelse af NO_x-dannelse. NO_x-dannelse blev modelleret post-proces, ved brug af resultater fra modellering af forbrændingsprocessen. Driftsdata fra Affald+, et forbrændingsanlæg i Næstved, blev brugt til bestemmelse af indgangsbetingelser til beregningen. Store uenigheder mellem den modellerede NO_x-dannelse og målinger fra Affald+ blev fundet. Store forskelle på de predikterede temperaturer i fyrrummet og målte temperaturer blev fundet. Disse temperaturforskelle kan være skyld i overestimeringen af NO_x-dannelsen.

Ved brug af SEM-CM algoritmen, blev en skeletmodel for "Selective Non-Catalytic Reduction" (SNCR) processen udviklet. Det bedste kompromis mellem modelstørrelse og nøjagtighed blev fundet for skeletmodellen bestående af 21 specier og 50 reaktioner.

Reduktionseffektiviteten af NO_x med NH_3 i et SNCR system blev evalueret gennem målinger på et affaldsforbrændingsanlæg i Næstved. Ydermere blev gassammensætningen i SNCR-zonen målt. Udover sædvanlige forbrændingsprodukter (CO_2 og H_2O), blev store koncentrationer af CO målt. CO-koncentrationer i nærheden af 6000ppm, i området hvor SNCR-processen foregår, blev målt.

SNCR processen blev modelleret i CFD. Dette blev gjort post-proces forbrændingsmodelleringen. Til modellering af SNCR processen blev den udviklede skeletmodel benyttet. Til modellering af forbrændingsprocessen blev driftsdata fra nævnte affaldsforbrændingsanlæg i Næstved brugt. Der blev fundet store forskelle på den predikterede effektivitet af NO_x-reduktionen og den målte. Den store forskel mellem den predikterede effektivitet af NO_x-reduktionen og den målte, kan skyldes en unøjagtig beskrivelse af CO koncentrationerne i CFD modellen. Da SNCR-kemien er yderst afhængig af CO koncentrationen, kan en unøjagtig beskrivelse af CO koncentrationen føre til stor unøjagtighed i beskrivelsen af NO_x-kemien.

Contents

Chapter 1

Introduction

Managing the large amounts of municipal solid waste that is produced daily is a significant challenge, and R&D efforts to resolve the problems are increasing. Traditionally, the municipal solid waste has been disposed at landfills due to the low cost. In many regions this is no longer possible as an increase in municipal solid waste generation is experienced. This has generated a shift in municipal solid waste handling, from disposal at landfills to extraction of energy through combustion. One of the main combustion technologies for solid waste is grate-firing. This technology is widely recommended as one of the most competitive, as it enables the use of a wide range of fuels, both biomass and solid waste, with varying moisture content and the requirements to the fuel preparation and handling are limited.

Combustion of solid waste, similar to combustion of other solid fuels, emits nitrogen oxides (NO_x). The emission of NO_x continues to be a major environmental concern [1] as it is an acid rain precursor and participates in formation of photochemical smog, which is problematic in urban areas [1] [2]. Furthermore, studies indicate that the gaseous NO_2 has significant impact on the human health [3].

Nitrogen oxides are formed either from oxidation of the N_2 in the combustion air or from oxidation of organically bound nitrogen in the fuel [1]. For solid fuels such as waste, which has a significant content of organic nitrogen, the dominating source of NO is the NO formed from organically bound nitrogen in the fuel [1]. In grate combustion of waste, most of the nitrogen bound in the fuel is released during devolatilisation of the fuel in the fuel-bed, mostly as NH_3, HCN and aromatic N-compounds [4].

Due to the effects on the environment and on the human health minimising the NO_x emissions from combustion processes is of utmost importance. This can be achieved through modelling of the combustions process in commercial CFD codes. The scope of this research is to develop a reliable simplified model for NO_x formation, as well as for reduction by SNCR, and implement it in CFD. Following the project the model can help to improve B&W Vølunds NO_x control strategies and the design of future W-t-E boilers.

1.1 Grate firing combustion technology

The prime objective of a waste combustion plant is to burn the waste in an environmentally safe manner. This means that the burnout of the flue gas and bottom ash needs to be maximized, and the formation of air, water and soil pollutants be prevented

as much as possible.

A secondary - but equally important - objective is maximization of the energy recovery. The incinerator is equipped with a steam boiler, the energy recovery takes place by raising the steam temperature, which is passed to a turbine/generator set for electricity and, possibly, heat production. In such a plant the steam production rate should be as constant as possible to secure operation of the turbine and uniform electricity production; consequently a constant thermal conversion rate in the furnace/boiler system is essential.

Boilers for waste-fired power plants are normally water tube boilers, in Europe they most often have four passes: three vertical radiation passes and one convection pass. The first of the radiation passes is integrated in the furnace as the post-combustion chamber. The convection pass, in which the evaporators, the superheaters and the economizers are located, may be vertical or horizontal.
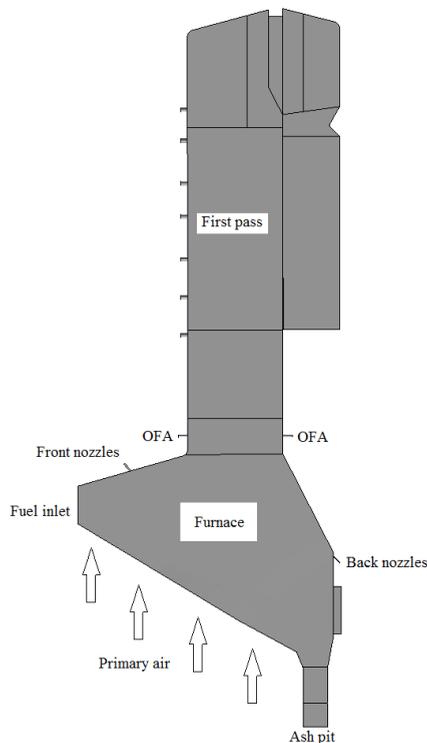
Figure 1.1: Schematic drawing of the furnace, first and second pass of a Waste-to-energy plant.

The addition of combustion air, both primary and secondary combustion air, plays an important role in the efficiency of the W-t-E plant and in securing complete combustion of the fuel [5]. In modern W-t-E plants the combustion air is added in three different locations; primary air under the grate, secondary air through nozzles in the front and back roof of the furnace and over-fire air nozzles initially in the first pass.

This is schematically shown in Figure 1.1.

The main objective of the primary air, together with the movement of the grate, is to significantly increase the mixing of the combustibles and increase waste conversion [5]. The primary air is injected from under the grate perpendicular to the movement of the fuel; consequently the bottom of the fuel is exposed to preheated primary air while the top of the fuel is within the furnace. For effective combustion it is important to mix the fuel well as it is transported down the grate. Typically the grate is split into 4 zones and a predefined fraction of the total primary air distributed to each zone. Effective control of the primary air distribution to each zone helps to control the combustion. The primary air added in the first section primarily contributes to the drying of the fuel, while the primary air added in the second and third part of the grate provides the needed air and heat for devolatilization of the fuel. The primary air added in the fourth section mainly provides the needed oxygen for complete burn-out of the fuel.

Effective secondary air injection is extremely important in optimisation of the gas combustion in the freeboard, to secure complete burnout and to secure low emissions [5]. The secondary air introduced through nozzles in the front roof secures staging of the gas combustion in the front part of the furnace which helps to reduce NO$_x$ emissions [5]. Furthermore, the injection of combustion air in the front roof creates recirculation in the furnace increasing the residence time of particles and combustibles in the furnace thereby securing complete burn-out of the waste and lowering CO emissions.
Injection of secondary air in the lower part of the first pass, this is denoted over-fire air (OFA), acts to secure complete burn-out and reduce the emissions due to the staging effect. The arrangements of the over-fire air jets can provide an effective highly turbulent environment at the exit of the furnace due to horizontal recirculation zones. This causes a prolonged residence time of combustibles securing complete burn-out. Furthermore, the OFA jets secures a more evenly distributed gas temperature in the cross sectional area of the first pass [5]; consequently the effectiveness of the reduction of formed NO$_x$ in a SNCR system can be increased.

The grate, located in the bottom of the furnace, has three important functions. The grate has to secure lengthwise transport of the fuel from the inlet to the ash pit, distribute the primary combustion under the grate and mix the fuel to secure complete burn out. These can be classified into four main groups; Stationary sloping grates, Travelling grates, Reciprocating grates and Vibrating grates [5]. In this study the focus will be put on W-t-E plants equipped with a reciprocating grate. This type of grate transports the fuel from the inlet to the ash pit by reciprocating movements mixing the fuel more effectively compared to the other grate types[5].

1.2 NO$_x$ emission

1.2.1 Atmospheric NO$_x$ chemistry

NO$_x$ is found to be a precursor for acid rain. In the atmosphere NO undergoes a series of reactions through which nitrate is formed; an aqueous solution of nitrate is a highly corrosive mineral acid (nitric acid). Firstly NO reacts with hydroperoxyl to form NO$_2$ and hydroxyl [6]:

$$NO + HO_2 \rightarrow NO_2 + OH \tag{1.1}$$

The formed NO_2 is photochemically broken down to form NO and ozone according to reaction 1.2.

$$NO_2 + hv(\lambda \leq 420\text{nm}) \rightarrow NO + O(^3P)$$
$$O(^3P) \rightarrow O_2 \overset{M}{+} O_3 \tag{1.2}$$
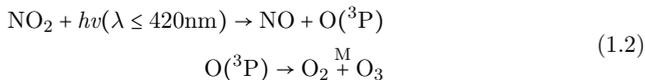
The formed NO from reaction 1.2 reacts with hydroperoxyl again to form NO_2 according to reaction 1.1.

The formed ozone reacts with NO_2 to form nitrate, which leads to acid rain [6], according to reaction 1.3.

$$NO_2 + O_3 \rightarrow NO_3 + O_2 \tag{1.3}$$

Acid rain has a great influence on the ecosystem as it promotes acidification of soil, forest and the aquatic ecosystems, consequently affecting the wildlife, crops and forests [7].

1.2.2 Human health issues

Several animal studies have been performed to determine the impact of NO_2 exposure on the human health. Extrapolation of results and observations from these studies can give an insight in the health issues related to NO_2 exposure on the human body. Because of the difference between mammalian species, the exact effects on the human body caused by NO_2 exposure has not exactly been determined. However, because of basic physiological, metabolic and structural similarities in all mammals, the results and observations from studies of several animal species indicate that NO_2 exposure can cause similar types of effects in humans [3]. Animal studies on NO_2 exposure show signs of a number of different effects in several animal species. Most notably the studies show negative effects on the host defence against infectious pulmonary diseases, lung metabolism, lung function and lung structure [3].

Long-term exposure to high concentrations of NO_2 has been reported to result in morphological lung lesions for several species of laboratory animals. Furthermore, destruction of alveolar walls in lungs from animals in a limited number of studies. The destruction of the alveolar walls causes emphysema in humans.

NO_2 can act as a strong oxidant in the oxidation of unsaturated lipids with peroxides as the dominant product. Both ascorbic acid (vitamin C) and alpha-tocopherol (vitamin E) inhibit the peroxidation of unsaturated lipids. When ascorbic acid is sealed within bilayer liposomes, NO_2 oxidizes the sealed ascorbic acid. Furthermore, NO_2 can also oxidize membrane proteins. The oxidation of either of the two, the membrane lipids or proteins, can result in the loss of cell permeability control[3].

The respiratory tract has two main objectives; to ensure efficient exchange of gases, mainly O_2 and CO_2, and to provides the body with a first line of defence against inhaled viable and non-viable airborne agents. It has been shown that exposure to NO_2 can result in a decrease in the effectiveness of these defence mechanisms, thereby increasing the susceptibility to infectious respiratory diseases. The parameters that are affected by NO_2 exposure are the functional and biochemical activity of cells in lungs, alveolar macrophages, immunological competence, susceptibility to respiratory infections, and the rate of mucociliary clearance [3].

Even though the exposure of humans NO$_2$ has not been proven to cause any of the mentioned health issues above, the animal studies highly indicate a number of human health issues related to NO$_2$ exposure. Limiting the NO$_x$ is therefore of great importance.

1.2.3 Legislations on NO$_x$ emissions from W-t-E plants

Legislation on emission from European companies is decides by the European Union based on what can be achieved by "Best Available Techniques" denoted. BAT. The legislations on emissions of NO$_x$ are a part of the BREF-documents[8]. These documents are revised every 8th year, hence new technologies becomes a part of the legislation. The BREF-documents and the BAT are specified for approximately 30 industries, among these waste incineration.

The BREF documents include emissions and the used of resources by companies. The BREF documents are, according to the Industrial Emissions Directive (IED) which came into force in Denmark on January 7 2013, binding for companies that incorporate the requirements in their environmental impact assessments. Companies are required to comply with the new requirements within 4 years after the publication of the BREF-documents[8].

The current BREF-documents dates back to 2010. These states that the NO$_x$ emission must be limited to 200 mg/Nm^3 for new build Waste-to-energy plants, while the NO$_x$ must be limited to 250 mg/Nm^3 for existing plants[8]

As stated above revised BREF documents will come every 8th year; revised BREF documents are expected in 2018[8]. A draft of the revised BREF documents were provided by DAKOFA (Dansk Kompetencecenter for Affald og Ressourcer[8]). According to the revised BREF-documents emission of NO$_x$ must be limited to 50-120 mg/Nm^3 for new build Waste-to-energy plants, while the NO$_x$ must be limited to 50-150 mg/Nm^3 for existing plants[8]. The values are daily average. The exact value is determined by local authorities.

1.3 Formation of NO$_x$

NO$_x$ can be formed by three different mechanisms, which depend on the process conditions, fuel etc.[9]. The mechanisms are:

- Thermal NO$_x$

- Prompt NO$_x$

- Fuel NO$_x$

A simplified reaction path diagram of the major steps in the formation of thermal NO, prompt NO and fuel NO is shown in figure 1.2.
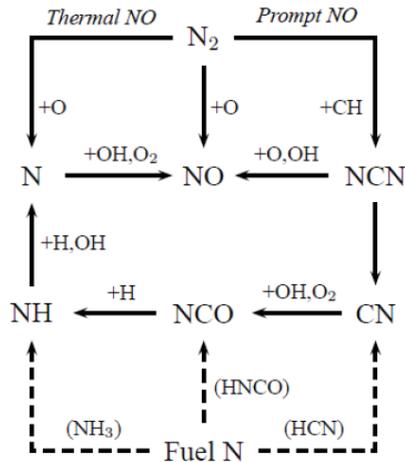
Figure 1.2: Simplified reaction path diagram of the major steps in the formation of thermal NO, prompt NO and fuel NO [10].

Thermal NO_x is formed by oxidation of the atmospheric nitrogen, prompt NO_x is formed through reaction between atmospheric nitrogen and hydro carbon radicals from the fuel and fuel NO_x is formed from the nitrogen bound in the fuel[9].
Each of these mechanisms will be presented and examined in the following sections.

1.3.1   Thermal NO_x mechanism

Thermal NO_x is formed through oxidation of nitrogen from atmospheric air. The formation is highly temperature sensitive and happens at relatively high temperatures [9]. The oxidation is described from the widely accepted Zeldovich two-step mechanism 1.4 and 1.5 [11]. At high temperature oxygen dissociates or reacts with free radicals to form free oxygen atoms, these attack nitrogen molecules to start a chain reaction forming NO. This reaction mechanism was first proposed by Zeldovich (1947), hence it is called the Zeldovich mechanism, and has been shown below.

$$N_2 + O \rightleftharpoons NO + N \tag{1.4}$$

$$N + O_2 \rightleftharpoons NO + O \tag{1.5}$$

In some cases the Zeldovich mechanism under-estimates the NO formation [12]. In these cases the mechanism is extended to include an additional reversible reaction 1.6. The mechanism including the additional reversible reaction is referred to as the *Extended Zeldovich mechanism*.

$$N + OH \rightleftharpoons NO + H \tag{1.6}$$

The extended Zeldovich mechanism is very depended on the temperature. At temperature below 1600-1800K the thermal NO formation by the extended Zeldovich mechanism is significantly reduced. Furthermore, Thermal NO_x is not as predominant at fuel-rich environments due to the low amount of available oxygen[9]. The initial step of the Zeldovich mechanism, the attack of an oxygen atom on the triple bond in N_2 (reaction 1.4) has a high activation energy of about 75kcal mol^{-1}, consequently this is the rate limiting

step in thermal NO formation only significant at higher temperatures [10].

At lower temperatures, below 1800K, and a stoichiometric ratio of 1.2 it has been shown that thermal NO$_x$ account for lees than 15% of the total NO$_x$ formation. At a slightly reduced stoichiometric ratio; 1.0, the thermal NO$_x$ was found to account for less than 1% for the formed NO$_x$ [9]. These measurements have, however, been performed during coal combustion. Similar behaviours are expected for biomass combustion as thermal NO$_x$ is formed from atmospheric nitrogen, therefore independent of the fuel type.

1.3.2 Prompt NO$_x$ mechanism

The prompt NO$_x$ is formed through reactions between the atmospheric nitrogen and hydrocarbon radicals in fuel rich regions of flames. The formation of NO$_x$ through the prompt NO$_x$ mechanism was first proposed by Fenimore (1971)[11].
The formation of NO$_x$ through the prompt reaction mechanism is describe by the 3 overall reactions 1.7, 1.8 and 1.9.

$$N_2 + CH_x \rightleftharpoons HCN + N + ... \tag{1.7}$$

$$N_2 + C_2 \rightleftharpoons 2CN \tag{1.8}$$

$$N + OH \rightleftharpoons NO + H \tag{1.9}$$

From these three reactions it is postulated that reaction 1.7 is the dominating reaction. Of the hydrocarbon radicals the methylidyne (CH) is especially interesting as it is sufficiently reactive to attack molecular nitrogen thereby initiating the prompt NO formation reactions [10]. The HCN formed from this reaction follows the same reaction pathway as HCN formed from devolatilisation of the fuel; the HCN is therefore included in the fuel NO$_x$ mechanism described in the following section. A schematic drawing of the major reaction pathways of prompt NO$_x$ and fuel NO$_x$ has been proposed by Miller and Bowman [13] and is seen in figure 1.3
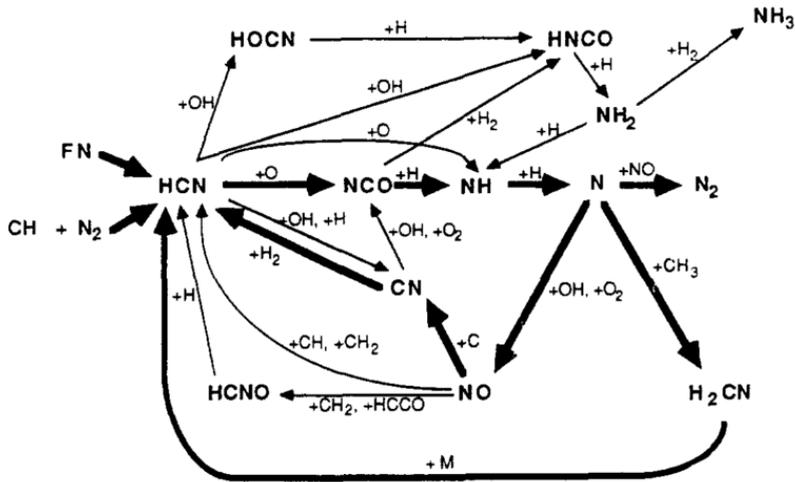
Figure 1.3: The major reaction patchway for the formation of prompt and fuel NO_x proposed by Miller and Bowman [13]. The bold line represents the most important reactions.

It has been estimated that the HCN formed from reaction 1.7 accounts for 90% of the prompt NO_x formed[9]

The prompt NO_x mechanism requires, as seen in reaction 1.7, a hydrocarbon radical to be initiated, consequently the prompt NO_x mechanism is much more predominant in fuel-rich regions[9].

The prompt NO_x mechanism is neglected in many models as it is only significant in highly fuel-rich regions. Furthermore, the prompt NO_x mechanism only accounts for a small fraction of the total NO_x formed; the prompt mechanism accounts for approximately 15% of the total NO_x produced[9].

There are uncertainties about the rate data of the overall reactions leading to formation of prompt NO_x. At present time the prompt NO_x is by default calculated from a global kinetic parameter derived by De Soete [14] in Fluent[15]. De Soete showed that the overall prompt formation rate can be found from equation 1.10.

$$\frac{d[NO]_{prompt}}{dt} = (\text{Overall prompt NO}_x \text{ formation rate})$$
$$- (\text{Overall prompt N}_2 \text{ formation rate}) \tag{1.10}$$

Under fuel-rich conditions, where prompt NO_x formation has a slight significance, the oxygen radical concentration is high and N radicals almost exclusively react to form NO_x. The prompt NO_x formation rate can therefore be expressed as equation 1.11 [15].

$$\frac{d[NO]}{dt} = k_{prompt}[O_2]^a[N_2][FUEL] \cdot e^{-E_a/RT} \tag{1.11}$$

1.3.3 Fuel NO$_x$ mechanism

Fuel NO$_x$ is formed by oxidation of fuel bound nitrogen. An accepted assumption is that the general scheme for fuel NO$_x$ mechanism includes a partial or total transformation of the nitrogen bound in the fuel into a series of nitrogen intermediates; these intermediates are HCN, NH$_3$ CN, NH and N, followed by a double competitive reaction path. One of the reaction paths transforms the formed nitrogen intermediates into NO via an attack from an oxygen species. In the second reaction path the nitrogen intermediates are transformed into molecular nitrogen by attack of (mainly) NO itself [11] [14].
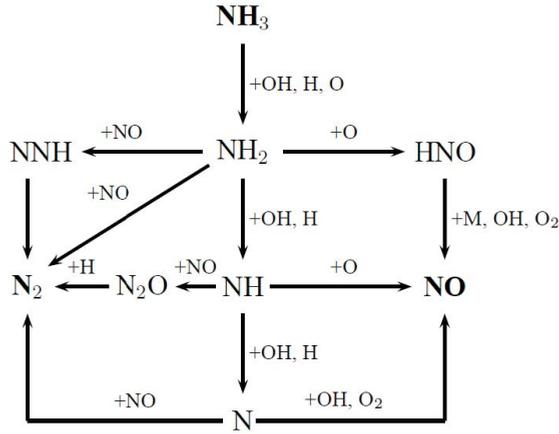
Figure 1.4: Reaction path diagram for the oxidation of NH$_3$[10]

The formation proceeds through the formation of HCH or NH$_3$. Hence these compounds are oxidized to NO$_x$ according to reaction 1.12. A competing reaction 1.13 reducing the formed NO$_x$ has a great influence on the overall NO$_x$ formation. The competing reactions, reaction 1.12 and 1.13, form the overall reaction sequence for fuel NO$_x$ formation[14] [9].

$$HCN + O_2 \rightarrow NO + ...$$
$$NH_3 + O_2 \rightarrow NO + ... \tag{1.12}$$

$$HCN + NO \rightarrow N_2 + ...$$
$$NH_3 + NO \rightarrow N_2 + ... \tag{1.13}$$

From the overall reaction 1.12 and 1.13 it is seen that HCN and NH$_3$ react to form either NO or N$_2$. The ratio between these two products depends on the local conditions[9]. In fuel-rich regions a large amount of N$_2$ is formed compared to the amount of NO. This is due to the low oxygen availability which means that the formed NO is used as oxidant for NH$_3$, amongst others, thereby reducing NO to molecular nitrogen N$_2$ [16] [9]. In fuel-lean regions the HCN and NH$_3$ are oxidised to NO, because oxygen is used as oxidant for NH$_3$.

In combustion processes at lower temperatures; as is the case for waste incineration plants, fuel NO formation is the dominating NO$_x$ formation mechanism. Typically

more than 80% of the formed NO_x originates from fuel bound nitrogen[9]. Fuel NO_x is formed more rapidly compared to thermal NO_x due to the weaker N-H and N-C bonds than the strong triple bonds which must be broken during thermal NO_x formation[17].

1.4 NO_x reduction methods in Waste-to-Energy plants

1.4.1 Primary NO_x reduction measures

The aim of primary NO_x reduction techniques is to decrease the amount of NO_x formed during devolatilisation and combustion of the fuel and combustible gases. This can be done using a number of different approaches. The different approaches are similar in the way that they either limit the availability of oxygen in the primary combustion section of the boiler unit or lower the combustion temperature. The limited availability of oxygen acts to limit the formation of fuel-NO_x, while a lowering of the combustion temperature limits the formation of thermal NO_x and fuel-NO_x formation; fuel NO_x formation is strongly temperature dependent[1].

There are four major primary NO_x reduction methods which are applied industrially either alone or in combination. These reduction methods are marked by the red box seen in figure 1.5[18]:
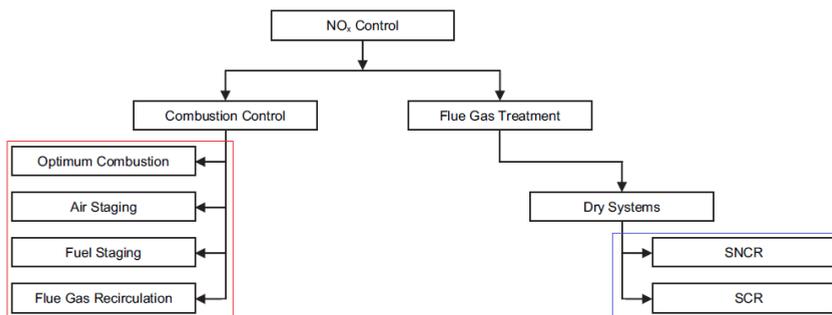
Figure 1.5: The primary control measures are marked by the red box, while the secondary measures are shown in the blue box. Other primary and secondary measures are available. However, the shown measures are the ones used in solid waste incineration on a grate. (Modified from [19])

According to some literature primary reduction methods can reduce the formation of NO_x with 50-80% [16].

Staged combustion

The principal of staged combustion is to limit the formation of NO_x by limiting the availability of oxygen in the zone just above the fuel layer during devolatilisation, while an excess amount of oxygen is available in a second zone further up in the combustion chamber. In modern grate-fired power plants burning biomass the ratio between primary air; which is responsible for the devolatilization of the fuel, and the secondary air; responsible for the oxidation of the combustible gases and char, tends to be 4/6 in the

favour of the secondary air, while the ratio in older grate-fired units tends to be 8/2 in the favour of the primary air[20]. The approach is illustrated in figure 1.6.
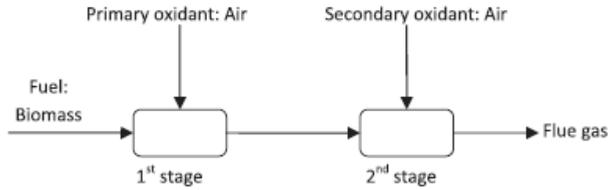
Figure 1.6: Principal of staged combustion air supply [21]

The primary air is injected into the system from under the grate and the secondary air is injected from the ceiling. A schematic drawing of a combustion chamber is seen in figure 1.7
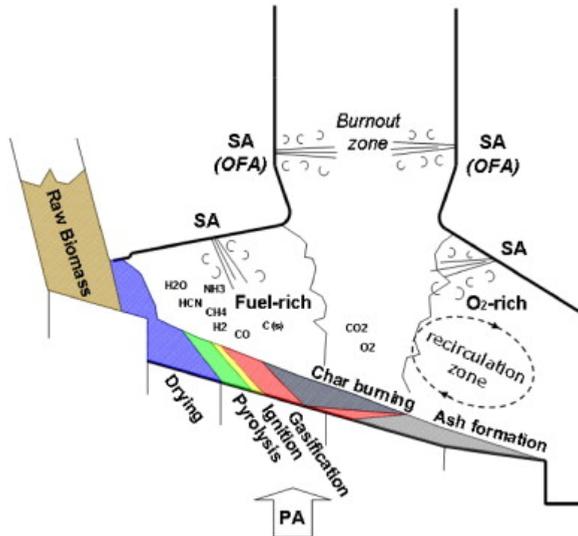
Figure 1.7: A schematic drawing of a typical combustion chamber in a grate-firing solid waste power plant. The location of the primary (PA) and secondary air (SA) is seen as well [20].

From figure 1.7 it is seen that the combustion chamber is split into two zones; a fuel rich zone and an oxygen rich zone. In the fuel rich zone a limited amount of oxygen is available. The limited availability of oxygen in the primary combustion zone will cause NO to act as an oxidant for CO, CH$_4$, HCN and NH$_i$ ($0 > i < 4$) thereby reducing NO to molecular nitrogen N$_2$. These reduction reactions proceed according to reaction 1.14

and 1.15 amongst others [16].

$$NO + NH_2 \rightarrow N_2 + H_2O \tag{1.14}$$

$$NO + CO \rightarrow CO_2 + 0.5N_2 \tag{1.15}$$

The limitation of oxygen in the fuel rich zone induces an increase in CO formation due to incomplete combustion. In the oxygen-rich zone the secondary air acts to decrease the temperature and oxidise the unburned carbohydrates, thereby limiting the formation of thermal NO_x and increasing the burn-out.

In the oxygen rich zone an overstoichiometric amount of oxygen is available in order ensure total burn-out of the char produced from devolatilisation in the fuel rich zone, hence more heat is being produced.

Enhanced air mixing

Proper design of the secondary air injection can enhance the mixing of the combustibles. The Over-Fire Air (OFA) acts to ensure burn-out of all carbohydrates. Effective design of the OFA ensures good mixing and prolongs the residence time, as seen in figure 1.8, of the combustibles in the burn-out zone ensuring complete burn out.
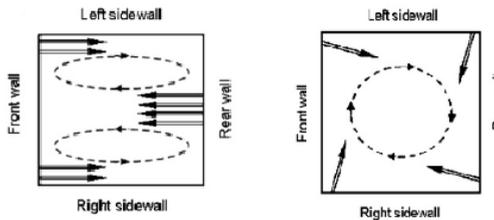
Figure 1.8: Examples of OFA designs to ensure good mixing and prolonged residence time of the combustibles in the burn-out zone[20]

Two different OFA configurations are shown in figure 1.8.

Flue gas recirculation (FGR)

In flue gas recirculation a part of the flue gas from the combustion is injected into the furnace again, as illustrated in figure 1.9.

After the hot flue gas has passed through the economiser it is recirculated into the furnace again. The recirculated flue gas acts to decrease the temperature in the furnace thereby degreasing the thermal NO_x formation. Furthermore, as the oxygen and nitrogen mass fraction in the flue gas is lowered, compared to atmospheric air, the partial pressure of oxygen and nitrogen in the furnace is reduced, hence the NO_x formation is limited[22].
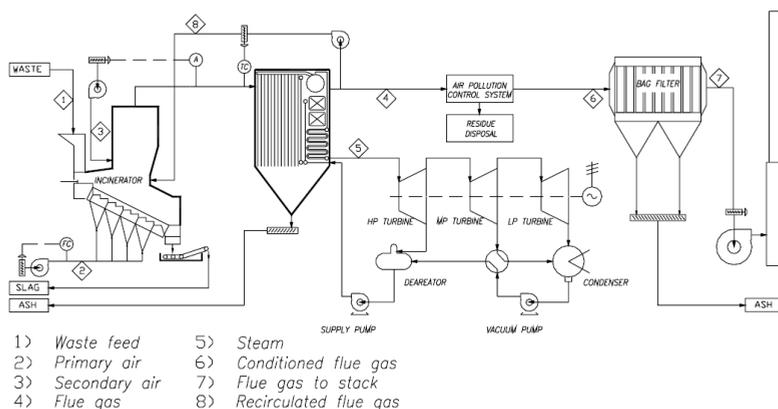
Figure 1.9: Schematic drawing on a grate-firing solid waste incineration plant with flue gas recirculation[22]

1.4.2 Secondary NO$_x$ reduction measures

The primary NO$_x$ reduction methods, mentioned in the previous section, only limit the formation of NO$_x$ to a certain degree. Due to the tight legislations on NO$_x$ emissions sufficient NO$_x$ reduction is not possible when primary NO$_x$ reduction methods are used alone[18]. For further reduction in NO$_x$ emissions secondary NO$_x$ reduction methods are used. The secondary NO$_x$ control methods used in Waste-to-Energy plants are shown in figure 1.5. The aim of these methods is to reduce the formed NO$_x$ through chemical reactions with a reduction agent. In many industries aqueous solutions of ammonia or urea are used for NO$_x$ reduction. The reduction of NO$_x$ using an aqueous solution of ammonia follows reaction 1.16, while reduction of NO$_x$ using an aqueous solution of urea follows reaction 1.17

$$4NH_3 + 4NO + O_2 \rightarrow 4N_2 + 6H_2O \qquad (1.16)$$

$$CO(NH_2)_2 + 2NO + 0.5O_2 \rightarrow 2N_2 + CO_2 + 2H_2O \qquad (1.17)$$
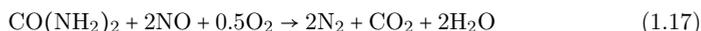
The reduction of NO$_x$ is done catalytic through Selective Catalytic Reduction (SCR) or non catalytic through Selective Non-Catalytic Reduction (SNCR).
The use of a catalyst decreases the temperature window in which the optimal reduction occurs by several hundred degrees. This allows for better control, thereby more optimal reduction. The reduction using SNCR occurs by direct injection of the reducing agent dissolved in water into the first-pass, whereas reduction by SCR happens by injection of the reducing agent after heat exchange in the boiler. This ensures a more stable temperature. The SNCR concept will be discussed in detail in section 1.4.3.
Due to the use of a catalyst the SCR process is economically less feasible compared to the SNCR process.

1.4.3 Selective Non-Catalytic Reduction

Prior to 1972 homogeneous reaction between NH$_3$ and NO, NO and O$_2$ and NH$_3$ and O$_2$ had been studied extensively. Each of these three reactions were predicted by the

literature to react to a negligible extent [23]. Not before 1972 a mixture of NH_3, NO and O_2 was studied. The mixture behaved rather different from the sum of the parts[24]. The presence of O_2 was shown to enable NH_3 to selectively reduce the NO to atmospheric nitrogen leaving the O_2 largely unreacted[23]. This process is referred to as the "Thermal DeNO$_x$" process.

Presently the Thermal DeNO$_x$ process is a widely used and effective method for NO$_x$ reduction by injection of amines (-NH-)containing selective reducing agents such as NH3 or urea into the flue gases [25].

In this part of the thesis NO$_x$ reduction by injection of a reducing agent into the first pass of the boiler, Thermal DeNO$_x$ process, will be reviewed; the optimal operating window and kinetics for the reduction will be examined. Furthermore, the concept of selective non-catalytic reduction using different reducing agents will be addressed.

Two different strategies exists for secondary NO$_x$ control; the Thermal DeNO$_x$ process and the RAPRENO$_x$ process [13]. These after-treatment processes reduce the formed NO$_x$ by homogeneous gas-phase reactions. The thermal DeNO$_x$ process uses ammonia or urea as reducing agent, which is injected into the exhaust gas in a limited temperature window, while the RAPRENO$_x$ process uses cyanuric acid as reducing agent [13].

The choice of reducing agent is important for the modelling purpose as these behave differently. The most commonly used reagents are ammonia, urea and cyanuric acid. Brouwer and Heap[26] made a schematic drawing of the NO$_x$ reduction by these reagents shown in figure 1.10
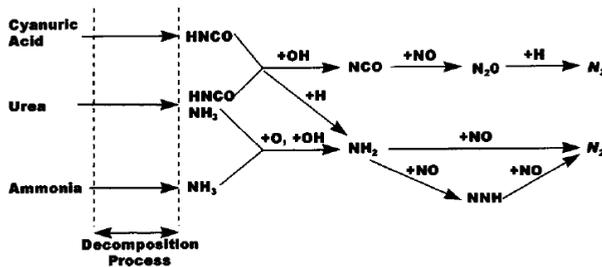
Figure 1.10: Schematic figure of the proposed simplified pathway for NO$_x$ reduction by ammonia, urea and cyanuric acid [27]

Ammonia

The most used reducing agent for the reduction of NO$_x$ is ammonia, due to a lower price compared to urea. After injection through a nozzle into the first pass, ammonia and water are simultaneously evaporated to form gaseous ammonia and water. The gaseous ammonia reacts homogeneously with NO to form atmospheric nitrogen [13] according to the simplified scheme seen in figure 1.11.
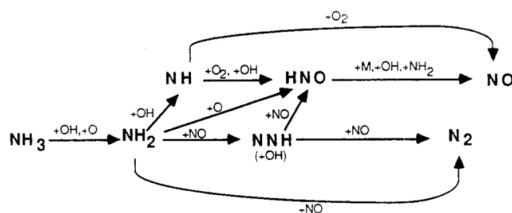
Figure 1.11: The most important reactions shown as a reaction pathway diagram for the thermal DeNO$_x$ process [13].

At higher temperature; above approximately 1100°C [13], the gaseous ammonia decomposes to form additional NO thereby contributing to the overall NO$_x$ emission.

Urea

Urea behaves differently compared to ammonia as this is a salt. Consequently simultaneous evaporation of water and urea is not happening. The urea evaporation/decomposition is not understood in detail and a number of assumptions are therefore applied [28]. After injection of urea in the combustion gases the aqueous urea solution is heated to the boiling point of water at which the water is evaporated [29]. When all the water has evaporated the urea undergoes thermal breakdown producing ammonia according to reactions 1.18, 1.19 and 1.20.

$$(NH_2)_2CO(aq) \rightarrow (NH_2)_2CO(l) + H_2O(l) \tag{1.18}$$

$$(NH_2)_2CO(l) \rightarrow (NH_2)_2CO(g) \tag{1.19}$$

$$(NH_2)_2CO(g) \rightarrow NH_3(g) + HNCO(g) \tag{1.20}$$
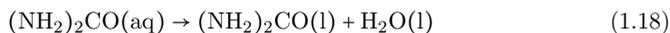
According to Birkhold et al.[29] the rate of reaction 1.19 can be determined from equation 1.21.

$$1 \cdot 10^{12} \cdot e^{-V/RT_d} \tag{1.21}$$

Here V is the heat of evaporation and T$_d$ the temperature of the droplet. The heat of evaporation has been determine to 87.4kJ/mol [29].
After decomposition of urea the product (ammonia) will enter into the ammonia reaction pathway shown in figure 1.11.
45% of the formed urea will according to Miller and Bowman[12] decompose to isocyanic acid [13]. This will act to reduce the NO$_x$ similar to cyanuric acid.

Cyanuric acid

Cyanuric acid (C$_3$H$_3$N$_3$O$_3$) decomposes thermally to isocyanic acid and small amounts of ammonia. According to Miller and Bowman cyanuric acid decomposes into 2.7 parts of isocyanic acid and 0.3 parts of ammonia. The isocyanic acid enters into the pathway as stated in figure 1.10. The formed isocyanic acid reacts with a species M in the gas phase to form cyanate. The formed cyanate is the compound responsible for the NO$_x$ reduction due to its reaction with NO to form N$_2$O.

1.4.4 Operating window of the thermal $DeNO_x$ process

As urea decomposes to ammonia after injection of the urea solution into the hot exhaust gasses, the temperature window at which these two components reduce NO_x most effectively are similar. Experimental data from degradation of NO_x with ammonia has been performed by Lyon and Hardy [30] as shown in figure 1.12
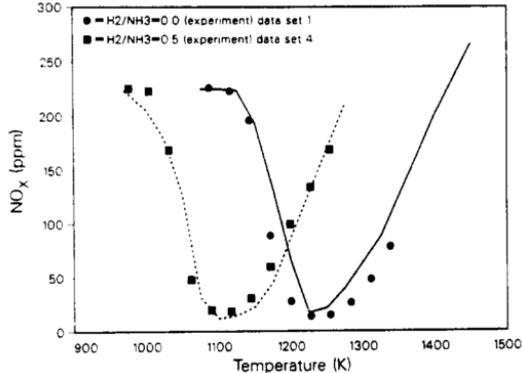
Figure 1.12: The effect of hydrogen upon the thermal $DeNO_x$ temperature operating window. The experimental data (the filled boxed) have been obtained by Lyon and Hardy [24]. These have been compared with a kinetic model (the lines) developed by Bowman and Miller [13].

As seen in Figure 1.12 the reduction of NO_x with NH_3 occurs in a tight temperature window around 950°C. Furthermore, it is seen that the presence of combustibles, in this case H_2, moves the temperature window.

A well cited model used extensively to describe the reduction of NO_x with NH_3 is the global model by Brouwer and Heap [26]. The model assumes the reduction occurs through 2 competing reactions shown in reaction 1.22 and 1.22.

$$NH_3 + NO \rightarrow N_2 + H_2O + H \tag{1.22}$$

$$NH_3 + O_2 \rightarrow NO + H_2O + H \tag{1.23}$$

This global model describes the reduction chemistry well for most conditions. However, the presence of CO in the flue have been shown to move and narrowing the temperature window for reduction. This effect has not been captured well by the model.
In the next chapters of the thesis the NO_x reduction with NH_3 will be studied more extensively.

1.5 Scope of the thesis

The overall aim of this project is to develop and implement models that describe the formation and reduction of harmful NO_x gases in grate-firing combustion chambers in Babcock & Wilcox Vølund´s in-house CFD code, thereby facilitating predictions of the NO_x levels at any given point in the boiler. The research hypotheses are therefore:

- A simple, but precise, model for NOx formation in grate-firing boilers can be developed and implemented in the Babcock & Wilcox Vølund in-house combustion model.

- A model for NOx degradation, using appropriate SNCR systems, can be developed and implemented in the Babcock & Wilcox Vølund in-house combustion model.

- The implemented sub-models can precisely predict NO_x levels when compared with experimental results from a pilot scale grate-firing combustor and commercial solid waste grate-firing power plant.

The objectives will be met by dividing the project into a number of different tasks. The first task deals with the identification of an appropriate model for NO_x formation and degradation in the free-board. The second task involves development and validation of developed simplified models by comparing predictions with experimental and theoretical results. The third involves the implementation of the appropriate models in the BWV in-house CFD model. The fourth task deals with the evaluation of the implemented model.

Chapter 2

Modelling of NO$_x$ chemistry

In order to explain the formation of NO$_x$ during combustion of solid fuels numerous different kinetic mechanisms have been proposed. The mechanisms range from very simple global reaction kinetics describing the nitrogen chemistry in a limited parameter space to very detailed reaction mechanism where more than one hundred species and over five hundred reactions are included[31] which describe full combustion chemistry in the full parameter space.

In the following it will be shown that the formation and reduction of NO$_x$ is highly dependent on the temperature and oxygen concentration. Due to this dependency, the turbulent environment in the furnace and SNCR zone of a Waste-to-energy plant, and large differences in the local stoichiometry and temperature the use of CFD for accurate NO$_x$ predictions is essential[32]. The use of CFD as a prediction tool comes with disadvantages, detailed chemical models have been shown to highly increase the computational efforts[33] and the large number of reactions may complicate the analysis of results from CFD simulations; consequently the use of reduced models of global models in CFD can be an advantage. However, reduction of chemical models influence the performance of the models as shown in the following sections; consequently using reduced models is a trade off between computational time, easier understanding of the chemistry and modelling accuracy.

In the following sections a number of the more accurate Detailed Chemical Kinetic Models (DCKM) will be presented; the most promising detailed chemical kinetic model will be identified and used as starting mechanism for the development of skeletal models. Readily available skeletal models will be presented and analysed. Lastly, existing global models will be presented and analysed. Each of the models will be discussed in terms of accuracy and applicability for implementation in CFD.

2.1 Detailed Chemical Kinetic Models

A Detailed Chemical Kinetic Model, or Detailed Chemical Kinetic Mechanism, is composed of a particular type of reactions; Elementary reactions[34]. These are fundamental mechanistic steps, an elementary reaction is assumed to occur in a single step and to pass through a single transition state[34]. An example of an elementary reaction is the reaction between a hydrogen radical and an oxygen molecule:

$$H + O_2 \leftrightarrow O + OH \tag{2.1}$$
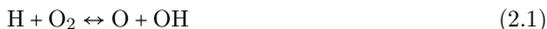
The rate constants connected to each elementary reaction in the detailed chemical kinetic model are not dependent on the conditions under which they were derived, however they are dependent on the temperature and in some cases the pressure[34].

In the literature a number of different detailed chemical kinetic model's have been proposed. Some of the more cited detailed chemical kinetic model's include the ones developed by Miller and Bowman [13], Glarborg et al. [35] and Mendiara and Glarborg [36].

2.1.1 The Miller and Bowman mechanism

Miller and Bowman developed a detailed chemical kinetic model in 1989. This detailed chemical kinetic model is one the most cited chemical kinetic models for NO_x formation and reduction during combustion of solids, especially coal and coal-derived fuels. The chemical model includes thermal, prompt and fuel NO_x formation. Besides including NO_x formation the model includes degradation of NO_x through the thermal DE-NO_x and RAPRENO$_x$ process [12]. Sensitivity analysis and rate of production analysis were performed in order to determine the main elementary reaction pathways for the nitrogen conversion process [12]. The proposed detailed chemical kinetic model consists of 234 reversible reactions [12].

The developed model was compared with experimental results obtained by Sun et al. [37] for NO, HCN, NH_3 and the total of the three before mentioned. The experiments were condicted in a jet-stirred reactor burning ethylene in air with a small quantity of added ammonia (1.5% of fuel by mass) [13]. The NO concentration as a function of the fuel/air equivalence ratio predicted by the Miller and Bowman mechanism has been compared with PSR data obtained through experiments, this is shown in Figure 2.1.
In Figure 2.2 a comparison between the HCN concentration as a function of the fuel/air equivalence ratio predicted by the mechanism and experimental Perfectly Stirred Reactor (PSR) data has been made, while the predicted NH_3 concentration has been compared with experimental PSR data in Figure 2.3.
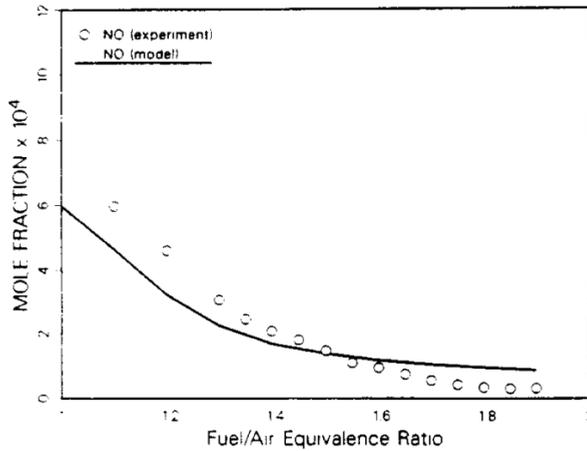
Figure 2.1: Comparison between the detailed chemical kinetic model proposed by Miller and Bowman [13] and experimental data obtained by Sun et al.[37]. The experiments were condicted in a jet-stirred reactor burning ethylene in air. The NO concentration as a function of the fuel/air equivalence ratio has been plotted for PSR simulations in CHEMKIN. Conditions: NH=2600ppmv, T=1750K and residence time=7msec.
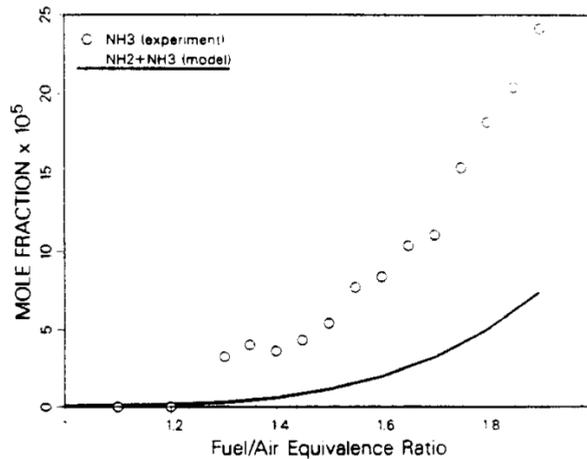
Figure 2.2: Comparison between the detailed chemical kinetic model proposed by Miller and Bowman [13] and experimental data obtained by Sun et al.[37]. The HCN concentration as a function of the fuel/air equivalence ratio has been plotted for PSR simulations in CHEMKIN.
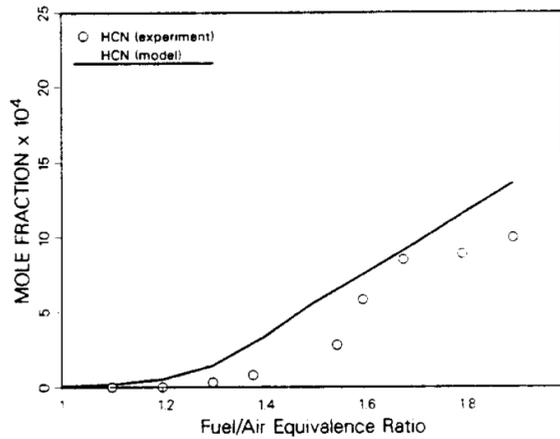
Figure 2.3: Comparison between the detailed chemical kinetic model proposed by Miller and Bowman [13] and experimental data obtained by Sun et al.[37]. The NH$_3$ concentration as a function of the fuel/air equivalence ratio has been plotted for PSR simulations in CHEMKIN.

The predicted NO and NH$_3$ concentrations agree well with the experimental data obtained by Sun et al. The prediction of the HCN on the other hand is less accurate. According to Miller and Bowman this is either due to measurement errors, inadequacies in the reaction mechanism or incompatibilities of the experimental conditions with the PSR model in CHEMKIN [12].

Figure 2.4: Comparison between the proposed detailed chemical kinetic model proposed by Miller and Bowman [13] and experimental data obtained by Sun et al.[37]. The sum of the NO, NH$_3$ and HCN (total fixed nitrogen) concentration as a function of the fuel/air equivalence ratio has been plotted for PSR simulations in CHEMKIN.

Further evaluation of the proposed detailed chemical kinetic model has been done

22

by comparing the predicted sum of HCN, NO and NH_3; the total fixed nitrogen, with the experimental data. This is seen in Figure 2.4.

A good comparison between the predicted total fixed nitrogen concentration and the experimental data is seen. A minimum in the nitrogen (NO, NH_3 and HCN) concentration is seen at an equivalence ratio between 1.2 and 1.4. This minimum is the key to a good NO_x control strategy [12]. The minimum arises due to fuel rich combustion in the beginning limiting the availability of oxygen thereby degreasing the NO formation, followed by a fuel lean combustion securing hydrocarbon, CO and H_2 burnout.

2.1.2 Mechanism proposed by Mendiara and Glarborg

Mendiara and Glarborg [36] developed a detailed chemical kinetic model for oxy-fuel combustion. In oxy-fuel combustion the combustion air consists of oxygen mixed with recycled flue-gases. This results in an oxygen rich and nitrogen free atmosphere, consequently the developed model only describes the fuel nitrogen formation. The model consists of 97 species and 779 reversible reactions [36]. The mechanism is mostly based on recent work on the methane/ammonia reaction system in flow reactors [38] and low pressure flames [39]. The reaction mechanism draws on results from oxidation of CO/H_2[40],C_1-C_2 hydrocarbons [39, 41–45], NH_3 [38, 39] and HCN[31], as well as interactions of these components[39, 43, 46].

Selected reactions are shown in the reaction path diagram 2.5

Figure 2.5: Reaction path diagram for nitrogen conversion during methane combustion under normal and oxy-fuel conditions [36]. The dashed lines are only important for the CO_2 experiments performed by Mendiara and Glarborg

Figure 2.5 shows the important pathways for the formation and destruction of NO. The dashed lines are only important at high CO_2 levels, while the solid lines denotes pathways which are important at regular CO_2 levels[36].

The mechanism proposed by Mendiara and Glarborg[36] was evaluated by comparison with experimental data. Experiments were conducted a 12mm internal diameter

laminar flow reactor made from alumina. The experiments covered oxy-fuel combustion of methane in the temperature range from 973K to 1773K. The comparison was done at fuel-lean, stoichiometric and fuel-rich conditions. The concentrations of methane at the inlet were around 2500 ppm and the equivalence ratio ϕ was varied between 0.13 and 1.55. The concentration of NH$_3$ was adjusted to 500 ppm. For For comparison the experiments were performed with both N$_2$ and CO$_2$ as bulk gas. The gas was pre-mixed before entering the reaction zone. After reaction the product gases were analysed in a series of continuous gas analysers [36]. The resulting gas concentrations are shown in Figure 2.6, 2.7 and 2.8.
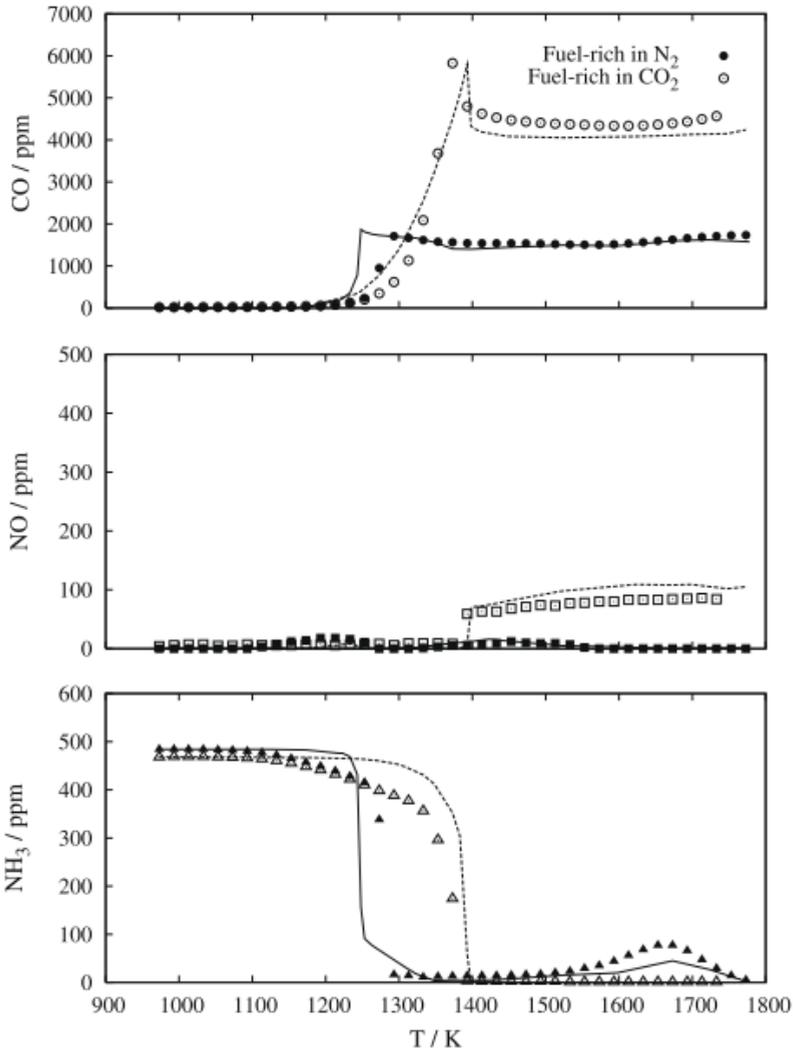
Figure 2.6: Model predictions compared with experimental data for oxidation of CH_4 in the presence of NH_3 in fuel-rich conditions as a function of temperature. The experimental data for N_2 and for CO_2 experiments are shown as closed and open symbols respectively. Conditions - N_2 experiments: CH_4=2515ppm, O_2=3479ppm, NH_3=484, N_2=99.35%, ϕ=1.55, Residence time=1296/T(K) - CO_2 experiments: CH_4=2519ppm, O_2=3505ppm, NH_3=468, N_2=9.14%, CO_2=90.21%, ϕ=1.55, Residence time=1296/T(K)
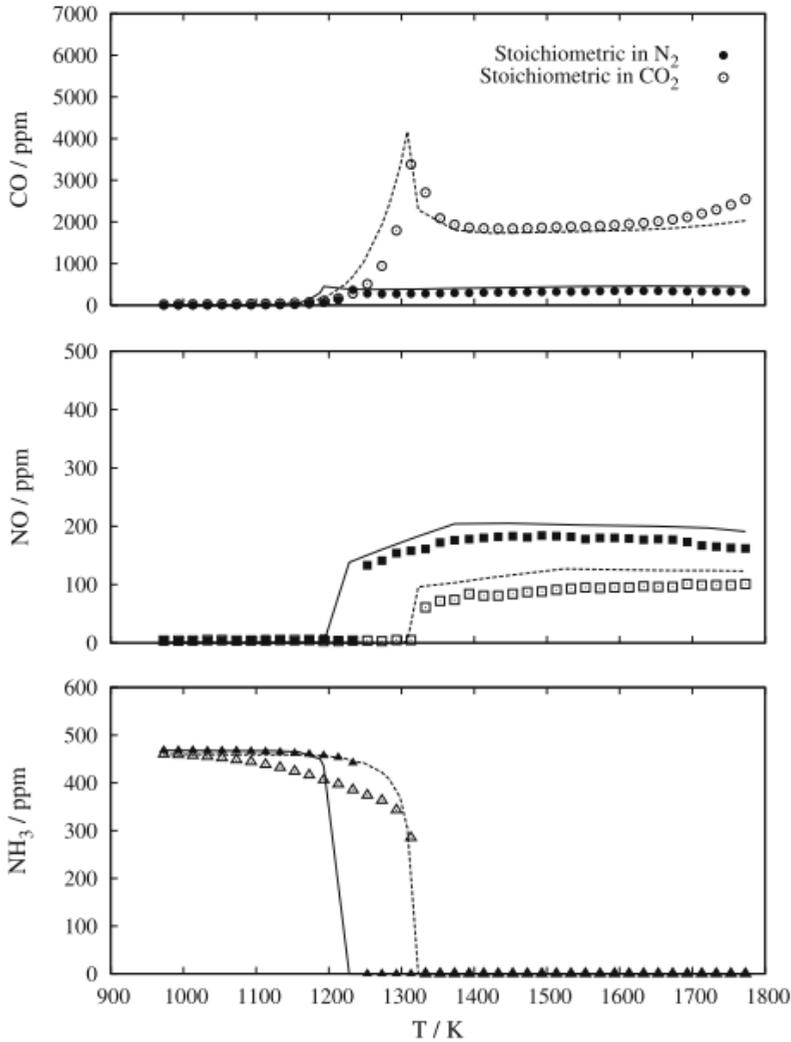
Figure 2.7: Model predictions compared with experimental data for oxidation of CH$_4$ in the presence of NH$_3$ in stoichiometric conditions as a function of temperature. The experimental data for N$_2$ and for CO$_2$ experiments are shown as closed and open symbols respectively. Conditions - N$_2$ experiments: CH$_4$=2513ppm, O$_2$=5036ppm, NH$_3$=468, N$_2$=99.20%, ϕ=1.07, Residence time=1296/T(K) - CO$_2$ experiments: CH$_4$=2512ppm, O$_2$=5014ppm, NH$_3$=460, N$_2$=10.65%, CO$_2$=88.55%, ϕ=1.07, Residence time=1296/T(K)
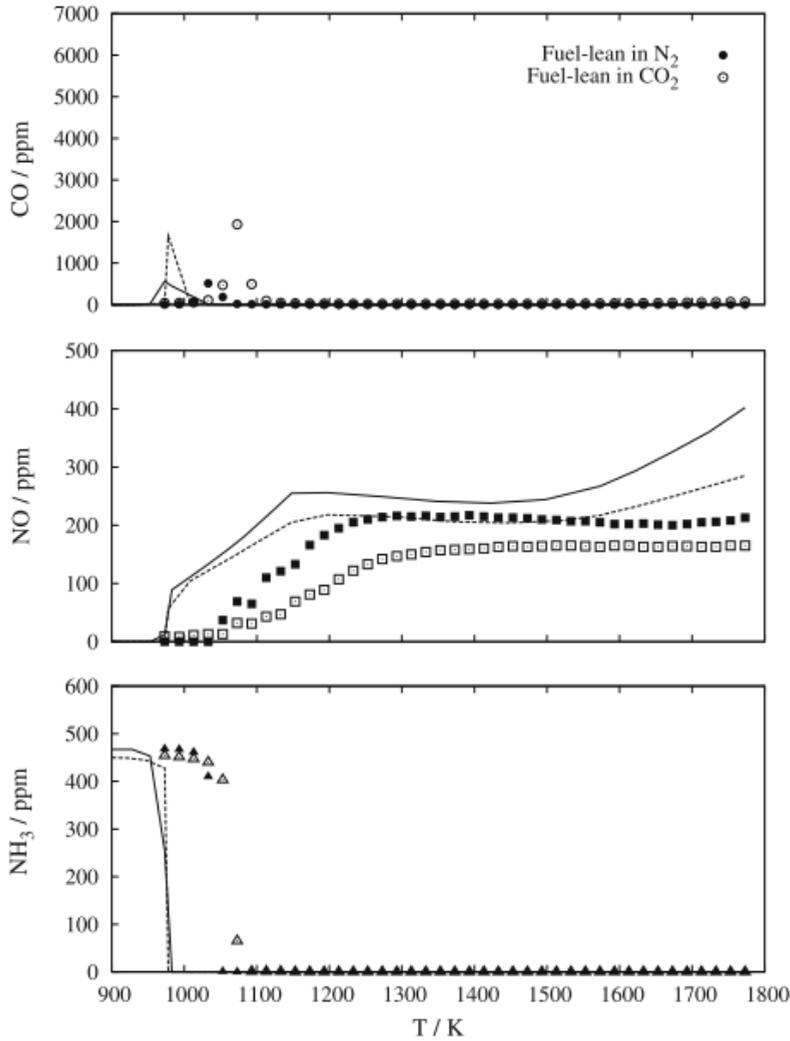
Figure 2.8: Model predictions compared with experimental data for oxidation of CH_4 in the presence of NH_3 in fuel-lean conditions as a function of temperature. The experimental data for N_2 and for CO_2 experiments are shown as closed and open symbols respectively. Conditions - N_2 experiments: CH_4=2508ppm, O_2=40062ppm, NH_3=468, N_2=95.69%, ϕ=0.13, Residence time=1296/T(K) - CO_2 experiments: CH_4=2512ppm, O_2=40133ppm, NH_3=450, N_2=5.59%, CO_2=90.10%, ϕ=0.13, Residence time=1296/T(K)

Figure 2.6 shows results comparing the proposed detailed chemical kinetic model with experimental data for fuel-rich conditions, Figure 2.7 shows results comparing the proposed detailed chemical kinetic model with experimental data for stoichiometric conditions, while Figure 2.8 shows results comparing the proposed detailed chemical

kinetic model with experimental data for fuel-lean conditions.

The presence of CO$_2$ seems to enhance the NH$_3$ consumption rate under fuel-rich and stoichiometric conditions. It is indicated that the presence of high levels of CO$_2$ enhances the formation of NO under reducing conditions, while it inhibits the NO formation under stoichiometric and fuel-lean conditions [36].

The essential features of the nitrogen chemistry is captured by the model developed by Mendiara and Glarborg. At fuel-lean conditions the model, however, predicts an increase in NO concentration at temperature above 1600K, which does not coincide with the experimental results.

2.1.3 Mechanism proposed by Skreiberg et al.

In the study by Skreiberg et al. the oxidation of NH$_3$, the most important NO$_x$ precursor during waste combustion on a grate [38] as shown is section 5, was studied under fuel-rich conditions and moderate temperatures [38]. A detailed chemical kinetic model for oxidation of NH$_3$ in the presence of H$_2$, CO and CH$_4$ was developed. The mechanism draws on previous studies on NH$_3$ oxidations performed by Miller and Bowman[13], Dean and Bozzelli [47] and Coda Zabetta et al.[48], selective non-catalytic reduction of NO by NH$_3$ presented by Glarborg et al.[49] and Miller and Glarborg[50] and hydrocarbon-nitroc oxide interactions presented by Glarborg et al.[43].

The developed mechanism was validated against experimental data presented by Hasegawa and Sata [51] on NH$_3$ conversion in a flow reactor under conditions ranging from slightly lean to very fuel-rich. Their experiments covered the fuels hydrogen (0 to 80 vol%), carbon monoxide (0 to 95 vol%), and methane (0 to 1.5 vol%)under temperatures ranging from 300 to 1330 K, and NO levels ranging from 0 to 2500 ppm.

The effect of temperature on the NH$_3$ and NO concentrations during oxidation of a fuel-rich gas mixture containing 1000ppm NO, 1000ppm NH$_3$, 5000ppm O$_2$, 25% CO and 9.1% H$_2$ was studied by Hasegawa and Sata [51] and compared with prediction using the mechanism proposed by Skreiberg et al.[38]. The comparison between experimental data and modelling prediction are shown in Figure 2.9.
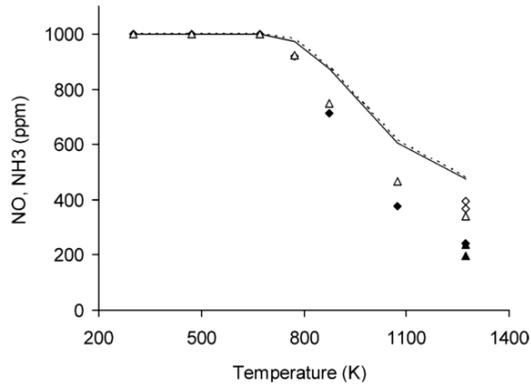
Figure 2.9: Predicted NO and NH_3 concentrations as a function of temperature determined by the detailed chemical kinetic model by Skreiberg et al. [38] compared with experimental data presented by Hasegawa and Sata [51]. NH_3 concentrations are shown as open symbols (experimental data) and dashed lines (predicted). NO concentrations are shown as closed symbols (experimental data) and solid lines (predicted). Inlet concentrations: 1000ppm NO, 1000ppm NH_3, 5000ppm O_2, 25% CO, 9.1% H_2 and N_2 balance. The residence time was ranging from about 1s to about 4s depending on the temperature.

The conversion of NH_3 and NO is initiated at around 700K and the conversion of NH_3 and NO increases with temperature. The model accurately predicts the temperature for onset of reaction. The degree of conversion is, however, not captured accurately as the model predicts a lower degree of conversion of NH_3 and NO. Furthermore, the model does not describe the increased consumption rate of NO compared to the consumption rate of NH_3 accurately.

In Figure 2.10 the effect of O_2 concentration on the NH_3 and NO concentrations during oxidation of a fuel-rich gas mixture containing 1000ppm NO, 1000ppm NH_3, 25% CO and 9.1% H_2 at 1273K was studied by Hasegawa and Sata [51] and compared with predictions using the mechanism proposed by Skreiberg et al.[38].
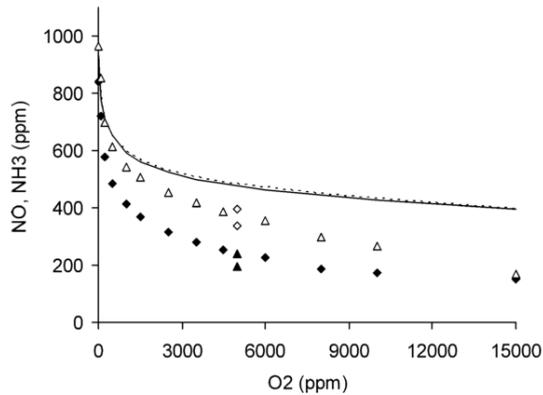
Figure 2.10: Predicted NO and NH$_3$ concentrations as a function of oxygen level at 1273K determined by the detailed chemical kinetic model by Skreiberg et al. [38] compared with experimental data presented by Hasegawa and Sata [51]. NH$_3$ concentrations are shown as open symbols (experimental data) and dashed lines (predicted). NO concentrations are shown as closed symbols (experimental data) and solid lines (predicted). Inlet concentrations: 1000ppm NO, 1000ppm NH$_3$, 25% CO, 9.1% H$_2$ and N$_2$ balance.

Both the model and the reported data shows an increase in the NH$_3$ and NO conversion with increasing O$_2$ concentrations. Similarly to the conversion of NH$_3$ and NO with increasing temperature, the model underpredicts the degree of conversion for NH$_3$ and NO with increasing O$_2$ concentrations, most pronounced for NO.

The effect of CO concentration on the oxidation and reduction of NH$_3$ and NO during oxidation of a fuel-rich NO, NH$_3$ and H$_2$ gas mixture at 1273K was studied by Hasegawa and Sata [51] and compared with predictions using the mechanism by Skreiberg et al.[38] in Figure 2.11.
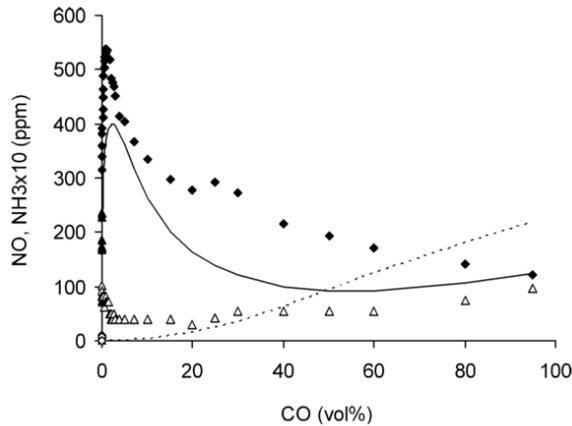
Figure 2.11: Predicted NO and NH$_3$ concentrations as a function of the CO concentration at 1273K determined by the detailed chemical kinetic model by Skreiberg et al. [38] compared with experimental data presented by Hasegawa and Sata [51]. NH$_3$ concentrations are shown as open symbols (experimental data) and dashed lines (predicted). NO concentrations are shown as closed symbols (experimental data) and solid lines (predicted). Inlet concentrations: 1000ppm NO, 1000ppm NH$_3$, 5000ppm O$_2$ and N$_2$ balance.

The trends of the the experimental data are well described by the model, the absolute value of the NO concentration is, however, underpredicted.
As seen in Figure 2.11 a high conversion of NO is achieved at low CO levels. With increasing CO concentrations the conversion of NO decreases due to the increased production of chain carriers caused by CO[38]. The conditions in Figure 2.11 corresponds to conditions during NO$_x$ reduction using NH$_3$[38].

The mechanism by Skreiberg et al.[38] describes the trends in the NH$_3$ oxidation and NO reductions chemistry well. However, the absolute values of the NH$_3$ and NO concentrations are not predicted accurately[38] by the mechanism by Skreiberg et al..

2.1.4 Mechanism proposed by Glarborg et al.

The newly developed detailed chemical kinetic model by Glarborg et al., consisting of 150 species and 1389 reactions, has been developed based on the work on nitrogen chemistry reported over the last 40 years [10]. The recent advances in the knowledge of thermochemistry and the reaction rates from theoretical work has been taken into account. The most important subsets of the mechanism has been validated against experimental data [10].
The most important reactions in the mechanism have been determined from studies on the chemistry of C$_1$-C$_2$ hydrocarbons [52][53], amines [54], cyanides [31] and hydrocarbon-nitrogen interactions [43][36][55]. Parts of the mechanism that date back to the 1980's as part of the previously discussed mechanism by Miller and Bowman are used[10][13]

The thermal NO modelling capability of the detailed chemical kinetic model by Glarborg et al. has been compared with selected experimental data by Homer and Sutton [56] in Figure 2.12.
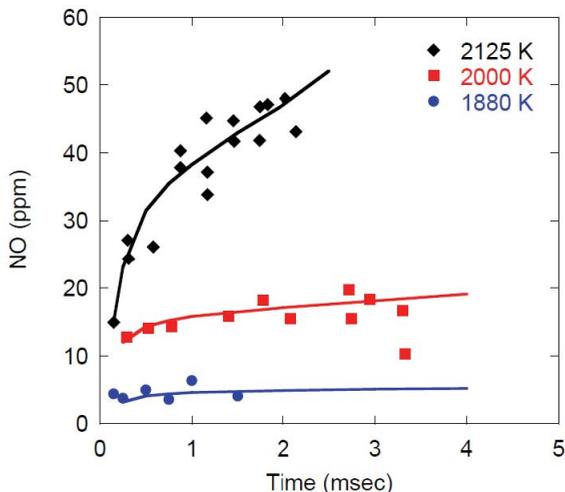
Figure 2.12: Comparison between measured NO profiles and predicted NO profiles in the post-flame zone of an atmospheric pressure H$_2$-O$_2$-N$_2$ premixed laminar flame. The experimental data was reported by Homer and Sutton [56] and the predicted NO profiles were determined using the mechanism by Glarborg et al. [10]. Black line: T=2125K, Inlet composition= 25% H$_2$, 17.5% O$_2$, 57.5% N$_2$. Red line: T=2000K, Inlet composition= 23% H$_2$, 16.1% O$_2$, 60.9% N$_2$. Blue line: T=1880K, Inlet composition= 21.1% H$_2$, 14.7% O$_2$, 64.2% N$_2$.

The measurements of NO concentration profiles in ambient pressure premixed hydrogen-oxygen-nitrogen flames reported by Homer and Sutton were conducted over a range of temperatures and stoichiometries as seen in Figure 2.12.The agreement between the measured NO profiles and the predictions using the mechanism are good for the three chosen temperatures and stoichiometries.

The capability of the mechanism to accurately predict the prompt NO formation was accessed by comparison between reported measurements and predicted NO mole fractions in Figure 2.13.
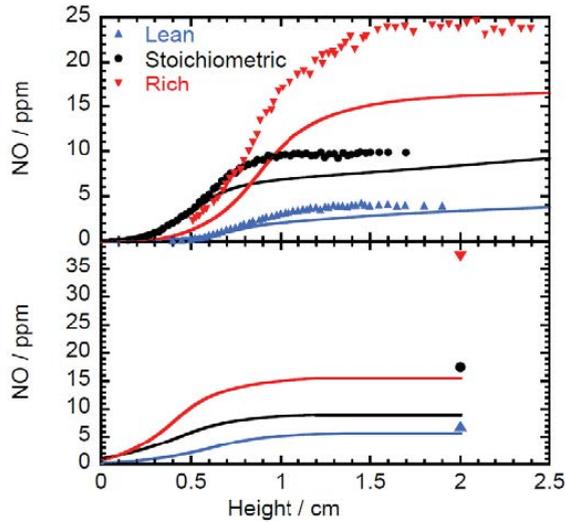
Figure 2.13: Comparison between measured NO mole fractions [57][58][59][60] and predicted NO mole fractions in low-pressure premixed methane-air-nitrogen flames. The experimental data is denoted by symbols, while the lines denote modelling predictions using the mechanism by Glarborg et al. [10]. The conditions at which the measurements by Lamoureux et al. [57][58][59] were performed (top picture) - Red symbols: ϕ=1.25, T_{max}=1845K - Black symbols: ϕ=1, T_{max}=1875K - Blue symbols: ϕ=0.8, T_{max}=1825K, P=40torr. The conditions at which the measurements by Berg et al. [60]were performed (bottom picture) - Red symbols: ϕ=1.28, T_{max}=1980K, P=30torr - Black symbols: ϕ=1.07, T_{max}=1920K, P=25torr - Blue symbols: ϕ=0.81, T_{max}=1750K, P=25torr

As seen from the 6 comparisons between data and model predictions in Figure 2.13 model predictions are quite accurate under slightly lean conditions. A slight under-prediction of the prompt NO formation is achieved at stoichiometric conditions, while the largest discrepancy is seen under fuel-rich conditions, the calculated prompt NO is about a factor of two below the measured [10].

The formation of NO is largely controlled by the oxidation of NH_3 released from the fuel [1] due to the relative low temperature of the combustion and the speciation of the NO_x precursors released from the bed, see Figure 5.10. The detailed chemical kinetic model by Glarborg et al. has been compared with experimental data reported by Mendiara and Glarborg [36] as shown in Figure 2.14.
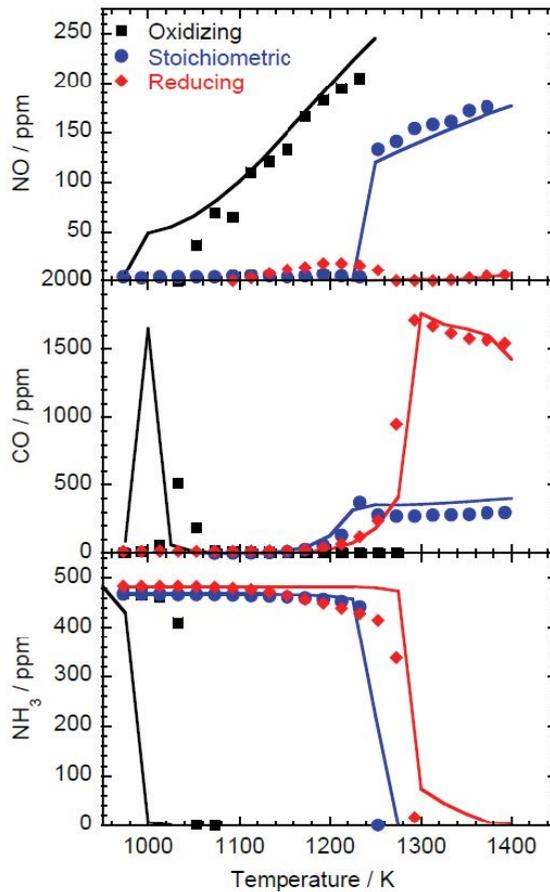
Figure 2.14: Comparison between measured NO concentrations [36] and predicted NO concentrations from oxidation of a mixture of CH$_4$ and NH$_3$ as a function of the stoichiometry and temperature. The experiments were conducted in a 12mm inner diameter alumina reactor at P=1.05atm and with a residence time τ=1295/T(K) in the isothermal zone. The symbols denote the experimental data and the solid lines denote the modelling predictions. The inlet concentrations are; Reducing: λ=0.645, CH$_4$=2508ppm, O$_2$=3480ppm, NH$_3$=484ppm, N$_2$=balancing - Stoichiometric: λ=0.935, CH$_4$=2513ppm, O$_2$=5040ppm, NH$_3$=468ppm, N$_2$=balancing - Oxidizing: λ=7.69, CH$_4$=2515ppm, O$_2$=40100ppm, NH$_3$=468ppm, N$_2$=balancing.

The capability of the mechanism to describe the formation of fuel-NO has been examined in Figure 2.14. The comparison has been made for oxidation of CH$_4$ doped with NH$_3$ as a function of the stoichiometry and temperature, as these conditions are more representative for a practical combustion system [10]. The fuel-NO formation under reducing conditions is negligible for the entire temperature interval as the rate of NH$_3$ consumption is slow until all CH$_4$ is converted to CO [10]. For stoichiometric condi-

tions the fuel-NO formation is accurately described by the mechanism with fuel-NO formed at temperatures above approximately 1250K. For oxidizing conditions the fuel-NO is formed at temperatures as low as 1050K. The mechanism accurately describes this formation.

The mechanism slightly underpredicts the onset temperature of NH$_3$ oxidation at oxidising conditions.

The general agreement between experimental data and model predictions using the detailed chemical kinetic model by Glarborg et al. is good as seen in Figure 2.12, 2.13 and 2.14. Not only does the mechanism describe the trends well, but the absolute values of the NO and NH$_3$ concentrations are accurately predicted for the specific conditions.

2.1.5 Evolution of the reviewed detailed chemical kinetic models

In this section numerous detailed chemical kinetic models were presented. All the models draws on previous studies by Miller and Bowman [13] or on models developed on the basis of this. The most recent of the presented models models is the model by Glarborg et al.[10]. For skeletal model development the model by Glarborg et al.[10] was used as it is the most recent model.

2.2 Simplified models for NO$_x$ formation

For the purpose of simulating chemistry in CFD reduced kinetics are of interest. Use of reduced kinetic models decreases the computational expenses compared to using detailed kinetic models. This is especially important when the CFD simulations are being used industrially, due to the limited amount of time available.
In the literature numerous simplified models have been proposed. Three different types of models have been developed; one type involves a systematic reduction of a detailed kinetic model (skeletal model), a second which applies steady state and partial equilibrium approximations to further reduce models and a third type uses experimentally derived empirical expressions (global models)[61]. The empirical models have been derived under certain conditions which make them unreliable under conditions not similar to the conditions at which they were developed. Extrapolation of these models needs to be done with care [61]. The systematically reduced models, if reduced properly, should be valid over the entire range of conditions, as these models are based on detailed kinetic models.

2.2.1 Skeletal models

A skeletal model is a systematically reduced model; a reduction of a detailed chemical kinetic model, where only the main reaction paths are included [61]. Redundant species and reactions are eliminated by different algorithms; see chapter 3. Hence, a skeletal model consists of elementary reactions, whereas a global model, introduced in the next section, consists of global reactions.The fundamental mechanistic step of the detailed chemical kinetic model are retained in the skeletal model. An overview of different reduction algorithms are presented in chapter 3.

Skeletal model by Houshfar et al.

Houshfar identified a detailed chemical kinetic model; the detailed chemical kinetic model developed by Mendiara and Glarborg [36] consisting of 81 species and 730 elementary reactions, for reduction.

Houshfar et al. reduced the detailed chemical kinetic model proposed by Mendiara and Glarborg[36] thereby developing three skeletal models with varying size using the DARS[62] chemical reaction system analysis tool; a slightly reduced model consisting of 52 species and 430 reactions, a medium reduced model consisting of 35 species and 198 reaction and a highly reduced model consisting of 26 species and 91 reactions. The models are applicable for low-, medium-, and high temperature ranges respectively.

The highly reduced skeletal mechanism performs well at high temperatures, while predictions of the NO$_x$ formation at medium and low temperatures (T≤ 1150°C) are not consistent with predictions using the detailed chemical kinetic model as seen in Figure 2.15.
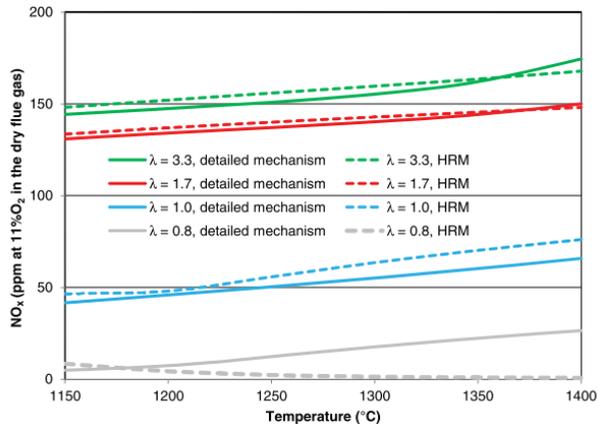
Figure 2.15: Predictions of the NO$_x$ emission in ppm using the highly reduced model consisting of 26 species and 91 reactions compared with predictions using the detailed chemical kinetic model as a function of time [62] (Corrected to 11% O$_2$ in the dry flue gas. τ=1s)

It is believed that the highly reduced model will deviate even more than the medium reduced model at lower temperatures, see Figure 2.16.
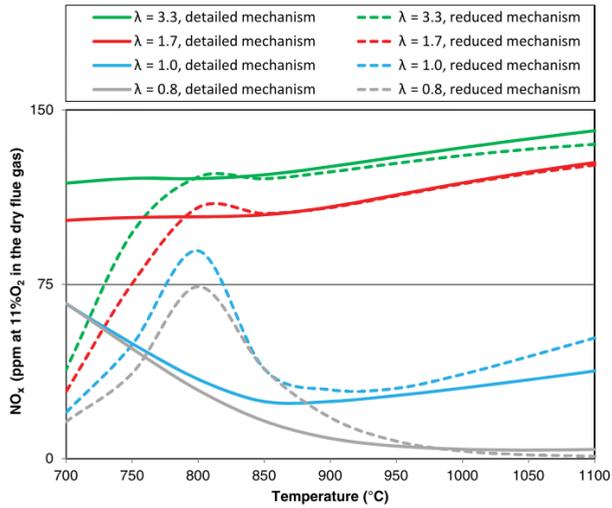
Figure 2.16: Predictions of the NO$_x$ emission in ppm using the medium reduced model consisting of 35 species and 198 reactions compared with predictions using the detailed chemical kinetic model as a function of time [62] (Corrected to 11% O$_2$ in the dry flue gas. τ=1s)

The predictions of the NO$_x$ emission using the medium reduced model at higher temperatures (T $\geq$ 950°C) is reasonable for the four different levels of excess air. At low temperatures (T $\leq$ 950°C) the predictions of the NO$_x$ emission using the medium reduced skeletal mechanism differs from predictions using the detailed chemical kinetic model. At low temperatures and reducing conditions ($\lambda < 1$) the predictions from the medium reduced model and the detailed chemical kinetic model contradict.

The slightly reduced model accurately predicts the formation of NO$_x$ as seen in Figure 2.17.
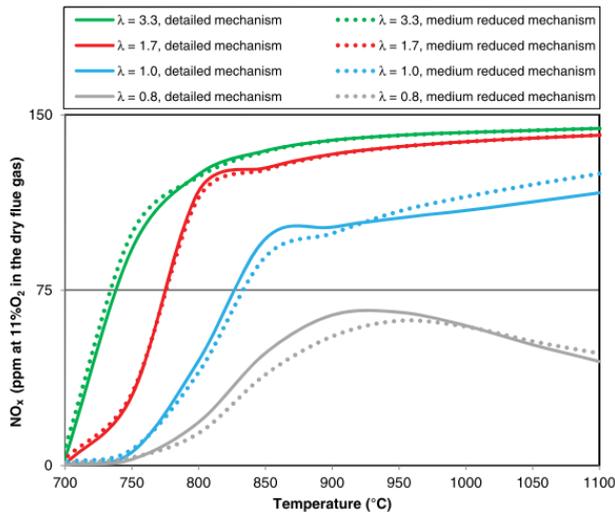
Figure 2.17: Predictions of the NO$_x$ emission in ppm using the highly reduced model consisting of 52 species and 430 reactions compared with predictions using the detailed chemical kinetic model as a function of time [62] (Corrected to 11% O$_2$ in the dry flue gas. τ=0.01s)

The models developed by Houshfar et al. predict the NO$_x$ emission reasonably accurate at high temperatures and oxidising conditions. At lower temperatures and reducing conditions the predictions using the models, except the slightly reduced skeletal model, differ from the NO$_x$ predictions by the detailed chemical kinetic model used for comparison.

2.2.2 Analytically reduced models

A common approach of model reduction involves a two-stage procedure. First, a skeletal mechanism is developed by removing all redundant species and reactions using a suggested reduction algorithm. Second, the skeletal mechanism is further reduced by order of magnitude approximations, resulting in the analytically reduced mechanism. These approximations could be steady state approximation or partial equilibrium approximation.

Model proposed by Pedersen et al.

Pedersen et al. reduced the detailed chemical kinetic model developed by Glarborg et al. [35] that consists of 184 elementary reaction, where 144 reactions constitute to the nitrogen chemistry[61]. The reduction was done through a well-established reduction method which has been used for a number of other systems e.g. Glarborg et al.[63]. The reduction was done in 7 steps summarized as:

- 1. Determination of the main reaction path

- 2. Elimination of redundant species

- 3. Elimination of redundant reactions

- 4. Identification of irreversible reactions

- 5. Elimination of non-selective irreversible reaction channels

- 6. Identification of species in steady state

- 7. Identification of reactions in partial equilibrium

Special emphasis was put on minimising the number of species rather than minimising the number of reactions[61].

The model was developed for coal combustion; consequently the main NO$_x$ precursor to be oxidised is HCN. For biomass combustion the main NO$_x$ precursor is NH$_3$[32]. The reduction was done by elimination of reaction channels contributing with less than 10% to the oxidation of HCN. This reduced the number of species by 10% while reducing the number of reactions by 67 reactions[61]. Further reductions were performed until a model consisting of 19 species, 11 nitrogen species and 37 reactions was achieved. Of the 11 nitrogen species 7 species were assumed in steady state. These species are CN, HOCN, HNCO, NCO, NH$_2$ and N. The 4 remaining species are the active ones; these are HCN, NH$_3$, NO and N$_2$ [61]. The resulting reduced model is schematically represented in Figure 2.18.
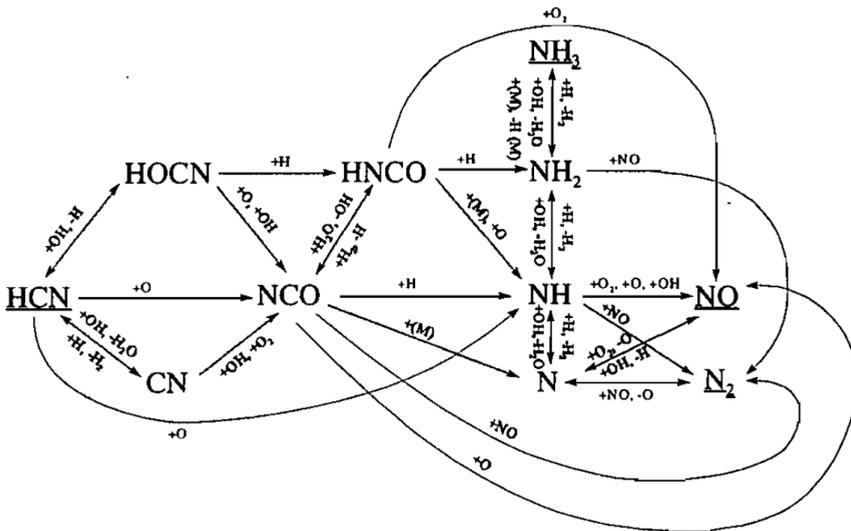
Figure 2.18: Reaction diagram for the reduced HCN oxidation model proposed by Pedersen et al.[61]. The underlined species are <u>not</u> in steady-state [61]

The proposed models were verified by PFA and CSTR simulations under conditions typical of pulverised coal combustion using the developed models and the detailed chemical kinetic model from which they were developed. Three different cases were simulated for validation of the proposed HCN model.

- The reduced HCN model coupled with a proposed CO/H$_2$ model. In the Figure 2.19, 2.20, 2.21 and 2.22 this approach is denoted "reduced".

- The HCN model is decoupled from the CO/H$_2$ model. In the Figure 2.19, 2.20, 2.21 and 2.22 this approach is denoted "decoupled".

- A 3 step CO/H$_2$ model is used with decoupling of the HCN chemistry. In the Figure 2.19, 2.20, 2.21 and 2.22 this approach is denoted "3 step".

Each case is compared with the detailed chemical kinetic model proposed by Glarborg et al [63]. In Figure 2.19 and 2.20 the HCN oxidation model is compared with the detailed chemical kinetic model at varying oxygen concentrations. The simulations have been performed in both a CSTR and a PFR.
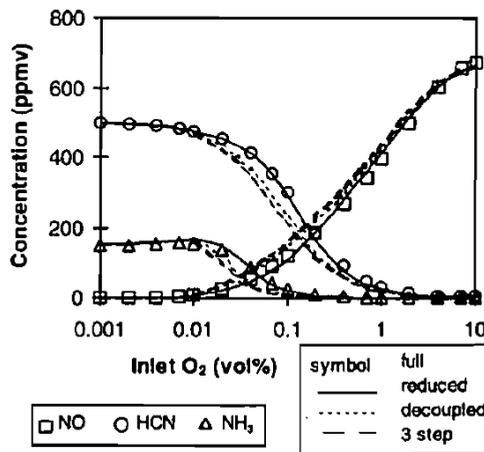
Figure 2.19: CSTR simulation of HCN oxidation models [61]. (T=1900K, τ =3ms, [CO]=[H$_2$]=[H$_2$O]=4vol%, [CO$_2$]=6vol%, [HCN]=500ppmv, [NH$_3$]=150ppmv)[61]
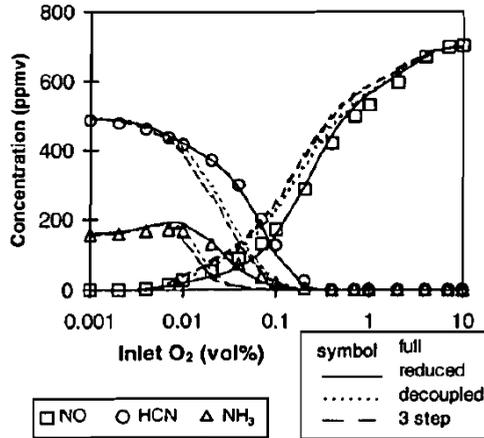
Figure 2.20: PFR simulation of HCN oxidation models [61]. (T=1900K, τ =3ms, [CO]=[H$_2$]=[H$_2$O]=4vol%, [CO$_2$]=6vol%, [HCN]=500ppmv, [NH$_3$]=150ppmv)[61]

The model by Pedersen et al. agrees very well with the detailed chemical kinetic model proposed by Glarborg et al. [35]. However, when the model is decoupled from the CO/H$_2$ chemistry a slightly higher conversion of HCN and NH$_3$ is experienced. The higher conversion experienced, when using the decoupled models, is a consequence of chain terminating HCN oxidation at these particular conditions employed[61].

It was shown that for the decoupled models at inlet O$_2$ concentrations in the range of 0.01-1 vol% the hydrogen radical concentration is significantly higher than for the detailed chemical kinetic model [61]. Only minor differences are experienced in the CO and H$_2$ concentrations between the decoupled models and the detailed chemical kinetic model [61].

For further evaluation of the reduced model the temperature was varied at constant oxygen levels. The result from this is shown in Figure 2.21 and 2.22.
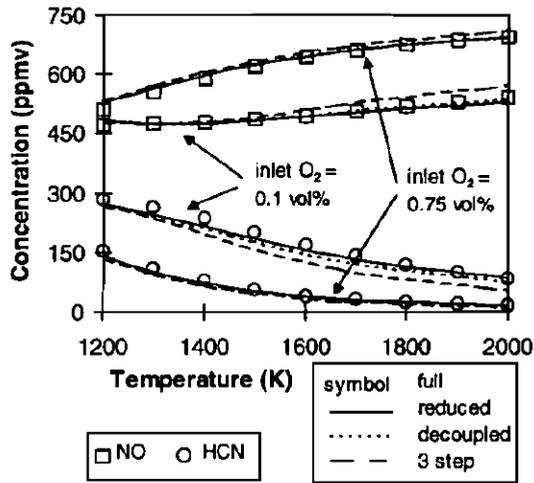
Figure 2.21: CSTR simulation of HCN oxidation models [61]. (τ =2ms, [CO]=1vol%, [H$_2$]=0.5vol%, [H$_2$O]=6vol%, [CO$_2$]=10vol%, [HCN]=300ppmv, [NO]=500ppmv)
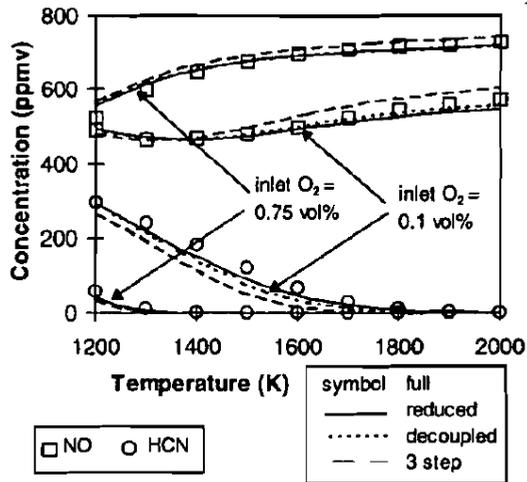
Figure 2.22: PFR simulation of HCN oxidation models [61]. (τ =2ms, [CO]=1vol%, [H$_2$]=0.5vol%, [H$_2$O]=6vol%, [CO$_2$]=10vol%, [HCN]=300ppmv, [NO]=500ppmv)

The comparison between the reduced model and the detailed chemical kinetic model has been done at two oxygen levels, 0.1 vol% and 0.75vol%. The result shows very good agreement between the reduced model and the detailed chemical kinetic model. This is the case for a temperature range between 1200K and 2000K, which is the range at which one would expect to see NO formation in a waste incineration plant; see section 5. The reduced model was furthermore compared with global models developed by Fenimore[11],

Wendt[64], Mitchell and Tarbell[65] and De Soete[14] in Figure 2.23.
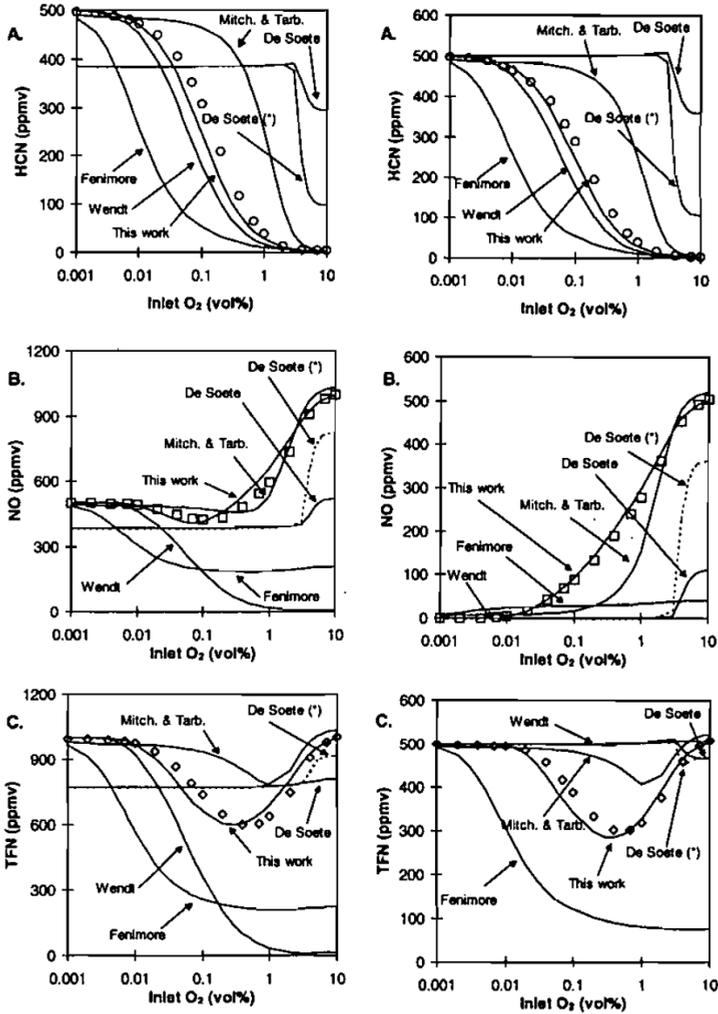
Figure 2.23: CSTR simulations of HCN oxidation. The conditions are; T=1800K, τ = 5ms. [CO]=[H$_2$]=4vol%, [CO$_2$]=[H$_2$O]=6vol%, [HCN]=[NO]=500ppmv. TFN denotes the total fixed nitrogen, while the symbols denote the DCKM

The simulations have been performed in a CSTR with varying oxygen concentrations. The deviation between the reduced model and detailed chemical kinetic model, denoted by symbols, are minor and for the given conditions a good accuracy of the skeleton model is achieved. The global model, on the contrary, performs poorly. None of the models describes the system to a reasonable degree.

In Table 2.1 the condition under which the model proposed by Pedersen et al.[61] has been evaluated is shown.

Table 2.1: Conditions under which the model proposed by L. S. Pedersen et al. has been evaluated

Temp. (K)	Oxygen level	Other matters
1900	0.001-10 vol%	CSTR sim., τ =3ms, [CO]=[H$_2$]=[H$_2$O]=4vol%, [CO$_2$]=6vol%, [HCN]=500ppmv, [NH$_3$]=150ppmv
1900	0.001-10 vol%	PFR sim., τ =3ms, [CO]=[H$_2$]=[H$_2$O]=4vol%, [CO$_2$]=6vol%, [HCN]=500ppmv, [NH$_3$]=150ppmv
1200-2000	0.1 and 0.75vol%	CSTR sim., τ =2ms, [CO]=1vol%, [H$_2$]=0.5vol%, [H$_2$O]=6vol%, [CO$_2$]=10vol%, [HCN]=300ppmv, [NO]=500ppmv
1200-2000	0.1 and 0.75vol%	PFR sim., τ =2ms, [CO]=1vol%, [H$_2$]=0.5vol%, [H$_2$O]=6vol%, [CO$_2$]=10vol%, [HCN]=300ppmv, [NO]=500ppmv
1800	0.001-10 vol%	CSTR sim., T=1800K, τ = 5ms$v$. [CO]=[H$_2$]=4vol%, [CO$_2$]=[H$_2$O]=6vol%, [HCN]=[NO]=500ppmv
[32] 1400	λ =0.8, 1 and 1.5	Isothermal plug flow conditions, [HCN]=1000ppm
[32] 1800	λ =0.8, 1 and 1.5	Isothermal plug flow conditions, [HCN]=1000ppm

[3.5mm]

Further reduction of the analytically reduced model by Pedersen et al.

Hansen and Glarborg [32] used the analytically reduced N-scheme by Pedersen et al.[61] as starting point for a further reduction. The objective of the work done by Hansen and Glarborg was to develop a simple approach to estimate the radical concentrations and combine this with the skeletal model by Pedersen et al.[32]. The radical estimation tool developed by Hansen and Glarborg has been developed for combustion of devolatilisation gas compositions typical for solid fuels ranging from bituminous coal to biomass [32].

Pedersen et al. determined correlations for the OH and O concentrations during a combustion of CO/H$_2$. It was shown that these concentrations can be determined from concentrations of H and major species H$_2$, O$_2$ and H$_2$O [32]. The three major species are also part of the NO formation scheme produced by Pedersen et al. The main purpose of the work done by Hansen and Glarborg was to determine the H radical concentration from the major species, H$_2$, O$_2$ and H$_2$O, along with temperature and stoichiometry; the correlation needs to apply under the following conditions:

- Oxidation of four different solid fuels; bituminous coal, sub-bituminous coal, lignite and poplar wood

- Temperature in the range from 1200 to 2000K

- Excess air ratio in the range from λ=0.6 to λ=2.0

- Oxygen in the oxidizer stream in the range from 1 to 21vol%

- Integration in time; this is possibly also used by ANSYS Fluent to describe chemistry in the fine structure (EDC)[32]

The combustion can be split into two parts; an initial radical build up period (induction period) followed by consumption of the radical as the fuel is being consumed. In the study by Hansen and Glarborg it was found difficult to describe both of these periods with only one correlation. For this reason separate description of the radical concentration was developed; one for the radical build-up and one for the radical consumption Pedersen et al.[61] proposed an expression for formation of H_2O and H from H_2 and O_2. A similar relationship was used by Hansen and Glarborg. They found that the H radical concentration in the radical build-up period could be described reasonably well by equation 2.2

$$[H] = Q_1 \cdot \frac{[H_2O] - [H_2O]_{in}}{[H_2]} \qquad (2.2)$$

The relation equation 2.2, is valid for combustion of fuel where H_2 is released in significant quantities, such as biomass. The inlet water vapour concentration is included in order to account for no radical H before radical build-up [32]. The constant Q_1 is depended on the process conditions. It was found, through simulations in CHEMKIN, that the parameter Q_1 can be determined from equation 2.3.

$$Q_1 = (\alpha(T) \cdot \lambda^{\beta(T)} \cdot \sqrt{[O_2]_{in}} \qquad (2.3)$$

α and β are described by second order polynomials dependent on the temperature.
The H radical concentration during radical consumption has been developed on the basis of a three step mechanism proposed by Pedersen et al.[61].

$$CO + H_2O \rightleftharpoons CO_2 + H_2$$
$$H + H + M \rightleftharpoons H_2 + M \qquad (2.4)$$
$$3H_2 + O_2 \rightleftharpoons 2H + 2H_2O$$
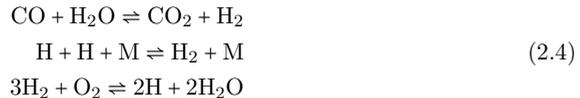
It is assumed that the reactions are irreversible and [H] is in quasi-steady state. The following expression, 2.5 for the H radical concentration was obtained by Hansen and Glarborg.

$$[H] = \sqrt{\frac{k_{2.4,3}[H_2]^3[O_2]}{k_{2.4,2}[M]}} \qquad (2.5)$$

The rate constants are obtained from the work of Pedersen et al.[61]. These are, however, replaced by a parameter Q_2 in equation 2.6 in order to obtain a better description of the H radical concentration.

$$[H] = Q_2 \sqrt{\frac{[H_2]^3[O_2]}{[M]}} \qquad (2.6)$$

In equation 2.5 the total gas concentration [M] is calculated from the ideal gas equation [32]. The parameter Q_2 is found by employing expression 2.7.

$$Q_2 = \frac{\gamma(T) \cdot \lambda + \eta(T)}{[Q_2]_{in}} \qquad (2.7)$$

A satisfactory determination of the radical H concentration at a given time is found to be the minimum of the radical H concentration found from equation 2.2 and equation 2.6; the H radical concentration during radical build up phase and the H radical concentration during radical consumption phase respectively.

$$[H] = \min\Big([H]_{build-up}, [H]_{consumption}\Big) \qquad (2.8)$$

It was shown through simulations that at very fuel-rich conditions; $\lambda \leq 0.6$ and temperature below 1400K the expressions for Q_1 and Q_2 are less accurate, leading to less accurate predictions of the radical H and NO concentration [32].

As previously described, the OH and radical O concentrations are linked with the radical H concentration. These concentrations can be determined from partial equilibrium and steady-state considerations [32]. The OH concentration is linked with the H concentration through reaction 2.9.

$$OH + H_2 \rightleftharpoons H_2O + H \tag{2.9}$$
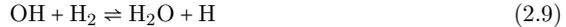
Reaction 2.9 is found to be close to partial equilibrium. The OH concentration can therefore be determined from equation 2.10.

$$[OH] = \frac{[H][H_2O]}{K_{2.9}[H_2]} \tag{2.10}$$

Where the rate constant has been determined to $K_{2.9} = (1.424 \cdot 10^{-2})T^{0.3301}\exp(8052/T)$. The radical O concentration was determined from 4 reactions.

$$
\begin{aligned}
O + OH &\rightleftharpoons H + O_2 \\
O + H_2 &\rightleftharpoons OH + H \\
OH + OH &\rightleftharpoons H_2O + O \\
H + O + M &\rightleftharpoons OH + M
\end{aligned}
\tag{2.11}
$$

Through partial equilibrium assumptions the O concentration can be determined by 2.12

$$[O] = \frac{N_O}{D_O}$$

$$D_O = k_{2.11,1}[OH] + k_{2.11,2}[H_2] + (k_{2.11,3}/K_{2.11,3})[H_2O] + K_{2.11,4}[H][M] \tag{2.12}$$

$$
\begin{aligned}
N_O = (k_{2.11,1}/K_{2.11,1})[H][O_2] + (k_{2.11,2}/K_{2.11,2})[OH][H] \\
+ k_{2.11,3}[OH]^2 + (k_{2.11,4}/K_{2.11,4})[OH][M]
\end{aligned}
$$

The simplifications developed by Hansen and Glarborg[32] were compared with a detailed chemical kinetic model developed by Mendiara and Glarborg [36] and the skeletal mechanism by Pedersen et al.. PFR simulations were performed for evaluation purposes. In Figure 2.24 and 2.25 the model simplifications are evaluated for a case where NO is formed from HCN.
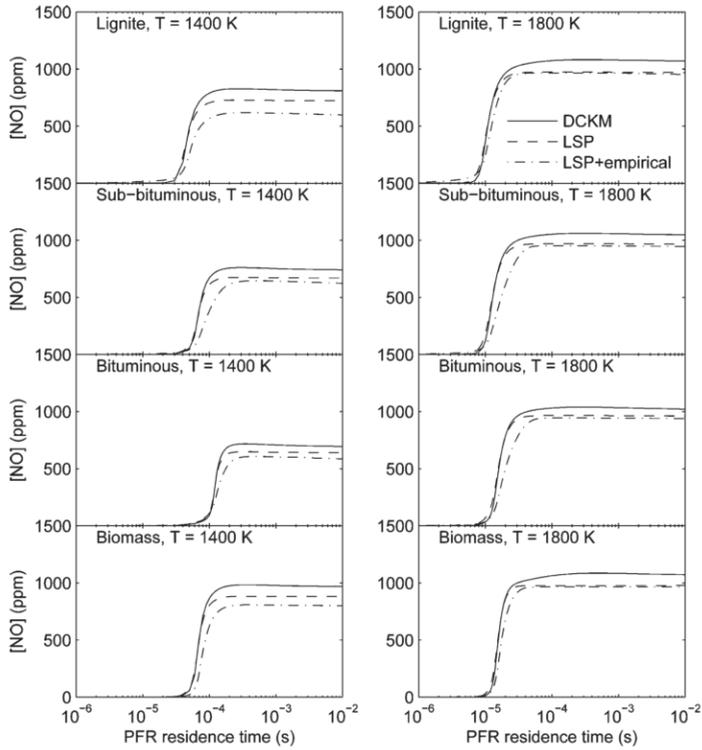
Figure 2.24: NO concentrations predicted by the skeletal mechanism by Pedersen et al. with modifications by Hansen and Glarborg, the skeletal mechanism by Pedersen et al. [61] and the detailed chemical kinetic model developed by Mendiara and Glarborg [36] during combustion of gaseous volatiles from different solid fuels with excess air of $\lambda = 0.8$ and temperatures of 1400K and 1800K. The nitrogen volatiles are represented as 1000ppm HCN. The calculations have been performed under isothermal conditions assuming plug-flow [32]. Input data for the simplified models; the major species, have been determined from the detailed chemical kinetic model. (——=DCKM,- - - =LSP model and - · - · - =LSP with modifications by Hansen and Glarborg)

Figure 2.25: NO concentrations predicted by the skeletal mechanism by Pedersen et al. with modifications by Hansen and Glarborg, the skeletal mechanism by Pedersen et al. [61] and the detailed chemical kinetic model developed by Mendiara and Glarborg [36] during combustion of gaseous volatiles from different solid fuels with excess air of $\lambda = 0.5$ and temperatures of 1400K and 1800K. The nitrogen volatiles are represented as 1000ppm HCN. The calculations have been performed under isothermal conditions assuming plug-flow [32]. Input data for the simplified models; the major species, have been determined from the detailed chemical kinetic model. (——=DCKM,- - - =LSP model and - · - · · - =LSP with modifications by Hansen and Glarborg)

From Figure 2.24, where the excess air is $\lambda = 0.8$, it is seen that the final level is generally well described. The difference in NO concentration between the model by Pedersen et al. with estimations of the radical pool concentration, the model by Pedersen et al. and the detailed chemical kinetic model is generally low for all fuels at both temperatures; within $\pm 30\%$ [32]. However, it is seen that the reduced models slightly underestimate the NO concentration for all cases. It is more pronounced at the lower temperature. The underestimation is enhanced when the radical pool concentration is estimated by the tools developed by Hansen and Glarborg.

From Figure 2.25 it is seen that the models predict the NO concentration quite accurately at 1800K, even under highly reducing conditions. However, for the lower temperature predictions of the NO concentration for bituminous coal and sub-bituminous coal by estimation of the radical pool concentration is highly overestimated. This might be due

to a higher ratio of hydrocarbons to hydrogen in the volatiles. Estimation of the radical pool is based on H$_2$/O$_2$ reactions. The high fractions of hydrocarbons causes a less precise prediction of the O/H radical pool [32]. The cause of the error is mainly due to errors in the estimation of the H radical concentration [32].

The same simulations have been performed for a case where NO is formed by NH$_3$. This is shown in Figure 2.26 and 2.27.
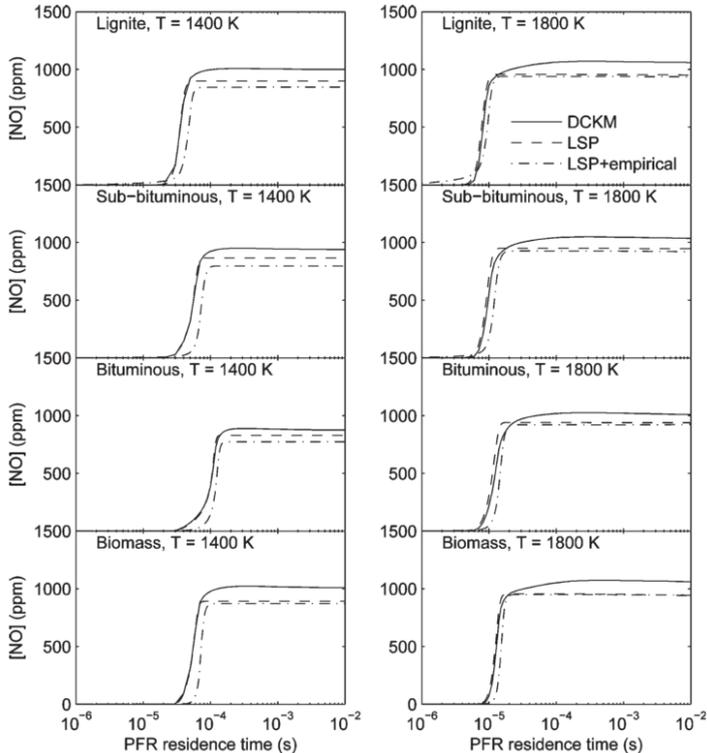
Figure 2.26: NO concentrations predicted by the model by Pedersen et al. with modifications by Hansen and Glarborg, the model by Pedersen et al. [61] and the detailed chemical kinetic model developed by Mendiara and Glarborg [36] during combustion of gaseous volatiles from different solid fuels with excess air of $\lambda = 0.8$ and temperatures of 1400K and 1800K. The nitrogen volatiles are represented as 1000ppm NH$_3$. The calculations have been performed under isothermal conditions assuming plug-flow [32]. Input data for the simplified models; the major species, have been determined from the detailed chemical kinetic model. (——=DCKM,- - - =LSP model and - · - · · - =LSP with modifications by Hansen and Glarborg)

49

Figure 2.27: NO concentrations predicted by the model by Pedersen et al. with modifications by Hansen and Glarborg, the model by Pedersen et al. [61] and the detailed chemical kinetic model developed by Mendiara and Glarborg [36] during combustion of gaseous volatiles from different solid fuels with excess air $\lambda = 0.5$ and temperatures of 1400K and 1800K. The nitrogen volatiles are represented as 1000ppm NH$_3$. The calculations have been performed under isothermal conditions assuming plug-flow [32]. Input data for the simplified models; the major species, have been determined from the detailed chemical kinetic model. (—=DCKM,- - - =LSP model and - · · · · - =LSP with modifications by Hansen and Glarborg)

Similarly to the NO predictions using HCN as NO$_x$ precursor, a similar conclusion of the prediction capability by the reduced skeletal model by Hansen and Glarborg was achieved for predictions using NH$_3$ as sole NO$_x$ precursor.
Simulations show that the predictions of the NO level from formation of NO from both HCN and NH$_3$, using the estimation tools developed by Hansen and Glarborg, are good in good agreement with the original skeletal mechanism for the specific conditions[32].

Model proposed by Glarborg et al.

Glarborg et al.[63] used the detailed chemical kinetic model proposed by Miller and coworkers as basis for a reduced nitrogen chemistry model. The detailed chemical kinetic model was reduced to a skeletal model by Peters and coworkers [66] [67] and Bilger et

al. [68] and further reduced by Glarborg et al.

It was identified by Glarborg et al. that the key to a good description of both the fuel oxidation and nitrogen chemistry process is the modelling of OH, O and CH$_3$ [63]. In this study the concentrations of the previously mentioned species are obtained through simplifying assumptions. The OH concentration is obtained from partial-equilibrium of reaction 2.13 according to equation 2.14.

$$OH + H_2 \rightleftharpoons H_2O + H \tag{2.13}$$
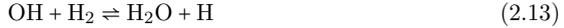
$$[OH] = k_{b2.13}[H_2O][H]/k_{f2.13}[H_2] \tag{2.14}$$

Where k_{fi} and k_{bi} are the forward and backward rate constants of reaction i.

It was shown that the partial-equilibrium approximation is a fairly good approximation for OH under most conditions. However, at low temperatures and fuel-rich conditions the assumption for OH is not accurate [63].

The concentration of O and CH$_3$ has previously been obtained in different ways by Paczko et al. [67] and Bilger et al. [68]. The simplification approaches used by Paczko et al. and Bilger et al. was shown to be limited to a narrow condition range. Glarborg et al. used a complex steady-state approximation for CH$_3$ (equation 2.15).

$$
\begin{aligned}
[O] &= (w_{f1} + w_{b2} + w_{f4})/(k_{b1}[OH] + k_{f2}[H_2] \\
&\quad + k_{b4}[H_2O] + k_{f1}[CH_4] \\
&\quad + k_{f16}[CH_3])
\end{aligned}
$$

$$
\begin{aligned}
[CH_3] &= (w_{f10} + w_{f11} + w_{f12})/(k_{b10}[H_2] \\
&\quad + k_{b12}[H_2O] + k_{f13}[H] + k_{f16}[O]) \\
&\quad + (k_{f18} + k_{f19})[OH])
\end{aligned}
\tag{2.15}
$$

Where w_{fi} and w_{bi} are the forward and backwards rate constants of reaction i respectively; i refers to the reaction number in the work done by Glarborg et al. [63].

For the nitrogen species steady-state balances for N, NH, NCO and CN was used to eliminate a number of reactions, consequently obtaining the following rate-of-production terms for HCN and NO:

$$
\begin{aligned}
w_{NO} &= -2w_{54} - 2w_{57} + w_{61} + w_{66} \\
&\quad + w_{67} - w_{68} - w_{69} - w_{70} \\
&\quad - w_{71} - w_{72} - w_{73} \\
&\quad - w_{74} - w_{77}
\end{aligned}
$$

$$
\begin{aligned}
w_{HCN} &= -w_{61} - w_{66} - w_{67} - w_{68} \\
&\quad + w_{69} + w_{70} + w_{71} + w_{72} \\
&\quad + w_{73} + w_{74} + w_{77}
\end{aligned}
\tag{2.16}
$$

The reduced model was evaluated by comparing PFR calculations for the reduced model with calculations using a detailed chemical kinetic model. Furthermore, the skeletal model, from which the reduced model is developed, has been compared with the reduced and detailed chemical kinetic model as well. The calculations were performed using the PSR-code from the CHEMKIN library [63]. The results from the comparison are shown in Figure 2.28.
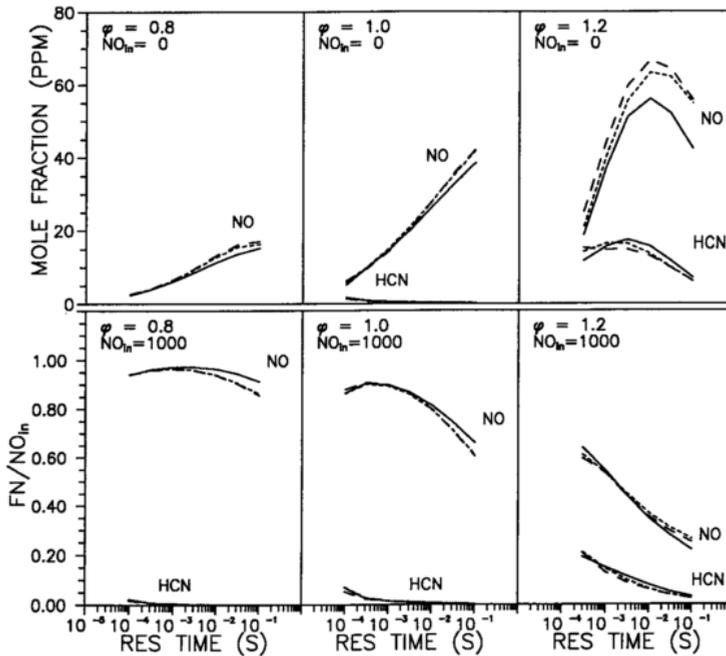
Figure 2.28: Predicted concentrations of NO and HCN for combustion of methane with and without NO addition. (T=1700 K, P=1 atm, ϕ=0.8, 1.0 and 1.2, —=DCKM, - - - =Skeletal mechanism, $\cdots$ =Reduced model)

It was shown that in the range of $0.7 \leq \phi \leq 1.4$ the model predicts the major species and the key radicals, such as O and CH$_3$, and the formation and destruction of NO very well; this is seen in Figure 2.28. However, for fuel-rich conditions ($\phi \geq 1.5$) the CH$_i$ radical concentrations are over-predicted due to neglection of the C$_2$ chemistry [63]. The model predicts the NO formation and destruction fairly good. However, at low temperature and under fuel-rich conditions the accuracy of the reduced model deteriorates due to the neglection of the C$_2$ chemistry.

2.2.3 Global models

The most simple models for chemistry representation are the global models. These models consist of global reactions, a transition between a set of reactants to a set of products not necessarily representing any mechanistic structure[34], consequently the global models do not necessarily represent the true nature of a reaction. The models are usually very limited in the number of species and reactions, hence the computational demand is dramatically lowered compared to detailed chemical kinetic model's or skeletal models. The most cited global schemes that have been developed include the schemes proposed by De Soete [14], Mitchell and Tarbell [65] and Brink et al. [69]. The De Soete global scheme is by default used in ANSYS Fluent to describe fuel NO$_x$ formation [15].

The De Soete global model

The De Soete model is based on the general global fuel NO$_x$ mechanism seen in Figure 2.29, describing the transformation of fuel bound nitrogen to gaseous NO$_x$ precursors followed by either oxidation or reduction of the precursor.

$$AZ \longrightarrow \cdot XN \underset{+NO}{\overset{+OX}{\longrightarrow}} \begin{matrix} NO \\ N_2 \end{matrix}$$
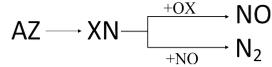
Figure 2.29: Overall mechanism by DeSoete (modified from [14]).

The primary nitrogen compound, the fuel nitrogen, has been denoted AZ and the nitrogen intermediate compounds, the NO$_x$ precursors, are denoted XN.

Through experiments where the operational conditions have been kept constant the De Soete model has been validated [14]. According to the De Soete model two competitive reactions are forming NO and N$_2$ trough intermediates; these are NH$_3$, HCN etc. The rate of formation of NO and N$_2$ through the intermediate XN$_i$, where XN$_i$ denotes one NO$_x$ precursor, is found from equation 2.17, 2.18 and 2.19:

$$V_{1,i} = k_{1,i} X_{AZ}^{e_i} X_{RH}^{f_i} \tag{2.17}$$

$$V_{2,i} = k_{2,i} X_{XN_i}^{g_i} X_{O_2}^{h_i} \tag{2.18}$$

$$V_{3,i} = k_{3,i} X_{XN}^{m_i} X_{NO}^{n_i} \tag{2.19}$$

where V$_{1,i}$, V$_{2,i}$ and V$_{3,i}$ denote the rate of production of the precursor, NO and N$_2$ respectively. X denotes the mole fraction of each species.
By summation, $\sum V_{2,i}$ and $\sum V_{3,i}$, the overall formation rate of NO and N$_2$ respectively can be found. The overall formation rate of NO and N$_2$ is reduced to expression 2.20 and 2.21.

$$V_A = k_A X_{AZ}^{a} X_{O_2}^{b} \tag{2.20}$$

$$V_B = k_B X_{AZ}^{c} X_{NO}^{d} \tag{2.21}$$

where k$_A$ and k$_B$ are the overall reaction rate constants for the formation of NO and N$_2$ respectively, while X_{AZ} is the mole fraction of the primary fuel nitrogen compound, the fuel nitrogen. It was shown that the reaction order in oxygen was 1 at low oxygen concentrations and 0 at high oxygen concentrations. The order of oxygen is denoted b in equation 2.20.

The above expressions 2.20 and 2.21 only describe the formation of Fuel NO$_x$ and N$_2$. Combined with the thermal NO$_x$; the Zeldovich mechanism, and overall NO$_x$ formation term can be set up.

$$\frac{dX_N O}{dt} = V_A - V_B + V_C - V_D \qquad \text{(NO formation rate)} \tag{2.22}$$

$$\frac{dX_N O}{dt} = -V_A + V_B - V_C + V_D \qquad \text{(N$_2$ formation rate)} \tag{2.23}$$

where V_C and V_D are the mean reaction rates of formation and decomposition of NO by the Zeldovich mechanism respectively[14].

Experiments from an ammonia/ethylene/oxygen/argon flame in the temperature interval of 1800K to 2400K give the following formation rates [14].

$$V_A = 4 \cdot 10^6 X_{NH_3} X_{O_2}^b \exp(-32000/RT) \quad (\text{sec}^{-1}) \tag{2.24}$$

$$V_B = 1.8 \cdot 10^6 X_{NH_3} X_{NO} \exp(-27000/RT) \quad (\text{sec}^{-1}) \tag{2.25}$$

The rate constants k_A and k_B are determined experimentally, consequently the value of these constants depend on the conditions where the experiments have been conducted. The validity of the De Soete model is limited to the conditions under which it was developed or conditions similar to these. Extrapolation beyond conditions of development should be done with care.

It has been shown that the De Soete model has severe shortcomings under fuel-rich conditions; see Figure 2.23. The main problem with the De Soete model is that NO is only formed when sufficient oxygen is available to make the oxidation faster than the reduction reaction [32]. Under fuel-rich conditions the NO yield is greatly underestimated.

The Mitchell and Tarbell global model

Mitchell and Tarbell used the same analogy as De Soete. It was experienced that the De Soete model failed to predict the strong temperature dependency on the two competing ammonia reactions 2.26 and 2.27, hence 2.29.

$$NH_3 + O_2 \rightarrow NO + H_2O + 1/2H_2 \tag{2.26}$$

$$NH_3 + NO \rightarrow N_2 + H_2O + 1/2H_2 \tag{2.27}$$
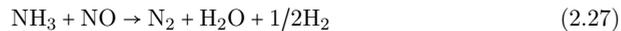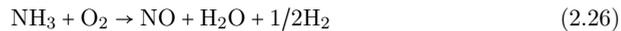
New rate parameters where therefore proposed. Selected kinetic data for NO$_x$ formation introduced by Mitchell and Tarbell is shown in Table 2.2

Table 2.2: Selected reactions in the reaction mechanism proposed by Mitchell and Tarbell [65]

Reaction	rate form	rate constant
2.26	$\frac{-k_6 y_{NH_3} y_{O_2}}{1+k_{den} y_{O_2}} \frac{T}{RT}$	$k_6 = 3.48 \cdot 10^{20} \exp(-100,000/RT)$
		$k_{den} = 6.90 \cdot 10^{-6} \exp(42,000/RT)$
2.27	$-k_7 y_{NH_3} y_{NO} \frac{T}{RT}$	$k_7 = 7.8 \cdot 10^{13} \exp(-75,500/RT)$

The rate constants for the reactions 2.26 and 2.27 have been fitted to experimental data for selective non-catalytic reduction process; these experiments were conducted in a temperature interval from 1100K to 1300K [69].
Furthermore Mitchell and Tarbell proposed that fuel nitrogen is converted into HCN which is subsequently converted into ammonia[65]

$$N_c(s) \rightarrow HCN \tag{2.28}$$

$$HCN + H_2O \rightarrow NH_3 + CO \tag{2.29}$$

Mitchell and Tarbell proposed a model consisting of 12 reactions in total, which include heterogeneous reactions for the description of char oxidation and reduction of NO by

heterogeneous reaction with char[65]. As can be seen in Figure 2.23 and 2.30 the global model by Mitchell and Tarbell has some shortcomings.

The global model by Mitchell and Tarbell has been specifically developed for coal combustion; it is assuming HCN as NO_x precursor. For application in waste combustion a model assuming NH_3 as NO_x precursor should be used; see section 5.

Global model proposed by Brink et al.

The global model developed by Brink et al. assumes that the mechanism is similar to the mechanism proposed by De Soete and Mitchell and Tarbell. This model, however, has been developed for biomass combustion, as it assumes the fuel bound nitrogen is released, during combustion, as NH_3. This assumption is supported by numerous studies where devolatilisation products from biomass have been measured. In these studies around 5% for the total amount of volatiles was released as HCN while 95% was released as NH_3[69]. Furthermore, as for the De Soete and Mitchell and Tarbell model, it is assumed that the gas from devolatilisation mainly consists of CO_2, CO, H_2O and H_2, meaning that all other hydrocarbons have been neglected [69]. These assumptions mean that only 2 reactions are needed to describe NO_x formation; these reactions are 2.26 and 2.27.

The difference between the De Soete and Mitchell and Tarbell model and the model proposed by Brink et al., other than neglecting the presence of other nitrogen intermediates than NH_3, is the different rate expressions. Through simulations of the NO_x level using a comprehensive model, the KILPINEN97[70], at temperature ranging from 900K to 1900K and oxygen levels ranging from 1% to 10% an empirical model was set up with rate expressions for the formation and degradation of NO_x as seen in 2.30 and 2.31 respectively.

$$r_1 = 1.21 \cdot 10^8 T^2 e^{-8000/T} [NH_3][O_2]^{0.5}[H_2]^{0.5} \tag{2.30}$$

$$r_2 = 8.73 \cdot 10^{17} T^{-1} e^{-8000/T} [NH_3][NO] \tag{2.31}$$

It was shown through an evaluation of the model developed by Brink et al. that this model underestimates the reaction between NH_3 and NO under fuel-rich conditions, while under fuel-lean conditions it is in better agreement with the comprehensive model as seen in Figure 2.30
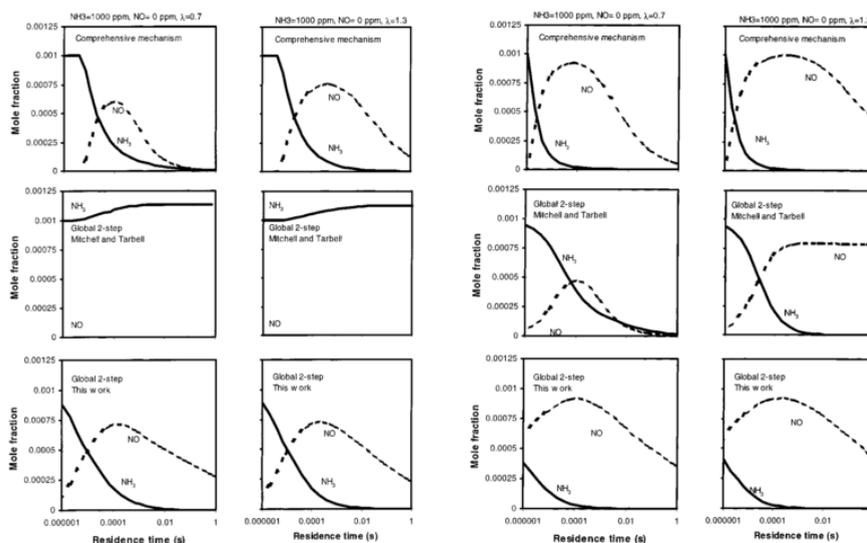
Figure 2.30: Comparison between the model developed by Brink et al., the global model by Mitchell and Tarbell [65] and the KILPINEN97 detailed chemical kinetic model. Oxidation of NH$_3$ occurs in a typical biomass pyrolysis gas containing 1000 ppm NH$_3$[69]. The 6 figures to the left show predictions at 1100K, while the 6 figures to the right show predictions at 1500K. The simulations were performed at λ=0.7 and λ=1.3

It was concluded through this study that the model proposed by Brink et al. performed better than the Mitchell and Tarbell model under reducing conditions, whereas the model performed worse under oxidising conditions. It was therefore concluded, similar to other studies, that empirical models are only valid under the conditions where they are developed, typically a limited region of operation.

Brouwer and Heap global model for Selective Non-Catalytic Reduction of NO$_x$

In order to describe the reduction of NO$_x$ by injection of ammonia-additives effectively with use of limited computational efforts Brouwer and Heap developed a global model for selective non-catalytic reduction of NO$_x$. The model has been developed by reduction of a Detailed chemical kinetic model. The detailed chemical kinetic model used in order to obtain the proposed model was developed by Miller and Bowman [13]. This detailed chemical kinetic model consists of 213 reactions.

It was identified that the principle NO reduction pathway occurs by reaction with NH$_2$ forming N$_2$ for ammonia and by reaction with HCO forming N$_2$O as intermediate for the cyanuric acid. When using urea both pathways are important [26]. This knowledge was used to develop the reduced mechanism. The mechanism assumes instantaneous breakdown of the reactants into ammonia and iso-cyanic acid (HNOC). Urea breaks down to into both ammonia and iso-cyanic acid in the ratio 1.1 moles of NH$_3$ to 0.9 moles of HNCO due to the fact that HNCO subsequently reacts along the ammonia

pathway [26]. For this reason cyanuric acid breaks down to 0.3 moles of NH$_3$ and 2.7 moles of HNCO [26]. The reaction pathway for reduction of NO with ammonia, cyanuric acid and urea is schematically shown in figure 2.31.
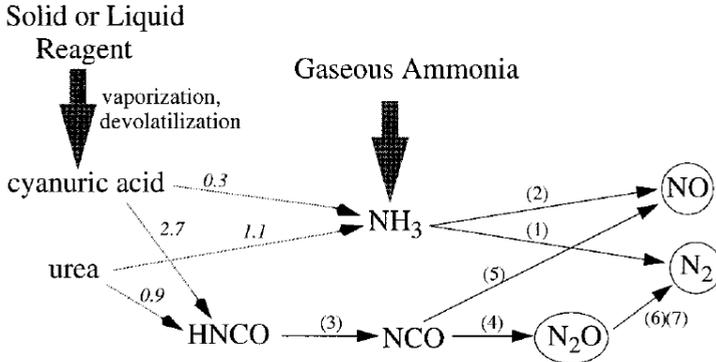
Figure 2.31: Schematic drawing of the reduced model [26]. The numbers in parentheses correspond to the reaction number in table 2.3

The numbers in parenthesis in figure 2.31 refers to the reaction number in table 2.3. The reduced mechanism proposed by Brouwer and Heap consists of 6 species and 7 irreversible finite-rate reactions. The reaction mechanism can be seen in table 2.3.

Table 2.3: Reduced model for selective non-catalytic reduction of NO$_x$ using ammonia, UREA or cyanuric acid proposed by Brouwer and Heap [26]. Units are: A=cm$\cdot$mol$\cdot$s$\cdot$K, E$_a$ = cal/mol.

Reaction	A	B	E$_a$
1. NH$_3$ + NO → N$_2$ + H$_2$O + H	$4.24 \cdot 10^8$	5.30	83,600
2. NH$_3$ + O$_2$ → NO + H$_2$O + H	$3.5 \cdot 10^5$	7.65	125,300
3. HNCO + M → H + NCO + M	$2.4 \cdot 10^{14}$	0.85	68,000
4. NCO + NO → N$_2$O + CO	$1.0 \cdot 10^{13}$	0.0	-390
5. NCO + OH → NO + CO + H	$1.0 \cdot 10^{13}$	0.0	0
6. N$_2$O + OH → N$_2$ + O$_2$ + H	$2.0 \cdot 10^{12}$	0.0	10,000
7. N$_2$O + M → N$_2$ + O + M	$6.9 \cdot 10^{23}$	-2.50	64,760

The first two reactions describes the ammonia chemistry. Reaction number 1 describe the degradation of NO which is favoured at lower temperature. Reaction number 2 describes the formation of NO from NH$_3$ and O$_2$ which is favoured at high temperatures. Reaction 3 through 7 describes the iso-cyanic acid chemistry. Reaction 3 describes the degradation of HNCO into NCO. HCO can subsequently react with OH and form NO through reaction 5. The desired reaction in the HNCO pathway is reaction 4 where NCO reacts with NO to form N$_2$O. The N$_2$O formed through reaction 4 reacts with OH or a third body to form N$_2$ through reaction 6 and 7.
Generally global reaction mechanisms, as the mechanism proposed by Brouwer and Heap, does not work well of a wide range of conditions. However, as the SNCR process is

limited to a narrow temperature window and oxygen level the global reaction mechanism works well for this process [26], as indicated in figure 2.32.
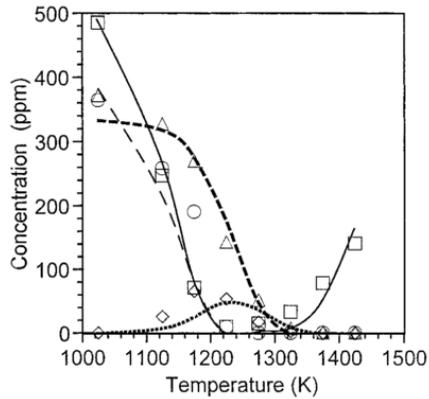
Figure 2.32: Comparison between a detailed chemical kinetic model and the reduced model for NO reduction by ammonia, urea and cyanuric acid. The symbols represents the detailed chemical kinetic model ($\square$=NO, $\triangle$=HNCO, $\bigcirc$=NH$_3$, $\diamond$=N$_2$O) and the line represents the reduced model (——=NO, — —=NH$_3$, - - - - =HNCO, $\cdots$=N$_2$O) [26]

It is seen that the reduced model describes the ammonia, urea, cyanuric acid and NO chemistry very well in the limited temperature window. Furthermore, it is seen that a minimum in NO concentration is obtained in the temperature range from approximately 1200K to 1300K agreeing with what was stated in a previous section.

The model was evaluated by Brouwer and Heap for the three reduction agents. This was done by comparison with experimental results found in the literature.
In figure 2.33 the reduced mechanism using ammonia as reducing agent has been compared with the full mechanism and experimental data obtained by Lyon [30].
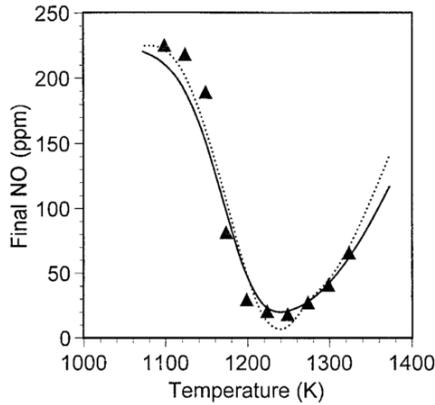
Figure 2.33: Comparison between a detailed chemical kinetic model, the reduced model for NO reduction by ammonia and experimental data obtained by Lyon [30] ($\cdots$=DCKM, —=Reduced model, ▲=Data from Lyon) [26]

The initial conditions for this comparison is 225ppm NO, 450ppm NH$_3$ and 1.23% O$_2$. It is seen that the reduced model predicts the reduction and the temperature dependence just as good as the detailed chemical kinetic model.
In figure 2.34 the reduced model for NO reduction using cyanuric acid as reducing agent has been compared with the detailed chemical kinetic model and experimental data obtained by Catan and Siebers [71]
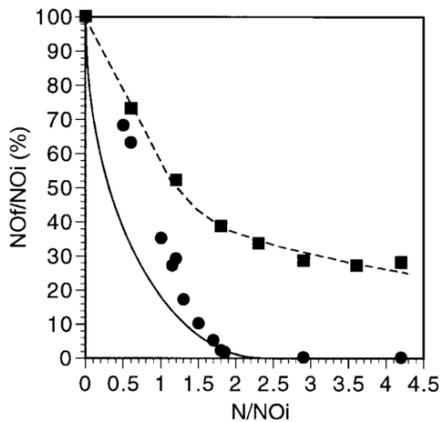
Figure 2.34: Comparison between a detailed chemical kinetic model, the reduced model for NO reduction by cyanuric acid and experimental data obtained by Caton and Siebers [71] with and with out CO. The line represent data from modelling using the reduced model (- - - -=with CO, —=without CO) and the symbols represent the data obtained by Caton and Siebers (■=with CO, ●=without CO) [26]

The data from Caton and Siebers were obtained in a 1.6 cm ID quartz reactor were simulated exhaust gasses was used and NO was reduced by injection of vaporised

cyanuric acid at 740K. The mixing limitations were considered small, therefore the experiment is though to simulated a situation of premixed reactants [26]. It is seen that the reduced model describes the NO reduction at these conditions using cyanuric acid as reducing agent with reasonable accuracy.

The reduced model was tested using urea as reduction agent. This was done by comparison with the detailed chemical kinetic model and experimental data obtained by Teixeira et al. [72]. The results from the comparison is seen in figure 2.35.
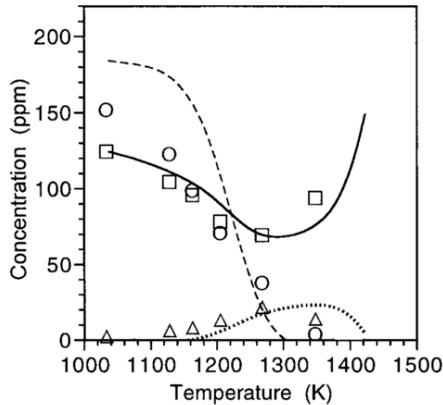
Figure 2.35: Comparison between the reduced model for NO reduction by urea and experimental data obtained by Teixeira et al. [72] with and with out CO. The line represent data from modelling using the reduced model (——=NO, - - - - =NH_3, $\cdots$=N_2O) and the symbols represent the data obtained by Teixeira et al. ($\square$=NO, $\bigcirc$=NH_3, $\triangle$=N_2O) [26]

The data was obtained by injection of a 2.4 wt % urea/water solution through an atomiser into the throat of a furnace with controlled injection temperature and temperature profile [26]. As seen in figure 2.35 the predictions using the reduced model shows good agreement with the data obtained by Teixeira et al. At lower temperature a slight overestimation of the NH_3 is however experienced. Furthermore, at elevated temperature a slight shifting in the peak of NO reduction and N_2O emission levels is experienced [26].

All in all a good agreement between the reduced model, the detailed chemical kinetic model and the experimental data is seen. This reduced model is therefore applicable for NO reduction simulations.

A urea decomposition model was proposed by Rota et al. [73]. The model consists of 2 simultaneous reactions decomposing gaseous urea into ammonia and isocyanic acid according to reaction 2.32 and 2.33.

$$CO(NH_2)_2 \rightarrow NH_3 + HNCO \qquad (2.32)$$

$$CO(NH_2)_2 + H_2O \rightarrow NH_3 + CO_2 \qquad (2.33)$$

The rate of reaction 2.32 and 2.33 is determined by the Arrhenius equation with pre-exponential factor and activation energy as stated in table 2.4 [73].

Table 2.4: Pre-exponential factor and activation energy for the Arrhenius equation related to the two step urea decomposition model [73]

Reaction	A	b	E
	m mol s K	-	J/mol
2.32	$1.27 \cdot 10^4$	0	65048.109
2.33	$6.13 \cdot 10^4$	0	87819.133

Included in the two step NO reduction by NH_3 is the effect of CO on the reduction. It has been shown that CO shifts the temperature window of the reduction reaction towards lower temperatures. This has been shown in Figure 2.36
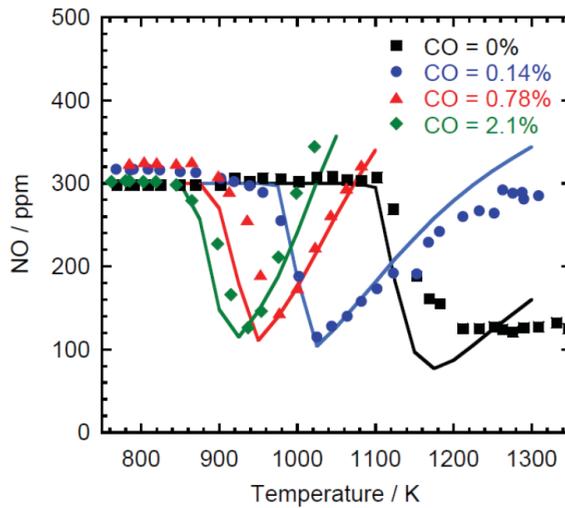
Figure 2.36: Comparison of experimental data [74] and modelling predictions for the reduction of NO with NH3 in a quartz flow reactor; effect of CO. The symbols denote the experimental data, the full line denote modelling predictions using the mechanism by Glarborg et al.[10]. Inlet concentrations: NO=300ppm, NH$_3$=300ppm, O$_2$=4%, H$_2$O=4,5%, N$_2$=balance. Residence time= 150ms at 1200K (constant molar rate)

Brouwer and Heap included this effect as a correction to reduction temperature used in the Arrhenius expression [26] as shown in equation 2.34 and 2.35.

$$k_i = A_i \cdot (T + S(CO)) \cdot \exp\left(\frac{-E_i}{R(T + S(CO))}\right) \tag{2.34}$$

$$S(CO) = 17.5 \cdot \ln(X_{CO} \cdot 10^6) - 68 \tag{2.35}$$

2.3 Modelling of NO$_x$ formation in commercial CFD codes

In recent times a greater focus has been put on modelling of NO$_x$ formation using commercial CFD codes; such as ANSYS's Fluent and CFX. Using various different approaches the formation of NO$_x$ during combustion in coal fired power plant, Waste-to-Energy plants, methane combustion and wood stoves has been simulated [75], [2], [76], [77], [78], [79], [80], [81], [82].

Frank and Castaldi[2] simulated the combustion of solid waste in a waste-to-energy plants with total throughput of fuel of 6980 kg h^{-1} using a detailed chemical kinetic model. In order to simplify the model the bed was not simulated in CFD; a stand-alone bed model was used. The devolatilisation gases, produced from devolatilisation of the solid waste, are introduced to the free board through the boundary conditions. Therefore the model only simulates the flow, temperature and species fields in the free board, first and second pass.

In order to model the chemistry in the free board the GRI 3.0 mechanism[83] was used. This mechanism consists of 50 species and 309 reactions; three species, AR, C$_3$H$_7$ and C$_3$H$_8$, were removed from the original GRI 3.0 mechanism in order to overcome the 50 species limitations in the 13.0 version of Fluent which was used in this study. The GRI 3.0 mechanism is a well-known model developed for methane combustion [2].

The interaction between the turbulence and chemical kinetics was accounted for by the use of the Eddy Dissipation Concept model, while the turbulence was modelled by use of the realizable $k - \epsilon$ turbulence model[2].

The primary model settings are shown in Table 2.5.

Table 2.5: Primary model settings for modelling of municipal solid waste combustion and NO$_x$ formation performed by Frank et al. [2]

	Frank and Castaldi
Mesh size	800,000 mostly hexahedral
Solver setting	Steady state, Pressure based solver Gravity enabled, Compressible flow
Turbulence model	Realizable $k - \epsilon$ with standard wall function
Reaction model	Eddy Dissipation concept, RANS model DCKM with 50 species and 309 reaction (modified GRI 3.0)

The inlet boundary conditions were determined through calculations using a bed model. The grate was split in 4 parts corresponding to drying, devolatilisation, gasification and char combustion. It was assumed that 30% of the NO$_x$ precursors are released on the first 30% of the grate[2].

In the study the fuel nitrogen in the inlet boundary conditions was varied to determine the most realistic fuel-nitrogen precursor. The results from the study showed that fuel nitrogen to NO conversion in the specific study was about 33% and that either HCN or NH$_3$ provide exit NO concentrations within 5% of each other. The study concluded that NO$_x$ precursor speciation was not significant to the final NO concentration for this particular case study[2]. The modelling results were not compared to full scale measurements.

In a recent study Bugge et al. [81] developed a model to simulate the formation of NO_x during combustion of wood in a wood stove. Like the model developed by Frank and Castaldi[2], the wood stove model uses the Eddy dissipation concept model to describe the interaction between turbulence and chemistry.

In order to accelerate the simulation time Bugge et al. used a skeletal model consisting of 36 species and 214 reactions. The skeletal model has been developed by a detailed chemical kinetic model containing 81 species and 1401 reaction in a study by Løvas et al [84]. To describe the radiative heat transfer the discrete ordinates model was used. The primary model settings are shown in Table 2.6.

Table 2.6: Primary model settings for modelling of NO_x formation in a wood stove performed by Bugge et al. [81]

	Bugge et al.
Mesh size	256,000 tetrahedral
Solver setting	Steady state
Turbulence model	$k - \epsilon$ with log-law wall function
Reaction model	Eddy Dissipation concept, RANS model skeletal model with 36 species and 214 reaction [84]
Radiation model	Discrete ordinates method (DO)
Soot model	Moss and Brookes model
Wall settings	Isothermal with temperature 673K

In this model the heterogeneous reactions in the solid fuel layer were not modelled. The wood logs were represented as volumes in the geometry; the decomposition of the fuel was modelled stand alone providing a combustible gas to the computational domain. The composition of the combustible gas was changed over time as the fuel is decomposed[81]. Due to the fact that the volatile release from the wood logs is time dependent with respect to mass flow and gas composition a model for the gas release was developed. As the mass flow of volatiles released is dependent on the heat flux from combustion of the volatiles, the surface which is most visible to the flames consequently has the highest volatile release rate [81]; this is taken into account in the developed model.

The simulations of the NO_x showed that the skeletal mechanism used in the study over predicted the prompt NO_x formation compared to simulations using a detailed chemical kinetic model.

In another study by Bugge et al. [76] simulations using the 36 species skeletal mechanism were compared with simulations using a skeletal mechanism containing 49 species and a detailed chemical kinetic model containing 81 species, from which the two skeletal mechanism were developed [76] [84]. It was found through the study that the 36 species mechanism corresponds well with the detailed chemical kinetic model at higher temperature i.e. temperature above 1073K, but at lower temperatures; at temperature of 873K, the NO_x comcentration was overestimated [76]. Furthermore, it was concluded

that the 49 species mechanism corresponds well with gas predictions from the detailed chemical kinetic model [76].

Adamczyk et al. studied the effects of the reburning process on the NO$_x$ emission in a pulverized coal boiler using CFD [79]. The modelling performed in this study used simple reaction kinetics as seen in Table 2.7; the primary model settings are also shown in the table.

Table 2.7: Primary model settings for modelling of NO$_x$ formation in a pulverized coal boiler fitted with reburning performed by Adamczyk et al. [79]

Adamczyk et al.	
Mesh size	Not stated
Solver setting	Steady state
	Eddy Dissipation/Finite-rate, RANS model
	Default Fluent NO$_x$ model
Reaction model	Two step volatile combustion
	One step global reburning reaction
	Three step heterogeneous char combustion mechanism

The heterogeneous char combustion was described by 3 reactions; char reacts with O$_2$, H$_2$O and CO$_2$ producing CO and H_2 as seen in reaction 2.36, 2.37 and 2.38.

$$C(s) + 0.5O_2 \rightarrow CO \tag{2.36}$$

$$C(s) + H_2O \rightarrow CO + H_2 \tag{2.37}$$

$$C(s) + CO_2 \rightarrow 2CO \tag{2.38}$$

The volatile combustion was described by a two step homogeneous oxidation reaction as seen in reaction 2.39 and 2.40. Furthermore, H$_2$ conversion into H$_2$O was described by a single step global reaction 2.41.

$$C_iH_kO_jN_mS_n + x_1O_2 \rightarrow x_2CO + x_3H_2O + x_4SO_2 + x_5N_2 \tag{2.39}$$

$$CO + 0.5O_2 \rightarrow CO_2 \tag{2.40}$$

$$H_2 + 0.5O_2 \rightarrow H_2O \tag{2.41}$$
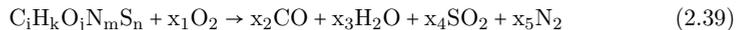
The interaction between chemical kinetics and turbulence was modelled by the Eddy Dissipation/Finite-rate model; this model describes the interaction reasonably well for a two step action mechanism but fails to describe the chemistry accurately when a more complex reaction mechanism is used [85].

In this study the reburning process was of special interest. Gas produced from gasification of sewage sludge was investigated as a secondary gaseous fuel for NO$_x$ reduction; the gas was assumed to have the composition $Y_{CO} = 0.27$, $Y_{CO_2} = 0.22$, $Y_{H_2} = 0.003$, $Y_{CH_4} = 0.006$, $Y_{N_2} = 0.49$ taken from an earlier work [86]. The syngas was either introduced through the primary oxidizer ducts or through the over fire air ducts. The amount of syngas accounted for 10% or 20% of the chemical energy from the coal [79].

The combustion of the methane in the gasification gas follow the global reaction 2.42 for simplification reasons.

$$CH_4 + 2O_2 \rightarrow CO_2 + 2H_2O \tag{2.42}$$

The formation of NO_x was determined from the default NO_x model in Fluent. The thermal NO_x was determined by the extended Zeldowich mechanism, while global reaction kinetics were used to determine the prompt NO_x as described in section 6.2. The fuel NO_x was determined from the well cited De Soete global kinetics 6.2.

It was concluded that for the four cases studied the NO_x formation was below the required level according to the Polish legislation. The results from the CFD modelling were, however, not compared with full scale measurements.

King et al. [75] simulated NO_x in low NO_x burner with radial swirlers with central fuel injection using Fluent 6.3. The simulations were performed in Fluent 6.3, and earlier versions of Fluent. The geometry used in the study contained 8 identical swirler vanes and fuel injection holes[75]. The primary model settings are seen in Table 2.8.

Table 2.8: Primary model settings for modelling of NO_x formation in low NO_x radial swirlers with central fuel injection performed by King et al.[75]

King et al.	
Mesh size	850,000
Solver setting	Steady state
Turbulence model	$k - \epsilon$ model
Reaction model	Non-premixed combustion model with equilibrium pdf model 16 species combustion model which is default in Fluent Default NO model (Zeldowich and De Soete) [75]

In order to obtain a grid-independent solution a mesh size of 850,000 element was used. The turbulence chemistry interaction was modelled, as for the other studied cases, with the well established $k - \epsilon$ model.

The combustion was simulated by use of a 16 species mechanism, which is default in Fluent. The before mentioned studies all used a RANS method in order to determine the temperature, species concentration etc. in each element. King et al. used a pdf method for temperature and species properties based on the assumption of chemical equilibrium [75]. NO_x formation was predicted, like in the study by Adamczyk, by the De Soete mechanism and the Zeldovich mechanism. The model was used for investigation of various different burner configurations.

Gas-phase freeboard combustion was investigated by Andersen et al.[82] by both experiments and CFD simulations. The study involved an investigation of NO_x simulations in Fluent using a number of different NO_x mechanisms, both global and skeletal, and a number of combustion mechanisms, global and skeletal. In Table 2.9 each of the CFD models, which have been compared to experiments, are shown.

Table 2.9: Primary model settings for modelling of NO$_x$ formation in a 50kW axisymmetric non-swirling natural gas fired combustion setup performed by Andersen et al. [82]

Andersen et al.	
Mesh size	Not stated
Solver setting	Steady state
Methane combustion model (RANS)	Two step methane combustion mechanism coupled with EDM[26] Four step Jones and Lindsted mechanism coupled with EDC[87] Skeletal mechanism used by Yang and Pope coupled with EDC [88]
NO$_x$ model (RANS)	De Söete model[14] Mitchell and Tarbell[65] model Brink et al. model[69] NO skeletal model proposed by Pedersen et al.[61]

Each of the four NO$_x$ mechanisms were combined with each of the three combustion mechanisms. The NO$_x$ simulations were performed both as a post-processing procedure and solved in conjunction with the combustion. It was concluded that all of the models found NO$_x$ trends equal to the experimental values for both simulation points; for setting 1 the exit oxygen concentration was predicted to be 6.7 % dry, while for setting 2 the exit oxygen concentration was found to be 0.7% dry. The combustion was slightly over-stoichiometric for both settings.

2.4 Summary

In this chapter the most promising NO$_x$ models have been presented and discussed. Depending on the problem chemical models with increasing complexity are used. The chemical models are typically divided into 3 groups:

- Detailed Chemical Kinetic Models

- Skeletal models

- Analytically reduced models

- Global models

The Detailed Chemical Kinetic Models are the most complex models. These models are composed of up to several thousand elementary reactions. These models are valid for all possible conditions. Due to the large size of these models, these are typically avoided for CFD purposes.

The skeletal models are reduced model composed of a lower number of elementary reactions. The skeletal models are reduced from detailed chemical kinetic models, these models have been developed specifically for a small parameter space. These models are being used increasingly for CFD purposes due to the relative high accuracy and the relative small size; consequently the computational time is dramatically reduced compared to detailed chemical kinetic models.

Global models are the least complex of the models types, hence the size of these are

typically very small. These models are often experimentally derived empirical models which have been developed under very specific conditions; hence the models are valid under a narrow span of conditions. Extrapolation of these models outside the range of development needs to be done with care. Global models have been used in a vast number of CFD studies due to the small size and low computational time.

A number of the more cited detailed chemical kinetic model's were presented and discussed in this chapter, these detailed chemical kinetic model's where proposed by Miller and Bowman[13], Mendiara and Glarborg[36], Skreiberg et al.[38] and Glarborg et al.[10]. One of the most cited detailed chemical kinetic model's is the model developed by Miller and Bowman. This model consists of 234 reversible reactions. This has been developed for conditions typically found in combustion systems and tested over a relatively broad range of temperatures, pressures, stoichiometries, and fuel types [13].
The model by Mendiara and Glarborg captures the essential features of the nitrogen chemistry very well. These are the NH_3 oxidation and NO reduction. At fuel-lean conditions the model predictions, however, do not coincide with experimental results[36].
The mechanism by Skreiberg et al.[119] describes the trends of the NH_3 oxidation and NO reductions chemistry well. Absolute values of the NH_3 and NO concentrations are not predicted accurately[119] by the model.
The model by Glarborg et al.[10] shows the most promising performance. The general agreement between model predictions and experimental results is good. The model describes the the trends of the nitrogen chemistry well. Furthermore, absolute values of the NO and NH_3 concentrations were predicted well by the model.

Several reduced models have been presented, all developed for different purposes. The analytically reduced model by Pedersen et al.[61], 19 species and 37 reactions, was developed to describe nitrogen chemistry during coal combustion. The modelling by the model and the detailed chemical kinetic model, from which it was developed, were in good agreement for the investigated parameter space. The model, however, has been developed for prediction of the HCN oxidation. Since HCN only accounts for a minor part of the NO_x precursors during waste combustion (see chapter 5) this model might not be applicable in waste combustion systems system. The model was further reduced by Hansen et al.[32] estimating radical concentrations from the major species concentrations.
Glarborg et al. developed a analytically reduced model based on the detailed chemical kinetic model from Miller and coworkers. This skeletal model was developed in the same fashion as models from from Peters and coworkers[66], [67] and Bilger et al.[68]. The model has been shown to predict the major species and the key radical accurately in the range $0.7 \leq \phi \leq 1.4$. For fuel-rich conditions; $\phi \geq 1.54$, and low temperatures the accuracy of the model deteriorates due to the neglect of the C_2 chemistry.
Houshfar et al.[62] reduced the detailed chemical kinetic model by Mendiara and Glarborg resulting in 3 skeletal models with varying size especially developed for nitrogen chemistry during biomass combustion. It was reported that the lower and medium sized skeletal models performed well at high temperatures, while deteriorating at low temperatures. The large sized skeletal model performed well in the temperature range from $700°C$ to $1100°C$. For CFD purposes this model will cause large computational expenses.

Global models by De Soete[14], Mitchell and Tarbell and Brink et al.[69] were presented and discussed in this chapter. Overall the global models perform very well in the range

of development; typically the range of development is very limited. For all the 3 proposed models predictions of the nitrogen chemistry at fuel-rich conditions are accurate.

Prediction of the NO$_x$ formation in combustion systems has been performed in the past by Frank and Castaldi[2], Bugge et al.[81], Adamczyk et al.[79], King et al.[75] and Andersen et al.[82]. For most of the studies the predictions using CFD were not compared with experimental results from the simulated plant. Andersen et al. compared the predicted NO concentrations with experimental measurements and concluded that the CFD model was capable of capturing the trends in the system, but accurate NO predictions was not possible.

Chapter 3

Strategies for the development of skeletal model

In the previous chapter it was shown that the readily available simplified models predicting the nitrogen chemistry during combustion of biomass does not describe the formation of NO to the desired degree over the entire parameter space; the readily available Detailed Chemical Kinetic Models for accurate prediction of the nitrogen chemistry are too large for effective simulation using CFD. Therefore, the development of a new skeletal model for NO formation is needed. An important step in the project is the development of a NO_x model with a limited size, that consequently enables B&W Vølund to model the nitrogen chemistry using an in-house CFD model; this tool can be used for optimization of boiler design and combustion air injection for low NO_x emission.

Skeletal model reduction is intended for removal of any species in the chemical kinetic model that are not important for the simulation of the desired targets i.e. the species of interest [89]. The aim of the skeletal model reduction is to reduce the size of the chemical kinetic model whilst retaining the prediction accuracy of the model.
The reduction can be split in two stages. In the first stage the redundant species are identified and removed. This is followed by an identification and removal of the redundant reactions that do not influence the modelling accuracy significantly [89]. This means that, even if one is only interested in predicting a small number of species, one might need to include a large number of intermediate species in order to describe the species accurately [89].
Skeletal reduction has been going on for several years and include methods such as [89]:

- Sensitivity-based methods

- Graph-based methods

- Optimization in model reduction

- Lumping methods

3.1 Sensitivity-based methods

A developed sensitivity-based method is the connectivity method. This method identifies the redundant species by investigation of the Jacobian of the system. The system is

described from equation 3.1.

$$\frac{dY}{dt} = f(Y, x), \quad T(t_0) = Y_0 \tag{3.1}$$

The concentrations are denoted Y, the initial concentrations are denoted Y_0 and x is the parameter vector, which may include rate coefficients. [89]

The redundant species are identified based on a value B_i (equation 3.2) which characterizes the length of the direct link of species i to a group of important species [90].

$$B_i = \sum_j ((Y_i/f_i)(\partial f_i/\partial Y_i))^2 \tag{3.2}$$

Here $(Y_i/f_i)(\partial f_i/\partial Y_i)$ is an element in the normalised Jacobian matrix that describes the percentage of change of the production rate of species j as a consequence of a change in concentration of i [89].

The higher the value of B_i the stronger a connection between the group of important species and the species i [90]. Consequently a species with a high B value is a necessary species in the description of the important group of species [89]. The method is iterative and summed over all the necessary species [89, 90]. The Jacobian matrix is essentially local, meaning that one value is obtained at each set of condition, therefore the method needs to be repeated over the whole range of conditions e.g. temperature, pressure and concentration. Species that are redundant over the whole range of conditions can be removed from the mechanism. Furthermore, different models can be developed for different sets of conditions.

The disadvantage of the connectivity method is that B_i values are not directly related to the final simulation error [89], consequently the accuracy of the reduced model can only be validated by comparison of simulations from the reduced model with simulations using the full kinetic model.

Within a model reduced by the connectivity method there might still be reactions that are redundant for the description of the desired species. These can be identified by a sensitivity analysis. The local rate sensitivity matrix, $F = (\partial f_i/\partial k_j)$ where f_i is the rate of production of species i and k_j is the rate constant of reaction j, is investigated by changing the rate constant and monitoring the production rate [89].

3.2 Graph-based methods

A species A can be strongly coupled to a species B directly or indirectly. They are directly coupled if they appear together in a fast reaction, and they are indirectly coupled if they both are coupled strongly to a species C. If an indirect coupling is experienced removal of a single species might require the removal of a whole group of species that are strongly coupled to the single species [91]. Such a relation can also mean a group of species needs to be kept in the skeletal model.

Graph-based methods are based on the identification of groups of species that are internally coupled and important in the description formation/degradation of species of importance[89]. This method is similar to the sensitivity-based methods with exceptions.

Using the Directed Relations Graph (DRG) approach, an edge exists between two notes if and only if the removal of one species induces significant error to the production/consumption rate of the other species [91]. Here the notes represent species. This can be seen in figure 3.1.
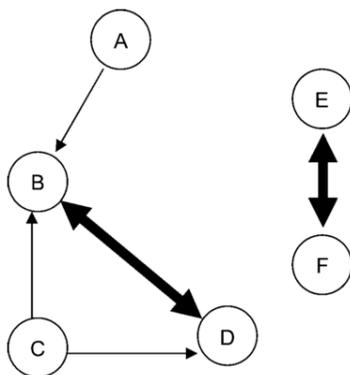
Figure 3.1: Example of a directed relation graph showing typical relations of the species [91]

The removal of B from the mechanism shown in figure 3.1 will therefore induce a significant error in the consumption rate of A. The width of the arrow represents the direct influence of one species on the other [91]. This is quantified by equation 3.3.

$$r_{AB} \frac{\sum_{i=1,I} |v_{A,i} R_i \delta_{Bi}|}{\sum_{i=1,I} |v_{A,i} R_i|} \tag{3.3}$$

$$\delta_{Bi} = \begin{cases} 1 & \text{if the i}^{\text{th}} \text{ elementary reaction involves species B} \\ 0 & \text{otherwise} \end{cases} \tag{3.4}$$

Here $\sum_{i=1,I} |v_{A,i} R_i|$ is the production rate of A and $\sum_{i=1,I} |v_{A,i} R_i \delta_{Bi}|$ is the production rate of A for the reactions where the species B is involved.

A threshold ϵ is defined such that if $r_{AB} < \epsilon$, where ϵ is predefined, no connection between A and B of significant importance occur and B has no influence on the production/consumption rate of A. The accuracy of the skeletal model will therefore depend on the chosen value of ϵ. In figure 3.2 the dependence of the threshold value and the size of the skeletal model can be seen.
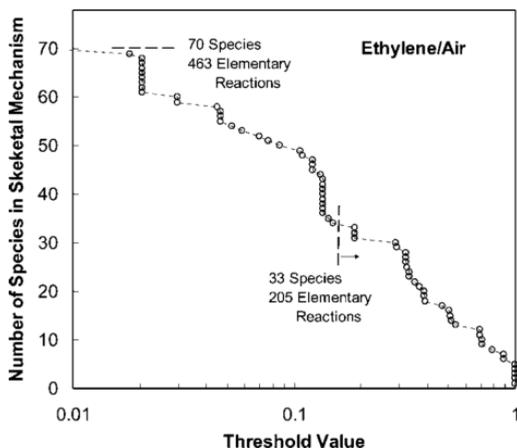
Figure 3.2: The dependency of the threshold value on the number of species in the developed skeletal model. The jumps in species number is due to the existence of strongly coupled groups [91]

By increasing the threshold, ϵ the model decreases in size. An increase in the ϵ-value means that the species B needs to induce a larger change in the production/consumption rate of A to be included in the reduced model; consequently a lower number of species are included in the reduced model. A large ϵ-value will most likely result in a less accurate model.

It was suggested by Lu and Law[91] that by using a two stage reduction a skeletal model with a lower number of species can be achieved. In a two stage reduction a different threshold number is used for the two reduction stages; in the second stage a large threshold number is used in order to gain further reduction in species number [89] [91].

3.3   Lumping methods

In some systems the skeletal reduction methods do not give the sufficient reduction to meet the computational requirements. In such a system it might be necessary to use a lumping method in order to achieve the needed reduction in computational expenses [89]. Species with similar structure, reactivity e.g. are lumped together. Furthermore, lumping can also be performed mathematically based on either linear or non-linear transformations, where a linear approach is the typical choice in combustion [89].
In mathematical lumping the vector of variables is transformed into a new vector of variables through a suitable transformation function as shown in equation 3.5.

$$\hat{Y} = h(Y) \tag{3.5}$$

Here Y is the vector of concentrations, $\hat{Y}$ is the new vector of concentrations and h is the transformation matrix [89]. The dimension of the new vector of concentrations is smaller than the dimension of the original vector of concentrations, hence the kinetic model is reduced and the number of ordinary differential equations (ODEs) that needs

to be solved is lowered.

$$\frac{d\hat{Y}}{dt} = \hat{f}(\hat{Y}, \hat{k}), \qquad \hat{T}_{t_0} = \hat{Y}_0 \tag{3.6}$$

Here $\hat{k}$ is the transformed parameter vector.

Battin-Leclerc[89] gives an example on lumping within the n-heptane scheme, where alkyl radicals react with oxygen through the following reactions.

$$R\cdot_1 + O_2 \to R_1 OO\cdot \tag{3.7}$$

$$R\cdot_2 + O_2 \to R_2 OO\cdot \tag{3.8}$$

$$R\cdot_3 + O_2 \to R_3 OO\cdot \tag{3.9}$$

$$R\cdot_4 + O_2 \to R_4 OO\cdot \tag{3.10}$$

Here the lumped alkyl concentration is defined as 3.11

$$[R\cdot] = [R\cdot_1] + [R\cdot_2] + [R\cdot_3] + [R\cdot_4] \tag{3.11}$$

The lumping corresponds to a reaction scheme as seen in reaction 3.12

$$R\cdot + O_2 \to ROO\cdot \tag{3.12}$$

As seen the four elementary reactions can be described as one global reaction. This means that the reaction rate constant can be described using a weighted mean of the elementary reaction rate constants according to equation 3.13

$$k' = \frac{k_1[R\cdot_1] + k_2[R\cdot_2] + k_3[R\cdot_3] + k_4[R\cdot_4]}{[R\cdot]} \tag{3.13}$$

The advantage of using the strictly mathematical lumping method is that the parameters used can be completely derived from the original kinetic equation. Therefore no fitting of data is required [89].

3.4 On-the-fly reduction

Most reduction methods rely on the reduction to a single skeletal model for description of chemistry over a whole range of conditions. On-the-fly reduction relies on the incorporation of full kinetics schemes in a CFD code and reduction of these models according to the local conditions while the calculations are proceeding [92]. These reduction methods therefore develop numerous skeletal models according to the local conditions. Some on-the-fly reduction methods will briefly be reviewed in this section. These reduction methods are:

- In-Situ Adaptive Tabulation (ISAT)

- Dynamic Adaptive Chemistry (DAC)

- Tabulation of Dynamic Adaptive Chemistry (TDAC)

The In-Situ Adaptive Tabulation (ISAT) reduction method developed by Pope typically reduces the CPU time by three orders of magnitude [93]. It can be used on full kinetic models, skeletal models and highly reduced models.

The final composition ϕ^1 can be calculated from the initial composition ϕ^0 over a time-step Δt according to equation 3.14

$$\phi^1 = \phi^0 + \int_0^{\Delta t} S dt \qquad (3.14)$$

Here S is the chemical source term.

At the beginning the ISAT table is empty. The first table entry consists of the initial composition ϕ^0, the mapping ϕ^1 which has been calculated from direct integration of equation 3.14, a mapping gradient $A = \partial\phi^1/\partial\phi^0$ and a hyper-ellipsoid of accuracy [85]. The hyper-ellipsoid of accuracy is the elliptical space around ϕ^0 where linear approximation to the mapping is accurate to a specified tolerance ϵ_{tol} [94].

A queried composition can be found by interpolation from equation 3.15

$$\phi_q^1 = \phi^1 + A(\phi_q^0 + \phi^0) \qquad (3.15)$$

Here q denotes a query. ϕ_q^0 therefore denotes the queried initial composition vector. As seen in equation 3.15 the queried composition is calculated from interpolation using the mapping gradient A. This interpolation is only valid if the initial query point ϕ_q^0 is within the hyper-ellipsoid of accuracy around ϕ^0. If this is not the case a direct integration is performed and the mapping error is calculated as seen in equation 3.16

$$\epsilon = |B(\phi_{DI}^1 - \phi_q^1)| \qquad (3.16)$$

Here B is a scaling factor. If the error is smaller than the specified tolerated error ϵ_{tol} the interpolation ϕ_q^1 is accurate and the hyper-ellipsoid of accuracy is grown to include the initial query composition ϕ_q^0. If the error is larger a new table entry is added and calculated by direct integration [15] [94].

The DAC reduction method rely on the directed relation graph (DRG) method as described in a previous section. In this method the local conditions are evaluated followed by a reduction of the full kinetic model according to these conditions through the DRG method [92]. The method identifies the reduntant species according to the local thermo-chemical conditions. This means that a reaction is only included in the reduced scheme if all reactants and products are active species and the inactive species will keep a constant mass fraction. Even though the inactive species are not included "chemically" they are important in the determination of the third-body concentration and the pressure-dependent reactions [92].

Liang et al. [92] proposed a formulation of the kinetics equations that minimizes the size of the ODE system without neglecting the third body effects. In a system that consists of m active and n inactive species the formulation can be expressed as equation 3.17.

$$\begin{cases} y_1^a = f_1 = (X(T, p, y_1^a \Pi, y_m^a, y_1^i \Pi, y_n^i)) \\ \vdots \\ y_m^a = f_m = (X(T, p, y_1^a \Pi, y_m^a, y_1^i \Pi, y_n^i)) \\ y_m^a = f_{m+1} = (X(T, p, y_1^a \Pi, y_m^a, y_1^i \Pi, y_n^i)) \end{cases} \qquad (3.17)$$

Here a denotes the active species and i denotes the inactive species.

In order to distinguish the active reactions from the inactive reactions the subroutines

for calculating rate constants in CHEMKIN have been modified in such a way that a binary flag mark the active reactions [92].
The DAC method typically reduces the computational time with a factor of 2 or 3 [15]. Compared to other methods this is low reduction in the computational time.

The most recent on-the-fly reduction method is the Tabulation of Dynamic Chemistry (TDAC) method that combines the two before mentioned methods[89].

3.5 Simulation Error Minimization Connectivity method (SEM-CM) for mechanism reduction

The ignition time delay and the flame speed are two features that are frequently modelled in combustion processes [95]. The method developed by Nagy et al. [95] is based on the elimination of redundant species in such a way that the ignition time delay, the flame velocity profile or concentration profile only deviate slightly, or within a given tolerance, from the original full mechanism. The SEM-CM bases the removal of redundant species on the inspection of the jacobian. Any element in the normalised jacobian of a complex model provides information of the changes in the time-derivative of the concentration of a species j if the concentration of species i is perturbed [95]. This is seen in equation 3.18.

$$J_{ij} = (c_i/f_i)(\partial_{f_i}/\partial_{c_i}) \tag{3.18}$$

In equation 3.18 f_i denotes the concentration of species j.
The Connectivity Method (CM) uses the squared of the jacobian to determine the strength of the direct link from a species i to a group of important species as shown in equation 3.19 [96].

$$B_i = \sum_{j \in \text{group}} J_{ij}^2 \tag{3.19}$$

Here the value B characterises the strength of the direct link from a species i to a group of important species[96]. The higher the value of B the stronger the link between the species i and the group of important species. Once the B value for all species i has been calculated the species with the highest B_i value is included in the group of important species j. The calculation of the B_i value is repeated until a gap appears between the B_i values. The species with a B_i value above the gap are necessary/important species and are included in the reduced model. The species with a lower B_i value are redundant species. Species are removed from the mechanism if it is redundant at each time it is investigated. As the redundant species are removed so are all reactions in which these species are participating [95].
The Connectivity method only yields one or a few reduced models. It was found by Nagy et al. that for mechanisms with a large number of species no gap in the B_i values appears for most conditions [95]. For each investigated time it is therefore not clear when to terminate the iteration [95]. The role of the important species, species that need to be modelled by the reduced model, diminishes as species are added to the group [95]. This means that the error when modelling the important species might not decrease as more species are added to the reduced model. Due to these two drawbacks the Connectivity method was modified by Nagy et al. to include an error function that monitors the advancement and efficiency of the reduction process [95].
Calculating the error function of important species i at time t_j can be done using

equation 3.20

$$\delta_i(t_j) = 2\frac{c_i^{red}(t_j) - c_i^{full}(t_j)}{c_i^{full}(t_j) + c_{i,max}^{full}} \tag{3.20}$$

Here $\delta_i(t_j)$ denotes the error of species i at times t_j, $c_i^{full}(t_j)$ and $c_i^{red}(t_j)$ denote the concentration of species i at times t_j according to the full and the reduced model respectively, and $c_{i,max}^{full}$ denotes the maximum concentration of species i in the selected time span according to the full mechanism [95].

In some cases it can be an advantage to do the reduction based on the maximum error instead. This is calculated using equation 3.21 and 3.22 [95].

$$\delta_{i,max} = \max_j |\delta_i(t_j)| \tag{3.21}$$

$$\delta_{max} = \max_i \delta_{i,max} \tag{3.22}$$

Here $\delta_{i,max}$ denotes the maximum error of the important species and δ_{max} denotes the overall maximum error.

In cases where the concentration of certain important species are more important it can be of interest to do the reduction based on the root mean square errors of the important species rather than the maximum. The root mean square error is calculated from equation 3.23 and 3.24 [95].

$$\delta_{i,rms} = \left(n_t^{-1} \sum_j \delta_i(t_j)^2 \right) \tag{3.23}$$

$$\delta_{rms} = \left(n_{imp}^{-1} \sum_i \delta_{i,rms}^2 \right) \tag{3.24}$$

In equation 3.23 and 3.24 n_t denotes the number of time points and n_{imp} denotes the number of important species.

The CM algorithm identifies and removes redundant species instead of redundant reactions. If the reaction A+B→C, which is assumed irreversible, is considered and A is the important species, the CM algorithm only selects species B since this species is the only species affecting the consumption rate of A. Since C has no influence on the consumption rate of A it is not selected, and the reaction A+B→C will be deemed redundant as one species in the reaction is redundant. This is avoided in the algorithm by Nagy et al. by selecting a set of species instead of single species. These combinations of species are called complementary sets [95]. A complementary set consists of the species that have been deemed redundant but will yield at least one additional reaction by selection [95]. In the example above species B and C will be a complementary set of reactions.

A schematic figure of the reduction algorithm developed by Nagy et al. is shown in figure 3.3.
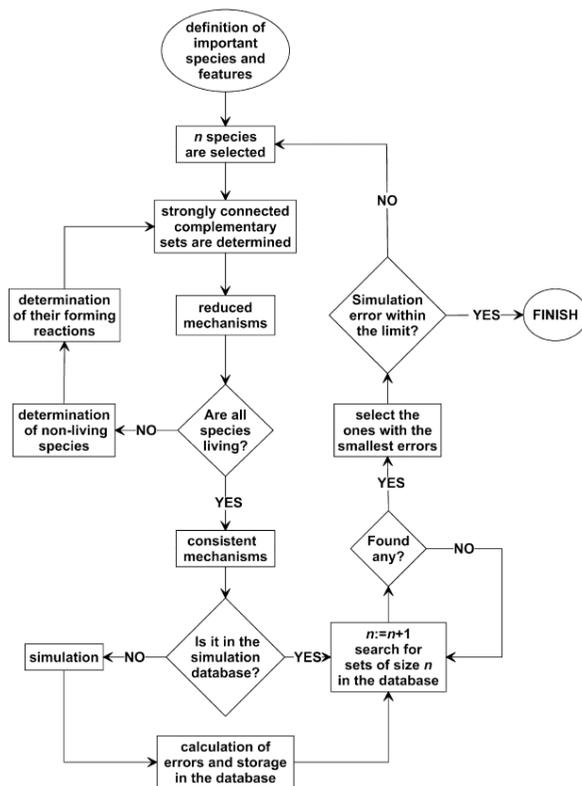
Figure 3.3: Flowchart of the SEM-CM reduction algorithm developed by Nagy et al. [95]

To start any mechanism reduction a set of time points, spatial points and important species for the reduction are selected. The time point are usually chosen within a time span of 1/4 to 4 times the ignition time delay.

The first step in the reduction are simulations using the full mechanism carried out at several selected time and spatial points. The concentration sets and the normalised jacobian matrices for each of the preselected time and spatial points are saved. The reduction will be performed in each of these time and spatial points,and the error between the reduced models and the full model will be calculated in these points.

Next step in the reduction is the identification of complementary sets of species. As described before, a complementary set of species consists of one species which has already been selected and a species which has not yet been selected but will yield at least one additional reaction. At the beginning of the reduction the complementary sets of species must contain one of the important species, which was selected before reduction.

After the identification of the complementary sets of species these are ranked according to the strength of the direct link from the complementary sets to the group of important

species using the equation 3.25

$$C_k = \frac{1}{n_k} \sum_{i \in set} B_i = \frac{1}{n_k} \sum_{i \in set} \sum_{j \in group} J_{ij}^2 \qquad (3.25)$$

Here n_k denotes the number of species in the complementary set and j is part of the group of important species. The complementary sets are ranked according the C_k value. In equation 3.25 the sum is divided by n_k to make sure that complementary sets where a lot of species are included are not ranked higher that complementary sets with only a few species.

Since two or more complementary sets can have similar strong links to the group of important species a number of the complementary sets, defined by the depth level m, are tested to find the optimal way of reduction [95]. After ranking of the complementary sets, they are added to the group of important species one by one to create a number of extended sets of species. The number of extended sets corresponds to the depth level m and the number of time points n_t (m x n_t).

Before the extended sets is evaluated through simulations, each of the extended sets are checked if all species are *living*. Species are defined as *living* if the initial concentration of the species is non-zero or if the species are produced in a chemical reaction already in the mechanism. If all the species are living the mechanism is *consistent*. If some species are non-living the reactions that produce the non-living species are identified and the complementary sets of these reactions are identified. The newly found complementary sets are ranked by calculation of $\bar{C}_k$ 3.26

$$\bar{C}_k = \frac{1}{n_k} \sum_{i \in set} \bar{B}_i = \frac{1}{n_k} \sum_{i \in set} \sum_{j \in q} \max_{l \le k} \bar{J}_{ij}(tl)^2 \qquad (3.26)$$

Here q denotes the group of non-living selected species. Equation 3.26 is similar to equation 3.25 but the last summation is only done for the non-living selected species. When all selected species are living all mechanisms are consistent.

The last step is detemining the efficiency of all the reduced models through simulation. The errors are calculated for each species set and saved in a database.

The steps described above are repeated adding new species until a reduced model with an error below the specified has been produced. All mechanisms are saved in a database during the reduction, which means that a mechanism with a given error can always be found after reduction has been terminated.

The procedure above only considers removal of redundant species. For further mechanism reduction redundant reactions are removed. In the study by Nagy et al. this is done by Principal Component Analysis (PCA) of the rate sensityvity matrix **F** [95] as described in section 3.1.

3.6   Path flux analysis (PFA) method for model reduction

The Path Flux Analysis method developed by Sun et al.[97] is similar to the DRG method described in an earlier section. The description here is based on the absolute

reaction rate for the reduction, see equation 3.3, the PFA method uses production and consumption fluxes to determine the most important reaction pathways [97]. The production flux (P_A) of species A is calculated by equation 3.27 while the consumption flux (c_A) of species A is calculated by equation 3.28.

$$P_A = \sum_{i_1,I} \max(v_{A,i} \cdot \omega_i, 0) \tag{3.27}$$

$$c_A = \sum_{i_1,I} \max(-v_{A,i} \cdot \omega_i, 0) \tag{3.28}$$

In equation 3.27 and 3.28 $v_{A,i}$ and ω_i denote the stoichiometric coefficient of species A in the i'th reaction and the reaction rate of reaction i respectively.

The production and consumption flux of A related with species B is calculated using equation 3.29 and 3.30 respectively.

$$P_{AB} = \sum_{i_1,I} \max(v_{A,i} \cdot \omega_i \cdot \delta_B^i, 0) \tag{3.29}$$

$$c_{AB} = \sum_{i_1,I} max(-v_{A,i} \cdot \omega_i \cdot \delta_B^i, 0) \tag{3.30}$$

δ_B^i can have the value 1 or 0 depending on the reaction. If species B participates in reaction i δ_B^i has the value 1, while δ_B^i has the value 0 if not. Equations 3.29 and 3.30 denote the rate of production and consumption of species A, respectively, due to the existence of species B.

Similar to the DRG approach the interaction coefficients for the production and consumption of species A via species B is calculated by equation 3.31 and 3.32.

$$r_{AB}^{pro-1st} = \frac{P_{AB}}{\max(P_A, C_A)} \tag{3.31}$$

$$r_{AB}^{con-1st} = \frac{C_{AB}}{\max(P_A, C_A)} \tag{3.32}$$

Equation 3.31 and 3.32 only considers production and consumption of species A via species B of first generation. A different definition of the interaction coefficient in the PFA method was introduced to take second, third etc. generation into account as shown in equation 3.35.

$$r_{AB}^{pro-2st} = \sum_{M \neq A,B} \left(r_{AM_i}^{pro-1st} r_{M_iB}^{pro-1st} \right) \tag{3.33}$$

$$r_{AB}^{con-2st} = \sum_{M \neq A,B} \left(r_{AM_i}^{con-1st} r_{M_iB}^{con-1st} \right) \tag{3.34}$$

$$r_{AB} = r_{AB}^{pro-1st} + r_{AB}^{con-1st} + r_{AB}^{pro-2st} + r_{AB}^{con-2st} \tag{3.35}$$

M_i denotes an intermediate species. Equation 3.35 is used to evaluate the importance of species B on the production and consumption of species A.

The size of the reduced models from the PFA method depends on a preselected threshold value ϵ. A species or a set of species is deemed important if $\epsilon \leq r_{AB}$. The size of the reduced models can therefore be decided by the modeller by changing the ϵ.

The difference between the DRG method and the PFA method can be explained by

a thought case. In figure 3.4 the targeted species is A, M_1 to M_8 are intermediate species and B, C, D, X and Y are products. The numbers on the arrow denote the ratio of the flux of A to each of the intermediates and products.
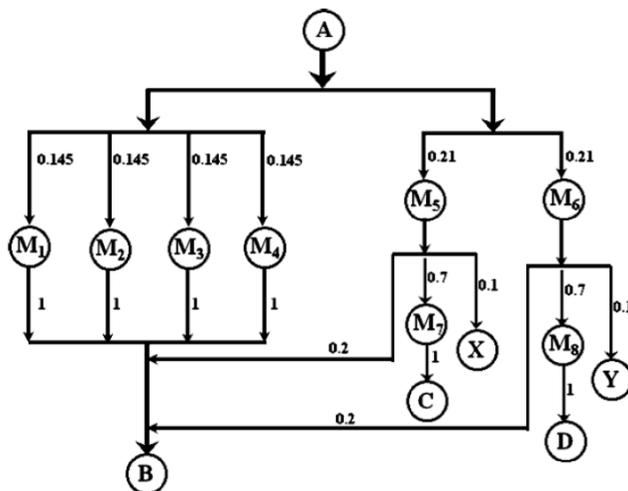
Figure 3.4: A schematic drawing of the flux relation between different species. Taken from the study performed by Sun et al. [97]

Assuming the goal of the reduction is to create a model consisting of 5 to 6 species, the DRG method includes the species A, M_5, M_6, M_7, M_8, C and D as this method only accounts for the first generation. Using the DRG method the reaction route including M_1 to M_4 to B is not included due to the lower ratio of flux of A in the first reaction step.

Using the PFA method the species A, M_1, M_2, M_3, M_4 and B are selected. First species B is selected via the indirect relation through the intermediates. After this the intermediates are selected from B [97].

Simple calculations done by Sun et al. show that the reduced model created by the DRG (and DRGEP) method only captures 29.4% of the targeted flux, while the model created by the PFA method captures 66.4% of the targeted flux [97]

3.7   Summary

In this chapter a number of reduction methods have been presented. These include sensitivity-based methods and graph-based methods. Emphasis was put on the simulation error minimization connectivity method by Nagy et al. [98] and the path flux analysis by Sun et al. [97]. Due to availability and stated performance of these two reduction methods they have both been used in this study for model reduction for the Detailed Chemical Kinetic Model developed by Glarborg et al.[10]; see section 4.3.

Chapter 4

Developing a skeletal model for the NO formation in a W-t-E plants

4.1 Estimating gas composition for model reduction

As described in the previous section the reduction of detailed chemical kinetic model using either the SEM-CM or the PFA method relies on a set of preselected targeted or important species. These are the species of certain interest. In this study it is desired to model the formation of NO_x. The reduction of detailed chemical kinetic models using the SEM-CM- or PFA algorithm relies of simulations of either the species concentrations of the important species or determination of the rate of formation/consumption of the targeted species. Both methods uses a starting gas composition that the the species concentrations or determination of the rate of formation/consumption is determined based on. In this section a gas composition that will serve for this purpose will be estimated. It is believed that the most reliable skeletal model will be achieved if a gas composition that resembles the devolatilisation gas composition of MSW. This will be estimated based on previous models and laboratory measurements.

The gas composition from devolatilisation of MSW will be estimated on the basis of stoichiometric calculations and experimental values from pyrolysis experiments.

The devolatilisation gas composition is estimated using a modification of a model by Østberg et al., which was developed for coal reburning [99]. This model uses the ultimate weight loss and ultimate analysis as input parameter.

The composition of a given fuel is represented as shown in equation 4.1. For simplification the sulphur and alkali content in the fuel is neglected.

$$C_cH_hO_oN_n \tag{4.1}$$

It is assumed that all hydrogen and oxygen, as well as part of the carbon and nitrogen, are released as volatiles. Since a fraction of the carbon is not released as volatiles c is replaced by α in equation 4.2 where α represents the amount of carbon released as volatiles. This also means that the fraction of the total carbon found as fixed carbon is $c_{char} = c - \alpha$. It is furthermore assumed that a fraction of the total nitrogen is bound in the char corresponding to the fraction of total carbon in the char.

As seen in equation 4.2 it is assumed that all the oxygen bound in the fuel is used to oxidize carbon to CO and CO_2.

The corresponding composition of the volatiles from devolatilisation of MSW is determined from equation 4.2.

$$C_\alpha H_h O_o N_{\alpha/c \cdot n} \rightarrow \beta CO + \gamma CO_2 + ((h - 4\sigma - 4\phi)/2)H_2$$
$$+ \sigma CH_4 + \phi/2 \cdot C_2H_4 + 0.8(\alpha/c \cdot n)NH_3 + 0.8(\alpha/c \cdot n)HCN \tag{4.2}$$
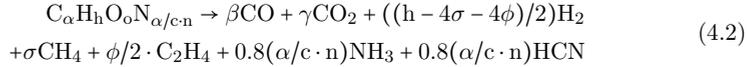
From measurements, performed in this study, at a full scale Waste-to-Energy it was shown that the gas composition just above the fuel bed was similar to the one predicted by model above (see section 5)

4.1.1 Determining the ratio between CO_2 and CO in the devolatilisation gas

It has been shown through experiments of high temperature pyrolysis of biomass, conditions similar to those in a waste-to-energy plant, that the devolatilisation gas consists of a small fraction of CO_2 [100] [101]. From a waste with a composition $C_c H_h O_o N_n$ the volatile composition can be found from equation 4.2. c, h, o and n are found directly from the proximate and ultimate analysis. C is the amount of carbon in both the volatiles and the char. The amount of carbon found as volatiles is determined by equation 4.3 using data from proximate and ultimate analysis of the fuel.

$$\alpha = c - c_{char} \tag{4.3}$$

As seen in equation 4.2 the oxygen in the fuel is split between CO and CO_2. The parameters β and γ in equation 4.2 are determined from a oxygen mole balance as shown in equation 4.4, where β and γ are the stoichiometric coefficients for CO and CO_2 respectively.

$$o = \beta + 2 \cdot \gamma \tag{4.4}$$

In the studies by Zanza et al.[100] [101] and Vilas et al. [102] it was shown that for biomass the ratio between CO_2 and CO, denoted ω, in the devolatilisation gas varies between 0.1 and 0.2.

$$\frac{\gamma}{\beta} = \omega \in [0.1 : 0.2] \tag{4.5}$$

According to Fagbemi et al. the ratio between CO_2 and CO decreases with increasing temperatures due to an increase in the heterogeneous reaction between C(s) and CO_2 to produce CO [103].

4.1.2 Hydrocarbons in the devolatilisation gas

In equation 4.2 it is assumed that the light hydrocarbons are represented by C_2H_4 and CH_4. This assumption is in agreement with measurements performed at a full scale Waste-to-Energy plant, see section 5. The pyrolysis gas composition for selected fuels, at similar temperature and heating rates as experienced in waste-to-energy plants, has been determined in several studies. The resulting compositions from selected studies are shown in table 4.1 and 4.2.

Species	Kaminsky[104] Plastics 790°C Fluidized bed	Li et al. [105] MSW 850°C lab scale Rotary kiln	Kaminsky et al.[106] Digested sewage sludge 750°C Fluidized bed	Hajaligol et al. [107] Cellulose 1000°C lab scale reactor	Leung et al.[108] Wood powder 1000°C lab scale reactor	Tire powder 1000°C lab scale reactor	Zanzi et al.[101] Straw Free-fall reactor	Straw pellets Free-fall reactor
H_2	0.29	0.43	0.22	0.49	0.17	0.25	0.44	0.39
CO	0.03	0.29	0.24	0.34	0.45	0.03	0.46	0.48
CO_2	0.012	0.15	0.06	0.03	0.08	0.01	0.05	0.05
CH_4	0.46	0.12	0.20	0.07	0.10	0.40	0.05	0.24
C_2H_4	0.15	0.05	0.04	0.03	0.03	0	0	0.001
C_2H_6	0.04	0.03	0.02	0.03	0	0	0	0
CH_3OH	dna	dna	dna	0.013	dna	dna	dna	dna
CH_3CHO	dna	dna	dna	0.016	dna	dna	dna	dna
Other $C_xH_yO_z$	0.02	dna	1.7(wt%)	0.38(wt%)	dna	dna	0.001	0

Table 4.1: Laboratory pyrolysis measurements for selected fuels. The compositions have been presented as mass fractions.

Species	Birch 800°C Free-fall reactor	White quebracho 800°C Free-fall reactor	Zanzi et al.[100] Straw pellets 800°C Free-fall reactor	Bargasse 850°C Free-fall reactor	SCAR 850°C Free-fall reactor	Fagbemi et al.[103]* Wood 900°C Cylindrical reactor	Straw 900°C Cylindrical reactor
H_2	0.17	0.16	0.13	0.15	0.13	0.25	0.25
CO	0.51	0.50	0.46	0.56	0.53	0.54	0.53
CO_2	0.08	0.09	0.13	0.09	0.12	0.05	0.05
CH_4	0.16	0.18	0.18	0.16	0.13	0.12	0.12
$C_2H_4 + C_2H_2$	0.06	0.05	0.06	0.05	0.06	0.04	0.06
C_2H_6	0.03	0.03	0.03	0.03	0.03	-	-
CH_3OH	dna	dna	dna	dna	dna	dna	dna
CH_3CHO	dna	dna	dna	dna	dna	dna	dna
Benzene + toluene	0.01	0.02	0.02	0.02	0.01	dna	dna

*=C_2H_6 is included in $C_2H_4 + C_2H_2$ mole fraction
dna=Data Not Available
SCAR=Sugar Cane Agricultural Residue

Table 4.2: Laboratory pyrolysis measurements for selected fuels. The compositions have been presented as mass fractions.

The studies show a significant release of ethene and ethane during the pyrolysis. Ethane is neglected due to simplifications. In the study by Hajaligol [107] a significant amount of methanol was measured, compared with the amount of methane. Smaller alcohols are not included in the devolatilisation gas composition model.

In order to determine the methane and ethene average molar ratio in a devolatilisation gas from combustion of waste the amount of carbon, which is not used to produce CO and CO_2, is determined by equation 4.6.

$$\theta = \sigma + \phi = \alpha - (\beta + \gamma) \tag{4.6}$$

Where θ is the sum of the moles of carbon molecules in CH_4 and C_2H_4, ϕ is the mole fraction of carbon atoms in C_2H_4 and σ is the moles of carbon in CH_4. From the molar fractions of methane and ethene in table 4.1 and 4.2 a ratio between ethene and methane can be determined to range from 0.2 to 0.4; consequently the fraction of moles of carbon used for ethene compared to methane ϵ range from 0.4 to 0.8 as twice the moles of carbon are used in the ethene structure compared to the methane structure.

$$\frac{\phi}{\sigma} = \epsilon \in [0.4 : 0.8] \tag{4.7}$$

The amount of CH_4, σ, is found by solving equation 4.8. Solving this equation relies on the determination of other species, e.g. ethene.

$$\sigma = \frac{\theta}{1 + \epsilon} \tag{4.8}$$

4.1.3 The NO_x precursors

From measurements of the NO_x precursor speciation discussed in section 5 it is seen that the NH_3 accounts for the majority of the NO_x precursor concentration; NH_3 account for more than 80%, while the HCN accounts for less than 20% of total amount of precursors released. It is assumed that this ratio is valid for all MSW. The precursor speciation has, to the knowledge of the author, not been evaluated in other studies. All nitrogen, expect the fraction found in the char, is converted to NH_3 and HCN in the ration 4/5 according to equation 4.9 and 4.10.

$$NH_3 = \left(\frac{\alpha}{c} \cdot n \right) \cdot 0.8 \tag{4.9}$$

$$HCN = \left(\frac{\alpha}{c} \cdot n \right) \cdot 0.2 \tag{4.10}$$

Since the fraction of nitrogen in the fuel is significantly smaller than the hydrogen content, the hydrogen used for production of NH_3 and HCN is neglected.

4.1.4 Estimated devolatilisation gas

Using the calculation procedure shown in previous subsections the devolatilisation gas composition for a number of fuels have been estimated. The devolatilisation gas compositions estimated from ultimate and proximate analysis of municipal solid waste, a mixture of municipal solid waste (MSW) and refuse derived fuel (RFD) and cardboard are shown in table 4.3.

Table 4.3: The estimated composition of gas from devolatilisation of four selected fuels. The composition has been estimated by equation 4.2 using the assumptions presented above.

Composition of gas from devolatilisation of different fuels

	Ryu et al. [109] MSW (Vol % dry)	Frey et al. [110] 75% MSW & 25% RFD (Vol % dry)	Sørum et al. [111] Cardboard (Vol % dry)	Goddard et al. [112] MSW (Vol % dry)
CO	43.5	44.0	46.9	38.0
CO_2	6.5	6.6	7.0	5.6
CH_4	10.0	1.5	16.2	16.3
C_2H_4	3.4	0.5	5.3	5.4
H_2	35.6	46.6	24.4	32.5
NH_3	0.88	0.64	0.16	1.79
HCN	0.22	0.16	0.04	0.44

The composition of different types of biomass has been reported in the literature. Vilas et al. [102] reported pyrolysis gas compositions of wheat straw and poplar wood found through free-fall pyrolysis experiments at high heating rates [100] [101]. The results from this study are comparable with the estimated devolatilisation gas shown in table 4.3.

The average devolatilisation gas composition is estimated from the composition of the four samples above and has been shown in table 4.4.

Table 4.4: The average devolatilisation gas composition determined from the 4 fuel samples [109] [110] [111] [112] using the model set up in this study.

	Mole fraction dry
CO	0.44
CO_2	0.07
CH_4	0.12
H_2	0.33
C_2H_4	0.04
NH_3	0.008
HCN	0.002

The estimated devolatilisation gas composition is in agreement with the 15 biomass samples which have been measured in 7 different studies. The gas composition from these studies are shown in table 4.1 and 4.2.

4.2 Effect of the estimated gas composition on model reduction

The reduction of a detailed chemical kinetic model to produce a skeletal model is based on an estimation of a starting gas composition (important species). The development of skeletal models is highly dependent on the choice of starting gas composition, since these most reductions are based on simulation of a parameter; ignition delay time, rate of formation etc., that is dependent of the choice of starting gas composition. Especially the SEM-CM reduction method is dependent on the composition since this reduction method is based on ignition delay time simulations; hence this is dependent on the starting gas composition.

The purpose of the section is to evaluate if the estimated devolatilisation gas composition, which is to be used for model reduction, is dependent on the formation of NO. It is believed that if the formation of NO is highly dependent on a species the accuracy of the estimation of this species needs to be high. In this section the proposed composition of the devolatilisation gas upon NO_x is evaluated through Perfectly Stirred Reactor (PSR) simulations. The parameters that are evaluated are:

- Ratio between CO and CO_2

- Composition of light hydrocarbons

- Precursor speciation

The effect of the above mentioned parameters were evaluated using the detailed chemical kinetic model by Glarborg et al. [10].

4.2.1 Effect of CO/CO_2 ratio in the devolatilisation gas

The effect of the choice of ω, the ratio between CO_2 and CO, is evaluated on the formation of NO. A robust model is essential as the reduction of the detailed chemical kinetic model, and the development of a skeletal model, is based on estimations of the devolatilisation composition which acts as input parameter for the reduction procedure. The evaluation is done through PSR simulations in CHEMKIN 10131. The reactor conditions are shown in table 4.5.

Table 4.5: The conditions in the PSR used to evaluated the effect of changes in the devolatilisation gas composition upon formation of NO_x. For the modelling the detailed chemical kinetic model by Glarborg et al.[10] was used.

Parameter	Value
τ	1s
P	1.0 atm
V	100 cm^3
Solver type	Steady state solver
Unit selection	Mole fraction

The combustion is simulated using the detailed chemical kinetic model developed by Glarborg et al. [10]. This model was presented in chapter 6.2. Included in this model is high temperature NH_3 oxidation.

(a) NO formation at T=900°

(b) NO formation at T=1200°

(c) NO formation at T=1500°
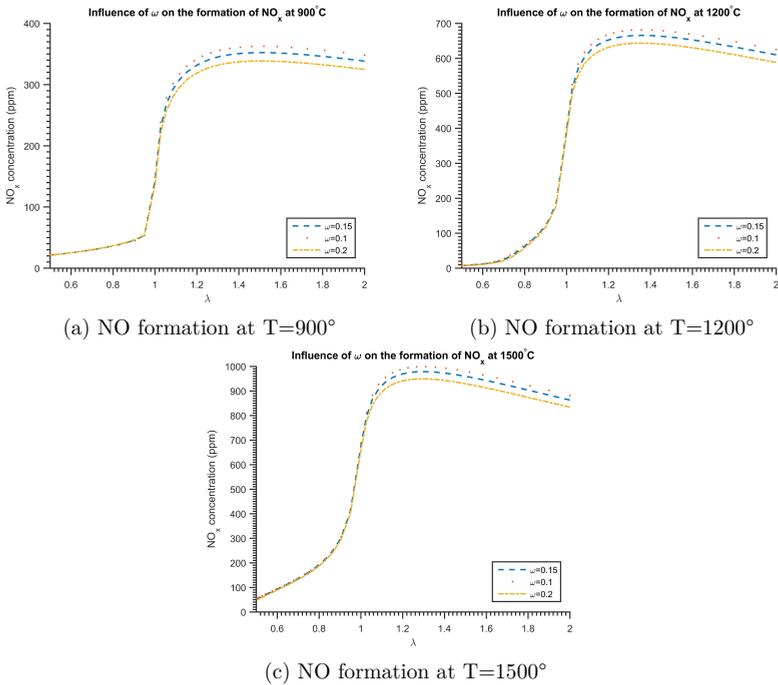
Figure 4.1: The formation of NO at T=900° and T=1500° found by simulation in PSR using CHEMKIN 10131. The Inlet composition of the gas to the PSR whas found using the simple model described in equation 4.2. The inlet gas composition was changes to see the effect of the choice of ω on the NO formation. The figure shows NO_x formation where ω has been set to 0.1, 0.15 and 0.2. The estimated devolatilisation gas composition is shown in table 4.4

In a reducing atmosphere no difference between the NO concentration after oxidation is experienced when ω is increased from 0.1 to 0.2. In an oxidizing atmosphere a slight difference is experienced. The difference in NO concentration when increasing ω from 0.1 to 0.2 is, however, less than 5%. Consequently the NO formation only slightly depended on the choice of ω within the allowed region.

4.2.2 The effect of the light hydrocarbons composition

As mentioned previously, it has been assumed that the light hydrocarbons released during devolatilisation are CH_4 and C_2H_4. As seen in table 4.1 and 4.2 smaller quantities of C_2H_6 are also released during devolatilisation of MSW. The effect of neglecting C_2H_6 on the NO formation is evaluated through PSR simulations using condition seen in table 4.5. Furthermore, in the study by Hajaligol et al.[107] significant amounts of CH_3OH was measured in the pyrolysis gas from pyrolysis of cellulose. An estimated ratio between CH_3OH and CH_4 of 1/5 was found. An alcohol level this high was only measured in one study. It was evaluated if a CH_3OH level corresponding to 1/5 of the CH_4 affects the formation of NO significantly. This was done by replacing an amount of

CH$_4$ corresponding to 1/5 of the initial amount with an equal amount of CH$_3$OH. The effect on the NO formation has been shown in figure 5.9

(a) NO formation at T=900°

(b) NO formation at T=1200°

(c) NO formation at T=1500°
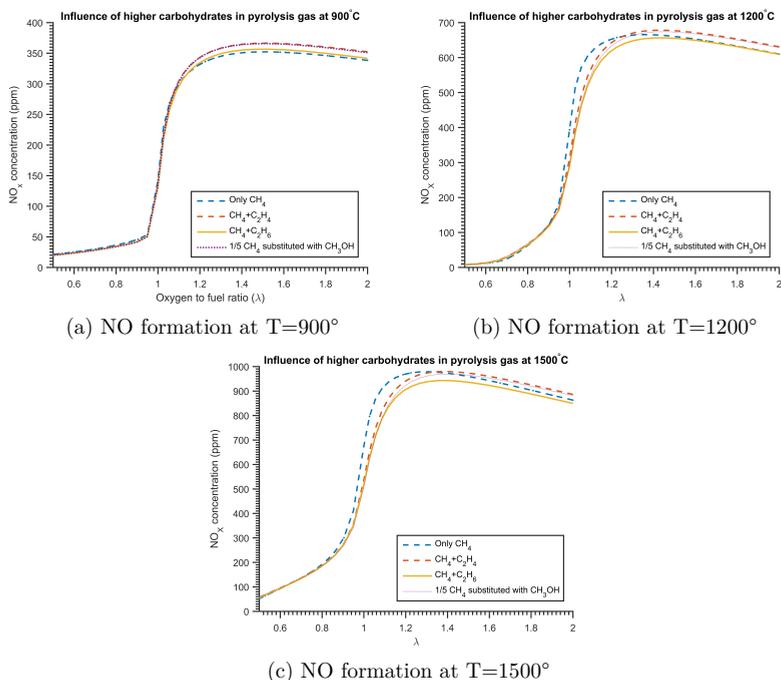
Figure 4.2: The formation of NO at T=900°, T=1200°, and T=1500° found by simulation in PSR using CHEMKIN 10131. The Inlet composition of the gas to the PSR whas found using the simple model described in equation 4.2. The inlet gas composition was changes to see the effect inclusion of higher hydrocarbons than CH$_4$.

The speciation of the light hydrocarbons with higher molar weights than CH$_4$ is relatively insignificant. No significant differences are seen in the predicted NO concentration when both C$_2$H$_4$ and C$_2$H$_6$ is present in the devolatilisation gas compared to a devolatilisation gas where only C$_2$H$_4$ is included. Furthermore, inclusion of an alcohol yields no significant difference in the NO$_x$ concentration. For simplification alcohols and C$_2$H$_6$ are not included in the devolatilisation gas composition model.

In the model the term 2·ϕ describes the ratio between C$_2$H$_4$ and CH$_4$. From previous studies shown in table 4.1 and 4.2, 2·ϕ has been estimated to range between 0.2 and 0.4. The influence of the choice of 2·ϕ has been evaluated through simulations for the condition of table 4.5. 2·ϕ was varied from 0.2 to 0.4 and the resulting NO concentrations are shown in figure 4.3.

(a) NO formation at T=900°   (b) NO formation at T=1500°
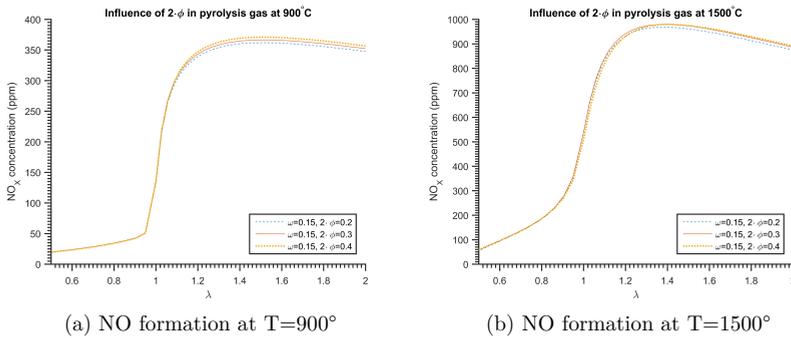
Figure 4.3: The formation of NO at T=900° and T=1500° found by simulation in PSR using CHEMKIN 10131. The Inlet composition of the gas to the PSR whas found using the simple model described in equation 4.2. The inlet gas composition was changes to see the effect of $2 \cdot \phi$ on the NO formation.

No significant differences in the NO concentration after oxidation of the devolatilisation gas with the two compositions ($2 \cdot \phi$=0.2 and $2 \cdot \phi$=0.4) is seen. At oxidizing conditions, where the largest difference occurs, the change in NO concentration is less than 5%. Consequently the choice of $2 \cdot \phi$ is believed to have no significant influence on the development of the skeletal model.

4.2.3 The effect of precursor speciation on the NO formation

It has been measured that the NO_x precursors during combustion of MSW consists of more than 80% NH_3 and less than 20% HCN. The speciation of the precursors were measured in this study at a full scale W-t-E plant. Measurements are shown in section 5. This assumption is evaluated as previously. In figure 5.10 the effect of the precursor speciation on NO_x formation is shown. 50% and 100% of the initial amount of NH_3 has been replaced by an equal amount of HCN to evaluate the effect of the choice of NO_x precursor.

(a) NO formation at T=900°

(b) NO formation at T=1500°
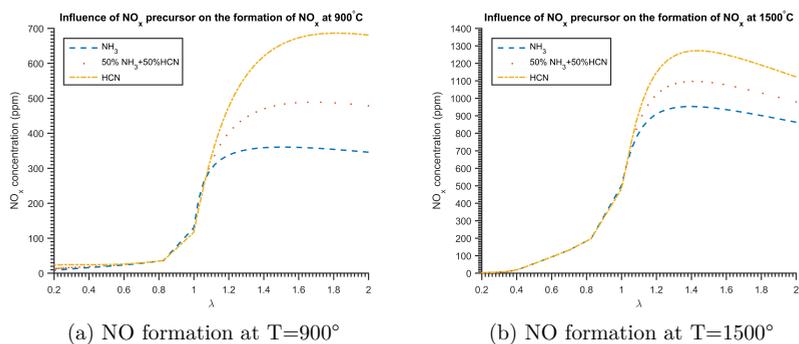
Figure 4.4: The formation of NO at T=900° and T=1500° found by simulation in PSR using CHEMKIN 10131. The inlet composition of the gas to the PSR has found using the simple model described in equation 4.2. The inlet gas composition was changes to see the effect of NO_x-precursor on the NO formation. The figure shows NO_x formation where all the NO_x-precursor is solely NH_3 and where 50% and 100% of the NH_3 has been substituted with an equal amount of HCN.

Correctly determining the precursor speciation is highly important in order to correctly calculate the NO concentration. At $\lambda \geq 1.1$ the choice of NO precursor has a great impact on the NO concentration. The difference decreases as the temperature is increased. At $\lambda \leq 1.1$ the choice of NO precursor becomes insignificant.

In the pyrolysis of biomass it has been shown that the NH_3 is released mainly as a primary product from pyrolysis [1]. For low rank coals, pyrolysed both at high and low heating rates, NH_3 was detected prior to HCN [113]. It is believed that this behaviour is due to direct cleavage of amino groups and amides during pyrolysis [1].Furthermore, it is proposed that, due to the dependence of heating rate on NH_3 formation, NH_3 is produced, along with the primary route, in a secondary reaction from HCN [114].

The heating rate and particle size has been shown to have substantial effects on the selectivity of NO precursors during pyrolysis. Increasing the particle size seems to favour the formation of NH_3 over HCN [1] [115] as this leads to an increased chance of secondary reactions [115]; hence the large particles and low temperatures in grate-firing W-t-E plants favour the formation of NH_3 over HCN.
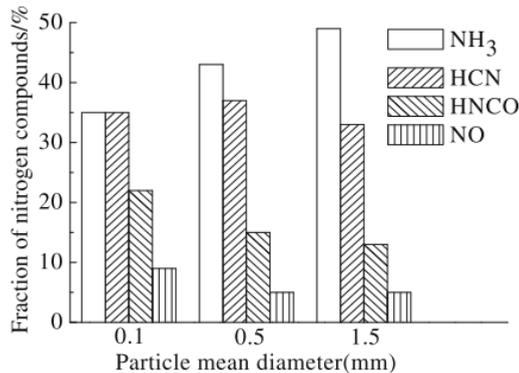
Figure 4.5: The speciation of nitrogen compounds formed during devolatilisation of straw an increasing particle sizes [115].The pyrolysis and gasification of wheat straw were carried out in a TG analyzer at a heating rate of 40°/min from room temperature to 800°C

A potential explanation for this behaviour is conversion of formed HCN to NH_3 by reaction with water[115].

$$HCN + H_2O \rightarrow NH_3 + CO \tag{4.11}$$

This reaction is favoured in larger particles due to longer diffusion paths for HCN in the particle [115]. During combustion of fine particles it has been shown that the dominating NO_x precursor is HCN [116] [117] [118]. HCN can represent up to 80% of the total amount of NO_x precursors during devolatilisation of fine particles [118], but as seen in figure 4.5 as the particle size is increased a substantial amount of NH_3 is formed, more that 50% of the total amount of NO_x precursors.

In grate fired Waste-to-Energy plants even larger particles are pyrolysed, giving rise to low internal heating rates. This favours the formation of NH_3 supporting the measurements that NH_3 is the main NO_x precursor during MSW combustion at grate-fired waste-to-energy plants.

4.3 Development of skeletal models for the NO formation using SEM-CM and PFA reduction methods

In this section the development of skeletal models will be reviewed. Furthermore the performance of the developed skeletal models will be evaluated. Each of the developed models, using the SEM-CM and the PFA reduction methods, respectively, will be analysed. Every reduction has been done based on the gas composition shown in table 4.4. The performance of each model will be evaluated through Perfectly Stirred Reactor calculations at 3 temperatures; 900°C, 1150°C and 1400°C and at an oxygen-to-fuel ratio ranging from λ=0.5 to λ=2. These conditions were chosen to cover most of the range of conditions found in the furnace of a W-t-E plant; see chapter 5.

4.3.1 Reduction strategy using the SEM-CM algorithm

The reduction of detailed chemical kinetic model by Glarborg et al. [10] was performed in two steps; initially a large skeletal model was created with a very low error, from this skeletal model 5 smaller skeletal models with varying size were created.

The large skeletal model with a very low error was created by combining skeletal models developed at a variety of conditions. The reduction is based on a simulation of the species profiles of the important species, it was found that the best reduction was achieved by reducing the models around the ignition time delay from 1/4 to 4 times the ignition delay time for each condition, for a gas with the composition as shown in Table 4.4 mixed with air at an oxygen-to-fuel ratio:

$$\tau_{sim} = \left[1/4 \cdot T_{ign} \; ; \; 4 \cdot T_{ign} \right]$$

$$\lambda = \left[0.1 \; 0.25 \; 0.5 \; 0.75 \; 1 \; 1.5 \; 2 \right]$$

At each of these oxygen-to-fuel ratios a reduction at 4 temperatures was done.

$$T = \left[1050 \; 1300 \; 1550 \; 1800 \; \right] K$$

This corresponds to $7x4$ reductions, hence 28 skeletal models were created each valid at only one of the 28 conditions. The reduction was performed at a depth level of 128, resulting in 28 skeletal models. These were merged to create 1 skeletal model valid in the whole parameter space. The results of the initial model reduction was a 56 species and 1160 reaction skeletal model with an root mean square error of 4% compared with the full model.

This skeletal model was used for further reduction. A single reduction of the skeletal model at all 28 conditions were performed using the same depth level. A larger skeletal model was created initially by merging 28 smaller skeletal models to limit the computational efforts, as reduction of detailed chemical kinetic model at all 28 conditions is very time consuming. The reduction of the 56 species and 1160 reaction skeletal model resulted in 5 skeletal models with increasing size as shown in table 4.6.

Model no.	Species	Reactions
1	32	162
2	36	225
3	38	251
4	38	570
5	46	500

Table 4.6: Developed skeletal models using the SEM-CM

All of these models are tested against the detailed chemical kinetic model in section 4.3.

4.3.2 Accuracy of the developed SEM-CM skeletal models

Skeletal models developed using the SEM-CM algorithm has been compared to the detailed chemical kinetic model developed by Glarborg et al. [10] at the conditions given above and are shown in figure 4.6.

In figure 4.6 the 3 figures to the left shows the NO formation at 900°C, 1150°C and 1400°C at increasing oxygen-to-fuel ratios, while the 3 figure to the right shows the NH_3 oxidation at increasing oxygen-to-fuel ratios.

All the developed models overpredict the NO formation slightly at oxygen-to-fuel ratios above approximately λ = 1.1 This is consistent for all the developed models and the overprediction might have been avoided if the SEM-CM reduction was conducted at additional over-stoichiometric conditions, as seen in section 3.5. For under-stoichiometric oxidation of the devolatilisation gas all models accurately predictions the NO concentration at temperatures above 1150°C. At 900°C the 32 species and 162 reactions skeletal model overpredicts the NO formation dramatically. It is expected that this model underperforms compared to the rest of the developed models due to the small size. At the 3 temperatures the 4 larger skeletal models performs well with a slight overprediction of the NO at large oxygen-to-fuel ratios ($\lambda > 1.1$)
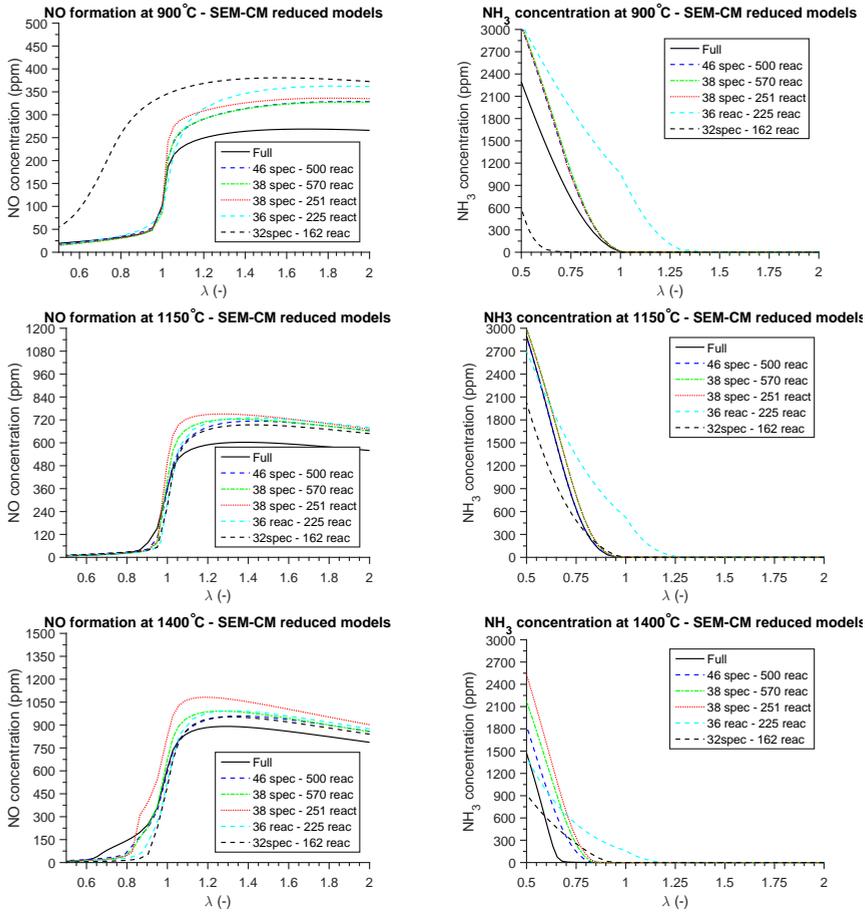
Figure 4.6: modelling of the formation of NO and oxidation of NH$_3$ as a function of the oxygen-fuel (λ) in a PSR with residence time $\tau = 20ms$ at 900, 1150 and 1400° using inlet gas composition shown in table 4.4. The NO$_x$ formation and NH$_3$ oxidation was modelled using the detailed chemical kinetic model by Glarborg et al. [10] and 5 skeletal models of varying size developed by the SEM method [95]

The predicted NH$_3$ concentration is higher at understoichimetric conditions for all the developed skeletal models except the 32 species and 162 reaction model. At low and high temperatures, T < 900°C and T > 1400°C, and very understoichiometric conditions, $\lambda = 0.5$, the predicted NH$_3$ using the skeletal models are relatively high compared to the NH$_3$ concentration predicted using the full model. At the same time the predicted NO concentration using the skeletal models are comparable with the NO concentration predicted with the full model. The underprediction of the NH$_3$ oxidation is be due to the removal of intermediate species during the model reduction.

The skeletal model with the best performance is the 46 species and 500 reaction model. This model best captures the NO formation and the NH$_3$ oxidation. However, the larger the model the longer the simulation time in a CFD code. For this reason it can

be of an advantage to use as small a model as possible. The best compromise between between modelling results and model size is the 38 species and 251 reaction skeletal model. Reducing the size more will induce large errors in either the NO formation or in the NH_3 oxidation.

4.4 Reduction strategy using the PFA algorithm

The reduction of the detailed chemical kinetic model by Glarborg et al. [10] resulted in 3 skeletal models with increasing size as shown in table 4.7.
A gas with the composition as shown in Table 4.4 mixed with air at an oxygen-to-fuel ratio:

$$\lambda = [0.1\ 0.25\ 0.5\ 0.75\ 1\ 1.5\ 2]$$

At each of these oxygen-to-fuel ratios a reduction at 10 temperatures was done.

$$T = [900\ 1000\ 1100\ 1200\ 1300\ 1400\ 1500\ 1600\ 1700\ 1800]K$$

The reduction was performed based on species importance on the production and consumption fluxes of a given production. A reduction at each temperature and stoichiometry was preformed. This corresponds to $10x7$ reductions, hence 70 skeletal models were created each valid at only one of the 70 conditions. These were automatically merged to create 1 skeletal models valid in the whole parameter space. The size of the final skeletal model was controlled by varying the interaction coefficient δ; the larger the interaction coefficient the smaller the mechanism (See chapter 3.

Model no.	Species	Reactions
1	32	207
2	38	265
3	50	409

Table 4.7: Developed skeletal models using the PFA method

All of these models are tested against the detailed chemical kinetic model in section 4.4.1.

4.4.1 Accuracy of the developed PFA skeletal models

Skeletal models developed using the PFA algorithm has been compared to the detailed chemical kinetic model developed by Glarborg et al. [10] at the conditions given above and are shown in figure 4.7.
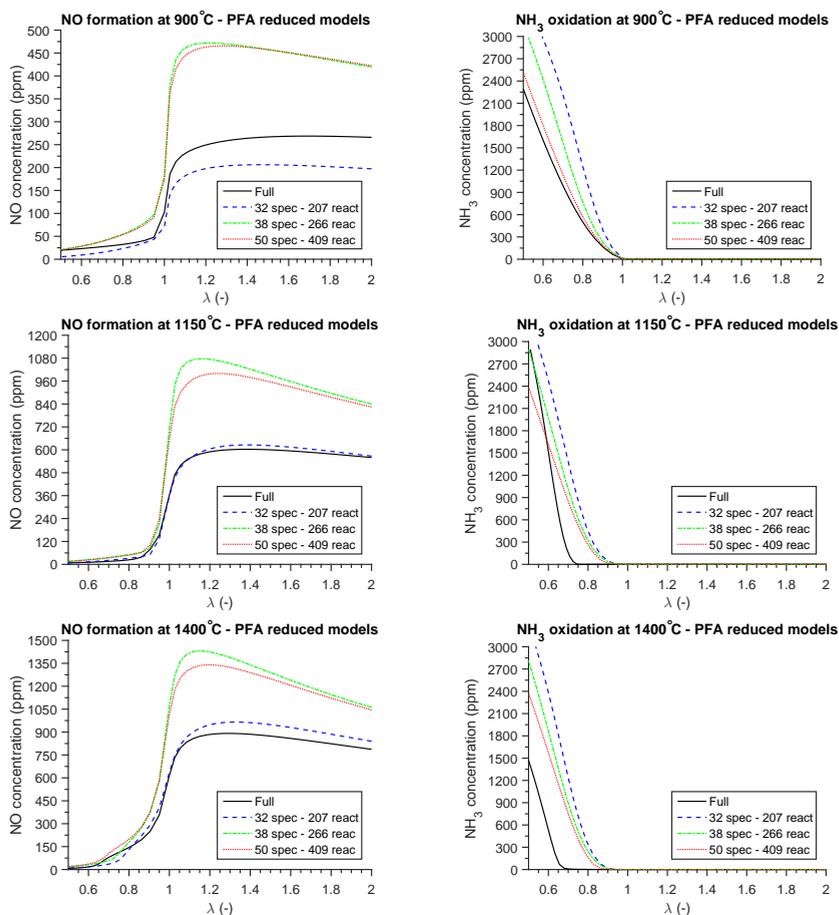
Figure 4.7: modelling of the formation of NO and oxidation of NH_3 as a function of the oxygen-fuel (λ) in a PSR with residence time $\tau = 20ms$ at 900, 1150 and 1400° using inlet gas composition shown in table 4.4. The NO_x formation and NH_3 oxidation was modelled using the detailed chemical kinetic model by Glarborg et al. [10] and 3 skeletal models of varying size developed by the SEM method [97]

The NO prediction using the larger skeletal models developed using the PFA algorithm, the 50 species and 409 reactions model and the 38 species and 266 reactions model, shows a large overprediction of the NO formation compared to the full model, especially at overstoichiometric conditions. The small model, 32 species and 207 reactions, predicts the NO formation accurate compared to the full model, slightly underpredicting the formation at low temperatures and slightly overpredicting the formation at high temperature.

The NH_3 oxidation, on the other hand, is poorly predicted by the small model. Large deviations in the NH_3 concentration between the full model and the small model at understoichiometric conditions are seen. A consequence of this might be unreliable results from CFD modelling. However, since the small models predicts the NO formation well

it is further analysed.

For further analysis of the most promising models, the 38 species and 251 reactions model developed using the SEM-CM algorithm and the 32 species and 207 reactions model developed using the PFA algoritm, PFR simulations were made comparing the models with the full model.
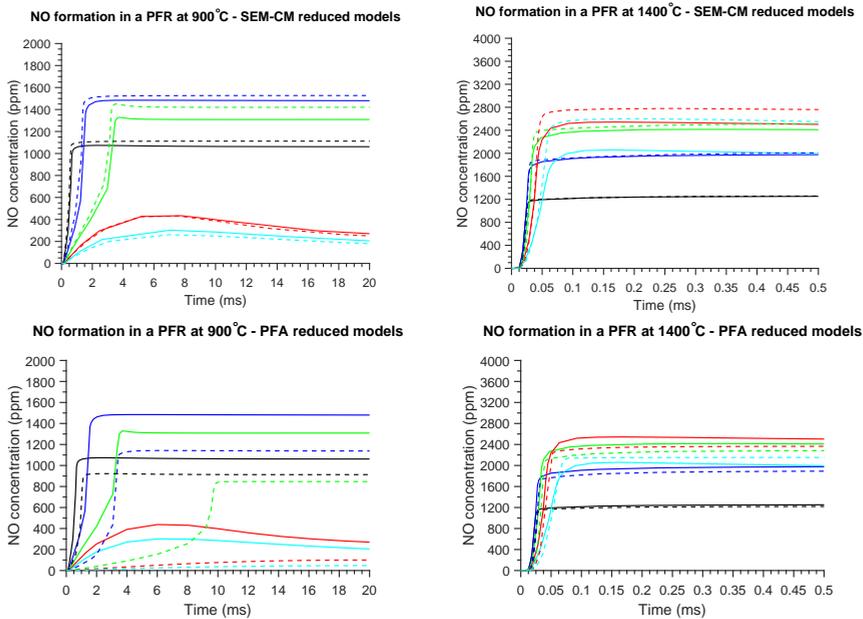
Figure 4.8: modelling of the formation of NO as a function of the reactor residence time in a PFR at 900 and 1400° and varying oxygen-to-fuel ratio (λ) using inlet gas composition shown in table 4.4. The NO_x formation was modelled using the most promising skeletal models developed in this study using the SEM method [95] and the PFA method [97]. -=Full model and −=skeletal model. Black:λ=2, Blue:λ=1.625, Green:λ=1.25, Red:λ=0.875 and Cyan:λ=0.5

The most extreme cases were modelled, this being at temperatures T=900°C and 1400°C. To the left in figure 4.8 results from low temperature simulations are shown while to the right results from high temperature simulations have are shown. The PFR simulations have been performed at 5 oxygen-to-fuel ratios, λ=2, 1.625, 1.25, 0.875 and 0.5, at residence times 20ms and 0.5ms for the low temperature and high temperature case respectively.
Results show that the SEM-CM reduced model is in good agreements with the full model for all oxygen-to-fuel ratios at both low and high temperature. The PFA reduced model, however, is in good agreement with the full model at high temperatures for all oxygen-to-fuel ratios but not at low temperatures. For $\lambda < 1.625$ the PFA reduced model does not capture the time depended formation of NO. At low oxygen-to-fuel ratios the NO is formed significantly slower with the PFA reduced model compared with the full model. However, similar NO concentrations are obtained after long residence times.

Similar plots were made for the NH$_3$ oxidation on PFR's.
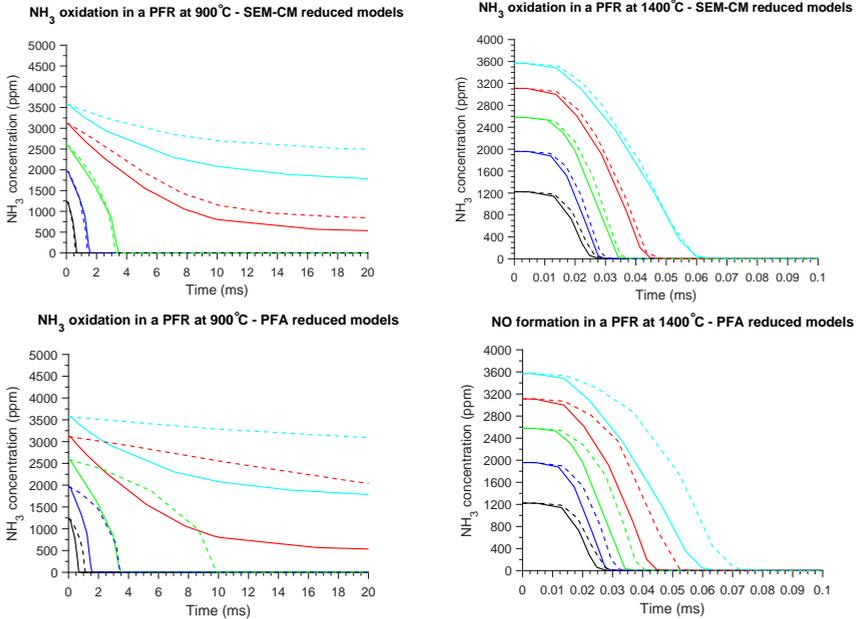
Figure 4.9: modelling of the oxidation of NH$_3$ as a function of the reactor residence time in a PFR at 900 and 1400° and varying oxygen-to-fuel ratio (λ) using inlet gas composition shown in table 4.4. The NO$_x$ formation was modelled using the most promising skeletal models developed in this study using the SEM method [95] and the PFA method [97]. -=Full model and --=skeletal model. Black:λ=2, Blue:λ=1.625, Green:λ=1.25, Red:λ=0.875 and Cyan:λ=0.5

High temperature oxidation of NH$_3$ is simulated relatively accurate using both skeletal models. Low temperature oxidation of NH$_3$ can not be modelled accurately at low oxygen-to-fuel ratios using the PFA reduced skeletal model as seen in figure 4.9, while low temperature oxidation of NH$_3$ is modelled with great success using the SEM-CM reduced model at all conditions.

Like for NO formation, at low oxygen-to-fuel ratios the NH$_3$ is oxidized significantly slower with the PFA reduced model compared with the full model. For this reason one is encouraged to use the SEM-CM reduced skeletal model to avoid significant simulation error in a CFD model. The particular difference between the two skeletal models is a consequence of the reduction method; the SEM-CM method is based on minimisation of the error on the important species profiles between the detailed chemical kinetic model and the skeletal model through simulations.

4.5 Summary

A number of skeletal models were developed from reduction of the detailed chemical kinetic model by Glarborg et al. [10] using both the simulation error minimization connectivity method (SEM-CM) and the path flux analysis method (PFA). The accuracy of the models were tested by comparing ideal reaction simulations, using CHEMKin, of the skeletal models and the detailed chemical kinetic model from which they were developed. It was shown that skeletal models developed using the SEM-CM algorithm with more that 36 species describe the NO_x formation well, while skeletal model with more than 38 species also describe the oxidation of NH_3 well.

Furthermore, it was shown that the 32 species skeletal model developed by the PFA algorithm describes the NO_x formation well. However, this model does not describe the oxidation of NH_3 to the desired degree.

Based on the accuracy of the skeletal models determined by ideal reaction simulations it was concluded that the 38 species and 251 reactions skeletal model developed using the SEM-CM algorithm offers the best compromise between model size and accuracy. This model will be used later in this thesis for NO_x formation simulation using CFD.

Chapter 5

Full scale measurements of the NO$_x$ precursors and major species concentrations above the grate at a Waste-to-Energy plant

This chapter includes a manuscript which has been submitted to the journal "Fuel" in the spring of 2017. The manuscript was accepted for publication on the 27th of February 2018; see comments from reviewer and editor in appendix B. The focus of this manuscript is measurements of the NO$_x$ Precursors and major species concentrations above the Grate at a Waste-to-Energy plant. The manuscript also include an evaluation of the influence of the speciation of the NO$_x$ Precursor on NO$_x$ formation.

5.1   Introduction

In order to achieve a satisfactory result from CFD modelling of NO$_x$ formation during combustion of waste in grate-fired waste-to-energy plants an accurate description of the temperature field in the free-board is essential, due to the dependency of the temperature on the low temperature fuel NO$_x$ chemistry [1][119]. Modelling of the temperature field in the free-board relies on an accurate determination of the boundary conditions, e.g., species concentrations, gas temperature and gas velocity from the bed into the computational domain. Most CFD models of grate-fired waste-to-energy (W-t-E) plants use a stand-alone model of the bed, describing the waste devolatilisation and the partial oxidation of volatiles. The volatile oxidation is strongly coupled to the combustion of gaseous species in the free-board due to the radiation onto the bed as indicated in figure 5.1.

Figure 5.1: Schematic overview of the procedure for CFD modeling of solid fuel combustion in grate-firing units

Coupling the devolatilisation of the fuel and partial oxidation of the volatiles in the bed with the combustion of gaseous species in the free-board has been applied with success in previous studies [5][109]. Recently the NO precursor concentrations were measured at a full-scale waste-to-energy plant [120]. However, the measurements were limited to two fixed positions above the grate. The objective of this study is to measure the gas temperature and species concentrations just above the fuel bed in a full-scale W-t-E plant. The gas species concentrations are measured by gas extraction and use of FTIR spectroscopy in four fixed positions above the bed. By suction pyrometer the gas temperatures were measured concurrently to the species concentrations. The results are useful for evaluation of bed models and will provide a more accurate description of the temperature field in the free-board. The species measurements include the NO_x precursors released from the bed. Based on the results, the importance of the partitioning of NO_x precursors on the formation of fuel NO_x in grate-fired W-t-E plants is discussed.

5.2 Plant and grate characteristics

Over a span of three days the gas composition and temperatures above the bed from combustion of municipal solid waste (MSW) were measured. All measurements were performed at Affald+, a W-t-E plant located in Næstved, Denmark. The W-t-E plant has a nominal waste capacity of 8.2t/h. During the days of measurements the plant was operated slightly below nominal capacity as seen in table 1. The plant uses the Dynagrate® grate technology. The grate is a single-lane grate, with dimensions 10.6x4m. The grate has been split into four zones with lengths of 2.8, 2.7, 2.7 and 1.8 meter, respectively. Predefined fractions of the primary air can be distributed to each zone.

5.2.1 Plant operation

During the three days of measurements, the waste-to-energy plant was running stable without any malfunctions or shut-downs. The plant was operated with an oxygen set point of 6 vol% (wet) and a steam production of 9.5 kg/s as shown in table 1. The

steam pressure was kept at a constant value of 55.6±0.1bar with a steam production of 9.±0.1kg/s corresponding to full capacity. During the measurement campaign the plant was operated under two different settings, as seen in table 5.1 and figure 5.2, to evaluate the effect of primary air distribution on the concentration profile of combustibles, water, CO_2 and NO_x precursors. The tonnage was changed between the two plant settings to accommodate the changes in heating value of the fuel. The tonnage is lower that the yearly average of 9 ton/h [121] due to the high heating value of the waste, which in the period of measurements contained large quantities of dry waste wood.

Table 5.1: Specifications of Affald+ line 4 during the three days of measurements.

	Air dist. 1	Air dist. 2
Waste feed (tons/h)	7.2±1.6	7.3±0.9
Avg. heating value (MJ/kg)	13.5±1.2	13.8±0.5
Avg. primary air (Nm3/h)	17,454±1808	20,215±2017
Fraction on grate section 1	0.20	0.20
Fraction on grate section 2	0.35	0.27
Fraction on grate section 3	0.35	0.43
Fraction on grate section 4	0.10	0.10
Avg. secondary air (Nm3/h)	10,851±326	10,847±300
Temp. primary air (°C)	45.5±3.2	45.9±3.6
Temp. secondary air (°C)	41.9±0.6	40.6±0.6
Avg. O_2 (% wet)	6.3	6.2
Steam production (kg/s)	9.5	
Steam temperature (°C)	400	
Steam pressure (bar)	55.6	
Grate dimension	10m long, 6m wide	

The average waste feed and heating value of the fuel for the period of measurements provide data for an estimation of the waste composition. The waste composition was estimated based on correlations between waste feed and heating value established over a long period of time by B&W Vølund. In table 5.2 the estimated waste composition has been shown.

Table 5.2: Estimated waste composition based in the fuel input (tons/h) and the lower calorific value of the fuel (MJ/kg).

Component	wt %
C	0.311
H	0.044
O	0.184
N	0.011
S	0.002
Cl	0.007
Moisture	0.275
Ash	0.166

The primary and secondary air flows were obtained from the plant control system. The changes in primary air distribution involved only sections 2 and 3 on the grate. The

fractions of air on grate 1 and 4 were unchanged as grate 1 acts to dry the waste and grate 4 mainly serves as ash transport; full conversion of the waste has occurred on the previous 3 sections.

Figure 5.2: The fraction of the total amount of primary air distributed under the grate for plant setting 1 and 2.

5.3   Gas phase composition and temperature measuring system

The flue gas composition was measured with a 6 meter water cooled probe. The temperature in the center of the probe and from end of the probe to the cooler was kept at 150°C to avoid water condensation. Prior to the O_2 analyzer the gas is cooled to 5°C to remove any water and aerosols. The system allows simultaneous IR, UV and O_2 measurements. Attached on the probe was a non-cooled suction pyrometer of equivalent length. This secured species concentration measurements and gas temperature measurements at equivalent locations at the same time. The concentrations of species CH_4, C_2H_2, C_2H_4, CO, CO_2, NH_3, HCN and H_2O were measured. The probe was inserted through an opening in the roof of the furnace in front of the fuel inlet. The probe was manually inserted into the furnace at a defined angle and distance. The species concentrations and gas temperature were measured at four predefined locations in the furnace close to the fuel bed. In figure 5.3 the four points of measurement have been shown as circles. Furthermore the size of each grate-section and distance from the measuring point to the grate are indicated. Depending on the position on the grate the fuel bed can be as thick as 1m. The opening is shown in figure 5.3 as a 45° cone in the front roof of the furnace. The insertion length and insertion angle of the water cooled probe is shown in table 2, corresponding to the measuring point shown in figure 5.3. The point closest to the fuel inlet (left in figure 5.3) is referred as measuring point 1, while the point closest to the ash pit (right in figure 5.3) is referred to as measuring point 4.
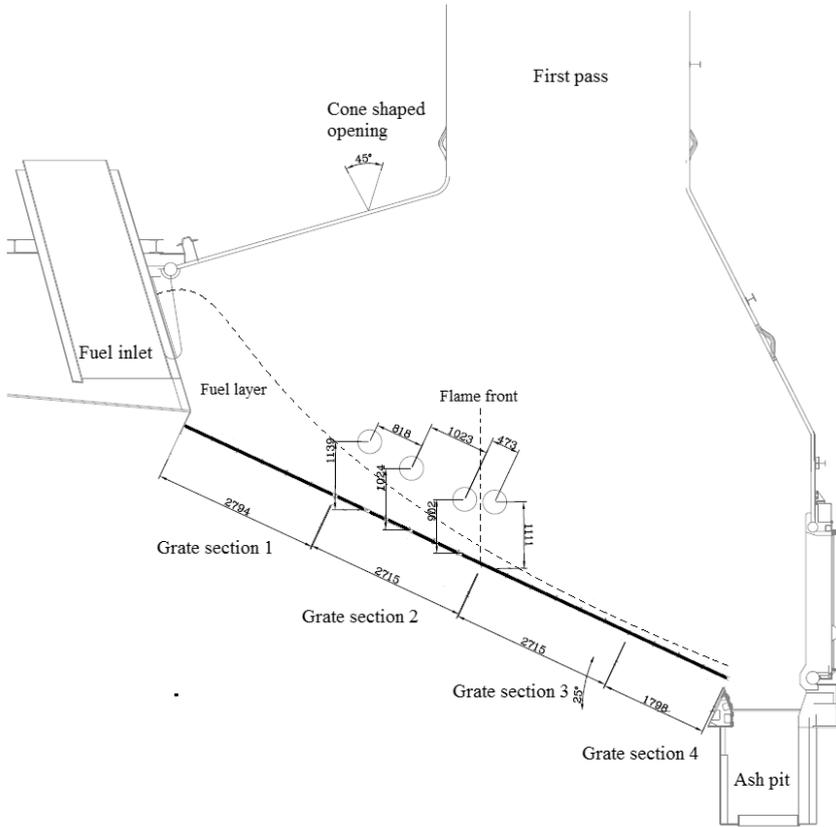
Figure 5.3: Schematic drawing of the furnace. The measuring points are shown as circles. Measuring point 1 is closest to the fuel inlet, while measuring point 4 is closest to the ash pit. The dotted line shows the predicted height of the waste layer, the thick solid line shows the grate surface and the vertical dotted line shows the flame front during the experiments

Table 5.3: The insertion length from the cone shape opening to the measuring point and insertion angle of the water cooled probe into the furnace. The points are shown in figure 5.3 as well.

Measuring point	Distance (m)	Angle °
1	4.4	0
2	5.0	9
3	6.0	18
4	6.0	23

Concentrations of the above mentioned species have been determined from FTIR absorption measurements with use of Bomen MB100 FTIR spectrometer with built-in IR

light source and external DTGC detector. The gas sampling was performed at a constant flow rate of 3 Nl/min controlled by an EL-Flow type Bronkhorst mass flow controller with a response time from 0% to 98% signal level of the gas sampling system of about 50s. Concentrations of CO, CO_2, hydrocarbons, NH_3, HCN and water were determined by FTIR measurements. The O_2 concentration was determined using a Siemens O_2 paramagnetic analyzer. The main sampling parameters were continuously logged by an Agilent BenchLink Data Logger. The temperature of the gas in the sampling line was kept constant at 150°C to avoid condensation of water and light tar products. To avoid blockage of the system, two thimble filters were installed along the heated line to remove particles, soot, heavy tars and aerosols. The system was leak tight and allowed for operation between 1000mbar and 500mbar, limited by the lowest pressure of the O_2 analyzer. After analysis of the flue gas by IR/UV absorption measurement the gas was cooled for water removal for determination of the O_2 concentration. A schematic overview of the measuring system is shown in figure 5.4.

Figure 5.4: Schematic overview of the gas phase composition and temperature measuring system.

Analysis of the spectral data was performed with an in-house software at the Technical University of Denmark[122]. The software uses the latest spectral databases HITRAN/HITEMP for analysis of IR spectral data in the spectral range from 400 cm^{-1} to 6000cm^{-1}. The pressure in the sampling system was determined and variations have been taken into account in the data analysis. The uncertainties in the measurements are mainly defined by the uncertainties in the spectral databases and by the S/N ratio in the measured spectra. The uncertainties are shown in table 3.

5.4   Measurement results

The measurements are analyzed and discussed in this section. The gas temperature profiles for both plant settings are shown in figure 5.5. In figure 5 the profile of the water vapor content in the flue gas for plant setting 2 is shown, while the species concentrations; CH_4, C_2H_2, C_2H_4, CO, CO_2, NH_3 and HCN are shown in figures 5.8-5.10. All measurements were performed at a distance approximately 50cm above the fuel bed depending on bed thickness

Table 5.4: The uncertainties in the extractive IR measurements. The uncertainty has been shown as relative %.

Species	Relative uncertainty
	Rel. %
H_2O	2
CO_2	3
CO	2
CH_4	3
C_2H_2	10
C_2H_4	7
HCN	8
NH3	5

5.4.1 Gas temperature profile

The gas temperature was measured continuously by a suction pyrometer attached on the side of the water cooled probe. The thermocouple was calibrated after the measurements at the thermometry facilities at DTU. The gas temperature profiles for both plant settings are seen in figure 5.5.
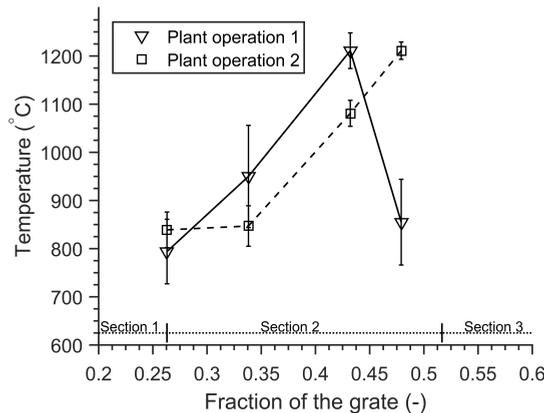
Figure 5.5: The gas temperature profile for the two plant settings (shown in table 1) measured by suction pyrometer. The grate sections of the Dynagrate® have been shown in the figure 5.3 as well.

The temperature increases along the grate from measuring point 1 to 3. The low temperature at the initial part of the grate is a consequence of fuel drying, as seen from the large water content in the flue gas shown in figure 5.7, and devolatilisation of the solid fuel. Lower gas temperatures are experienced in point 2 and 3 for the plant setting 2. This is attributed to a lower degree of oxidation in this region as a result of a lower fraction of the total primary air being provided on grate section 2 compared to that at plant setting 1, see figure 8 and 9. The maximum gas temperature for the two plant settings are in the same region; 1150-1250°C. The peak temperature is expected

to be a consequence of the char oxidation occurring in the region, this is supported by observations from the inspection window at the ash pit and figure 5.6, showing the position of the probe at measuring point 4. The location of the tip of probe is outside of the flame region during plant setting 1. This indicates that devolatilisation has been completed and char oxidation is occurring. The tip of the probe was in the flame region during plant setting 2 indicating combustion of the volatiles; this is supported by the higher temperature at measuring point 4 during this plant setting.

Figure 5.6: Picture of the combustion of waste on a grate at Affald+ during the measurements in this study. The probe is measuring in measuring point 4 during plant setting 2. The tip of the probe is outside of the flame region; the devolatilisation zone.

As a large fraction of the total primary air is provided under grate section 3 instead of grate section 2, during plant setting 2, the position of the peak gas temperature is moved towards the ash pit. The shift in gas temperature may cause a change in the release profile of species from the solid bed due to the dependency of temperature on the pyrolysis products formation [101][123] and on the position of the char oxidation on the grate.

5.4.2 Water concentration profile

Considerable water vapour concentrations in the flue gas will appear in regions where the fuel is dried. Drying of the fuel occurs initially in the combustion process for which reason the water content is expected to have a maximum above grate section 1.
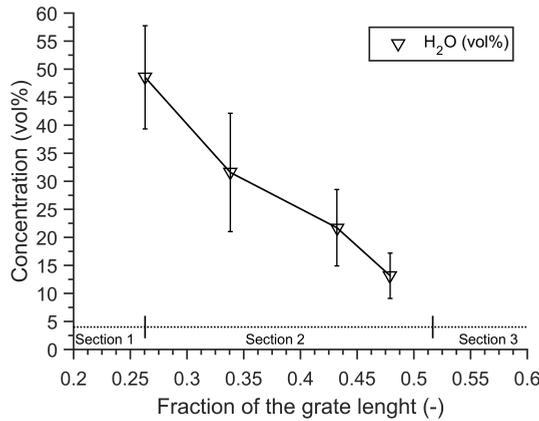
Figure 5.7: The water concentration profile above the fuel bed.

The water concentration decreases linearly from the beginning of grate section 2 to the end of grate section 2. The level is highest at point 1 due to drying of the fuel. Downstream of section 1, water is mainly formed by oxidation of volatiles and the concentration approaches zero above the latter part of the grate where char oxidation has terminated.

5.4.3 Concentration profile of CO and CO_2 along the fuel bed

The most pronounced difference between the CO and CO_2 concentration profiles for the two plant settings are the shapes as seen in figure 5.8. For plant setting 1 the concentration of CO gradually decreases, while the CO_2 concentration increases, from the initial part of grate section 2 to the latter part. For plant setting 2 the CO and CO_2 concentrations are somewhat constant along the grate section before the CO concentration drops to about 0% at measuring point 4; close to the intersection between grate section 2 and 3. Higher CO concentration at measuring point 3, the latter part of grate section 2, indicates a lower degree of oxidation due to the limited oxygen availability. This is a consequence of the lower amount of primary air supplied under grate section 2. The measurements indicate that the concentrations of CO and CO_2 at this point depend on the plant settings, i.e., the distribution of primary air on the second and third grate section.

(a) Plant operation 1

(b) Plant operation 2

Figure 5.8: The concentration profiles of CO, CO_2 and O_2 along the grate during plant operation 1 and 2 (table 1).

The O_2 concentration is very low corresponding to a fuel rich zone at measuring point 1, 2 and 3 as a result of under-stoichiometric oxidation of the gas released from the bed. However, during plant setting 1 significant amounts of oxygen was measured at measuring point 1 and 2 along with larger amounts of CO and hydrocarbons. This may be a consequence of insufficient mixing of the combustible gasses and the oxidizer. This phenomenon is more pronounced during plant setting 1 where a larger fraction of the total combustion air was supplied in the region where measurements were done. From point 3 to point 4 a significant decrease in the CO concentration and an increase in the O_2 concentration were measured for both cases due to larger oxygen availability. It is expected that the devolatilisation process has been completed at this point. This is supported by hydrocarbon measurements, as discussed below.

From position 3 to 4 a more pronounced decrease in the CO concentration is experienced for plant setting 2 as the CO concentration is higher in the initial part of the grate due to limited oxygen availability caused by the primary air distribution. The results indicate that the release profile of gaseous products, CO, hydrocarbons and NO_x precursors, from the bed is unaltered as the primary air distribution changes; it is merely the degree of oxidation that changes.

5.4.4 Hydrocarbon concentration profile along the fuel bed

The major combustible released from the waste bed is CH_4. Also substantial amount of C_2H_4 is produced, along with small amounts of C_2H_2 as shown in figures 5.9a and 5.9b.

(a) Plant operation 1
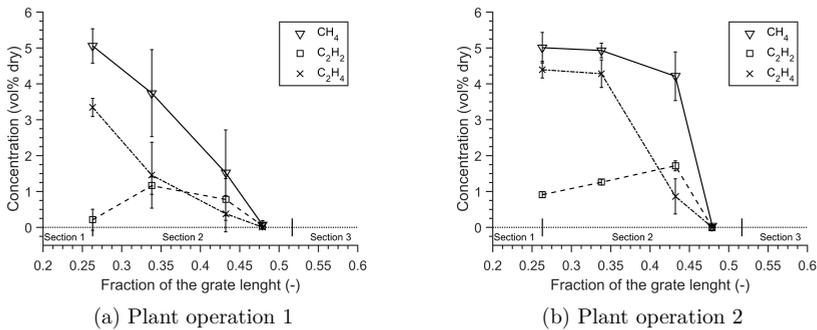
(b) Plant operation 2

Figure 5.9: The concentration profiles of the major hydrocarbon species during combustion of MSW along the grate during plant operation 1 and 2 (table 1).

It is evident that the concentrations of the major hydrocarbons are significantly lower at measuring point 2 and measuring point 3 under plant operation 1, presumably due to a larger supply of oxygen, promoting oxidation. The observations are supported by the CO and CO_2 measurements (figures 5.8a and 5.8b), which show a larger degree of oxidation for plant setting 1.

A roughly linearly decrease in the CH_4 and C_2H_4 concentrations from point 1 to point 4 was measured during plant setting 1, while the CH_4 concentration from point 1 to 3 was more or less constant during plant setting 2, presumably due to the lower oxygen availability. From point 3 to point 4, the CH_4, C_2H_4 and C_2H_2 concentrations decrease rapidly. At point 4 none of the major hydrocarbons were measured for any of the two plant settings, showing full oxidation of the combustible gasses from the bed. High CO_2 concentrations at this measuring point indicate that char oxidation is occurring. This is supported by figure 5.6 where it is seen that the position of the probe tip is outside the flame region.

Smaller amounts of C_2H_2 were measured above the bed during both plant settings. Initially the concentration is negligible compared to the CH_4 and C_2H_4 concentration. However, at the end of grate section 2 (measuring point 3) the C_2H_2 concentration exceeds that of C_2H_4. The larger C_2H_2 concentration at the end of grate section 2 is expected since it is an intermediate product of oxidation of higher hydrocarbons.

The composition of the hydrocarbons measured in this study is in agreement with measurements reported in literature. The gas compositions from rapid pyrolysis of biomass in a drop-tube reactor [101][100] and of digested sewage sludge in a fluidized bed [106] show a similar partitioning of hydrocarbons.

5.4.5 Concentration profiles of HCN and NH3 pre-cursors from the solid fuel bed

Concentration profiles of NO_x precursors from the waste bed have, to the knowledge of the authors, not previously been reported in literature. From a NO_x modelling perspective the concentration profiles of these species are essential to effectively model the NO_x formation in CFD. Concurrent to the hydrocarbon, CO, CO_2 and H_2O concentrations, the NH_3 and HCN profiles were measured and are shown in 5.10a and 5.10a.

(a) Plant operation 1
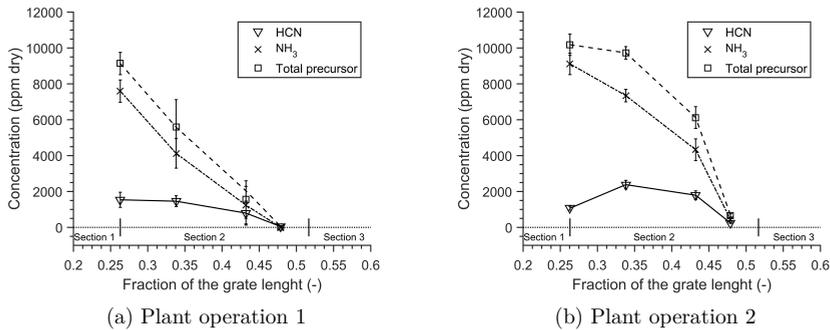
(b) Plant operation 2

Figure 5.10: The concentration profiles of the major NO$_x$ precursors during combustion of MSW as a function of the grate length during plant operation 1 and 2 (table 1.

The profiles for NH3 and HCN during plant setting 1 are similar to those of CH$_4$ and C$_2$H$_4$. The concentrations of NO precursors peak at a high level of approximately 10000ppm at point 1, after which they decrease to low levels at point 4, as seen in 5.10a and 5.10a

For plant setting 2 a constant total precursor concentration was measured from point 1 to point 2 after which the concentration drops to about 0 at point 4. The NH$_3$ concentration drops linearly from point 1 to 3, whereas the HCN concentration initially increases from point 1 to 2. Again, the concentration profiles of the precursors during plant setting 2 follow a trend similar to CH$_4$.

According to literature the majority of the total NO$_x$ precursors are released as NH3 during biomass and waste combustion [1]. The present measurements support this finding, as less than 1/5 of the total amount of precursor was identified as HCN. The error induced by modelling the fuel-NO$_x$ formation using NH3 as the sole NO$_x$ precursor is evaluated in section 5.

5.5 Comparison with previous measurements at W-t-E plants

The gas composition and gas temperature from drying, devolatilisation and char combustion of waste on a moving grate have previously been reported by Bøjer et al. [124] from Vestforbrændingen plant. These measurements were conducted at a waste-to-energy plant with a hydraulically forward-acting grate with a nominal waste capacity of 26t/h and a grate size of 13.1x9.75m. In the study the emphasis was put on measuring the release of alkali; besides alkali, only CO, CO$_2$ and NO concentrations were measured.
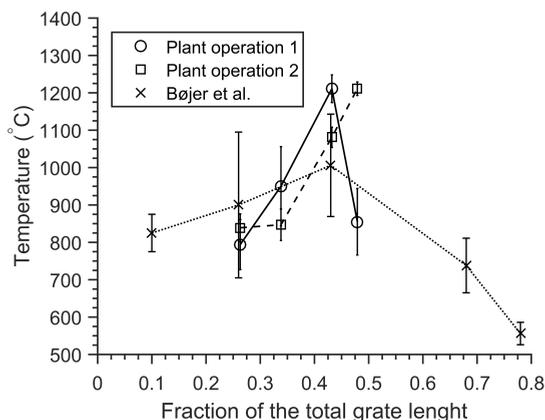
Figure 5.11: The measured gas temperature at both plant operations compared with gas temperatures measured by Bøjer et al. at Vestforbrændingen [124].

Comparison between the gas temperatures measured in this study and measurements performed by Bœjer et al. is shown in figure 5.11. Similar temperatures were found in both plants; Bøjer et al. measured the temperatures at a W-t-E plant with a different grate technology and a nominal capacity approximately 3 times larger than Affald+. At both plants the highest gas temperature was obtained at a location approximately 45% down the grate. However, the gas temperature is significantly higher in the present study. The higher gas temperature is suspected to be due to a number of differences between the two studies. The heating value of the fuel was higher by approximately 3MJ/kg in this study. During the measurements dry waste wood was mixed with the MSW increasing the homogeneity of the fuel, as a consequence lower fluctuations in the position of the flame front occurs. Bøjer at al. measured the gas temperatures close to the side walls; the cooling effect of walls may affect the gas temperature. Also differences in the primary air distribution might affect the gas temperatures. Lastly, in this study the reaction zone was very narrow, for this reason a sharp increase in the gas temperature is seen. This was supported by IR-camera inspections. A broad reaction zone was experienced by Bøjer et al. [124], corresponding to a flat gas temperature curve as seen in figure 5.11. It is suspected that the homogeneity of the fuel and differences in the control strategy can explain the low fluctuation in the position of the flame front during measurements at Affald+.
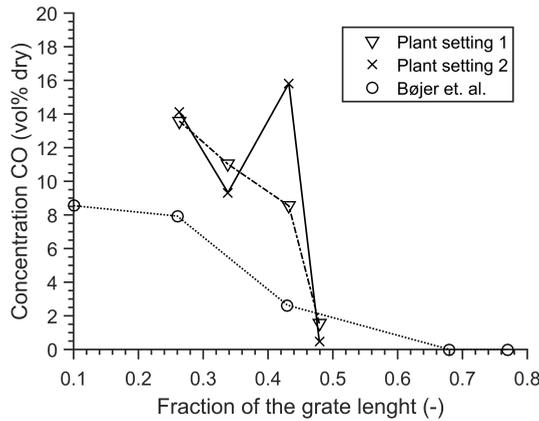
Figure 5.12: The CO concentration for both plant settings obtained in this study. These have been compared with measurements obtained by Bøjer et al. at Vestforbrændingen [124].

In figure 5.12 the CO concentration as a function of the grate length found in this study has been compared with results found by Bøjer et al. [124]. They reported peak CO and CO_2 concentrations of approximately 8 and 15 vol % dry, respectively. The results indicate that the release of volatiles and oxidation of these species occur over a larger part of the grate for the measurements during operation at Vestforbrændingen as CO was depleted after approximately 70% of the total grate length, while CO concentrations reach about 0% after approximately 50% of the grate length at Affald+. The differences might be due partly to differences in primary air distribution under the grate. Due to differences in the primary air distribution, heating value of the fuel, lower gas temperatures and large fluctuations in the position of the flame front, large standard deviations in the CO concentrations were experienced by Bøjer et al [124].
The total hydrocarbon peak concentration was estimated by Bøjer et al. on the basis of measurements of the CO and CO_2 concentration profiles to be approximately 10 vol% dry [124]; this is similar to the measured levels in this study. In both studies the hydrocarbons are depleted after the initial half of the grate.

Despite the differences (size, grate technology) between the W-t-E plants, the measured species concentrations in the two test campaigns show significant similarities. Devolatilisation of the fuel occurs on the first half of the grate and gas temperatures peak after approximately half of the total grate length. These similarities indicate robustness in gas temperatures as well as composition and concentrations of gasses released from the waste bed in grate fired W-t-E plants.

5.6 The influence of precursor speciation on the NO_x formation

A robust bed model is essential for a correct prediction of the NO_x formation in CFD. In particular the composition of gasses released from the fuel bed is an input parameter

to a CFD model. In this section the influence of the choice of precursor on the NO$_x$ formation is evaluated. The evaluation is done through Perfectly Stirred Reactor (PSR) simulations in CHEMKIN 10131, using reactor conditions as shown in table 5.5. The combustion is simulated using the detailed chemical kinetic model developed by Mendiara and Glarborg [36]. Included in this mechanism is high temperature NH$_3$ and HCN oxidation.

Table 5.5: The inlet gas composition used in PSR simulations in CHEMKIN 10131. The gas composition was determined based on the extractive IR measurements.

Species Vol	Concentration %
CO	13.6
CO$_2$	11.6
CH$_4$	5.1
C$_2$H$_4$	3.3
NH$_3$	0.8
HCN	0.2
N$_2$	65.4

The composition of the inlet gas for the PSR simulations, shown in table 4, was determined based on the extractive IR measurements conducted on Affald+; these are shown in figure 5.8 to figure 5.10. The composition was found at normal primary air configuration (plant setting 1) at measuring point 1. Even though it has been shown in previous measurements that the gas above the bed contains a significant amount of H$_2$ [105], this species could not be quantified in the present work and was neglected in the simulations. N2 account for the majority of the devolatilisation gas due to supply of atmospheric air under the grate; NO formed in the bed is not included in the inlet gas. These assumptions might alter the NO$_x$ concentration after oxidation in the PSR reactor slightly but is not expected to influence the analysis of the precursor influence.

Figure 5.13: The influence of the precursor on the NO_x formation at T=800, 1000 and 1200°C for increasing λ. The pressure is 1 atm and the nominal residence time is 1s. The total precursor concentration was 10000ppm for all simulations. - NH3=9000ppm and HCN=1000ppm, — NH3=10000ppm and HCN=0ppm, — NH3=0ppm and HCN=10000ppm.

The calculations were performed at 800, 1000 and 1200°C, covering the expected range above the grate (figure 5.5). The simulations were done using three different inlet gas compositions; the composition shown in table 4, i.e., 80% NH_3 and 20% HCN, and compositions where all reactive N was NH_3 and HCN, respectively. The predicted formation of NO_x is shown in figure 5.13. As expected the NO concentration increases with increasing excess air ratio (λ) until a certain point where no more NO is generated and the gas is merely diluted by additional air. At values of λ below 1.1, the choice of precursor does not influence the final NO concentration in the temperature interval investigated. At high excess air ratios, the choice of precursor has a large impact on the predicted NO formation, with HCN oxidation yielding significantly higher levels of NO. At λ=1.5 the NO_x concentrations found from the PSR simulation are 128, 71 and 54% higher when HCN is used as precursor, compare to NH_3, for temperatures of 800, 1000 and 1200°C, respectively. Ammonia consumption yields NH_2 radicals, which can subsequently react with NO to form atmospheric nitrogen and water through reaction:

$$NH_3 + OH \leftrightarrow NH_2 + H_2O \tag{5.1}$$

$$NH_3 + O \leftrightarrow NH_2 + OH \tag{5.2}$$

$$NO + NH_2 \leftrightarrow N_2 + H_2O \tag{5.3}$$

Hydrogen cyanide is oxidized through a different sequence of reactions which has a higher selectivity for forming NO [1]. For modelling reliably the NO formation at high excess

air ratios it is thus important to determine the correct ratio between NH_3 and HCN. With decreasing temperatures the importance of an accurate precursor determination increases considerably.

5.7 Summary

The gas temperatures and concentration profiles of the major species above the fuel bed in combustion of waste at a grate-fired W-t-E plant were measured for two different plant operations. The gas temperature increased from 800°C at the initial part of the grate to a maximum value of 1200°C about halfway down the grate, with the position depending slightly on the primary air distribution. The gas released from the fuel bed consisted primarily of water, CO, CO_2, CH_4 and C_2H_4, with significant amounts of C_2H_2 detected downstream. The concentration profiles depended on the distribution of the primary air under the grate. A larger supply of combustion air in the early grate sections (section 2) enhanced oxidation, leading to lower levels of combustible gasses.

The measurements show that volatile nitrogen from the bed is mostly released as NH_3, with minor amounts of HCN. The concentration of the precursors was measured to about 1%vol above the initial part of the grate (section 2). Chemical kinetic modelling of NO formation at representative temperatures shows that at excess air ratios below 1.1 the NO yield is roughly independent of the choice of precursor. However, at higher values of λ the N-speciation influences the formation of NO significantly because HCN has a higher selectivity for forming NO. For this reason reliable determination of the partitioning of NO-precursors is important for predicting NO in grate-fired systems.

Chapter 6

Modelling NO formation in grate firing waste-to-energy plants using CFD

In the previous chapter a skeletal model for the NO_x formation was developed and tested using ideal reactor simulations. It was shown that the model performs reasonably well for conditions expected in the furnace and first pass of a W-t-E plant. In this section the skeletal model will be implemented in a CFD model, a NO_x formation simulation will be performed and the results will be compared to full-scale measurements.

In this study the commercial CFD code Fluent 18.1 has been used for NO_x formation simulations in a full-scale W-t-E plant. The mesh used in the modelling of the NO_x formation consists of approximately 2,500,000 cells. The high number of cells is needed to capture the flow from nozzles correctly. The geometry consists of both tetrahedral and hexahedral cells. The nitrogen chemistry was modelled post process the combustion process.

6.1 Turbulence modelling

The velocity and pressure in the boiler unit were solved using the simple RANS model, where the solution variables in the Navier-Stokes equations were decomposed into a mean term and a fluctuation term. The equations, the Reynolds-averaged Navier-Stokes equations (RANS), have the same form as the instantaneous Navier-Stokes equations but the solution variables now represent time averaged values instead of instantaneous values[85].

$$\frac{\partial \rho}{\partial t} + \frac{\partial}{\partial x_i}(\rho u_i) = 0 \tag{6.1}$$

$$\frac{\partial}{\partial t}(\rho u_i) + \frac{\partial}{\partial x_j}(\rho u_i u_j) = -\frac{\partial \rho}{\partial x_i} + \frac{\partial}{\partial x_j}\left(\mu\left(\frac{\partial u_i}{\partial x_j} + \frac{\partial u_j}{\partial x_i} - \frac{2}{3}\sigma_{ij}\frac{\partial u_l}{\partial x_l}\right)\right) + \frac{\partial}{\partial x_j}(-\rho\overline{u_i'u_j'}) \tag{6.2}$$

Here i and j denote the flow components (x,y,z) and x is the direction variable. Furthermore, an additional term is added that represents the effect of turbulence on the flow and pressure; the Reynolds stress $-\rho\overline{u_i'u_j'}$.

Numerous models are available in Fluent for calculation of the Reynolds stress. The most common models employ the Boussinesq hypothesis to model the Reynolds stress[125].

119

These models are the two equation models (standard k-ϵ, RNG k-ϵ, realizable k-ϵ etc.) meaning it includes two extra equations to represent the turbulent properties of the modelled flow. These models have some shortcomings when modelling the flow in highly swirling flows or modelling of not fully turbulent flows [125]. However, they are commonly used due to the general application[125] and the high stability. In this study the Reynolds stress is modelled by the realizable k-ϵ model.

6.2   Modelling of NO chemistry in turbulent flows using CFD

Different approaches can be taken when the interaction between fluid flow and chemistry are modelled in CFD. In this chapter different approaches for simulation of fast and slow chemistry will be presented and an evaluation of the different approaches in relation to NO_x chemistry will be made.

6.2.1   Species transport and chemical reactions

Chemical reactions, mixing- and transport of species can be modelled in ANSYS Fluent. These phenomena are modelled by solving the governing conservation equations which describe the convection, diffusion and reaction.

The transport of species is found by solving the conservation equation for each chemical species. In ANSYS Fluent the local mass fraction of each chemical species, denoted Y_i is predicted by solving the convection-diffusion equation for each of the Ith chemical species. The general form of the convection-diffusion equation is given below[15]:

$$\frac{\partial}{\partial t}(\rho Y_i) + \nabla \cdot (\rho \vec{v} Y_i) = -\nabla \cdot \vec{J_i} + R_i + S_i \tag{6.3}$$

In equation 6.3 R_i describes the net rate of production of species i by chemical reactions, S_i describes the net rate of formation/creation of species i from a dispersed phase or any user defined sources, while $\vec{J}$ describes the flux of species i. The flux of species i arises due to a gradient in temperature or species concentration.

By default the mass diffusion due to concentration gradients for a laminar flow is modelled by Fick's law 6.4

$$\vec{J_i} = -\rho D_{i,m} \nabla Y_i - D_{T,i} \frac{\nabla T}{T} \tag{6.4}$$

In equation 6.4 $D_{i,m}$ is the mass diffusion coefficient for species i in a mixture, while $D_{T,i}$ is the thermal diffusion coefficient. Equation 6.4 is only valid for a system within the laminar flow regime. For a system within the turbulent flow regime equation 6.4 is modified. Turbulence is considered by adding the turbulent diffusivity, also called the eddy diffusivity, to the first term in the Fick's law 6.4.

$$\vec{J_i} = -\left(\rho D_{i,m} + D_t\right) \nabla Y_i - D_{T,i} \frac{\nabla T}{T} \tag{6.5}$$

It is identified that the eddy diffusivity and the eddy kinematic viscosity, $v_t = \mu_t / \rho$, have dimensions which are similar - the dimensions are length divided by time. By

taking the ratio of these a dimensionless number, the turbulent Schmidt number, is obtained[126].

$$Sc_t = \frac{v_t}{D_t} = \frac{\mu_t}{\rho D_t} \tag{6.6}$$

where mu_t is the turbulent viscosity. The Schmidt number (6.6) is substituted into equation 6.5 and the modified mass diffusion is obtained 6.7

$$\overrightarrow{J_i} = -\left(\rho D_{i,m} + \frac{\mu_t}{Sc_t}\right)\nabla Y_i - D_{T,i}\frac{\nabla T}{T} \tag{6.7}$$

By introduction of the turbulent Schmidt number Sc_t in equation 6.4 an equation for the mass diffusion in a turbulent flow has been set up. By default the Schmidt number has been set to 0.7 in Fluent.

Above an expression for the diffusion $\overrightarrow{J_i}$ has been set up. However, in order to solve the convection-diffusion equation (6.3) an expression for the reaction R_i is also needed. In Fluent the reaction can be described from 3 default models depending on the system.

- Laminar finite-rate model

- Eddy-dissipation model

- Eddy-dissipation concept model

Each of these models have different advantages that will be described in the following and it will be discussed the suitability of each model.

The laminar finite-rate model

The laminar finite rate model computes the reaction term in the convection-diffusion equation solely using the Arrhenius expression. This means that this model ignores the effects of turbulent fluctuations. The model is accurate for laminar systems, but has a high inaccuracy in turbulent systems due to highly non-linear Arrhenius chemical kinetics [15].

The net formation of species i is calculated as the sum of the rate of formation or destruction of species i in the full range of N_R reaction that i participates in. The net rate of formation or destruction of i is measured in mass per time unit.

$$R_i = M_{w,i}\sum_{r=1}^{N_R}\widehat{R}_{i,r} \tag{6.8}$$

Here $M_{w,i}$ is the molar weight of species i and $\widehat{R}_{i,r}$ is the molar rate of formation or destruction of species i in reaction r.

The molar reaction rate is calculated from simple reaction kinetics expressions as shown in equation 6.9

$$\widehat{R}_{i,r} = \zeta(v''_{i,r} - v'_{i,r})\left(k_{f,r}\prod_{j=1}^{N}[C_{j,r}]^{(\eta'_{j,r}+\eta''_{j,r})}\right) \tag{6.9}$$

In equation 6.9 ζ represents the net effect of the third bodies on the reaction rate. $v''_{i,r}$ and $v'_{i,r}$ are the stoichiometric coefficients of the products and the reactants respectively, which means that the rate is negative if species i in reaction r is a reactant and positive if it is a product. $k_{f,r}$ is the forward rate constant for reaction r. $C_{j,r}$ is the molar

concentration of species j in reaction r and $\eta'_{j,r}$ and $\eta''_{j,r}$ are the rate exponent of species j in reaction r.

For the following second order reaction with rate constant k_f

$$a + b \rightarrow c$$

the molar reaction rate using equation 6.9 for a is as follows

$$\widehat{R}_i = (1 - 0)k_f[a]^1[b]^1$$

The rate coefficient for each reaction is computed from the Arrhenius expression 6.10

$$k_{f,r} = A_r T^{\beta_r} \exp\left(\frac{-E_a}{RT}\right) \tag{6.10}$$

In equation 6.10 A is the pre-exponential factor, β is the temperature exponent, E_a is the activation energy and R is the universal gas constant.

For reversible reactions Fluent can calculate the backwards reaction in two different ways. The net rate of reaction for a given species i is determined by summation of the rate of formation and destruction of species i according to equation 6.11

$$\widehat{R}_{i,r} = \zeta(v''_{i,r} - v'_{i,r})\left(k_{f,r} \prod_{j=1}^{N} [C_{j,r}]^{\eta'_{j,r}} - k_{b,r} \prod_{j=1}^{N} [C_{j,r}]^{v''_{j,r}}\right) \tag{6.11}$$

The backwards rate constant is determined, by default, from the forward rate constant and the equilibrium constant. The following relationship applies [127].

$$K_r = \frac{k_{f,r}}{k_{b,r}} \tag{6.12}$$

where K_r is the equilibrium constant for the reaction. The equilibrium constant for reaction r can be calculated from the change in Gibbs free energy [15] according to equation 6.13.

$$K_r = \exp\left(\frac{\Delta S_r}{R} - \frac{\Delta H_r}{RT}\right)\left(\frac{p_{atm}}{RT}\right)^{\sum_{i=1}^{N}(v''_{i,r} - v'_{i,r})} \tag{6.13}$$

The Gibbs free energy is calculated from an entropy and an enthalpy term. These terms are in Fluent calculated as shown in equation 6.15 and 6.16, which is another way of writing equation 6.14

$$\Delta S_r = S_{products} - S_{reactants} \qquad \Delta H_r = h_{products} - h_{reactants} \tag{6.14}$$

$$\frac{\Delta S_r}{R} = \sum_{i=1}^{N}(v''_{i,r} - v'_{i,r})\frac{S_i}{R} \tag{6.15}$$

$$\frac{\Delta H_r}{R} = \sum_{i=1}^{N}(v''_{i,r} - v'_{i,r})\frac{h_i}{RT} \tag{6.16}$$

Instead of calculating the backwards rate constant, as shown above, the backwards rate constant can be calculated from the Arrhenius expression if the reaction rate parameters are known.

The laminar finite-rate model calculates the rate constants for the number of reactions that has been specified. If some reactions are reversible, the reversible reaction rate is by default calculated from the equilibrium constant. However, if the reaction rate parameter for the backwards reaction is known it is possible to calculate the backwards reaction constant directly from the Arrhenius expression. The laminar finite-rate model does not consider fluctuations due to turbulence and is therefore only applicable for laminar systems.

The eddy dissipation model

The eddy dissipation model builds on the assumption that the rate of combustion is determined by the intermixing of molecular scale fuel and oxidizer eddies due to the very fast chemical reactions that occur in combustion reactions. The fuel and oxygen occur in separate eddies[128]. In the Eddy-Break up model the fluctuations of the product mass fraction were included in order to model turbulent combustion[129]. It was identified that a relationship between the fluctuations and the mean concentration of species occurs; consequently the fluctuations of the product mass fraction were replaced by the mean concentration[128].

According to the Eddy dissipation model the reaction rate of reaction r is determined by the minimum of three computed rates. The first rate evaluated is defined on the basis of the mean oxygen mass fraction [130]:

$$R_{O_2} = \overline{\rho} \frac{A_{eddy} \overline{Y}_{O2}}{v} \frac{\epsilon}{k} \tag{6.17}$$

A_{eddy} is a constant that depends on the structure of the flame and the rate of reaction between fuel and oxidizer; in Fluent the default value of A is 4.0, but will have to be tuned to get accurate solutions for some problems. $\overline{Y}_{O_2}$ is the local time-mean mass fraction of oxygen [128], ϵ is the dissipation of turbulent kinetic energy and k is the turbulent kinetic energy.

The second rate evaluated is defined on the basis of the fuel mass fraction similar to equation 6.17.

$$R_{fuel} = \overline{\rho} \frac{A_{eddy} \overline{Y}_{fuel}}{v} \frac{\epsilon}{k} \tag{6.18}$$

The third rate evaluated is defined on the basis of the concentration of the production mass fraction [130] [128]

$$R_p = \overline{\rho} \frac{A \cdot B}{1 + v_{O/f}} \overline{Y}_p \frac{\epsilon}{k} \tag{6.19}$$

where B is a constant [128]; the constant B have by default a value of 0.5 in Fluent, while $v_{O/f}$ is the stoichiometric oxygen to fuel mass ratio [130].
The controlling rate has been defined in Fluent as seen in equation 6.20 and 6.21

$$R_{i,r} = v'_{i,r} M_{w,i} A \rho \frac{\epsilon}{k} \min_{\Re} \left(\frac{Y_{\Re}}{v'_{\Re,r} M_{w_{\Re}}} \right) \tag{6.20}$$

$$R_{i,r} = v'_{i,r} M_{w,i} A B \rho \frac{\epsilon}{k} \frac{\sum_p Y_p}{\sum_j^N v''_{j,r} M_{w,j}} \tag{6.21}$$

where Y_p is the product mass fraction and $Y_\Re$ is the mass fraction of a particular react-ant. In the equation 6.20 and 6.21 the expression $\min_\Re$ denotes the rate of the reaction that causes the minimum reaction rate.

Reaction proceeds whenever turbulence is present, this means that reaction proceeds whenever $\epsilon/k > 0$ [15]. This model does not evaluate the reaction kinetics. Problems arise due to the fact that the temperature is not included in the evaluation of the reaction rate. This has been addressed by evaluation of both the rate of turbulent mixing and the Arrhenius rate of reaction. This model is denoted the Eddy dissipation/Finite-rate model in Fluent. When using the Eddy dissipation/Finite-rate model the reaction source term in the convection-diffusion equation (6.3) is determined from equation 6.22 [131].

$$R_{i,r} = \min\left(k_{eddy}\frac{\epsilon}{k}\min_\Re\left(\frac{Y_\Re}{v'_{\Re,r}M_{w_\Re}}\right), k_{eddy}B\frac{\epsilon}{k}\frac{\sum_p Y_p}{\sum_j^N v''_{j,r}M_{w,j}}, R_{i,\text{Arrhenius}_r}\right) \tag{6.22}$$

In equation 6.22. $k_{eddy} = v'_{i,r}M_{w,i}\rho A$

The Eddy dissipation model will likely produce inaccurate solutions due to the differences in the reaction rate from reaction to reaction. The eddy-dissipation model assumes every reaction has the same turbulent reaction rate. This means that this model should only be used for a global single step or two step reactions [15]. Furthermore, the Eddy dissipation model does not have the ability to model radicals which in many cases are the kinetically controlling species [131].

The eddy dissipation concept model

In order to model the interaction between turbulence and detailed chemical mechanisms in Fluent where reaction kinetics have a great influence on the reaction rate an extension of the Eddy dissipation model was developed[132]; such reactions can be pollution form-ation where the chemical kinetics have a domination role in the overall reaction rate. The Eddy Dissipation Concept (EDC) model developed by Magnussen [133] assumes that chemical reactions occur in fine structures of fluid volume[133] [134]. In these fine structures most of the dissipation of turbulent kinetic energy into heat occurs. The dissipation of turbulent kinetic energy into heat occurs according to the cascade model; energy is transferred from large eddies to small eddies before dissipation into heat in the small eddies[133] [134]. In these fine structures it is assumed that the reactants are mixed homogeneously, and these structures are therefore treated as continuously stirred tank reactors[133] at constant pressure [15]. According to the EDC model the fine structures are not evenly distributed in time and space. This means that at a certain time a large number of fine structures are available and at other times a low number of fine structures are available[134].The number of fine structures are largely dependent on the turbulence and since the chemical reaction is dependent on the availability of these structures the chemical reactions depend on the turbulence[134].

The volume fractions of the fine scales are found according to equation 6.23 [15]

$$\xi^3 = C_{xi}^3\left(\frac{v\epsilon_{\text{sub-grid}}}{k^2}\right)^{3/4} \tag{6.23}$$

In this equation C_{xi} is a volume fraction constant with the value 2.1377 and $\epsilon_{\text{sub-grid}}$ is the sub-grid scales dissipation of turbulent kinetic energy.

It is assumed that reaction occurs in the fine scales over a time period defined in equation 6.24 [15].

$$\tau = C_\tau \left(\frac{v}{\epsilon}^{1/2} \right) \tag{6.24}$$

In equation 6.24 C_τ denotes a time scale constant equal to 0.4082 , while $\frac{v}{\epsilon}^{1/2} = \tau_{\text{eta}}$ is the Kolmogorov time scale; the smallest time scale in turbulent flows.

The reaction term in the convection-diffusion equation is determined according to reaction 6.25 [15]

$$R_i = \frac{\rho \xi^2}{\tau \left(1 - \xi^3 \right)} (Y_i^* - Y_i) \tag{6.25}$$

The term Y_i^* refers to the mass fraction of species i in the fine-scales after reaction over a time period of τ . This is found using the Arrhenius reaction expression.

Using the Eddy dissipation model a detailed chemical kinetic scheme can be incorporated into Fluent. Due to the difference in time scales the system becomes stiff and computationally costly to solve. The model should therefore only be used when the assumption of fast chemistry is invalid. Hence, turbulent mixing is rate limiting and the Eddy dissipation model should be used[15].

Originally the EDC model has been developed as a CSTR concept. However, in order to minimize convergence problems integration in time (PFR) is often employed when the concept is implemented in commercial CFD codes such as FLUENT [32].

6.2.2 Modelling the combustion chemistry

Profound studies of the combustion of hydrocarbons have been performed over the last 5 decades. During these studies several simple global reaction schemes have been suggested to describe the oxidation of hydrocarbons during combustion. Furthermore, a number of detailed elementary reaction schemes have been suggested for a more thorough description of the oxidation of hydrocarbons.

Combustion of hydrocarbons can be described from a simple global reaction 6.26

$$C_mH_n + (m + n/2)O_2 \rightarrow mCO_2 + n/2H_2O \tag{6.26}$$
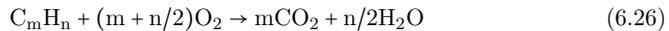
For implementation in CFD this is not adequate due to the lack of CO formation. It has been shown that the concentration of CO has a large impact on the formation of species such as NO_x [135]. Furthermore, by neglecting the formation of H_2 and CO the predicted flame temperature is highly overestimated [136]. Combustion models which at least have a two-step global reaction scheme with CO as an intermediate is needed. The most commonly used models to describe the combustion of hydrocarbons in CFD have been presented below.

The simplest combustion model is the Westbrook and Dryer Two-Step Mechanism [137] 6.27.

$$\begin{aligned} CH_4 + 1.5O_2 &\rightarrow CO + 2H_2O \\ CO + 0.5O_2 &\leftrightarrow CO_2 \end{aligned} \tag{6.27}$$
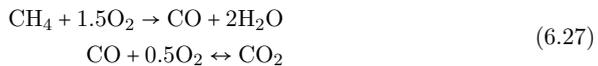
The first step in the Westbrook and Dryer mechanism is the breakdown of the fuel to form CO and H_2O. The formed CO is oxidized to CO_2 in the following reaction. This reaction is reversible, whereas the first reaction is irreversible. This combustion

mechanism is directly available in FLUENT as a standard combustion model [85]. A more complicated mechanism, however still very simplified, is the Jones and Lindstedt Four-Step Mechanism [87] shown in reaction scheme 6.28.

$$CH_4 + 0.5O_2 \rightarrow CO + 2H_2$$
$$CH_4 + H_2O \rightarrow CO + 3H_2$$
$$H_2 + 0.5O_2 \leftrightarrow H_2O \quad (6.28)$$
$$CO + H_2O \leftrightarrow CO_2 + H_2$$
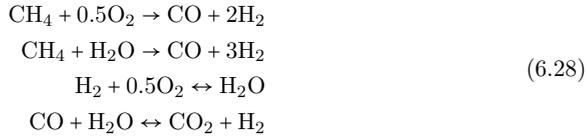
In some cases the Westbrook and Dryer Two step mechanism and the Jones and Lindstedt four-step mechanism have been merged [138]. The first two reactions in the Jones and Lindstedt mechanism describe the breakdown of the fuel, in this case methane. As seen in the reaction scheme, the first reaction is the dominant reaction under fuel lean conditions, whereas the second reaction under these conditions is less relevant. Under fuel rich conditions the second reaction is very important. The first two reactions are considered irreversible in this model. The third reaction is oxidation of the formed hydrogen from reaction 1 and 2. This reaction, along with reaction 4 which is a water-gas shift reaction, is considered reversible [136]. According to Brink et al. the backward rate of reaction 3 can be neglected due to its small importance in the temperature range between 1200K and 1800K [136]. Other authors have modified the kinetics of the backwards rate of reaction 3 from the original form to yield a more accurate result [33]. This mechanism is used regularly in the CFD modeling of industrial applications.

The two above mentioned mechanisms for the combustion of hydrocarbons (methane) are simplified global reaction schemes. More detailed reaction mechanisms have also been suggested, e.g. the reaction mechanism suggested by Glarborg et al. [41], involving 60 species and 424 elementary reactions. These reaction schemes are based on elementary reactions, therefore no equilibrium considerations, and a more accurate model is achieved. However, due to the complexity of the more accurate reaction mechanisms, the computational time is highly prolonged, and these mechanisms are not used commercially. Some studies have evaluated the accuracy of the two simple mechanisms, the Westbrook and Dryer mechanism and Jones and Lindstedt mechanism, by comparing these with a complex model, such as the model described by Glarborg et al. [41].

Andersen et al. [33] compared the accuracy of the Westbrook and Dryer mechanism and the Jones and Lindstedt mechanism for combustion of methane under oxy-fuel conditions. The results from this study showed that both the Westbrook and Dryer and the Jones and Lindstedt mechanism adequately predict the concentration of the major species CO_2 and O_2, thereby yielding satisfactory predictions of the heat release. The difference in accuracy between the two mechanisms is seen in the prediction of the CO concentration. The Westbrook and Dryer mechanism tends to overpredict the CO concentration, whereas the Jones and Lindstedt mechanism correctly predicts the CO concentration. However, the Jones and Lindstedt mechanism overpredicts the CO peak levels in some cases. Both models, however, predict the time for full conversion accurately [33].

Brink et al. concluded that the Jones and Lindstedt mechanism proves to be a good compromise between computational effort and accuracy [136]. The Jones and Lindstedt mechanism is more complex than the Westbrook and Dryer mechanism, but has a higher

degree of accuracy than the Westbrook and Dryer scheme and is used regularly in CFD modeling of industrial applications [119].

The choice of combustion model depends heavily on the required level of detail. For NO_x formation simulations it is required to capture the heat release and major species concentrations from hydrocarbon oxidation well. The global two step mechanism by Westbrook and Dryer [137] has been shown to describe the major species concentration adequately[33] [139]. In this study the main combustion was modelled by the global two step mechanism by Westbrook and Dryer:

$$CH_4 + 1.5O_2 \rightarrow CO + H_2O \tag{6.29}$$

$$CO + 0.5O_2 \rightarrow CO_2 \tag{6.30}$$

$$CO_2 \rightarrow CO + 0.5O_2 \tag{6.31}$$

The aim of this project was to developed a chemical submodel to describe the NO_x formation by implementing this in the in-house CFD model at B&W Vølund. Since the combustion process is described by the Westbrook and Dryer mechanism by B&W Vølund this was also done in this study.

Turbulence-chemistry interaction model used for modelling of the nitrogen chemistry

The choice of turbulence-chemistry interaction model depends on the specific problem. For modelling of highly complex problems where a complex multi step reaction mechanism is used; e.g. formation of emissions, the Eddy dissipation concept (EDC) has to be used. This model assumes that the reaction occurs in fine structures of the fluid volume; see section 6.2.1. For a more simple problem where the chemistry can be described by a simple global reaction mechanism the Eddy dissipation model (EDM) can be used. This model assumes the rate of reaction is determined solely by the mixing of fuel and oxidizer [128]. For a multi step global reaction this can cause some problems as the the rate of reaction of each reaction is not evaluated. The problem is fixed by using the Eddy-dissipation/Finite-rate model where both the mixing and the kinetics are evaluated and the limiting factor of these is used as rate of reaction.

Modelling of the NO_x formation is done in two steps; first the temperature-, pressure-, velocity- and turbulence profile is determined. The heat releasing reactions; the oxidation of hydrocarbons (CH_4), are simulated using the global methane oxidation mechanism by Westbrook and Dryer. The influence of the turbulence on the chemistry is modelled by the Eddy-dissipation/Finite-rate model. This model was chosen due to the stability of the model and the low computational time. Furthermore, it is only an advantage to use more advanced interaction models when the turbulent mixing is not rate limiting.

Secondly, on the basis of results from the main combustion NO_x chemistry was simulated. The prediction of emission formations was done using a skeletal model, which has been developed in this study. The interaction between chemistry and turbulence was modelled using the EDC model.

6.3 Estimations of the inlet boundary conditions from the fuel bed to the freeboard

Accurate predictions of the heat release, the species concentration and the velocities in the boiler heavily depend on the inlet boundary conditions from the waste bed to the freeboard. An accurate estimation of the species concentrations, the gas flow and gas temperature from the bed to the freeboard is essential. The waste undergo drying, pyrolysis and char oxidation as it travels from the fuel inlet to the ash pit; consequently the temperature, gas flow and gas composition change along the waste bed. The concentration-, flow-, and temperature profiles of the gas from the bed into the computational domain as a function of the grate length have in this study been estimated using an in-house model of the bed supported with full scale measurements performed; see chapter 5.

6.3.1 An overview of the structure of the bed model

According to the in-house bed-model developed at B&W Vølund [140], calculations of the properties of the gas and particles leaving the waste bed are based on mass- and heat balances. The waste bed is divided in rectangular sections and a mass and heat balance for each section is set up. In this study the waste bed was divided into 16 equally sized rectangular sections.

The approach used assumes that properties of the gas and particles that leave the bed are uniformly distributed in each of these sections. Due to the cooling of the walls on the fuel bed different rates of drying, devolatilisation etc. might be seen in full-scale W-t-E plants: consequently the gas and particles that leave the bed will not be uniformly distributed. Furthermore, the assumption of a well-mixed gas mixture leaving the bed may not be valid; it is expected that stratification will occur but this has not be investigated further.

Released from each bed section to the freeboard, according to the in-house bed-model developed at B&W Vølund, are species CH_4, CO, CO_2, O_2, H_2O and N_2. Furthermore, particles are released from the bed. These are modelled as spherical carbon particles in Fluent.

Part of the solid fuel does not undergo any reaction in one section, this part is transported by the grate to the following bed section acting as inlet to this control volume. Inlets to the control volume for a given bed section are the solid fraction from the previous control volume and the primary air provided to that specific section of the bed.

Part of the volatiles released in the solid waste are oxidized in the bed before entering the computational domain. This is included in the bed model causing an increase in the temperature of the gases leaving the bed. It was estimated, from the work by Dvirka[141], that a maximum of 30-35% of the total energy released by waste combustion occurs in the gas phase (Q_{pyr}) in the free board; 65-70% of the heat is released in the bed. This predefined number is defined in the bed model as the gasification rate. By comparing temperatures predicted by the bed model and measurements performed in this study; see chapter 5, it was estimated that 35% of the total energy released by waste combustion occurs in the gas phase. By using this value more consistency between predicted temperatures of the gases leaving the bed estimated by the bed model and

measured temperatures 0.5m above the grate was achieved; see Figure 6.8.

In order to make the bed model applicable for all fuel loads and number of grate sections distributions of the rate of evaporation, combustible gas release and combustion in the fuel bed are used. The rates are distributed in a domain defined by the incremented sum of supplied primary air normalised to the total primary air supplied under the grate; the domain is therefore [0;1].

Along with the mass balance, the heat balance is calculated too in order to adjust the temperature of the gases leaving the bed.

6.3.2 Inlet boundary conditions for the modelled case determined by the bed model

It has been decided to model the NO_x formation at Affald+ under operating conditions identical to the conditions during the experimental study determining the NO_x precursors and major species concentrations above the grate; see chapter 5. It was decided to model the formation during plant operation 1.

For determination of the inlet boundary conditions the heating value of the fuel, total amount of primary air, distribution of primary air under the grate, temperature of the primary air and waste composition need to be provided. For the particular case of interest these parameters have been shown in Table 5.1. The composition of the waste is assumed to be as shown in Table 6.1.

Table 6.1: The assumed composition of the waste during combustion for the case modelled

Element	Fraction (kg/kg)
C	0.305
H	0.041
O	0.176
N	0.013
Ash	0.174

Providing the bed model with the information about the waste composition (Table 6.1), the heating value of the fuel, total amount of primary air, distribution of primary air under the grate and temperature of the primary air(Table 5.1) the gas temperature, mass flow of gas and composition of the gas for each grate section can be achieved. It was decided in this study to divide each of the grate sections into additional 4 equally sized zones. In the CFD model the grate is therefore divided in 16 grate zones.

The mass flow of gases from the grate to the computational domain determined by the bed model based on data from Table 6.1 and 5.1 as a function of the number of grate zones has been shown in Figure 6.1.
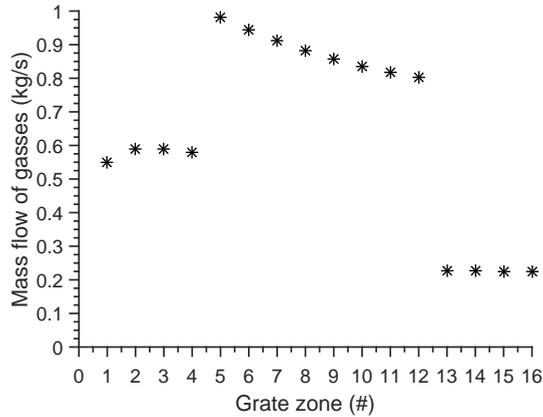
Figure 6.1: The mass flow of gases from the grate to the computational domain determined by the bed model based on data from Table 6.1 and 5.1 as a function of the number of grate zones.

The distribution of the mass flow of gases from the bed to the free board is identical to the distribution of primary air under the grate; see Figure 5.2 (left).

The temperature of the gas leaving the bed was calculated using the bed model as well. In Figure 6.2 the gas temperature entering the computational domain has been shown. The gas temperature approximately 0.5m above the bed was measured using a suction pyrometer and shown in Figure 5.5 in chapter 5. The peak temperature of the measured gases was found to be approximately 1200°C, while the peak temperature of gases leaving the bed predicted by the bed model was determined to be approximately 1700°C. The difference between the two temperatures is significant. This might be due to differences in location; the bed model estimates the temperature of the gas at the interface between bed and freeboard while the measurements were performed in the freeboard 0.5m above the bed. In section 6.5 the gas temperatures at 0.5m and 1.0m above the bed determined by the CFD model are compared with measurements.
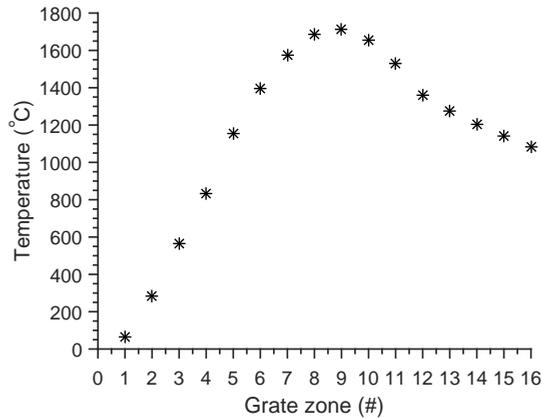
Figure 6.2: The gas temperature of the gas leaving the grate to the computational domain determined by the bed model based on data from Table 6.1 and 5.1 as a function of the number of grate zones.

The concentrations of specific species from the bed into the computational domain are shown in Figure 6.3.
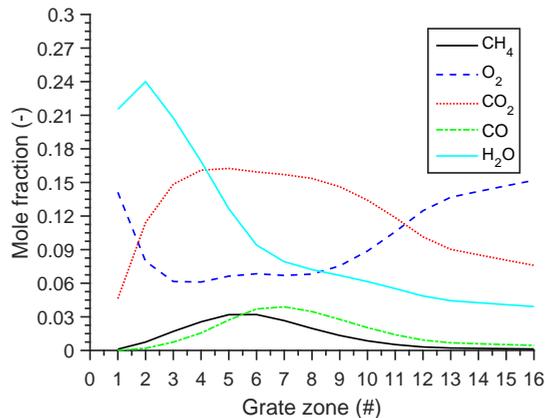
Figure 6.3: The mole fraction of each species from the grate to the computational domain determined by the bed model based on data from Table 6.1 and 5.1 as a function of the number of grate zones.

Figure 6.3 shows that full oxidation of the combustibles does not occur in the bed; the minimum mole fraction of oxygen entering the freeboard was determined to approximately 0.06. Measurements of the gas composition at 0.5m above the bed have been reported in chapter 5. A comparison between the gas composition at 0.5m and 1.0m above the bed determined by CFD modelling and full scale measurements has been done in section 6.5.

6.4 Post processing of the NO chemistry

The heat releasing reactions are modelled as shown in the previous sections. The combustion chemistry is modelled by the 2 step Westbrook and Dryer global mechanism with inlet boundary conditions determined by the In-house bed model. Due to the small mechanism the chemistry-turbulence interactions were modelled by the Finite-rate/EDM model, while the turbulence was modelled by the realizable k-ϵ model.

Based on the temperature-, turbulence-, velocity- and species- profiles the NO chemistry was modelled. After modelling of the combustion chemistry the transport equations of species CH_4, CO, CO_2, H_2O and O_2 were disabled; consequently the instantaneous concentrations of these species are used in the determination of the NO concentration profile. This procedure is only valid due to the assumption that the NO chemistry does not change the concentration of the main combustion species (CH_4, CO, CO_2, H_2O and O_2) or the temperature profile.

The NO chemistry was modelled using the 38 species and 251 reaction skeletal model developed in this study. The chemistry-turbulence interactions were modelled using the EDC model, while the turbulence was modelled using the realizable k-ϵ model.

As shown in chapter 4 the NO formation highly depends on the concentration of precursors in the free board. Furthermore it was shown in chapter 5 that the NO formation also depends on the precursor speciation with NH_3 the main precursor during waste combustion in a grate firing W-t-E plant. The concentration profile of NH_3 above the bed was measured in this study; see chapter 5. The release of NH_3 from the bed to the free board was adjusted to match the NH_3 concentrations measured at Affald+. A comparison between the measured NH_3 concentration and the NH_3 in the CFD model has been shown in Figure 6.9 in the following section. The concentration profile of NH_3 from the bed to the free board used during modelling of the NO formation has been shown in Figure 6.4.
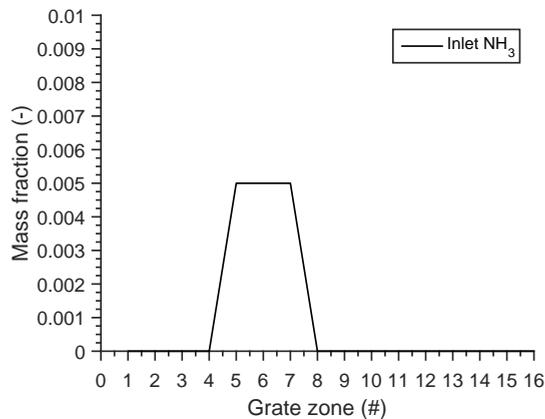
Figure 6.4: The mole fraction of NH_3 from the grate to the computational domain. The concentration profile was calibrated by using the measurements in chapter 5.

Measurements at Affald+ showed high concentrations of NH_3 on bed section 2 (see

chapter 5, in Figure 6.4 this corresponds to grate zone 5, 6, 7 and 8. Furthermore, no NH$_3$ was measured at grate section 3, which corresponds to grate zone 9, 10, 11 and 12 in Figure 6.4. The inlet mass fraction of NH$_3$ from the grate to the freeboard was assumed occurring only from grate zone 5, 6, 7 and 8 (grate section 2) which agree with measurements presented in chapter 5. The mass flow was adjusted to reach concentrations above the bed in agreement with measured concentrations.

6.5 Comparison between CFD predictions of NO$_x$ formations and NO$_x$ measurements at full-scale W-t-E plant

In the previous sections the modelling procedure was presented. The modelling was divided into two parts. First the heat releasing reactions, the main combustion, were modelled. Based on these results the NO chemistry was modelled post process. In this section results from the modelling of the NO formation at Affald+, a full scale W-t-E plant in Næstved, will be presented. The results will be compared with full scale measurements conducted at Affald+ which have been presented in chapter 5.
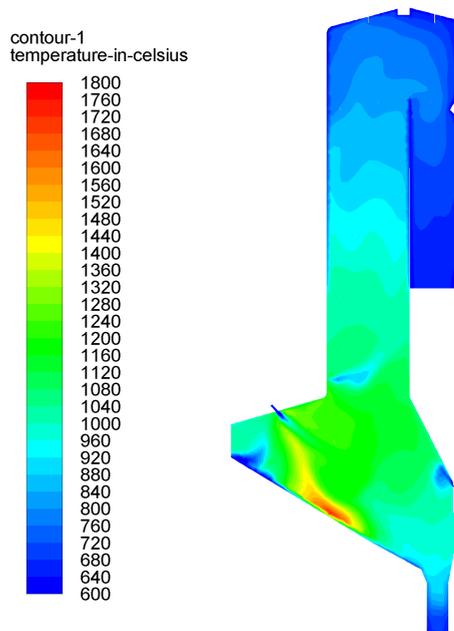
Figure 6.5: The temperature profile in the middle of the boiler determined by CFD calculations. Post processing of the nitrogen chemistry has been performed based on this temperature profile. The process conditions for the modelling have been shown in Table 5.1

The resulting temperature profile modelled in CFD using the previously described

sub-models and the process conditions shown in Table 5.1 has been presented in Figure 6.5.

A region of high temperature, above 1800°C, is predicted on grate section 2 and the first part of grate section 3 right above the grate. It is expected that thermal NO_x formation occurs in this region due to the high temperatures. This is supported by the NH_3 concentration profile from the bed to the free board (Figure 6.4), no NH_3 is released in this region, and the NO concentration profile shown in Figure 6.10. In the rest of the furnace temperatures are found between 1200°C and 800°C.

The oxygen profile, which the NO chemistry is highly dependent on, has been presented in Figure 6.6.
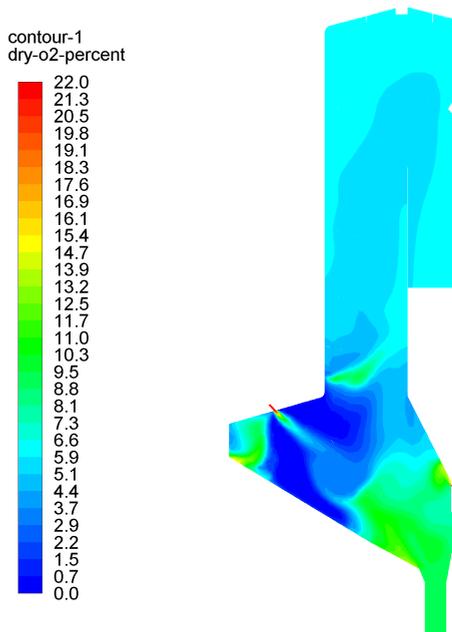
Figure 6.6: The oxygen profile in the middle of the boiler determined by CFD calculations. Post processing of the nitrogen chemistry has been performed based on this oxygen profile. The process conditions for the modelling have been shown in Table 5.1

According to the predictions the furnace is split into two zones; an oxygen poor zone from the fuel inlet to approximately half way down the grate and an oxygen rich zone from half way down the grate to the ash pit. This agrees with measurements at full scale W-t-E plants. In the oxygen poor zone locally high oxygen concentrations are found in the jet from nozzles in the front roof. At the fuel inlet the oxygen concentration was predicted to be approximately 10% dry. Initially in a combustion process the fuel is dried. During this process only small amounts of combustibles are released. It is expected that small amounts of combustibles are released close to the fuel inlet and thereby a low oxygen consumption. Consequently a higher oxygen concentration is found.

Above the injection of over fire air the oxygen concentration reaches 6% dry. This agrees with the measured value at Affald+; see Table 5.1 in chapter 5.

The velocity profile has been presented in Figure 6.7.
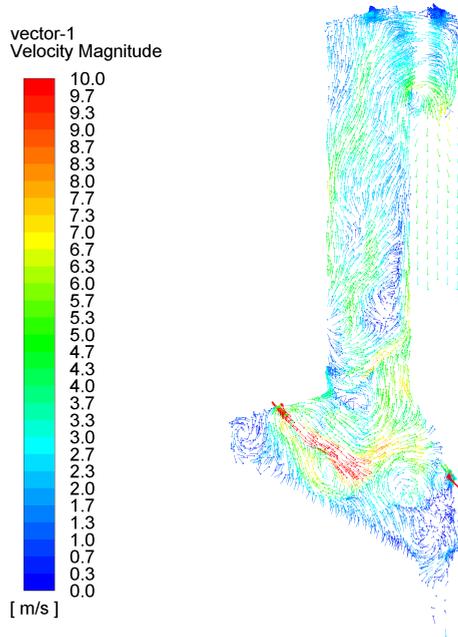
Figure 6.7: The velocity profile in the middle of the boiler determined by CFD calculations. Post processing of the nitrogen chemistry has been performed based on this velocity profile. The process conditions for the modelling have been shown in Table 5.1

The resulting velocity profile shows large recirculation zones in the furnace. A large recirculation zone is seen below the jet caused by the nozzles in the front roof. The recirculation of flue gases causes a flow of oxygen from the oxygen rich zone into the oxygen poor zone. The location of the recirculation zone corresponds to the location of peak gas temperatures in the furnace; see Figure 6.5.

The concentration profile of the major combustion species, precursors and temperatures were measured approximately 0.5m above the bed at a full scale W-t-E plant; see chapter 5. These measurements have been compared with predictions using CFD.

The temperatures at a height of 0.5m and 1.0m above the bed predicted by CFD and the measured values have been compared in Figure 6.8.
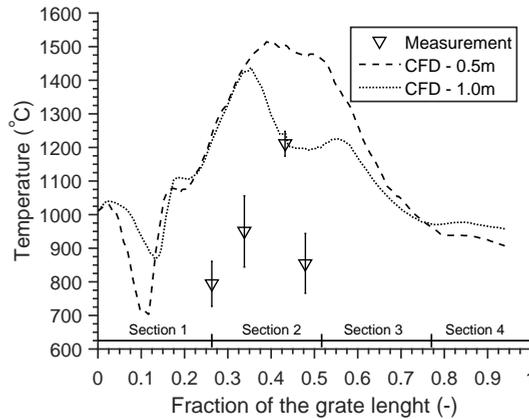
Figure 6.8: The gas temperatures above the grate determined by CFD at points along a straight line from the fuel inlet to the ash pit at an equal distance from both boiler walls. The gas temperature has been evaluated at a distance of 0.5m and 1.0m above the bed and compared with the gas temperatures measured at Affald+; see chapter 5. The process conditions for the modelling have been shown in Table 5.1

The predicted temperatures at the different heights simulated, 0.5m and 1.0m above the bed, have similar values between 0% and 35% and between 60% and 100% of the total bed length. On the contrary the predicted temperatures above the bed do not agree between 35% and 60% of the total bed length. This is expected to be due to the recirculation of colder flue gases induced by the nozzles in the front roof; cf. Figure 6.7.

The predicted and measured temperatures do not agree. The absolute values of the predicted temperatures are in general several hundred degrees higher than the measured. The temperatures at the height of 0.5m above the bed modelled by the CFD code are approximately 300°C higher than the measured temperatures. Model predictions of the position of the peak gas temperature above the bed are, however, in good agreement with measurements. The increased gas temperatures predicted by the CFD model might be due to kinetics or the lack of mixing of combustible gases and oxygen from the bed. The bed model assumes a perfectly mixed gas entering the free board from the bed. It is believed that stratification occurs which means that local fuel rich and fuel lean zones will be found above the bed. The mixing of the fuel and oxidizer decreases the reaction rate causing a prolonged combustion process thereby decreasing the local high temperature zones.

In Figure 6.9 the species concentrations at a hight of 0.5 and 1.0m above the bed predicted by CFD and the measured values have been compared.
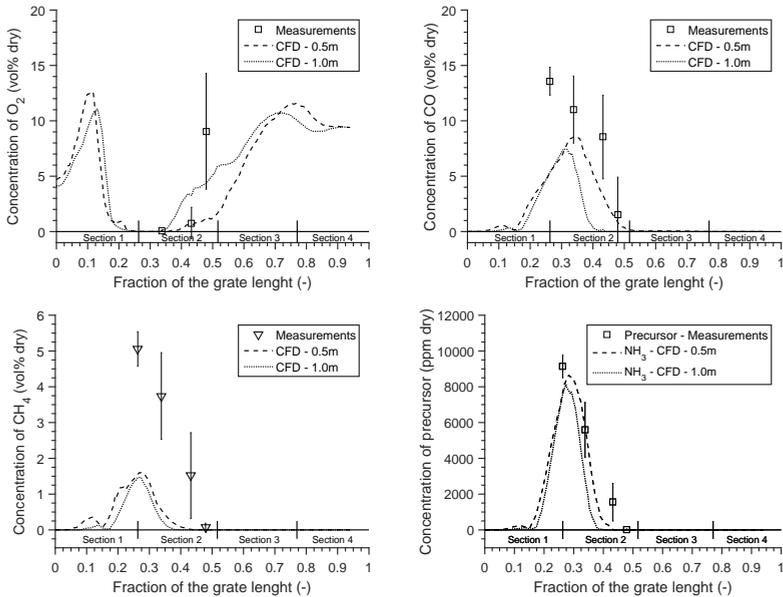
Figure 6.9: The species concentration above the grate determined by CFD at points along a straight line from the fuel inlet to the ash pit at an equal distance from both boiler walls. The species concentrations have been evaluated at a distance of 0.5m and 1.0m above the bed and compared with the species concentrations measured at Affald+; see chapter 5. The process conditions for the modelling have been shown in Table 5.1

The predicted oxygen concentrations are generally in good agreement with measurements. At the transition between grate section 2 and 3 the predicted oxygen concentrations are, however, slightly low compared to the measured.

The predicted concentrations of combustible gases, CO and CH_4, using the CFD model are in general significantly lower than the measured concentrations. The CFD model predicts a larger oxidation of the combustibles and therefore a larger energy release close to the bed. This is in good agreement with the temperatures shown in Figure 6.8. It is believed that this is due to the kinetics used in the CFD model or mixing phenomena as described above. Stratification above the bed causes local fuel rich and fuel lean zones above the bed. The mixing of these zones decreases the reaction rate causing a prolonged combustion process. Consequently higher concentrations are found 0.5m to 1.0m above the bed.

The inlet NH_3 was adjusted to yield the measured NH_3 concentrations. As seen in Figure 6.9 the predicted NH_3 and the measured NH_3 concentrations agree very well.

Based on the results presented in Figure 6.5, 6.6 and 6.7 the NO chemistry was modelled post process. This was done by disabling the calculation of flow, energy turbulence and transport of the major species (CH_4, CO_2, H_2O, O_2 and CO). The resulting NO_x concentrations in the modelled W-t-E have been presented in Figure 6.10.
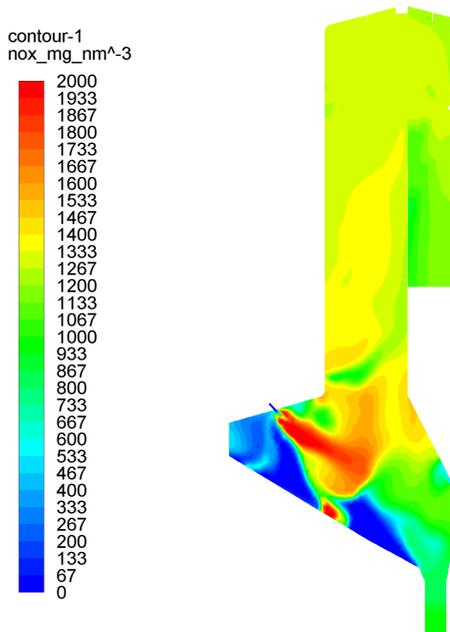
Figure 6.10: The NO_x profile in the W-t-E plants presented in mg/Nm^3 at 11% O_2. The process conditions for the modelling have been shown in Table 5.1

High concentrations of NO_x are found in the jets from the secondary air nozzles in the front roof. The high NO_x concentrations in the jet are due to high oxygen concentrations, high turbulence caused by the jet and high NH$_3$ concentrations; see Figure 6.6 and 6.9. The high NO_x concentrations just above the bed are believed to be caused by thermal NO_x formation due to the high temperature, above 1800° as shown in Figure 6.5, and oxygen flowing from the oxygen rich zone as seen in Figure 6.7 into the high temperature zone. Figure 6.10 indicates full oxidation of species in the furnace before the over fire air; consequently less staging occurs. The outlet concentration of NO_x was predicted to be 1168 mg/Nm^3 at 11% O_2.

The results show very high NO_x emissions compared to measured values at Affald+. Measurements from the plants environmental measurement unit show raw NO_x values ranging from 250 to 350 mg/Nm^3 at 11% O_2 depending on the plant operation, the fuel etc. The predicted NO_x emissions are roughly 4 times larger than the measured NO_x emissions during normal operation. It is believed that the overestimation of the NO_x emission using the developed skeletal model in combination with CFD is caused by the overprediction of the temperature from modelling of the combustion. The overprediction of the temperature might be caused by one or both the following:

- The global kinetics, the model by Westbrook and Dryer[137], have some short comings that might induce errors to the prediction of the combustion process [33]. Studies indicate that the neglection of the H$_2$ in the chemical model might cause an

overprediction of the temperature [136]. For better prediction of the combustion process a more advanced combustion model should be used.

- The bed model assumes a perfectly mixed gas entering the computational domain; consequently the reaction rate is controlled by the kinetics. However, it is believed that stratification might occur over the bed. Due to stratification mixing of the fuel and oxidizer from the bed becomes important. The controlling mechanism might change from kinetically controlled to mixing controlled. This could decrease the reaction rate thereby lowering the temperature in the high temperature zones.

6.6 Summary

The formation of NO_x was modelled using CFD. Modelling of NO_x was performed post process based on the temperature, main species, turbulence and velocity profile. The combustion process was modelled using a two step methane combustion model; Westbrook and Dryer global mechanism [137]. The chemistry-turbulence interaction of the combustion process was modelled by the Finite-rate/EDM model and the turbulence modelled using the realizable k-ϵ model. The temperatures and species concentrations from the fuel bed to the free board were modelled by a stand alone model developed at B&W Vølund. The mass flow of combustion air, heat value of the fuel and mass flow of fuel were determined from operational data from the plant.

The results from the modelling of the combustion process were compared with measurements conducted at the plant; see chapter 5. It was shown that temperatures in the furnace were overpredicted by the model, while species concentrations of the combustibles were underpredicted. This indicates an overprediction of the oxidation of these species. This could be caused by stratification above the bed or due to limitations of global the combustion kinetics.

The formation of NO_x was modelled post process based on the temperature, main species, turbulence and velocity profile. The NO chemistry was modelled using the 38 species and 251 reactions skeletal model developed in this study; see chapter 4. The chemistry-turbulence interaction of the NO_x formation process was modelled by the EDC model and the turbulence modelled using the realizable k-ϵ model. The NO_x precursor, NH_3, was included in the inlet gas entering the computational domain from the bed in concentrations that match the measured concentrations.

The results from modelling showed high concentrations of NO_x in the jet caused by the secondary air nozzles in the front roof of the furnace and in the high temperature region just above the bed. The NO_x emission modelled is approximately 4 times higher than measured at Affald+. It is believed that the large deviation between the modelled and measured emissions are caused by large errors in the prediction of the temperature profile in the furnace. This needs to be addressed before accurate predictions can be made.

Chapter 7

Full scale measurements of the SNCR performance

It is essential to validate a CFD model if the modelling approach is to be used as a design- or optimisation tool. In this chapter results from measurements performed at a full scale W-t-E plant will be presented and discussed. The measurements can be used as data for validation of a CFD model of a SNCR system for NO reduction at a W-t-E plant. The measurements performed include the effect of temperature, ammonia mass flow and droplet size of injected ammonia solution into the hot flue gas on the NO reduction efficiency. Furthermore, ideal reactor simulations were performed and compared with the measurements.

7.1   Plant and grate characteristics

The gas composition and temperatures in the SNCR zone at a Waste-to-Energy plant were measured. The measurements, as for the measurements reported in chapter 5, were performed at Affald+. The W-t-E plant has a nominal waste capacity of 8.2tonnes/h; the plant was operated slightly below nominal capacity (see Table 7.1). The plant uses the Dynagrate® grate technology. The grate is a single-lane grate, with dimensions 10.6x4m. The grate has been split into four zones with lengths of 2.8, 2.7, 2.7 and 1.8 meter, respectively. Predefined fractions of the primary air can be distributed to each zone to control the combustion and ensure complete burn out and low emissions.

7.2   Plant operation during measurements

The measurements were performed over 2 days during which the waste-to-energy plant was running stable without any malfunctions or shut-downs. An oxygen set point of 6 vol% (wet) was used during the two days. The plant was operated at full capacity, consequently the steam pressure was kept at a constant value of 55.6±0.1bar with a steam production of 9.6±0.2kg/s.

The tonnage is lower than the yearly average of 9 ton/h [16] due to the high heating value of the waste.

The conditions under which the plant was operated during the measurements have been shown in Table 7.1.

Table 7.1: Specifications of Affald+ line 4 during the days of measurements.

Waste feed (tons/h)	7.9±2.0
Avg. heating value (MJ/kg)	13.3±0.8
Avg. primary air (Nm3/h)	25,346±3025
Fraction on grate section 1	0.20
Fraction on grate section 2	0.35
Fraction on grate section 3	0.35
Fraction on grate section 4	0.10
Avg. secondary air (Nm3/h)	10,445±395
Temp. primary air (°C)	45.5±3.2
Temp. secondary air (°C)	41.9±0.6
Avg. O_2 (% wet)	6.0±0.6
Steam production (kg/s)	9.6±0.2
Steam temperature (°C)	400
Steam pressure (bar)	55.6
Grate dimension	10m long, 6m wide

The primary and secondary air flows were obtained from the plant control system. The distribution of primary air under the grate was adjusted according to plant setting 1 during another set of measurements reported in chapter 5. The distribution of primary air under the grate has been schematically illustrated in Figure 7.1.
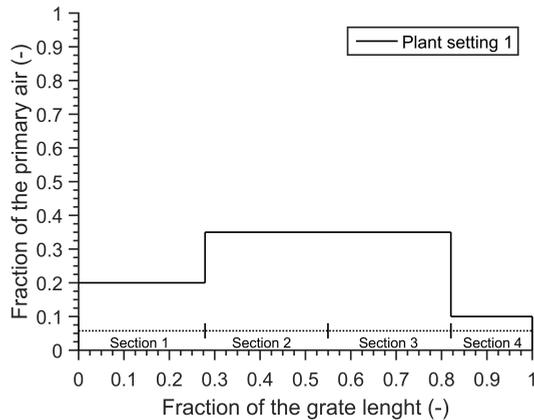
Figure 7.1: Fraction of the total amount of primary air distributed under the grate during the measurements.

Low amounts of primary air were provided to grate section 4 as this mainly serves as ash transport; full conversion of the waste has occurred on the previous 3 sections

7.3 Gas phase composition and temperature measuring system

The flue gas composition was measured with a 5 meter water cooled probe. Due limited access to the first pass measurements were performed by insertion of the probe through 35mm holes in the boiler wall intended for SNCR lances. Due to the small dimensions of the holes the probe was specially designed. The probe was designed at DTU Risø by Senior Scientist Sønnik Clausen.

The probe used for these measurements was different compared to the probe used for measurements in the furnace, as shown in chapter 5, due to lower temperatures in the SNCR zone and limited access to this volume. The temperature in the center of the probe was kept above 150°C to avoid water condensation. The temperature in the probe was controlled by evaporation of water in the probe; contrary to the probe used in the furnace where no evaporation on the cooling media occurred in the probe. This was achieved by minimizing the water flow through the probe.

Prior to the O_2 analyzer, see schematic drawing of the experimental setup in Figure 7.3, the gas is cooled to 5°C to remove any water and aerosols. The system allows simultaneous IR, UV and O_2 measurements. The concentrations of species CH_4, CO, CO_2, NH_3, O_2, NO and H_2O were measured. The probe was inserted through an opening in the boiler wall above the injection of the over fire air. The tip of the probe, the point of measurement, was inserted 2m into the pass. The location of measurement is shown in Figure 7.2. In Figure 7.2 the point of measurement has been shown as a red circle. The location of the SNCR levels have been shown as well.
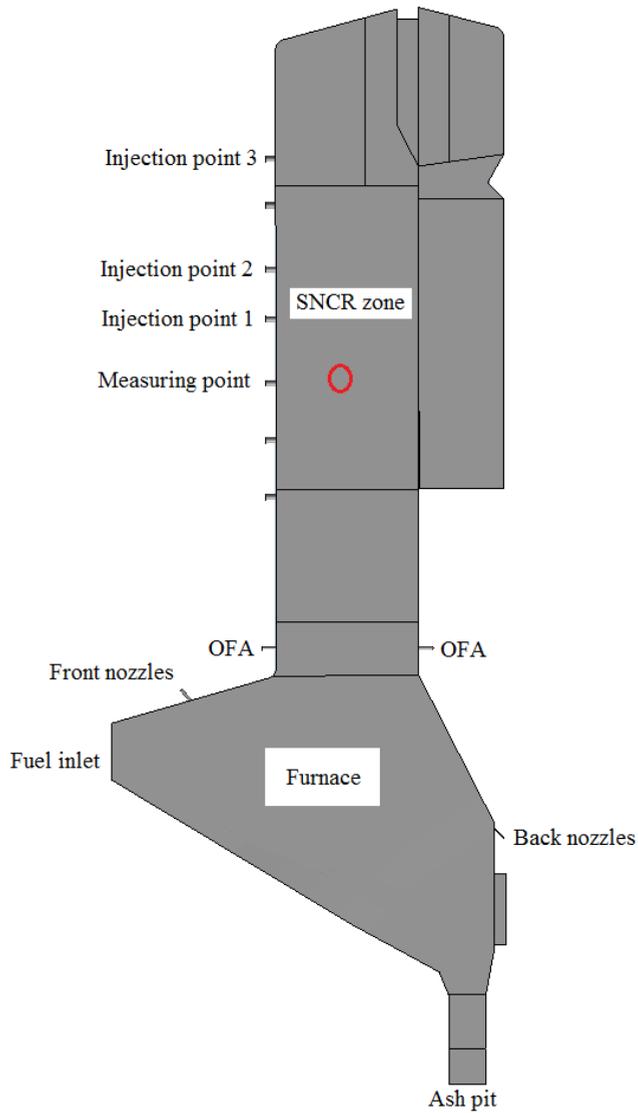
Figure 7.2: Schematic drawing of the furnace and first pass. The measuring point for flue gas determination is shown as a red circle. 7 SNCR levels have been installed in the first pass. Level 1 refers to the lowest SNCR level, while SNCR level 7 refers to the SNCR level with the largest distance to the quench; the transition from the furnace to the first pass. Insertion point 1=SNCR level 4, Insertion point 2=SNCR level 5 and Insertion point 3=SNCR level 7

Table 7.2: Injection of ammonia for NO_x reduction. The height above the quench. The injection points are also shown in Figure 7.2

Injection point	Height above quench (m)
1	9.9
2	11.35
3	14.25

Concentrations of the above mentioned species have been determined from FTIR absorption measurements with use of Bomen MB100 FTIR spectrometer with built-in IR light source and external DTGC detector. The gas sampling was performed at a constant flow rate of 3 Nl/min controlled by an EL-Flow type Bronkhorst mass flow controller with a response time from 0% to 98% signal level of the gas sampling system of about 50s. Concentrations of CO, CO_2, hydrocarbons, NH_3 and water were determined by FTIR measurements, while NO were determined by UV measurements. The O_2 concentration was determined using a Siemens O_2 paramagnetic analyzer. The main sampling parameters were continuously logged by an Agilent BenchLink Data Logger. The temperature of the gas in the sampling line was kept constant at 150°C to avoid condensation of water and light tar products. To avoid blockage of the system, two thimble filters were installed along the heated line to remove particles, soot, heavy tars and aerosols. The system was leak tight and allowed for operation between 1000mbar and 500mbar, limited by the lowest pressure of the O_2 analyzer. After analysis of the flue gas by IR/UV absorption measurement the gas was cooled for water removal for determination of the O_2 concentration. A schematic overview of the measuring system is shown in Figure 7.3.

Figure 7.3: Schematic overview of the gas phase composition and temperature measuring system.

Analysis of the spectral data was performed with an in-house software at the Technical University of Denmark[122]. The software uses the latest spectral databases HITRAN/HITEMP for analysis of IR spectral data in the spectral range from 400 cm^{-1} to 6000cm^{-1}. The pressure in the sampling system was determined and variations have been taken into account in the data analysis.

The uncertainties in the measurements (as for the uncertainties in the measurements done in the furnace) are mainly defined by the uncertainties in the spectral databases

and by the S/N ratio in the measured spectra. The uncertainties are shown in Table 5.4 in chapter 5.

After reduction of the NO_x in the SNCR zone the flue gas was analysed for NO and NH_3 by use of a laser based measuring tool installed at the power plant just after the economiser; an in-situ measurement tool. This enabled concurrent NO and NH_3 measurements before and after the SNCR system; consequently the efficiency of the SNCR system was evaluated. It should be noted that a delay of approximately 30 seconds between inlet flue gas measurements and outlet flue gas measurements were experienced due to the location of the laser based measuring tool. The analyser used for NO and NH_3 determination after the SNCR system was a Neo Monitors LaserGas^{TM} II SP[142] with NO and NH_3 detection limits according to Table 7.3.

Table 7.3: Neo Monitors LaserGas^{TM} II SP detection limit for NO and NH_3. Detection limits are specified as the 95% confidence interval for 1m optical path and gas temperature = 25°, pressure = 1 bar abs measured in N_2.

Species	Detection limit (ppm)
NO	10
NH_3	0.15

7.4 Measurements results

Before the measurements were performed tests to evaluate the best location for flue gas determination before the reduction zone were performed. Due to limited space SNCR level three was used for determination of the flue gas composition; see Figure 7.2. The NO concentration was measured at 4 distances from the boiler wall to evaluate any changes in the concentration. The NO concentration was measured 0.5, 1, 1,5 and 2m from the boiler wall. The resulting NO concentrations have been shown in Figure 7.4.
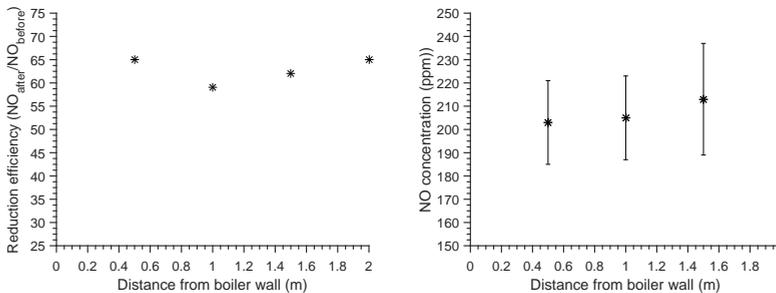
Figure 7.4: The reduction efficiency determined as a function of the measuring point. The inlet NO concentration into the SNCR zone was measured 0.5, 1, 1.5 and 2m from the boiler wall. The outlet NO concentraion from the SNCR zone was determined by the Neo Monitors LaserGas^{TM} II SP [142].

The measurements plotted in Figure 7.4 show no indications that the determination of the NO reduction efficiency depends on the location of measurements in the first pass.Furthermore, the concentrations of NO as a function of the distance from the

boiler wall indicates that the NO concentration does not depend on the location of measurements in the first pass. The concentration of NO increases slightly with distance from the boiler wall. However, differences between each measuring point are within the uncertainties.

It was decided that the measurements were to be performed at a distance of 2m from the boiler wall; hence the measurements were performed in the middle of the gas flow.

7.4.1 Flue gas composition in the SNCR zone

For accurate modelling predictions of the SNCR performance an accurate flue gas composition is needed. It will be shown in Figure 8.3 in chapter 8 that CO concentrations of 2000ppm in the flue gas can shift the SNCR temperature window by as much as 150K; hence an inaccurate flue gas composition might result in inaccurate modelling predictions. The gas composition was measured in SCNR level 3 and averaged over the entire time span. The resulting average gas composition has been shown in Table 7.4.

Table 7.4: The average flue gas composition measured at Affald+ in SNCR level 3, see Figure 7.2 using the specially designed probe. The gas species concentrations are shown as mole fractions. N_2 balances the composition.

Species	Avg. Mole fraction	Standard deviation
H_2O	0.256	0.027
CO_2	0.165	0.015
CO	1458 (ppm)	1545 (ppm)
CH_4	95 (ppm)	200 (ppm)
O_2	0.050	0.014
NO	110 (ppm)	19(ppm)

As expected the major species found in the flue gas are N_2, H_2O, CO_2 and O_2. The measurements showed significant amounts of CO at the measuring point. An average concentration of 1458ppm CO was measured. To further investigate the high CO concentration instantaneous CO concentration was plotted as seen in Figure 7.5.
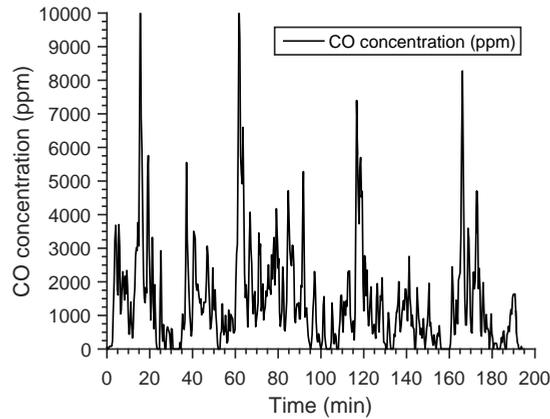
Figure 7.5: The instantaneous CO concentration measured in SNCR level 3, denoted "Measuring point" in Figure 7.2, 2m from the boiler wall. The CO concentration has been shown in ppm. The measurements were done using the specially designed cooled probe.

Over a span of 200 minutes the CO concentration at the point of measurement fluctuates from 0ppm to peak concentrations of above 1%. Only during a fraction of the time the CO concentration can be neglected. The CO concentration fluctuates between 1000 and 3000 ppm during the majority of the time. Neglecting CO during modelling of the SNCR performance at grate firing W-t-E plan will most likely cause large errors as CO in the flue gas changes the SNCR chemistry. As shown in chapter 8 the presence of 2000ppm in the flue gas during NO_x reduction using NH_3 changes the optimal reduction temperature by more than 150°C; see Figure 9.19. Therefore, the use of chemical model for the SNCR process that accurately predict the influence of CO on the NO reduction by NH_3 is important; hence the model developed in this study can be used. The model by Brouwer and Heap [26] will most likely not be able to predict the SNCR performance accurately(see Figure 8.3) as this does not correctly describe the influence of the CO on the reduction chemistry.

7.4.2 Temperature gradient in the Selective Non-Catalytic Reduction zone

As seen in section 1.4.3 the reduction efficiency of a SNCR system strongly depends on the reaction temperature, amongst others. Depending on the CO concentration the largest reduction of NO with NH_3 is found in the region between 1000K and 1250K, see Figure 8.3 and 8.4.

At the W-t-E plant IR based analysers were installed in SNCR level 3 and 6. At each level 2 analysers were installed, one in the right side and one in the left side of the pass. The measurements are in-situ continuous measurements. Suction pyrometer measurements were used to evaluate the accuracy of the IR measurements; consequently the IR measurements can be used during the rest of the measurements if the two methods are in agreement.

In Figure 7.6 the average flue gas temperature at the location of NH_3 injection measured by in-situ IR equipment and suction pyrometer, respectively, has been plotted.
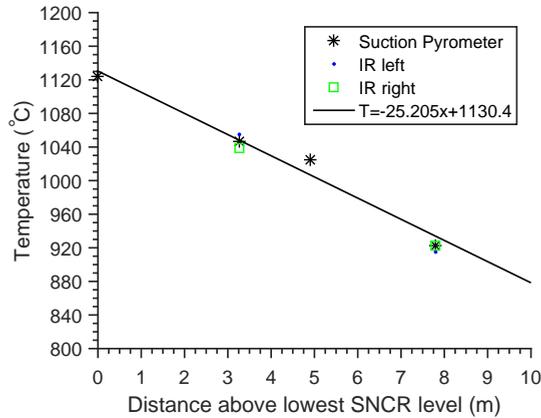
Figure 7.6: Temperature in the SCNR zone measured by suction pyrometer at a distance of 2m from the boiler wall. The measurements were performed at 4 heights above the quench. The temperatures have been compared with temperatures measured by IR equipments installed at the W-t-E.

The temperature measurements using the suction pyrometer were performed at a distance of 2m from the boiler wall to avoid the boundary layer between the boiler wall and the flue gas. In Figure 7.7 the influence of the boundary layer on the temperature is shown.

As shown in Figure 7.6 the suction pyrometer and IR measurements agree well, consequently the IR temperature measurements were used during the rest of the measurements.

From the suction pyrometer measurements the temperature gradient in the first pass was found. The temperature gradient in the first pass was determined to be -25.2°C/m. This result enables one to estimate the temperature at each ammonia injection point. The results from the temperature measurements will furthermore be used to calibrate the CFD model by adjusting the heat transfer coefficient of the boiler walls; see chapter 7.
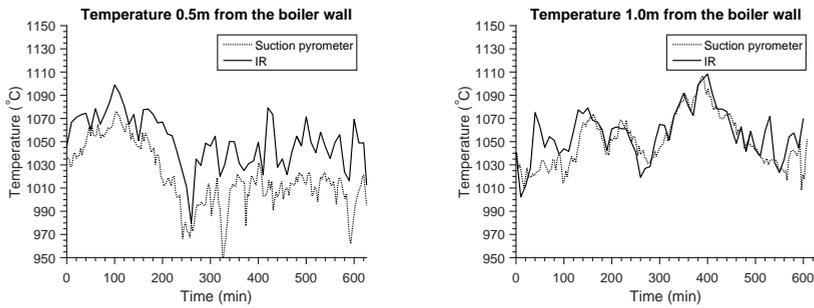
Figure 7.7: Comparison between suction pyrometer measurements and IR measurements at SNCR level 3. The temperatures measured by suction pyrometer in the left picture were performed at a distance of 0.5m from the boiler wall, while the temperatures measured by suction pyrometer in the right picture were performed at a distance of 1m from the boiler wall.

The temperatures measured by the suction pyrometer at a distance of 0.5m from the boiler wall are in general 25°C lower than the temperatures measured by the IR equipment due to the cooling of the boiler walls and the stagnant gas close to the walls. The temperatures measured by the suction pyrometer at a distance of 1m from the boiler wall are in general in good agreement with the temperatures measured by the IR equipment. Since the cross sectional area of the first 0.5m only accounts for 23% of the total cross sectional area of the first pass it was chosen to use the temperatures measured by the IR equipment as the average temperature of the whole cross sectional area; the temperature measured by the IR equipment is in fact the temperature in the middle of the pass.

7.4.3 Effect of temperature on the SNCR performance

The effect of temperature at the point of ammonia injection was evaluated by determining the reduction efficiency for injection of ammonia at 3 different positions. Ammonia was injected at injection point 1, 2 and 3; the injection points are shown in Figure 7.2. The NO concentration was measured before and after the ammonia injection and the reduction efficiency was determined. Due to fluctuations in temperature, gas composition etc. the reduction efficiency for each of the 3 injection points was determined as the average over a time period of 45min. The average reduction efficiency as a function of the temperature at the injection point is shown in Figure 7.8.
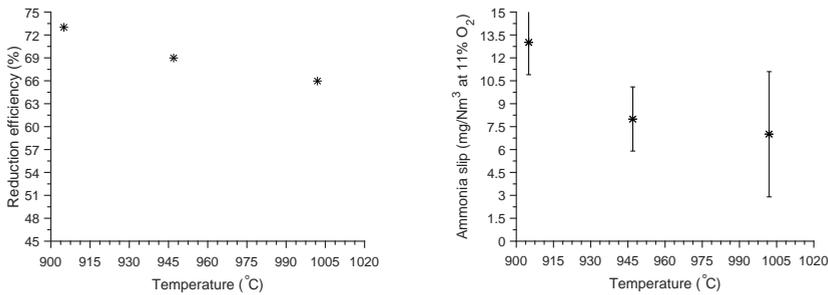
Figure 7.8: The efficiency $((1-[NO]_{\text{after reduction}}/[NO]_{\text{before reduction}})\cdot 100)$ and ammonia slip of the SNCR system as a function of the average temperature at the injection height. During the measurements 0.62l/min of 25% ammonia solution was injected for NO_x reduction corresponding to a NSR of 2.7. The air pressure in the nozzles was adjusted to 4bar.

In the temperature interval investigated the largest reduction in the NO was achieved by injection of ammonia solution at around 900°C. Increasing the temperature results in a small decrease in the efficiency. This could indicate that reduction occur in the presence of CO as the optimal temperature for NO_x reduction with ammonia without any CO present is approximately 950°C; see Figure 8.3. As the concentration of CO increases in the flue gas the optimal temperature decreases as shown in Figure 9.19. The presence of CO in the flue gas is supported by the flue gas composition measurements shown in Table 7.4.

As the NO reduction efficiency is increased by a reduction in temperature from 1000°C to 900°C the NH_3 slip is increased. This is expected due to the high normalised stoichiometric ratio (NSR), defined as n_{NH_3}/n_{NO}, as the rate of oxidation of NH_3 to NO is increased with temperature.

7.4.4 Effect of NH_3 concentration on the SNCR performance

The reduction efficiency is highly dependent on the NH_3 to NO ratio, the normalised stoichiometric ratio. Addition of a high concentration of NH_3 in the correct temperature window will yield a larger reduction cf. the model by Brouwer and Heap [26].

The effect of ammonia mass flow on the reduction efficiency at a full scale W-t-E plant was evaluated and results are shown in Figure 7.9. The injection height was kept constant during the measurements, while the amount of NH_3 injected was varied. For injection of ammonia SNCR level 5 was used. This level corresponds to an injection temperature of approximately 970°C. Each measurement is an average value over a time period of 45min.
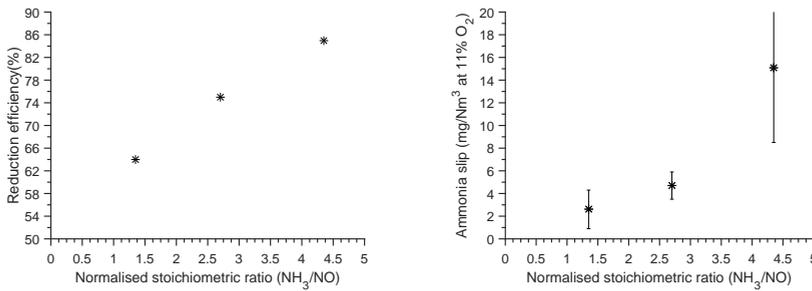
Figure 7.9: The efficiency $((1-[NO]_{\text{after reduction}}/[NO]_{\text{before reduction}})\cdot 100)$ and ammonia slip of the SNCR system as a function of the mass flow of 25% ammonia solution injected for NO reduction. During the measurements the injection height was kept constant at a height corresponding to an injection temperature of 970°C. The air pressure in nozzle was adjusted to 4bar.

As expected the reduction efficiency increases with increasing ammonia mass flow. The reduction efficiency was measured to 64% at a normalised stoichiometric coefficient of 1.35, to 75% at 2.7 and 85% at 4.35. The measurements were all performed at an ammonia injection temperature of approximately 970°C. As seen in Figure 7.8 the temperature at the point of injection is slightly higher compared to the optimal temperature. Higher efficiency with less NH_3 consumption is expected at lower temperatures.
The ammonia slip increases, as expected, with increasing ammonia flow. The slip is low at a mass flow of ammonia of 0.31 and 0.62l/min due to the high temperature at the injection point; unreacted NH_3 is oxidized to NO.

7.4.5 Effect of droplet size from ammonia injection on the SNCR performance

Ammonia is injected into the SNCR zone by air assisted nozzles (Turbotak^{TM} Atomizing Nozzles). The droplets are atomized by pressurised air in the nozzle head. By varying the air pressure the droplet size can be varied. Due to the dependency of the droplet size on the rate of evaporation[143] it was believed that the NO reduction efficiency is affected by the droplet size. The dependency of the droplet size of ammonia solution on the NO reduction efficiency was investigated by varying the pressure of the pressurised air. The pressurised air was adjusted to 2, 4 and 5 bars; this corresponds to a sauter mean diameter of the droplets of 40, 45 and 60μm respectively (see appendix D). Injection of ammonia was done at the same position during the three measurements. The injection was done in SNCR level 5; injection point 2 in Figure 7.2. In Figure 7.10 the results from measurements have been shown.
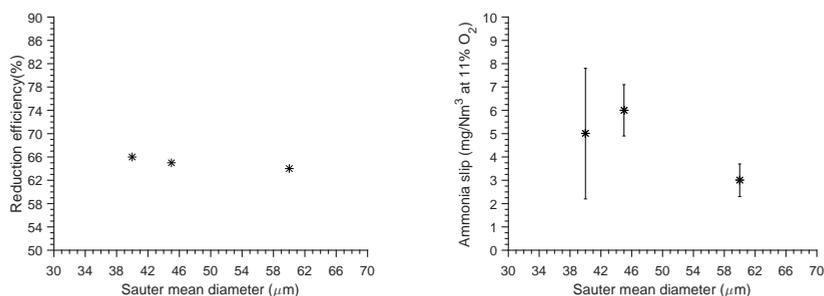
Figure 7.10: The efficiency $((1\text{-}[NO]_{\text{after reduction}}/[NO]_{\text{before reduction}})\cdot 100)$ and ammonia slip of the SNCR system as a function of the sauter mean diameter of the droplets injected into the flue gas for NO reduction. During the measurements the injection height was kept constant at a height corresponding to a temperature at the injection point of 970°C. The mass flow of 25% ammonia solution was constant at 0.62l/min corresponding to a NSR of 2.7.

The results indicate that the droplet size, in the range investigated, has no effect on the reduction efficiency. The reduction efficiency was determined to 66% during these measurements. This corresponds well to the reduction efficiency for similar conditions as shown in Figure 7.8 where the reduction efficiency was determined to 69%.
The results indicate that also the ammonia slip is unaffected by the droplet size of the ammonia solution injected for NO reduction. The ammonia slip for the 45μm droplet size is slightly higher than the ammonia slip for the 40 and 60μm droplet size, however within the standard deviation.

7.5 Modelling of the SNCR process using ideal reactor simulations

Previously in this section the results from full scale measurements of the SNCR performance have been presented. The effect of temperature, ammonia mass flow and droplet size of injected ammonia solution on the NO reduction efficiency was evaluated. In this section the NO efficiency as a function of the temperature will be modelled using a PFR model in CHEMKIN 10131. The NO efficiency as a function of temperature has been evaluated for 3 different CO concentrations and compared to the measurements presented in the previous section. The PFR model has been schematically presented in Figure 7.11.
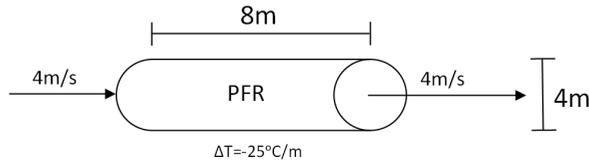
Figure 7.11: Modelling setup for CHEMKin modelling of the NO reduction with ammonia in a W-t-E plant. The reactor dimension is 8m long and 4m in diameter. This corresponds to the size of the first pass at Affald+. The flue gas velocity at Affald+ was found to be approximately 4m/s with a temperature gradient in the reaction zone of -25°C/m.

For each simulation a flue gas with composition as shown in Table 7.5 was used. As seen from Figure 7.11 the residence time in the reactor has been set to 2 seconds. A temperature gradient of -25°C/m in the reactor was defined based on temperature measurements at Affald+; see Figure 7.6.

Table 7.5: The average flue gas composition used for modelling of the SNCR system using CHEMKIN 10131. The gas species concentrations are shown as mole fractions. N_2 balance the composition.

Species	Mole fraction
H_2O	0.25
CO_2	0.165
O_2	0.05
NO	0.0001
NH_3	0.00027
CO	1500, 750 or 0 (ppm)
N_2	Balance

The inlet temperature to the reactor was varied from 800°C to 1050°C with flue gas compositions as shown in Table 7.5. The results from the modelling have been shown in Figure 7.12.
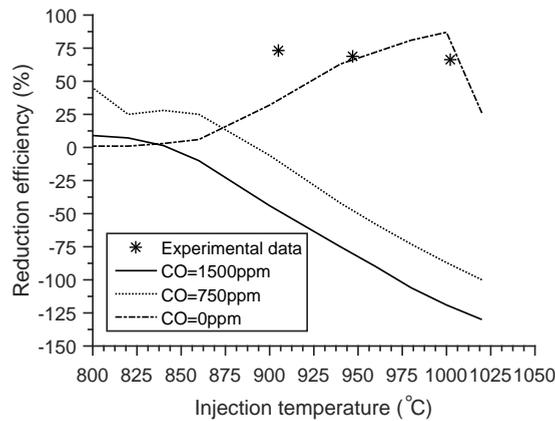
Figure 7.12: Modeling results from CHEMKIN modelling of the NO reduction with ammonia in the presence of CO as a function of temperature. The modelling was done in a PFR with temperature gradient of -25°C and gas velocity of 4m/s corresponding to the conditions in the SNCR zone at Affald+. Inlet gas composition: $H_2O = 25\%$, $CO_2 = 16.5\%$, $O_2 = 5\%$ and CO = 1500ppm (full line), 750ppm (dotted line), 0ppm (punctured line). N_2 balance. Reduction efficiency was defined as $((1-NO_{after}/NO_{before}) \cdot 100)$.

In the range of temperatures investigated, high CO concentrations lead to a very low or negative NO reduction. Compared to the measurement results the modelling results with high CO concentrations, CO=1500 and 750ppm, predict very low NO reductions. Modelling results with no CO in the flue gas yields higher NO reductions similar to the measured NO reductions. However, the results indicate that the temperature window is slightly shifted towards a higher temperature.

In the modelling of the SNCR process using ideal reactors the evaporation of the ammonia-water droplets was not taken into account. Due to the evaporation the actual reaction temperature is not the same as the injection temperature. Results in Figure 7.10 indicate that the reduction efficiency is independent of the droplet size; consequently the evaporation time is very low and most of the ammonia evaporates in the region where injection occur.

The predictions using a PFR model in CHEMKin and NO reductions efficiencies measured at Affald+ show differences. The PFR model assumes the inlet flue gas is perfectly mixed. This assumption might lead to errors as this is not the case in reality. It is believed that more reliable modelling predictions can be achieved by including mixing of the ammonia solution with the flue gas. This phenomena can be included by modelling of the SNCR performance in CFD.

7.6   Summary

The temperature and major flue gas species were measured in the SNCR zone of a full scale W-t-E plant. Furthermore, the concentration of CO and NO were measured. The temperature gradient from the lowest SNCR level to the highest was determined to

-25°C/m. High CO concentration of up to 6000ppm, with peak values of 10000ppm, were measured in the lower part of the SNCR zone. An average CO concentration of approximately 1500ppm was measured over a time span of 200 minutes. The high CO concentrations might shift the temperature window of the reduction reaction significantly.

The NO reduction efficiency as a function of the temperature at the point of ammonia injection was measured. The results showed decreasing efficiency with increasing temperatures from 905°C to 1002°C. The NO reduction efficiency decreased from 73 to 66%. As expected an increase in the ammonia mass flow resulted in an increase in the NO reduction efficiency, while the ammonia slip was increased as well. The NO reduction efficiency was increased from 64 to 85% by increasing the NSR from 1.35 to 4.35 at constant temperature at the point of ammonia injection. It was shown that the droplet size of the ammonia solution injected into the hot flue gas has got no influence on the efficiency of the NO reduction and the ammonia slip.

Ideal reaction simulations of the SNCR process was done. The results showed differences between the measured NO reduction efficiency and the modelled. It is believed that the neglection of the mixing of hot flue gases and ammonia solution injected into the first pass might induce modelling errors. The mixing phenomena can be included by using CFD.

Chapter 8

Development of a new SNCR skeletal model

As a consequence of the stringent legislations, that are expected to be tightened even more, on the NO_x emissions from Waste-to-Energy (W-t-E) plants, NO_x reductions using primary measures alone, e.g. staged combustion, might no longer be adequate. To comply with the legislation secondary NO_x reduction systems, Selective Catalytic Reduction (SCR) or Selective Non-Catalytic Reduction (SNCR), are used. The increasingly more stringent legislations lead to more advanced control of the secondary NO_x reduction system. Due to the relatively low cost of the SNCR system, compared to the expensive SCR, this is used as a secondary reduction system on a vast number of W-t-E plants. As input to the design and control of new advanced SNCR systems a CFD model of the system can be used.

In this section a new skeletal model for the reduction of NO_x in a SNCR system using aqueous ammonia will be presented and tested.

8.1 Development of a new skeletal model using the SEM-CM reduction algorithm

A number of skeletal models describing the formation of NO in W-t-E plants were developed using both the SEM-CM method and the PFA method and tested against a detailed chemical kinetic model (see chapter 4). It was found that the SEM-CM method produced skeletal models with a higher accuracy. Due to the superior performance of the SEM-CM method it was decided to use this for the development of a SNCR skeletal model.

As shown in chapter 4 the development of skeletal models using the SEM-CM algorithm requires knowledge about the gas composition as the model reduction occurs by minimization of the error between concentration profiles of the important species predicted by the starting model (detailed chemical kinetic model) and a produced skeletal model. Full scale measurements at a W-t-E plants capable for a turnover of 9.6 metric tonnes per hour were conducted to determine the gas composition at the transition to the SNCR zone. These measurements are described and discussed in chapter 7. Gas composition measurements were conducted over 3 days and results have been shown in table 8.1. The results from measurements of the gas composition at the transition to the SNCR

zone were used for model reduction, NH_3 was added to this gas composition at a molar fraction equal to the NO.

Species	Concentration
-	Vol % (dry), avg.
H_2O	25.6
CO_2	16.5
O_2	5.1
CO	0.15
CH_4	$9.5 \cdot 10^{-5}$
NO	0.013

Table 8.1: The average gas composition at the transition to the SNCR zone. The gas composition was determine through full scale measurements at a 9.6ton/h W-t-E plant (Affald+). N_2 and trace species balance the composition.

The reduction is based on minimization of the error predicted by the starting model (detailed chemical kinetic model) and the skeletal mode that is begin developed by simulation of the concentration profiles of the important species. It was found that the best reduction was achieved by reduction of the detailed chemical kinetic model around the ignition time delay from 1/4 to 4 times the ignition delay time.

$$\tau_{\text{sim}} = \left[1/4 \cdot \tau_{\text{ign}}; 4 \cdot \tau_{\text{ign}}\right] \tag{8.1}$$

Reductions were done at 5 temperatures ranging from 1073K to 1473K.

$$\text{T} = \left[1073 \quad 1173 \quad 1273 \quad 1373 \quad 1473\right]\text{K} \tag{8.2}$$

For reduction an NH_3 concentration corresponding to the NO concentration was used. A single reduction of the full mechanism developed by Glarborg et al. [10] at the 5 conditions above was performed. Due to the low number of conditions this was favoured over the development of mechanisms at each temperatures and combination of these to a large skeletal model; see chapter 4 for this procedure.

The reduction resulted in a skeletal model consisting of 21 species and 50 reactions and a skeletal model of 15 species and 34 reactions. As a consequence of the small size of the second skeletal model (15 species and 34 reactions) this broke down at a number of conditions, very inaccurately predicting the nitrogen chemistry and was discarded.

8.2 Accuracy of the developed SNCR skeletal model

A comparison between experimental data, the detailed chemical kinetic model developed by Glarborg et al. [10], the skeletal model developed in this study and the global model developed by Brouwer and Heap [26] has been plotted in figure 8.1.
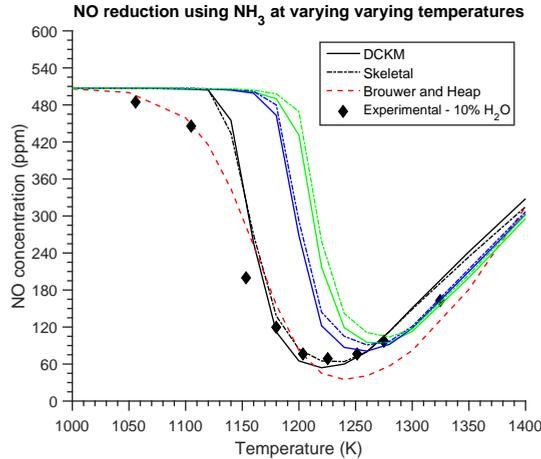
Figure 8.1: Comparison of experimental data [144] (at 10% H_2O) and modelling predictions for the reduction of NO with NH_3 in a laminar quartz flow reactor. The symbols denote the experimental data, the full line denote modelling predictions using the full mechanism[10], the dotted line denote modelling predictions using the developed skeletal model and the striped line denote modelling predictions using the global model by Brouwer and Heap [26]. Inlet concentrations: H_2O=10% (black) or 20% (blue) or 25% (green), NO=507ppm, NH_3=832ppm, O_2=4%, N_2=balance. Residence time= 370/T(K) (s)

A good agreement between the experimental data, the full model and the skeletal model at 10% water is seen. Both the full model and the skeletal model predicts the temperature at which the optimal NO_x reduction is achieved. An underprediction of the reduction is predicted by both models at low temperatures; below 1150K. Both the full model and the skeletal model predict a narrowing of the temperature window at larger water concentrations. Furthermore, a slight decrease in the reduction efficiency (NO_a/NO_i) is predicted at elevated water content in the flue gas by both the full model and the skeletal model.

The global mechanism by Brouwer and Heap [26] slightly overpredict the temperature at which optimal NO_x reduction is achieved; i.e. a higher optimal temperature is predicted at 10% H_2O. Compared to the full model and the skeletal model the global model by Brouwer and Heap accurately predicts the reduction efficiency at lower temperatures. At higher temperatures; T>1225K, the global mechanism slightly overpredict of the reduction efficiency.

Since water is not included in the global mechanism by Brouwer and Heap as shown in

Table 8.2, the global model should be used with caution when predicting NO_x reduction by ammonia at high water concentrations; above 20%. The developed skeletal model predicts the shift in optimal reduction temperature accurately, assuming that the full model is accurate.

Table 8.2: Reduced model for selective non-catalytic reduction of NO_x using ammonia proposed by Brouwer and Heap [26]. Units are: $A = cm \cdot mol \cdot s \cdot K$, E_a = cal/mol.

Reaction	A	B	E_a
1. $NH_3 + NO \rightarrow N_2 + H_2O + H$	$4.24 \cdot 10^8$	5.30	83,600
2. $NH_3 + O_2 \rightarrow NO + H_2O + H$	$3.5 \cdot 10^5$	7.65	125,300

As seen in Figure 8.1 the presence of water during reduction of NO_x with NH_3 causes a slight change in the optimal reduction temperature towards a higher temperature. Furthermore, a narrowing of the temperature window of the NO_x reduction reaction by increasing water concentration is seen.

Predictions with the full model, the skeletal model developed in this study and the global mechanism by Brouwer and Heap have been compared with experimental data from Kasuya et al. [145] and is shown in figure 8.2. In the experiments the effect of the O_2 concentration on the reduction of NO_x with NH_3 was investigated.

It is seen that the SNCR window is shifted towards lower temperatures when the oxygen concentration is increased. Furthermore, a widening of the temperature window is also seen. Both the full model and the skeletal model predict the shift in temperature and the widening of the temperature window fairly well for all the oxygen concentrations included in this study. At low oxygen concentrations; 1%, the full model and the skeletal model underpredict the reduction efficiency at high temperatures; T>1250K, while the global model by Brouwer and Heap accurately predicts the efficiency. At lower temperatures; T<1250K, the opposite trend is seen. The full model and the skeletal model predict fairly accurately the reduction efficiency, while the global model overpredicts the reduction efficiency. The onset temperature is predicted very accurately by the full model and the skeletal model, while the global model underpredicts the temperature onset by up to 100K.

For higher oxygen concentrations all models predict the reduction of NO_x fairly well. However, the full model and skeletal models underpredicts the optimal reduction temperature by up to 40K at 4 and 10% oxygen, while the global model predicts the optimal reduction temperature with reasonable accuracy.
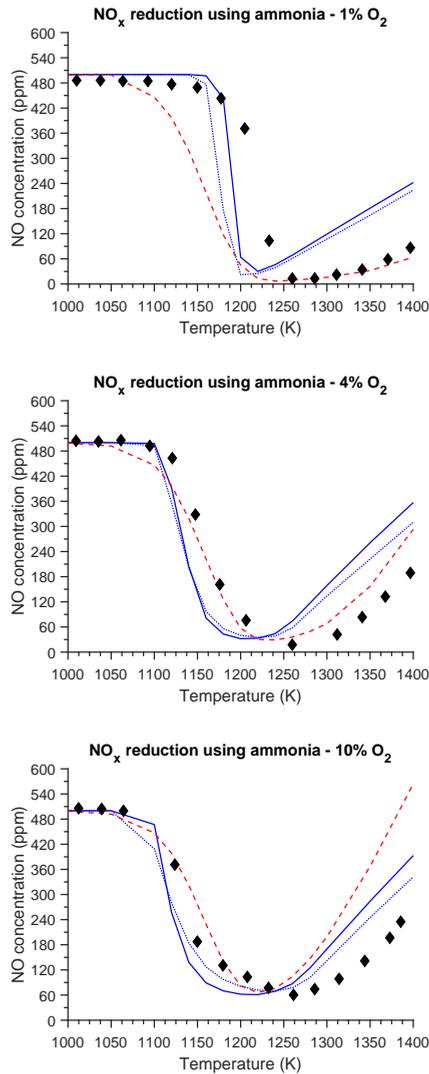
Figure 8.2: Comparison of experimental data [145] and modelling predictions for the reduction of NO with NH_3 in a quartz flow reactor. The symbols denote the experimental data, the full line denote modelling predictions using the full mechanism[10], the dotted line denote modelling predictions using the developed skeletal model and the striped line denote modelling predictions using the global model by Brouwer and Heap [26] Inlet concentrations: NO=500ppm±30, NH_3=1000ppm±60, H_2O=5%, N_2=balance. Residence time= 88/T(K) (s)

The increased oxygen concentration widens the temperature window and decreases the reduction efficiency, the ratio between the NO_x after and before reaction with am-

monia. This has been reported by Lu and Lu as well [146]. All models predict the decrease in reduction efficiency accurately.

The effect of CO on the reduction of NO_x with ammonia has been shown in figure 8.3. The full model by Glarborg et al. [10], the skeletal model developed in this study and the global model by Brouwer and Heap [26] has been compared with experimental data from Alzueta et al. [74]. In the experimental study the CO concentration was varied to investigate the effect on the NO_x reduction by ammonia.

Combustibles such as CO and H_2 have been shown to shift the temperature window towards lower temperatures as these replenish the radical pool [10]. The enhanced radical levels cause a higher degree of oxidation of NH_3 to NO, competing more effectively with the NO removal reactions and thereby narrowing the temperature window for the SNCR system[10]. The effect of the higher radical levels caused by CO flue gas is shown in figure 8.3.

Both the full model and the skeletal model accurately predict the onset temperature for CO concentrations up to approximately 1400ppm. At high CO concentrations; 7800ppm, the full model describes the onset temperature fairly accurate, while the developed skeletal model underpredicts the onset temperature by up to 80K. The global model by Brouwer and Heap breaks down when CO is introduced in the flue gas, over-predicting the onset temperature by more than 100K at 1400ppm CO and up to 200K at 7800ppm CO.

The narrowing of the temperature window caused by CO is well predicted by both the full models and the skeletal model. However, at high CO concentrations; 7800ppm, the skeletal model deviates notably from the full model and does not capture the narrowing of the temperature window fully. This is expected since the skeletal model is developed for CO concentrations up to 1500ppm.

The narrowing of the temperature window is not predicted by the global model by Brouwer and Heap. Brouwer and Heap include the effect of CO as a correction of the temperature used in the Arrhenius expression[26]; see equation 2.34 and 2.35 in chapter 6.2. The inclusion of the effect of CO on the reduction as a correction to the temperature results in a temperature window with the original shape but shifted towards a lower temperature. The narrowing of the window will not be captures by the method.
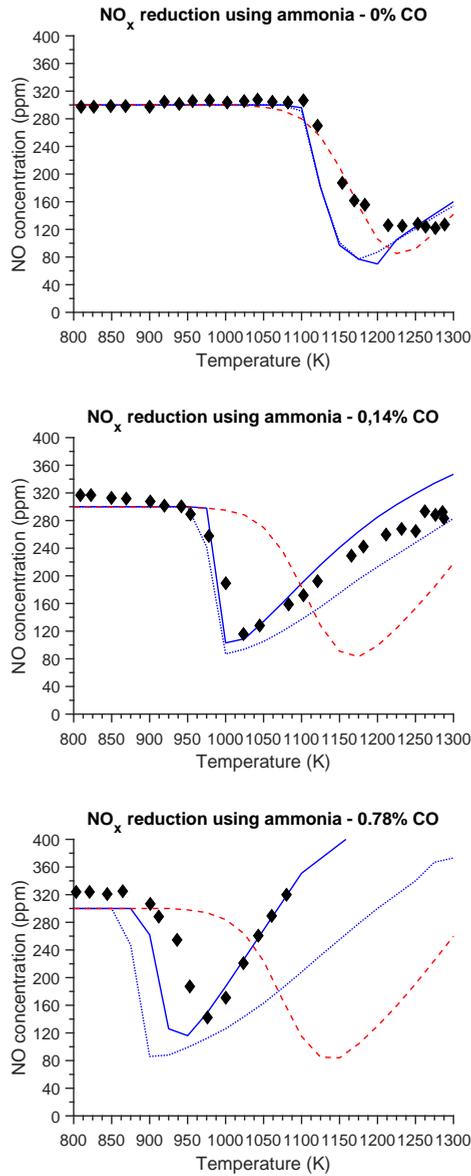
Figure 8.3: Comparison of experimental data [74] and modelling predictions for the reduction of NO with NH$_3$ in a quartz flow reactor; effect of CO. The symbols denote the experimental data, the full line denote modelling predictions using the full mechanism[10], the dotted line denote modelling predictions using the developed skeletal model and the striped line denote modelling predictions using the global model by Brouwer and Heap [26] Inlet concentrations: NO=300ppm, NH$_3$=300ppm, O$_2$=4%, H$_2$O=4,5%, N$_2$=balance. Residence time= 150ms at 1200K (constant molar rate)

From figure 8.1, 8.2 and 8.3 it is seen that the full model by Glarborg et al. [10] and the skeletal model developed in this study describe the SNCR process well for all the conditions. These models overpredict the onset temperature slightly at 10% water in the flue gas. The global model by Brouwer and Heap [26] underpredict the onset temperature at low oxygen concentrations, but perform fairly well for conditions without CO present. When CO is present in the flue gas the global model breaks down. Typically the H_2O content in the flue gas ranges from 20% to 30%. According to the detailed chemical kinetic model, see Figure 8.1, the variation in water content from 20% to 30% only have a limited effect on the SNCR process. A slightly narrowing of the temperature window is seen with increasing water content. Measurements from a full scale W-t-E plant showed average CO concentrations of 1500ppm in the SNCR zone; see chapter 7. Due to the high CO concentration in the SNCR zone it is essential to have a model that describes the influence of CO on the SNCR process. As shown in Figure 8.3 this is achieved by the developed skeletal model, but not achieved by the global model by Brouwer and Heap [26].

For modelling of the SNCR process it is recommended to use the global model by Brouwer and Heap [26] in all cases where full CO oxidation has occurred before the reduction zone. The limited size of the model makes it very useful, especially in CFD codes used industrially. If CO is present in the flue gas it is recommended to use either the full model by Glarborg et al. [10] or the skeletal model developed in this study. It can be an advantage to use the smaller skeletal model to reduce the computational expenses. For modelling of W-t-E plants it is recommended to use either the full model of the skeletal model due to the presence of CO in the reduction zone, as shown in section 7.

As seen in figure 8.1, 8.2 and 8.3 combustibles like CO have a major impact on the temperature window. The water concentration and oxygen concentration have minor effects on the optimal reduction temperature. For advanced control of the SNCR system it is important to have information of the CO level in the SNCR zone, thereby being able to achieve a better reduction as ammonia can be injected at the optimal temperature. In figure 8.4 the temperature at which the largest reduction of NO_x by NH_3 is achieved as a function of the CO concentration in the flue gas has been plotted. The results have been optained by PFR calculations in CHEMKIN using the detailed chemical kinetic model by Glarborg et al. [10]. The gas composition used for these calculations has been determined by full scale measurements at Affald+; see chapter 7.
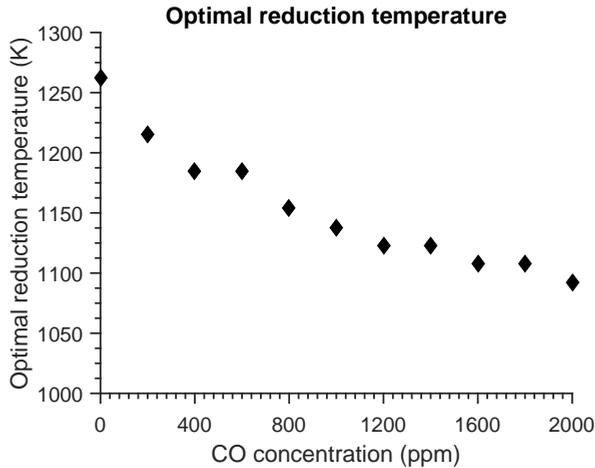
Optimal reduction temperature

Figure 8.4: The temperature at which the largest reduction of NO_x by NH_3 is achieved as a function of the CO concentration in the flue gas. The results are obtained by PFR simulations in CHEMKIN using the detailed chemical kinetic model by Glarborg et al. [10]. Inlet concentration: NO=300ppm, NH_3=300ppm, O_2=6%, H_2O=25%, CO=varied, N_2=balance. Residence time=0.1s

CO concentrations ranging from 0 to 2000ppm on average, with spike values above 6000ppm, was measured over a span of 3 days at the transition to the SNCR zone; see chapter 7. Elevated levels of up to 2000ppm CO in the flue gas in the SNCR zone, which is typically seen at W-t-E plants, can move the optimal reduction temperature by more than 150K. Ideally the CO concentration would be measured at strategic places in, or just before, the SNCR zone for better control of the SNCR process using the knowledge gained above.

8.3 Summary

In this chapter a 21 species and 50 reactions skeletal model describing the SNCR chemistry was developed using the SEM-CM algorithm. The model was tested against experimental data for varying O_2 concentrations and varying CO concentrations in the temperature interval from 800K to 1400K by ideal reactor simulations. It was shown that the developed model performs very well in the temperature interval of interest.

By ideal reactor simulations the effect of CO on the optimal NO_x reduction temperature by NH_3 was determined. It was shown that the optimal NO_x reduction temperature is decreased by more then 150K with 2000ppm of CO in the flue gas.

Chapter 9

Modelling of the SNCR system at a grate firing waste-to-energy plant using CFD

In a previous chapter a skeletal model for the NO_x reduction by ammonia was developed and tested using ideal reactor simulations. It was shown that the model performs well for conditions expected in the SNCR zone of a W-t-E plant. In this section the skeletal model will be implemented in a CFD model, a simulation of NO_x reduction by ammonia injection will be performed and the results will be compared to full-scale measurements.

The commercial CFD code Fluent 18.1 has been used for the NO_x reduction simulation in a full-scale W-t-E plant. The mesh used in the modelling of the NO_x reduction, like for the simulations of the NO_x formation, consists of approximately 2,500,000 cells. The high number of cells is needed to capture the flow from nozzles correctly. The geometry consists of both tetrahedral and hexahedral cells. The SNCR chemistry was modelled post process the combustion; the modelling was done based on the temperature-, turbulence- and velocity profiles from the combustion process. Furthermore, the concentration profiles of the major combustion species were used as well.

The modelling of the NO_x reduction has been done using plant data obtained from the W-t-E plant and from measurements at the plant; see chapter 7.

In this chapter the setup of the model will briefly be presented. The theory behind each of the models used, e.g. models for turbulence-chemistry interaction, has been presented in chapter 6. Estimation of the inlet gas composition and temperature from the bed to the free board will be presented. Furthermore, the results from modelling of the SNCR system will be compared with measurements presented in chapter 7.

9.1 Model setup

In this section the CFD model setup will briefly be presented. The motivation for using the specified combustion model, turbulence model and turbulence-chemistry interaction model in the modelling of the SNCR system has been stated in chapter 6.

9.1.1 Modelling the NO reduction chemistry in turbulent flow

Depending on the problem different procedures are used. For modelling of highly complex problems where a complex multi step reaction mechanism is used; e.g. formation of pollutants, the Eddy dissipation concept (EDC) has to be used. This model assumes that reaction occurs in fine structures of the fluid volume; see section 6.2.1. For simpler problems where the chemistry can be described by a simple global reaction mechanism the Eddy dissipation model (EDM) can be used. This model assumes that the rate of reaction is determined solely by the mixing of fuel and oxidizer [128]. For a multi step global reaction this can cause some problems as the the rate of each reaction is not evaluated. The problem is fixed by using the Eddy-dissipation/Finite-rate model where both the mixing and the kinetics are evaluated and the limiting factor of these used as rate of reaction.

Modelling of the NO_x reduction by ammonia is done in two steps; first the temperature-, pressure-, velocity and turbulence fields were determined. The oxidation of hydrocarbons (CH_4) was simulated using the global methane oxidation mechanism by Westbrook and Dryer. The influence of the turbulence on the chemistry is modelled by the Eddy-dissipation/Finite-rate model as the model offers good stability and low computational time. Furthermore, it is only an advantage to use more advanced interaction models when the turbulent mixing is not rate limiting.

On the basis of results from the main combustion NO_x reduction chemistry was simulated; the modelling was done by using the temperature-, turbulence-, velocity and concentration profiles of the major combustion species from the combustion process. The prediction of the reduction chemistry was done using a skeletal model which have been developed in this study; the model has been presented and tested in chapter 8. The interaction between chemistry and turbulence was modelled using the EDC model.

9.1.2 Estimation of the inlet gas composition and temperature from the bed to the free board

It has been decided to model the NO_x reduction using ammonia at Affald+ under operation conditions identically to the conditions during the experimental study determining the SNCR performance; see chapter 7.

For determination of the inlet boundary conditions the heating value of the fuel, total amount of primary, distribution of primary air under the grate, temperature of the primary air and waste composition was collected from the plant control system. The parameters of interest have been shown in Table 7.1. The composition of the waste is assumed to be as shown in Table 9.1.

Table 9.1: The assumed composition of the waste during combustion for the case modelled. The waste composition was estimated based on correlations between waste feed and heating value established over a long period of time by B&W Vølund. The parameter were collected during measurements a the full scale Waste-to-Energy plant; see chapter 7

Element	Fraction (kg/kg)
C	0.305
H	0.041
O	0.176
N	0.013
Ash	0.174

Providing the bed model with the information about the waste composition (Table 9.1), the heating value of the fuel, total amount of primary air, distribution of primary air under the grate and temperature of the primary air (Table 7.1), the gas temperature, mass flow of gas and composition of the gas for each grate section are modelled. It was decided, as in chapter 6.5, to divide each of the grate sections into additional 4 equally sized zones. The grate is therefore divided in 16 zones in CFD.

The mass flow of gas from the grate to the computational domain determined by the bed model based on data from Table 9.1 and 7.1 as a function of the number of grate zones has been shown in Figure 9.1.
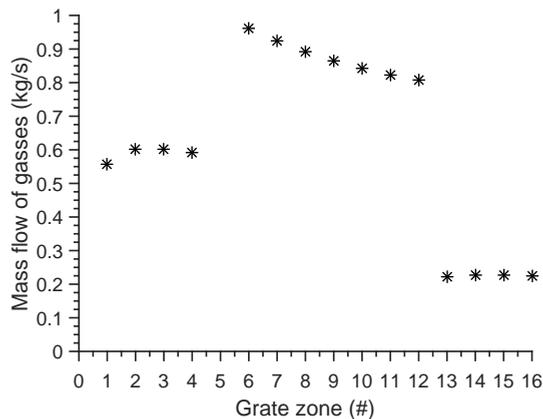
Figure 9.1: The mass flow of gases from the grate to the computational domain determined by the bed model based on data from Table 9.1 and 7.1 as a function of the number of grate zones.

The distribution of the mass flow of gases from the bed to the free board is similar to the distribution of primary air under the grate; see Figure 7.1 (left).

In Figure 9.2 the gas temperature entering the computational domain, determined by the bed model for the specific case, has been shown.
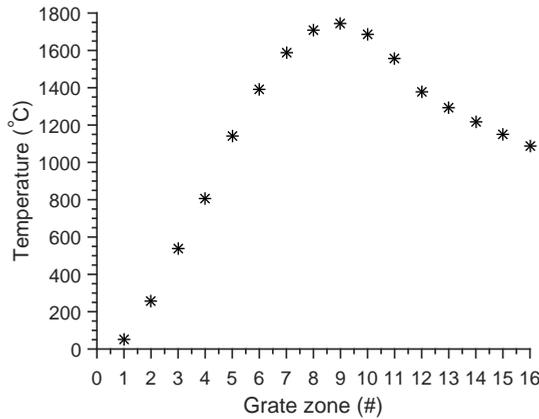
Figure 9.2: The gas temperature of the gas leaving the grate to the computational domain determined by the bed model based on data from Table 9.1 and 7.1 as a function of the number of grate zones.

The peak gas temperature above the bed was estimated to approximately 1800°. In chapter 6.5 it was shown that the gas temperature predicted by the bed model is several hundred degrees higher than the actual measured peak temperature at the W-t-E plant investigated. This is, however, not a problem for modelling of the SNCR performance as the chemistry of interest occurs up higher in the freeboard where much better agreement is observed, as shown in Figure 9.6.

9.1.3 Injection of ammonia-water solution for NO_x reduction

For NO_x reduction a solution of ammonia and water is injected into the flue gas through two Turbotak^{TM} Atomizing nozzles[147]. These nozzles use pressurised air for atomisation of the water-ammonia solution. The pressure of the air is used to control the sauter mean diameter of the particles. This specific nozzle has a hollow cone spray pattern. Injection of the water-ammonia solution was modelled in Fluent using data given in Figure D.1 in appendix D.

A very simple model for the injection of water-ammonia solution was used in this study. This was done as measurements showed no significant difference in the reduction efficiency with varying droplet size of the injected ammonia-water solution (see chapter 7); consequently it was assumed the evaporation of the ammonia-water solution was independent of the droplet size. The droplet evaporation is calculated using equation 9.1 [15].

$$\frac{dm_p}{dt} = k_c A_p \rho_{inf} \ln(1 + B_m) \tag{9.1}$$

Here m_p is the particle mass, k_c mass transfer coefficient, A_p is the droplet surface, ρ_{inf} is the bulk gas density and B_m is the Spalding mass number.

Due to the conical spray pattern the nozzles have been modelled as two circular surfaces

as shown in Figure 9.3. An inner surface where no injection of ammonia-water solution occur and an outer surface from where injection of ammonia-water droplets occur.
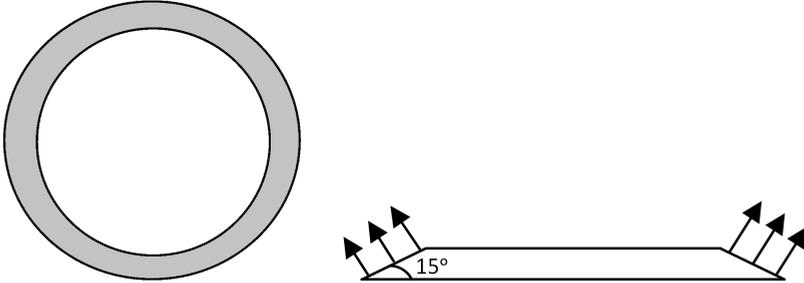
Figure 9.3: Schematic drawing of the modelling of the nozzle in CFD. The liquid is injected through the outer ring, the gray area, which has been angled at 15° relative to the boiler wall.

Injection of the water-ammonia droplets occurs from the surface between the inner and outer circle; the gray area in Figure 9.3. In order to capture the hollow cone spray pattern the surface was angled 15° relative to the boiler wall. The droplet size follows a Rosin-Rammler distribution around the sauter mean diameter, which is found from Figure D.1 in appendix D. The water-ammonia solution was modelled as two separate flows from the angled surface; pure water evaporating to water vapor and pure water evaporating to ammonia gas. Modelling the injection this way one assumes the evaporation of a water-ammonia solution occurs identically to the evaporation of pure water. Due to the low mass fraction of ammonia in the solution this assumption is reasonable.

The simulation of the reduction by ammonia injection was done for injection of 0.31 l/min of 25% water-ammonia solution to each nozzle, while the pressurized air was adjusted to 4.0bar. This setting corresponds to a mean sauter diameter of the injected droplets of 45μm. The concentration of ammonia in the mixture was set to 7.75 mass%.

9.2 Comparison between CFD prediction of the SNCR performance and measurements at a full-scale W-t-E plant

Submodels and the modelling procedures used for modelling of the reduction of NO_x by injection of ammonia in the SNCR process were presented in the previous sections and in chapter 6.5. An identical procedure as in chapter 6.5 was used for modelling of the nitrogen chemistry. First the combustion was modelled and based on these results the reduction of NO_x was modelled post process. In this section results from modelling of the NO_x reduction have been presented. The modelling of the NO_x reduction has been performed using a similar geometry as in chapter 6.5. The results were compared with full scale measurements conducted at Affald+; these are presented in chapter 7.

A schematic drawing of the boiler is seen in Figure 9.4. In this figure the injection level for the modelled case has been shown. Furthermore, the flue gas composition was

measured at the W-t-E plant and results have been presented in chapter 7. The position
of these measurements has been shown in Figure 9.4 as well. Results from the full scale
measurements will be used in this chapter to evaluate the modelling results.
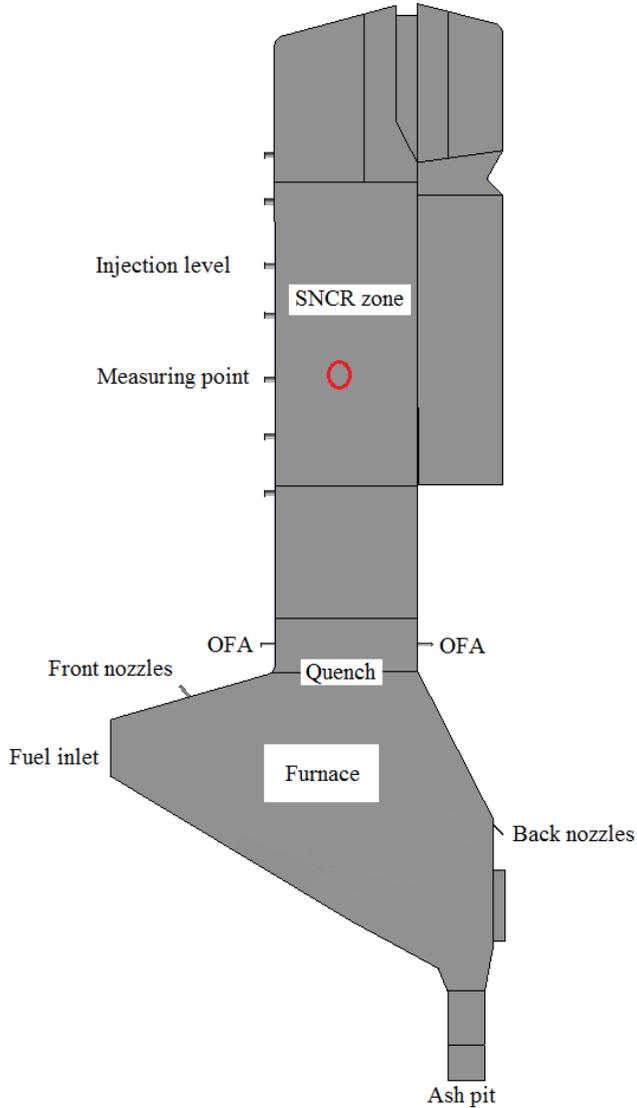
Figure 9.4: Schematic drawing of the furnace and first pass. The measuring point for
flue gas determination is shown as a red circle. 7 SNCR levels have been installed in
the first pass. Level 1 refers to the lowest SNCR level, while SNCR level 7 refers to the
SNCR level with the largest distance to the quench.

The resulting temperature profile from modelling of the combustion during plant

operation as shown in Table 7.1 using the previously described submodels has been shown in Figure 9.5.
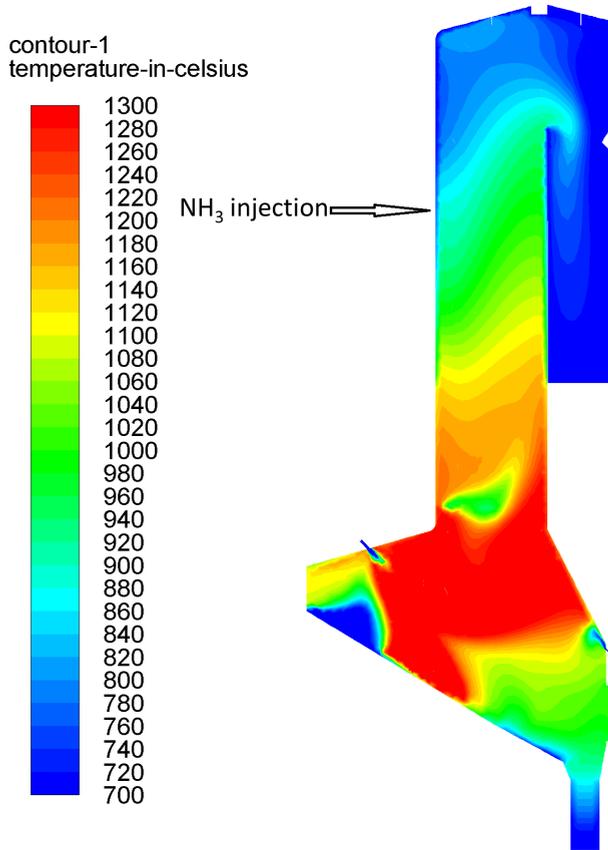
Figure 9.5: The temperature field in the middle of the boiler determined by CFD calculations for SNCR simulations. Post processing of the nitrogen chemistry has been performed based on this temperature field. The process conditions for the modelling have been shown in Table 7.1

A contour plot of the temperature from 700°C to 1300°C has been presented in Figure 9.5. The temperature is limited to 1300°C as the SNCR process is of interest in this specific simulation. After injection of over fire air the temperature gradually decreases from approximately 1200°C to approximately 700°C at the top of the first pass. The average temperature in the cross sectional area at each SNCR level was determined by CFD and compared with IR measurements in SNCR level 3 and 6 and suction pyrometer measurements performed at SNCR level 1, 3, 4 and 6. These results are shown in Figure 9.6.
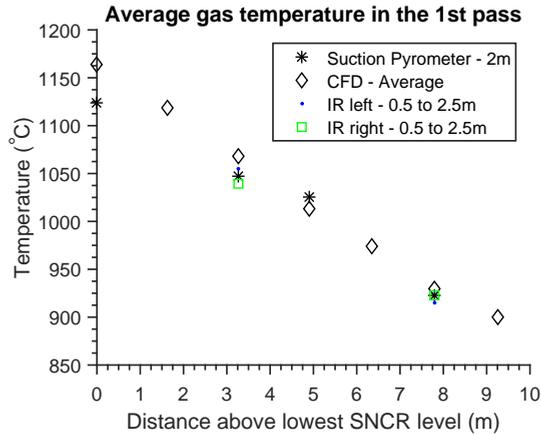
Figure 9.6: Comparison between the average gas temperature determined from the measurements presented in chapter 7 and predicted temperatures using CFD. The average temperature was predicted, using CFD, at each of the 7 SNCR levels; a schematic drawing of the placement of the SNCR nozzles have been presented in Figure 7.2. The position of the measurements has been shown in the figure as well.

In general a good agreement between the modelling results of the average gas temperature and the measurements have been achieved. At the lowest SNCR level the CFD model predicts temperatures that are 40°C higher than the measured temperatures. This can be due to errors in the estimation of the heat transfer coefficients of the boiler walls. Furthermore, the CFD model has been based on average values of the heating value, amount of combustion air etc. over 12 hours, while the measurements were conducted over a period of 30 minutes. Lower heating values of the fuel during temperature measurements in SNCR level 1 can also cause the differences between measurements and modelling results.

Measurements and modelling results agree well for SNCR level 3,4 and 6. At SNCR level 6 the CFD model predicts average temperatures which are 8°C higher than the measured.

The oxygen profile predicted by the CFD model has been presented in Figure 9.7.
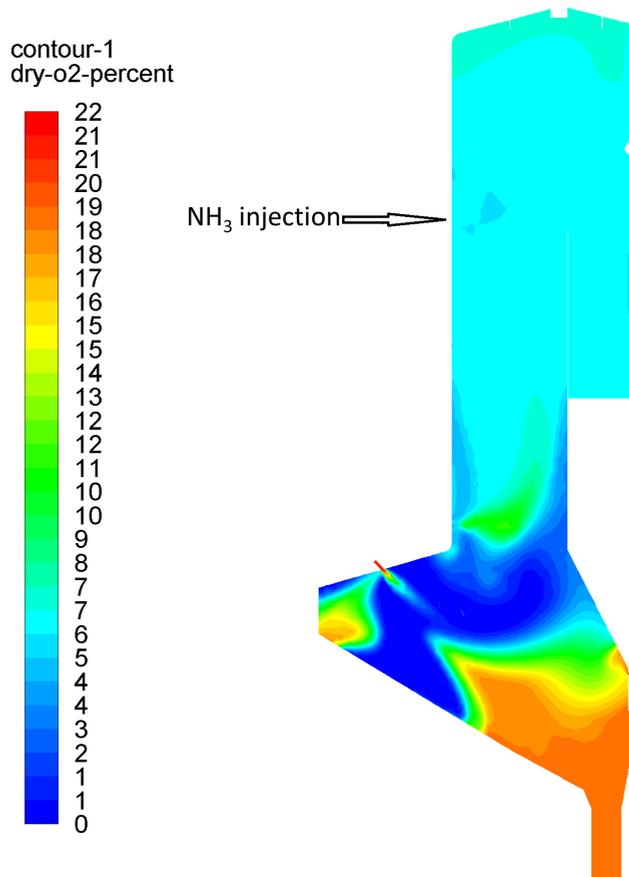
Figure 9.7: The O_2 field in the middle of the boiler determined by CFD calculations for SNCR simulations. Post processing of the nitrogen chemistry has been performed based on this temperature field. The process conditions for the modelling have been shown in Table 7.1

The SNCR performance is dependent on the oxygen concentration; the O_2 level slightly changes the temperature window as shown in Figure 8.2 in chapter 8. As seen in Figure 9.7 the oxygen concentration reaches a concentration of 6% dry after injection of over fire air. No large gradients in the oxygen concentration in the SNCR zone is seen. This is better seen in Figure 9.8, where the average O_2 concentration at each SNCR level predicted by the CFD model has been shown.
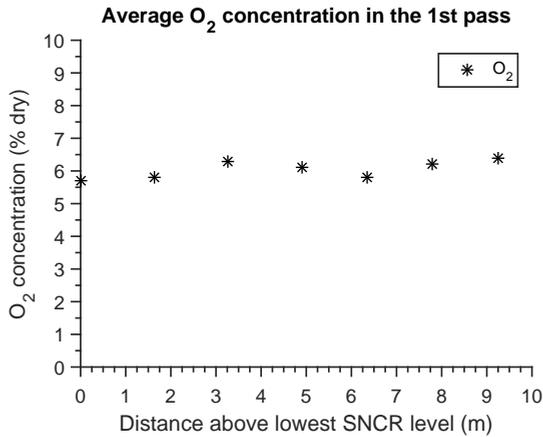
Figure 9.8: The average O_2 concentration at each SNCR level predicted by the CFD model; a schematic drawing of the placement of the SNCR nozzles have been presented in Figure 7.2.

The oxygen concentration at every position in the SNCR zone is predicted to be between 5% and 7% dry; the temperature window for reduction of NO_x with NH_3 do not significantly change within this O_2 range (see Figure 8.2 in chapter 8). A constant oxygen concentration is optimal for the SNCR performance. Furthermore, the predicted O_2 concentration in the SNCR zone agrees well with measurements presented in chapter 7.

The predicted reduction of NO_x by injection of NH_3 has been shown in Figure 9.9. In chapter 6.5 is was shown that the majority of the NO is formed in the jet, caused by injection of combustion air through the nozzles in the front roof. Due to the modelling procedure, post processing of the nitrogen chemistry, it is not possible to model the formation of NO_x followed by the reduction of the formed NO_x by ammonia injection. Modelling a phenomena post process is only valid if this does not change the species-, temperature or velocity field. By modelling the SNCR process post process the NO_x formation changes in the NO and NH_3 concentration profile in the furnace will occur. This will most certainly give inaccurate predictions. Due to this NO was included in the combustion air injected through the nozzles in the front roof. The concentration of NO in the combustion air was adjusted to reach a concentration of NO after the over fire air of 110ppm wet matching the measured NO concentrations during the SNCR measurements presented in chapter 7.
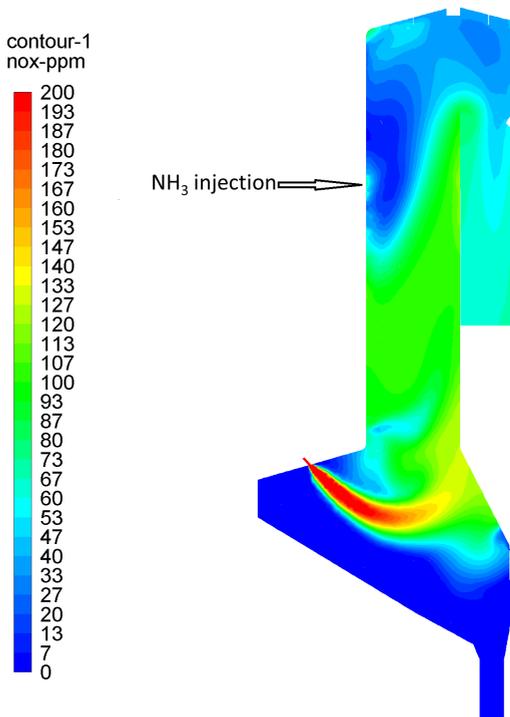
Figure 9.9: The NO field in the middle of the boiler determined by CFD calculations for SNCR simulations. The process conditions for the modelling have been shown in Table 7.1

Figure 9.9 shows reduction of the NO above the injection point as expected. The reduction, however, only occurs in half of the cross sectional area. This is due to limited ingress of the ammonia into the flue gas. The small ingress of ammonia into the flue gas is not expected. A requirement for a high NO_x reduction is good mixing of the NH_3 with the flue gas. Since less than half of the flue gas, according to the CFD model, is in contact with NH_3 a low reduction is expected. This is supported in Figure 9.13. In this figure it is also seen that the measured reduction efficiency is very high compared to the predicted. This indicates a large ingress of NH_3 into the flue gas.

The average NO concentration at each SNCR level was predicted by the CFD model and shown in Figure 9.10. This provided an overview of the NO reduction process.
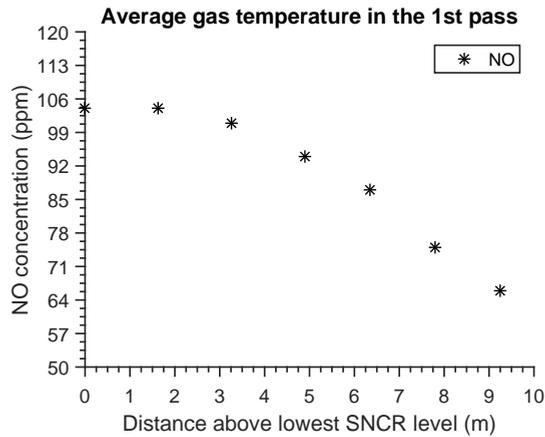
Figure 9.10: The average NO concentration at each SNCR level predicted by the CFD model; a schematic drawing of the placement of the SNCR nozzles have been presented in Figure 7.2.

A constant NO concentration of approximately 100ppm was predicted in SNCR level 1, 2 and 3. This corresponds to the amount of NO formed in the furnace. As stated before the NO was injected into the furnace through the nozzles in the front roof. The mass flow of NO into the furnace was adjusted to reach 105ppm. The model predicts a lower NO concentration in SNCR level 4 than the 105ppm. This is surprising as NH_3 is injected at SNCR level 5, a SNCR level above. This could indicate downwards velocities of some flue gas; the NH_3 is transported by the flue gas towards a lower SNCR level. From SNCR level 5 to 7 the NO concentration decreases correspond to reduction of NO_x emissions.

The NH_3 profile has been shown in Figure 9.11.
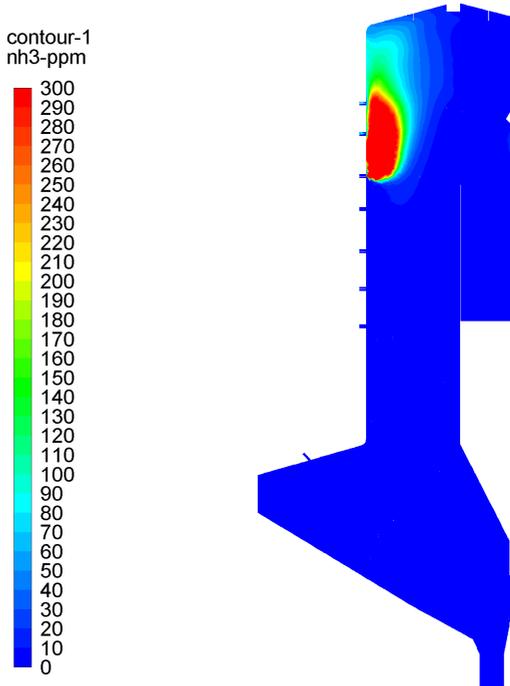
Figure 9.11: The NH$_3$ field in the middle of the boiler determined by CFD calculations for SNCR simulations. The process conditions for the modelling have been shown in Table 7.1

The average NH$_3$ concentration at each SNCR level was predicted by the CFD model and shown in Figure 9.10. As expected the NH$_3$ concentration is high around the injection point where reduction of the formed NO occurs.

The average NH$_3$ concentration is low in the SNCR level 1,2 and 3. However, concentrations of approximately 20ppm NH$_3$ in SNCR level 3 was predicted. This indicates downwards velocities from the NH$_3$ injection point. This is also supported by Figure 9.12. It is believed the high concentrations of NH$_3$ in SNCR level 4 is due to downwards velocities from the NH$_3$ injection point. The phenomena is not seen in Figure 9.11 since the shown NH$_3$ concentration field is shown for a vertical plane positioned between the right and left SNCR nozzles. The highest NH$_3$ concentration is found at SNCR level 5. This is expected as NH$_3$ is injected at this point. From level 5 to 7 the NH$_3$ concentration decreases as a consequence of reaction with NO.

Average NH$_3$ concentration in the 1st pass
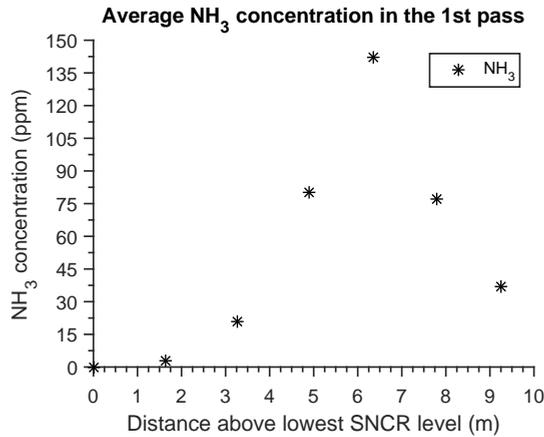
Figure 9.12: The average NH$_3$ concentration at each SNCR level predicted by the CFD model; a schematic drawing of the placement of the SNCR nozzles have been presented in Figure 7.2.

The reduction efficiency predicted by the CFD model was compared with the reduction efficiency measured at the W-t-E plant in Figure 9.13.
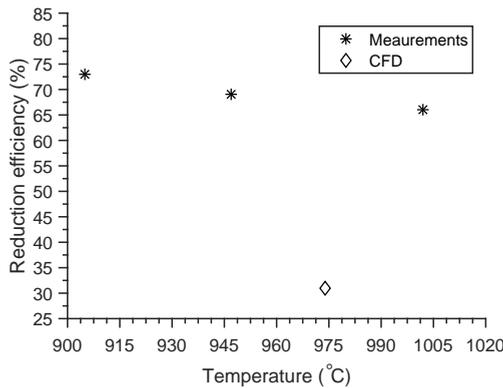
Figure 9.13: Comparison between measured SNCR efficiencies as a function of temperature and the predicted SNCR efficiency at 974°C using the CFD model. The measurements have been presented in chapter 7, while the process conditions for the modelling have been shown in Table 7.1

The full scale measurements showed a decreasing reduction efficiency with temperature from 73% to 66% in the temperature range from 905°C to 1002°C; the measurements have been commented in chapter 7. The measurements were conducted by extractive IR measurements. The efficiency is determined as an average value over a time span of 45 minutes. Furthermore, the temperature is also the average temperature at the injection point determined as an average value over a time span of 45 minutes using IR based measurements; see chapter 7.

The reduction efficiency was predicted using CFD to 31% at an injection temperature of 974°C. This is an underestimation of the reduction efficiency of more than 50%.

The reason for low reduction efficiency predicted by the CFD model was further investigated. The low efficiency predicted by the CFD model can be caused by one or more of the following:

- A recirculation zone in the first pass

- The neglection of CO in the SNCR zone

- Lack of ingress of the particles predicted by the CFD model

Figure 9.10 and 9.10 indicated recirculation of the flue gas in the first pass. This was further investigated by plotting the upwards velocity and the average temperature at the injection level. In Figure 9.14 and 9.15 the upwards velocity and along a horisontal line from the SNCR lance to the opposing boiler wall for both SNCR lances have been presented.

Vertical velocity at SNCR level 5
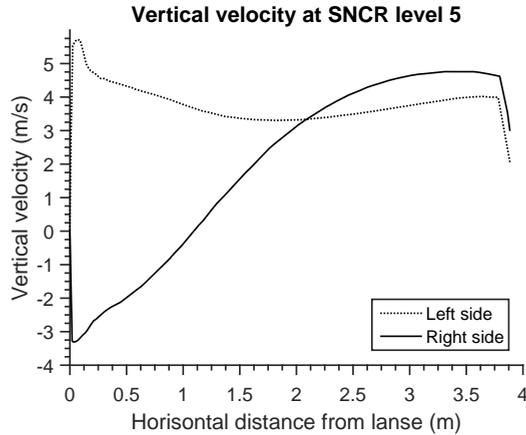
Figure 9.14: The vertical gas velocity, determined by CFD, along a line from the SNCR lance to the opposite boiler wall at SNCR level 5; see Figure 7.2 in chapter 7. The process conditions for the modelling have been shown in Table 7.1
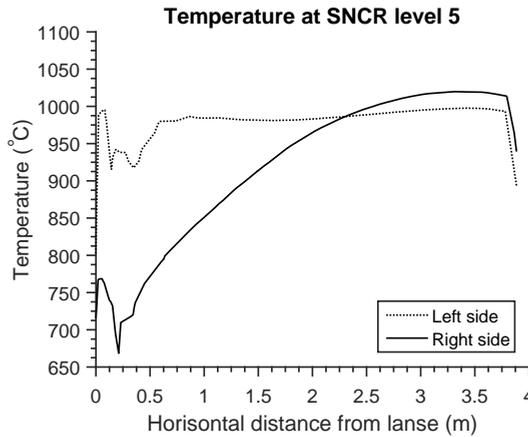
Figure 9.15: The gas temperature, determined by CFD, along a line from the SNCR lance to the opposite boiler wall at SNCR level 5; see Figure 7.2 in chapter 7. The process conditions for the modelling have been shown in Table 7.1

In Figure 9.14 it is seen that from 0 to 1.5 meters from the right SNCR lance the upwards velocity is negative; consequently the flue gas flows from the top of the first pass towards the furnace in the right side of the boiler. The upwards velocity in the left side of the first pass is positive. This means that a recirculation zone in the first 1.5 meters from ammonia injection into the pass occurs. Flue gases flow upwards in the left side of the pass while flowing downwards in the right side of the pass. This is supported by the temperature plot shown in Figure 9.15. It is seen that cold flue gases flow downwards towards the furnace in the right side part of the pass, consequently the temperature at the injection point in the right side is approximately 700°C while the temperature in the left side is approximately 1000°C due to an upwards flow of flue gases from the furnace. The actual temperature where reduction occurs is in fact not 974°C as stated above but approximately 700°C at the right lance and approximately 1000°C at the left lance, consequently the temperature is slightly high for optimal reduction at the left lance and too low for reduction at the right lance. A plot of the vertical gas velocity can support the claim that recirculation of the flue gas occurs in the first pass.
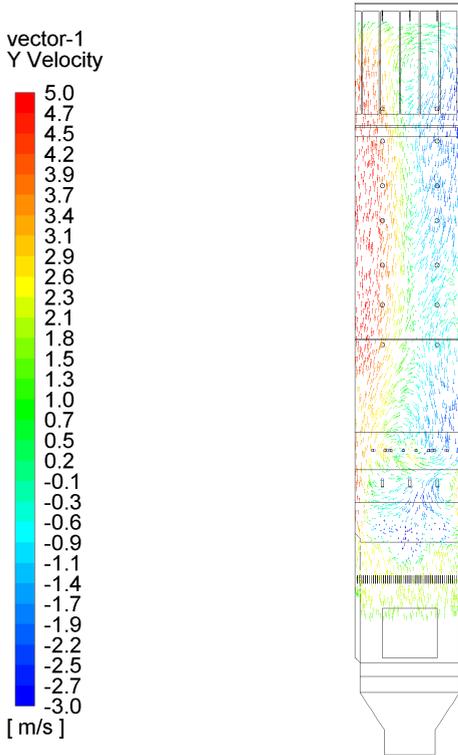
Figure 9.16: The velocity field 1 meter from the boiler wall determined by CFD calculations for SNCR simulations. The process conditions for the modelling have been shown in Table 7.1

The IR temperature measurements from the Affald+ were done in both the right and left side of the first pass; see Figure 9.6. The results from these measurements show no difference between the temperature in the right and left side of the first pass. This indicates that recirculation in the first pass does not occur at the W-t-E plant. Consequently the CFD model predicts a recirculation zone which is not seen in reality. The occurrence of the recirculation zone might be due to the mass flows of combustion air used in the CFD model. In order to determine the inlet mass flows data from the plant control system was averaged over 24 hours. This could cause problems as instantaneous operating conditions were not used; non-existing operating conditions.

In chapter 8 it was shown that small concentrations of CO have a great influence on the temperature window for NO_x reduction. Measurements on a full scale W-t-E plant, see chapter 7, showed peak CO concentrations in the SNCR zone of more than 2000ppm; see Figure 9.18. This can move the temperature window more that 150°C towards lower temperatures while narrowing the window; see Figure 8.4 and 8.3. In order to be able to effectively model the SNCR performance accurate predictions of the CO concentration

profile are needed. In Figure 9.17 the predicted CO profile has been shown.
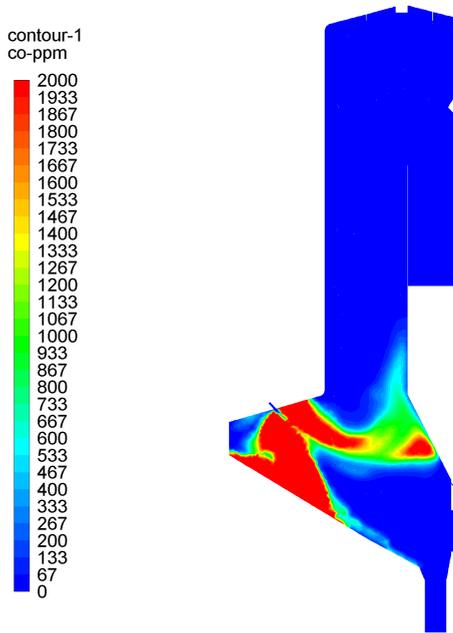
Figure 9.17: The CO concentration profile in the center plan of the boiler predicted by CFD calculations. The process conditions for the modelling have been shown in Table 7.1

Full oxidation of the combustibles before the first pass have been predicted by the CFD model. This does not correspond to measurements at a full scale W-t-E where concentrations of CO of more than 2000pmm were measured in the SNCR zone as shown in Figure 9.18. These CO measurements were performed in SNCR level 3, denoted "Measuring point" in Figure 9.4, at Affald+.
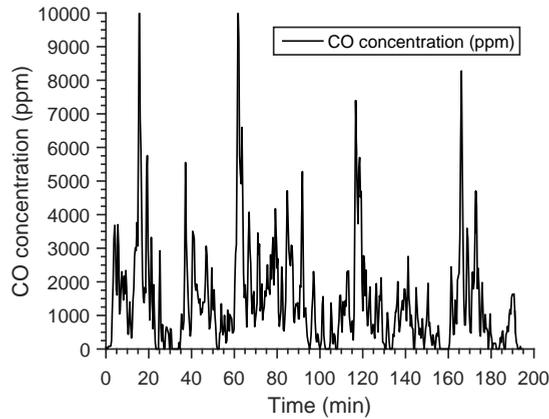
Figure 9.18: The instantaneous CO concentration measured in SNCR level 3, denoted "Measuring point" in Figure 9.4, 2m from the boiler wall. The CO concentration has been shown in ppm. The measurements were done using the specially designed cooled probe.

Peak CO concentrations of 1% was measured, while the average CO concentration was determined to approximately 1500ppm. Occasionally the CO concentration was measured to 0ppm. Since CO in the flue gas changes the temperature window for NO_x reduction process inaccurate prediction of the CO will dramatically effect the accuracy of the model.

It is believed that the under prediction of CO in the SNCR zone is due to either the combustion kinetics used in the CFD model or by stratification above the fuel bed, which is not accounted for in the CFD model. The combustion process is described by the simple Westbrook and Dryer [137] global mechanism, which is believed to be too simple to describe the process accurately. Stratification above the bed causes local fuel rich and fuel lean zones; the model assumed a perfectly mixed gas entering the freeboard from the bed. The mixing of these zones prolongs the combustion process, thereby increasing the life time of the CO released from the bed during devolatilisation or formed by partial oxidation of CH_4 in the furnace.

The effect of CO on the temperature window for the NO_x reduction with ammonia is shown in Figure 9.19.
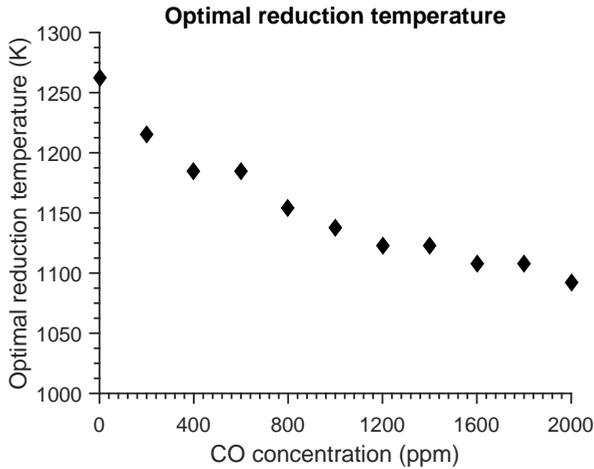
Figure 9.19: The temperature at which the largest reduction of NO_x by NH_3 is achieved as a function of the CO concentration in the flue gas. The results are obtained by PFR simulations in CHEMKIN using the detailed chemical kinetic model by Glarborg et al. [10]. Inlet concentration: NO=300ppm, NH_3=300ppm, O_2=6%, H_2O=25%, CO=varied, N_2=balance. Residence time=0.1s

Concentrations of up to 2000ppm of CO changes the temperature at which the optimal reduction occurs from approximately 950°C to approximately 800°C. It is believed that comparison between predictions from the CFD model and full scale measurements of the SNCR performance will not fully agree as long as accurate CO predictions can not be made.

Lastly the low predicted efficiency could be caused by a lack of ingress of ammonia-water droplets into the flue gas. The coverage of NH_3 injection was investigated by plotting the NH_3 concentration slightly above the injection point. The resulting NH_3 concentration in the cross sectional area slightly above the injection point has been shown in Figure 9.20.
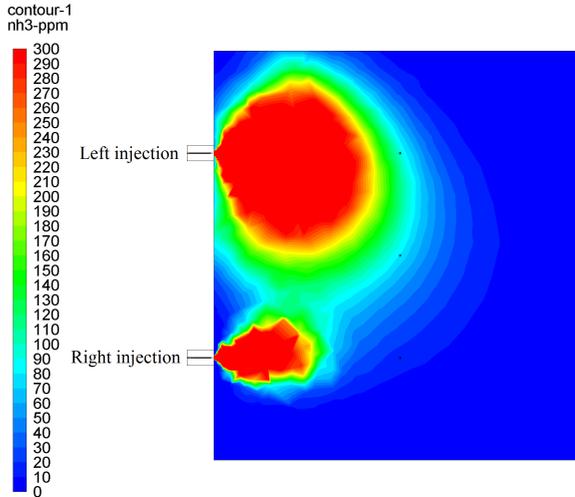
Figure 9.20: NH_3 concentration in the cross sectional area slightly above the injection point predicted by the CFD model. The NH_3 concentration has been specified in ppm.

In Figure 9.20 a plot of the NH_3 concentration in a cross sectional plane in the first pass is shown; the plane is seen from above. A larger part of the cross section area is covered by injection of NH_3 in the left lance. This is due to the upwards velocities investigated above. In the right side of the first pass downwards flowing flue gases cause the low ingress of the NH_3 into the first pass.

It is seen that the injection of NH_3 into the flue gas covers less that half of the cross sectional area. Assuming that the NO_x concentration is equally distributed in the whole cross sectional area high reduction efficiencies can not be achieved, since less that half of the total NO_x is exposed to any NH_3.

The measurements show high reduction efficiencies. An explanation of the high efficiency can be a higher ingress into the flue gas. The W-t-E plant used for data collection is stopped and cleaned approximately once every year. During the year of operation material build-up on boiler walls etc. occur. It can be imagined that material build-up on the nozzle or abrasion of the nozzle can change the characteristics of the droplets, thereby increasing the NH_3 ingress into the flue gas. By inspection of the nozzles after measurements at Affald+ some abrasion of the nozzle was identified.

It is believed the low reduction efficiency predicted by the CFD model is partly due to recirculation of flue gases in the SNCR zone, partly due to inaccurate predictions of the CO concentration field and partly due to the lack of ingress of NH_3 into the flue gas. It is of high importance to update the CFD model for better CO predictions. It is believed this might be done by changing combustion model or by accounting for stratification above the fuel bed as discussed in chapter 6. Furthermore, it would be of interest to evaluate the flow field in the first pass. Measurements suggest recirculation of flue gases does not occur. The inlet mass flow of combustion air used in the CFD model was determined as average values over 24 hours from the plant control system.

This might cause problems as instantaneous conditions were not used, a non-existing operating condition may have been simulated.

9.3   Summary

The reduction of NO_x was modelled using CFD. Modelling of the NO_x reduction process was performed post process based on the temperature, main species, turbulence and velocity profile. The combustion process was modelled using a two step methane combustion model; Westbrook and Dryer global mechanism [137]. The chemistry-turbulence interaction of the combustion process was modelled by the Finite-rate/EDM model and the turbulence modelled using the realizable k-ϵ model. The temperatures and species concentrations from the fuel bed to the free board were modelled by a stand alone model developed at B&W Vølund. The mass flow of combustion air, heat value of the fuel and mass flow of fuel were determined from operational data from the plant.

The reduction of NO_x was modelled post process based on the temperature, main species, turbulence and velocity profile. The reduction chemistry was modelled using the 21 species and 50 reactions skeletal model developed in this study; see chapter 8. The chemistry-turbulence interaction of the NO_x reduction process was modelled by the EDC model and the turbulence modelled using the realizable k-ϵ model. The NO_x concentration into the SNCR zone was adjusted to 110ppm based on the measurements of the flue gas composition.

The results from modelling of the NO_x reduction showed large differences between the predicted SNCR performance and the measured performance. The NO_x reduction efficiency was predicted to be 31% at an average injection temperature of 974°. The measured NO_x reduction efficiency was found to be between 73% and 66% determined in the temperature range 905°C and 1002°C. The predicted NO_x reduction efficiency is more than 50% lower than the measured. It is believed this to is due to a predicted recirculation of flue gases in the SNCR zone by the CFD model, by inaccurate predictions of the CO concentration field which the SNCR process is highly dependent on and the lack of ingress of NH_3 into the flue gas.

Chapter 10

Conclusion and future work

10.1 Conclusions from the study

A skeletal model for the NO_x formation in grate-fired Waste-to-Energy plants was developed using two different reduction algorithms. The reduction of the detailed chemical kinetic model was done using the simulation error minimization connectivity method (SEC-CM) and the path flux analysis method (PFA). A compromise between skeletal model size and performance was made. It was concluded that the 38 species and 251 reactions skeletal model developed using the SEM-CM was the most suitable for NO_x formation predictions for waste combustion in grate-fired Waste-to-Energy plants using CFD due to the relative small size and high accuracy.

The gas temperatures and concentration profiles of the major species above the fuel bed in combustion of waste at a grate-fired W-t-E plant were measured. These measurements serves to evaluate the predictions from a CFD model describing combustion of waste in a grate-fired W-t-E plant. It was determined that the gas temperature increases from 800°C at the initial part of the grate to a maximum value of approximately 1200°C. The position of the peak temperature over the fuel bed slightly depends on the primary air distribution under the bed. The gas released from the fuel bed consisted primarily of water, CO, CO_2, CH_4 and C_2H_4, with significant amounts of C_2H_2 detected downstream. The concentration profiles depended on the distribution of the primary air under the grate. A larger supply of combustion air in the early grate sections (section 2) enhanced oxidation, leading to lower levels of combustible gasses.
The measurements show that volatile nitrogen from the bed is mostly released as NH_3, with minor amounts of HCN. The concentration of the precursors was measured to about 1%vol above the initial part of the grate. Chemical kinetic modelling of NO formation at representative temperatures shows that at excess air ratios below 1.1 the NO yield is roughly independent of the choice of precursor. However, at higher values of the oxygen-to-fuel ratio (λ) the N-speciation influences the formation of NO significantly because HCN has a higher selectivity for forming NO. For this reason reliable determination of the partitioning of NO-precursors is important for predicting NO in grate-fired systems.

The formation of NO_x was modelled using CFD. Modelling of NO_x was performed post process based on the temperature, main species, turbulence and velocity profile from modelling of the waste combustion.
The results from the modelling of the combustion process were compared with meas-

urements conducted at the plant. It was shown that temperatures in the furnace were overpredicted by the CFD model, while species concentrations of the combustibles were underpredicted. This indicates an overprediction of the oxidation of these species. This could be caused by stratification above the bed or due to the global combustion kinetics. The formation of NO_x was modelled post process based on the temperature, main species, turbulence and velocity profile. The NO chemistry was modelled using the 38 species and 251 reactions skeletal model developed in this study. The results from modelling of the NO_x formation showed high concentrations of NO_x in the jet caused by the secondary air nozzles in the front roof of the furnace and in the high temperature region just above the bed. The NO_x emission modelled was approximately 4 times higher than measured at Affald+. It is believed that the large deviation between the modelled and measured emissions are caused by large errors in the prediction of the temperature profile in the furnace. This needs to be addressed before accurate predictions can be made.

A skeletal model for the reduction of NO_x by ammonia in a SNCR system was developed using the simulation error minimization connectivity method (SEC-CM). It was concluded that the 21 species and 50 reactions skeletal model developed using the simulation error minimization connectivity method was the most suitable for modelling of NO_x reduction by ammonia injection in grate-fired Waste-to-Energy plants using CFD due to the small size and high accuracy.

The concentrations of CO and NO in the SNCR zone of a full scale W-t-E plant were measured. High CO concentrations of up to 6000ppm, with peak values of 10000ppm, were measured in the lower part of the SNCR zone. An average CO concentration of approximately 1500ppm was measured, while average NO concentrations of 110ppm were measured.
The NO reduction efficiency as a function of the temperature at the point of ammonia injection was measured. The results showed decreasing efficiency with increasing temperatures from 905°C to 1002°C. The NO reduction efficiency decreased from 73 to 66%. As expected an increase in the ammonia mass flow resulted in an increase in the NO reduction efficiency, while the ammonia slip was increased as well. The NO reduction efficiency was increased from 64 to 85% by increasing the NSR from 1.35 to 4.35 at constant temperature at the point of ammonia injection.

Ideal reaction simulations of the SNCR process was done. The results showed differences between the measured NO reduction efficiency and the modelled. It is believed that the neglection of the mixing of hot flue gases and ammonia solution injected into the first pass might induce modelling errors. The mixing phenomena can be included by using CFD.

The reduction of NO_x was modelled using CFD. Modelling of the NO_x reduction process was performed post process based on the temperature, main species, turbulence and velocity profile determined by modelling of the combustion of waste. The reduction chemistry was modelled using the 21 species and 50 reactions skeletal model developed in this study.
The results from modelling of the NO_x reduction showed large differences between the predicted SNCR performance and the measured performance. The NO_x reduction efficiency was predicted to be 31% at an average injection temperature of 974°C. The

measured NO_x reduction efficiency was found to be between 73% and 66% determined in the temperature range 905°C and 1002°C. The predicted NO_x reduction efficiency is more than 50% lower than the measured. It is believed this is due to a predicted recirculation of flue gases in the SNCR zone by the CFD model and by inaccurate predictions of the CO concentration field which the SNCR process is highly dependent on.

Overall it has been shown that modelling of NO_x formation and reduction post process in CFD using skeletal models is a strategy that can be used. However, the accuracy of the results highly depend on the accuracy of the modelling of the combustion process.

10.2 Proposal for future work

Modelling of the nitrogen chemistry, both formation and reduction of NO_x, was done as post process. Consequently the nitrogen chemistry was modelled after modelling of the combustion process. Since the nitrogen chemistry is highly dependent on the temperature and oxygen concentration accurate predictions of the combustion process in essential for an accurate prediction of the nitrogen chemistry. In this thesis predictions of the NO_x formation and reduction showed poor agreement with measurements. It is believed that this is due to poor predictions of the combustion process. It is therefore recommended to update the CFD model for better prediction of this process. It is believed that the chemical model describing the combustion, in this study the Westbrook and Dryer model, is not sufficiently accurate for modelling of the temperature and oxygen profile for emission predictions. It is recommended to implement in CFD an existing chemical model that is more reliable or develop a more reliable chemical model. Development of a skeletal model for this purpose can be done by use of the SEM-CM algorithm used in this study.

An in-house model describing the fuel bed during waste combustion in a Waste-to-Energy plant has been used to predict the gas composition and gas temperature from the bed into the computational domain. Full scale measurements shows inconsistencies between predictions of the flue gas composition just above the fuel bed and full scale measurements above the bed. The inconsistencies between CFD predictions and full scale measurements indicate that the bed model does not correctly predict the gas composition and gas temperature into the computational domain. Furthermore, the model does not describe the release of NH_3 from the bed which is a very important parameter when modelling the NO_x formation chemistry. It is therefore recommended to develop a new bed model that describes the release of NH_3 and predicts gas compositions and gas temperatures that are consistent with measurements.

Predictions of the SNCR performance using CFD showed poor agreement with measurements from a full scale Waste-to-Energy plant. It is believed the absence of CO in the SNCR zone predicted by the CFD model causes the discord between predictions of the NO_x reduction and measurements. By introduction of CO concentrations of approximately 1500ppm in the SNCR zone it is believed the SNCR model can be evaluated. This however, does not solve the problem with the combustion model discussed above. This approach can only be used to evaluate the developed SNCR model.

It was shown in the thesis that the majority of the NO_x formed during waste com-

bustion in a grate-firing Waste-to-Energy plants occurs in the jet caused by injection of combustion air through nozzles in the front roof. It would be of great interest to evaluate if this is the case in full scale grate-firing Waste-to-Energy plants. Measurements to evaluate this can be performed at the Waste-to-Energy plant used for data collection in this study. As stated previously in this thesis, cone shaped opening in the front roof of the furnace has been installed at the plant. Insertion of water cooled probes through these openings are possible. The cone shaped openings are placed between the front roof nozzles and the quench. Measuring the gas composition at multiple points from the cone shaped openings and vertically down to the grate yields several measurements of the gas composition in the oxygen poor zone below the secondary air jet from the nozzles in the front roof, in the jet and above the jet. These measurements can be used to evaluate where NO_x is being formed.

Nomenclature

A	Pre-exponential factor
A_{eddy}	Constant used in the EDM and EDC model; Default value in Fluent is 4.0
B	A constant used in the EDM and EDC model; Default value in Fluent is 0.5
C_τ	Time scale constant used to calculate the reaction time in the Eddy dissipation concept (0.4082)
$C_{j,r}$	The molar concentration of species j in reaction r
C_{xi}	Volume fraction constant used in the calculation volume fractions of the fine scales with the value 2.1377
D_t	Eddy diffusivity/turbulent diffusivity
$D_{T,i}$	The thermal diffusion coefficient
$D_{i,m}$	The mass diffusion coefficient for species i in a mixture
E	The activation energy
K_r	Equilibrium constant for reaction r
$M_{w,i}$	Molar weight of species i
Q_{pyr}	Energy released in the gas phase
R	The universal gas constant
R_i	The net rate of production of species i by chemical reactions
S_i	Entropy for species i
S_i	The net rate of formation/creation of species i from a dispersed phase or any user defined sources
Y_i	Mass fraction of species i
Y_i^*	The fine-scale mass fraction after reaction over a time period of τ
Y_p	The product mass fraction
$Y_{\mathfrak{R}}$	Mass fraction of particular reactant

ΔH_i	Enthalpy change for reaction r
ΔS_r	Entropy change for reaction r
β	The Arrhenius temperature exponent
ϵ	The dissipation of turbulent kinetic energy
$\epsilon_{sub-grid}$	The dissipation of turbulent kinetic energy in the sub-grid scales
$\eta''_{j,r}$	The rate exponent for products of species j in reaction r
$\eta'_{j,r}$	The rate exponent for reactants of species j in reaction r
μ_t	Turbulent viscosity
$\overline{Y}_i$	The local time-mean mass fraction of species i
$\overrightarrow{J}$	The flux of species i
ρ	Density
$\widehat{R}_{i,r}$	The molar rate of formation or destruction of species i in reaction r
ζ	The net effect of the third bodies on the reaction rate
k	The turbulent kinetic energy
k_{eddy}	Term in the Eddy dissipation model $v'_{i,r}M_{w,i}\rho A$
$k_{f,b}$	The backwards reaction rate
$k_{f,r}$	The forward reaction rate
k_{prompt}	Rate constant for prompt NO_x formation
p_{atm}	Atmospheric pressure - 101325 Pa
$v''_{i,r}$	The stoichiometric coefficients of the products
$v''_{i,r}$	The stoichiometric coefficients of the reactants
v_t	Turbulent kinematic viscosity
$v_{O/f}$	The stoichiometric oxygen to fuel mass ratio
α	The amount of carbon released as volatiles
β	Stoichiometric coefficient of CO in devolatilisation reaction
γ	Stoichiometric coefficient of CO_2 in devolatilisation reaction
ω	The ratio between CO and CO_2 released during devolatilisation of biomass
ϕ	2 time the stoichiometric coefficient of ethene in devolatilisation reaction

σ	Stoichiometric coefficient of methane in devolatilisation reaction
τ	Residence time
θ	The sum of carbon molecules in methane and ethene from devolatilisation of biomass
c_{char}	Amount of carbon in the char
c	Amount of carbon bound in the fuel
h	Amount of hydrogen bound in the fuel
n	Amount of nitrogen bound in the fuel
o	Amount of oxygen bound in the fuel
P	Pressure
V	Volume
CFD	Computational Fluid Dynamics
DAC	Dynamic Adaptive Chemistry
DCKM	Detailed Chemical Kinetic Model
DO	Discrete ordinates method
DRG	Directed Relation Graph
EDC	Eddy Dissipation Concept
EDM	Eddy Dissipation Model
FGR	Flue Gas Recirculation
ISAT	In-Situ Adaptive Tabulation
MSW	Municipal Solid Waste
ODE	Ordinary differential equation
OFA	Over-Fire air
PFR	Plug Flow Reactor
PSR	Perfectly Stirred Reactor
RANS	Reynolds Averaged Navier-Stokes
SCR	Selective Catalytic Reduction
SNCR	Selective Non-Catalytic Reduction
TDAC	Tabulation of Dynamic Adaptive Chemistry
TFN	Total Fixed Nitrogen
W-t-E	Waste-to-Energy

Bibliography

[1] P. Glarborg, A. D. Jensen, and J. E. Johnsson. Fuel nitrogen conversion in solid fuel fired systems. *Progress in Energy and Combustion Science*, 29:89–113, 2003.

[2] A. Frank and M. J. Castaldi. CFD analysis of municipal solid waste combustion using detailed chemical kinetic modelling. *Waste Management & Research*, 32:745–754, 2014.

[3] Chemical Safety Information from Intergovernmental (INCHEM) Organizations. Environmental health criteria 188. (Accessed on 03-02-2017).

[4] C. Yin, S. K. Kær, L. Rosendahl, and S. L. Hvid. Modeling of pulverized coal and biomass co-firing in a 150 KW swirling-stabilized burner and experimental validation. *Proceedings of the International Conference on Power Engineering*, 09:305–310, 2009.

[5] C. Yin, L. Rosendahl, S.K. Kær, S. Clausen, S. L. Hvid, and T. Hiller. Mathematical modeling and experimental study of biomass combustion in a thermal 108 MW grate-fired boiler. *Energy and Fuels*, 22:1380–1390, 2008.

[6] B. J. Finlayson-Pitts and J. N. Pitts Jr. *Chemistry of the upper and lower atmosphere: Theory, experiments and applications*. Acedemic Press, San Diego, 2000.

[7] F. C. Menz and H. M. Seip. Acid rain in Europe and the United States: An update. *Environmental Science and Policy*, 7:253–265, 2004.

[8] DAKOFA. Dansk Kompetencecenter for Affald og Ressourcer -https://dakofa.dk/. (Accessed on 08-02-2018).

[9] S. C. Hill and L. D. Smoot. Modeling of nitrogen oxides formation and destruction in combustion systems. *Progress in Energy and Combustion Science*, 26:417–458, 2000.

[10] P. Glarborg, J. A. Miller, B. Ruscic, and S. Klippenstein. Modeling Nitrogen Chemistry in Combustion. *Progress in Energy and Combustustion Science (In press)*, pages 1–156, 2018.

[11] C. P. Fenimore. Formation of nitric oxide in premixed hydrocarbon flames. *Symposium (International) on Combustion*, 13(3):373–380, 1971.

[12] B. R. Bowman, D. T. Pratt, and C. T. Crowe. Effects of Turbulent Mixing and Chemical Kinetics on Nitric Oxide Production in a Jet-Stirred Reactor. *Fourteenth Symposium (International) on Combustion*, pages 819–830, 1973.

[13] J. A. Miller and C. T. Bowman. Erratum: Mechanism and modeling of nitrogen chemistry in combustion. *Progress in Energy and Combustion Science*, 16:347, 1990.

[14] G. G. De Soete. Overall reaction rates of NO and N_2 formation from fuel nitrogen. *Symposium (International) on Combustion*, 15:1093–1102, 1975.

[15] ANSYS FLUENT. theory guide. *Knowledge Creation Diffusion Utilization*, 15317, 2009.

[16] E. Houshfar, Ø. Skreiberg, T. Løvås, D. Todorović, and L. Sørum. Effect of excess air ratio and temperature on NOx emission from grate combustion of biomass in the staged air combustion scenario. *Energy and Fuels*, 25:4643–4654, 2011.

[17] H. B. Palmer and D. J. Seery. Chemistry of Pollutant Formation in Flames. *Annual Review of Physical Chemistry*, 24:235–262, 1973.

[18] K. Villani, J. De Greef, J. Goethals, I. Montauban, and H. Van Langenhove. Exploring the performance limits of non-catalytic De-NOx in waste. In *Fourth International Symposium on Energy from Biomass and Waste*, 2012.

[19] S. Mahmoudi, J. Baeyens, and J. P. K. Seville. NO_x formation and selective non-catalytic reduction (SNCR) in a fluidized bed combustor of biomass. *Biomass and Bioenergy*, 34(9):1393–1409, 2010.

[20] C. Yin, L. Rosendahl, and S. K. Kær. Grate-firing of biomass for heat and power production. *Progress in Energy and Combustion Science*, 34:725–754, 2008.

[21] E. Houshfar, Ø. Skreiberg, D. Todorović, A. Skreiberg, T. Løvås, A. Jovović, and L. Sørum. NO_x emission reduction by staged combustion in grate combustion of biomass fuels and fuel mixtures. *Fuel*, 98:29–40, 2012.

[22] G. Liuzzo, N. Verdone, and M. Bravi. The benefits of flue gas recirculation in waste incineration. *Waste Management*, 27:106–116, 2007.

[23] R. K. Lyon. The NH3-NO-O2 reaction. *International Journal of Chemical Kinetics*, 8(2):315–318, 1976.

[24] R. K. Lyon and J. E. Hardy. Discovery and development of the thermal $DeNO_x$ process. *Industrial & Engineering Chemistry Fundamentals*, 25(70):19–24, 1986.

[25] S. W. Bae, S. A. Roh, and S. D. Kim. NO removal by reducing agents and additives in the selective non-catalytic reduction (SNCR) process. *Chemosphere*, 65:170–175, 2006.

[26] J. Brouwer, M. P. Heap, D. W. Pershing, and P. J. Smith. A model for prediction of selective non-catalytic reduction of nitrogen oxides by ammonia, urea and cyanuric acid with mixing limitations in the presence of CO. pages 2117–2124, 1996.

[27] J. A. Caton and Z. Xia. The Selective Non-Catalytic Removal (SNCR) of Nitric Oxides from Engine Exhaust Streams: Comparison of Three Processes. *Journal of Engineering for Gas Turbines and Power*, 126(2):243–240, 2004.

[28] P. E. C. Burström, T. S. Lundström, B. D. Marjavaara, and S. Töyrä. CFD-modelling of selective non-catalytic reduction of NOx in grate-kiln plants. *7th international conference on CFD in minerals and process industries*, pages 1–6, 2009.

[29] F. Birkhold, U. Meingast, P. Wassermann, and O. Deutschmann. Modeling and simulation of the injection of urea-water-solution for automotive SCR DeNO$_x$-systems. *Applied Catalysis B: Environmental*, 70:119–127, 2007.

[30] R. K. Lyon. Kinetics and Mechanism of Thermal DeNO$_x$: A Review. *194th Annual ACS Meeting, Div. of Fuel Chemistry*, (15):433–443, 1987.

[31] P. Dagaut, P. Glarborg, and M. U. Alzueta. The oxidation of hydrogen cyanide and related chemistry. *Progress in Energy and Combustion Science*, 34:1–46, 2008.

[32] S. Hansen and P. Glarborg. A simplified model for volatile-N oxidation. *Energy and Fuels*, 24(13):2883–2890, 2010.

[33] J. Andersen, C. L. Rasmussen, T. Giselsson, and P. Glarborg. Global combustion mechanisms for use in CFD modeling under oxy-fuel conditions. *Energy and Fuels*, 23(11):1379–1389, 2009.

[34] F. Blurock and F. Battin-Leclerc. Modeling Combustion with Detailed Kinetic Mechanisms. In F. Battin-Leclerc, J. M. Simmie, and E. Blurock, editors, *Cleaner Combustion*, chapter 2, pages 17–58. Springer-Verlag, London, 1 edition, 2013.

[35] P. Glarborg, J. A. Miller, and R. J. Kee. Kinetic modeling and sensitivity analysis of nitrogen oxide formation in well-stirred reactors. *Combustion and Flame*, 65:177–202, 1986.

[36] T. Mendiara and P. Glarborg. Ammonia chemistry in oxy-fuel combustion of methane. *Combustion and Flame*, 156(10):1937–1949, 2009.

[37] W. H. Sun, J. P. Longwell, and A. F. Sorofim. Rich mixture reactions of nitrogen species in a stirred reactor with ethylene fuel. *Abstracts of papers of the american chemical society*, 193:95, 1987.

[38] Ø. Skreiberg, P. Kilpinen, and P. Glarborg. Ammonia chemistry below 1400 K under fuel-rich conditions in a flow reactor. *Combustion and Flame*, 136:501–518, 2004.

[39] Z. Tian, Y. Li, L. Zhang, P. Glarborg, and F. Qi. An experimental and kinetic modeling study of premixed $NH_3/CH_4/O_2/Ar$ flames at low pressure. *Combustion and Flame*, 156(7):1413–1426, 2009.

[40] C. L. Rasmussen, H. Hansen, P. Marshall, and P. Glarborg. Experimental measurements and kinetic modeling of $CO/H_2/O_2/NO_x$ conversion at high pressure. *International Journal of Chemical Kinetics*, 40(8):454–480, 2008.

[41] P. Glarborg and L. Bentzen. Chemical effects of a high CO_2 concentration in oxy-fuel combustion of methane. *Energy & Fuels*, (20):291–296, 2007.

[42] C. L. Rasmussen, K. H. Wassard, K. Dam-Johansen, and P. Glarborg. Methanol oxidation in a flow reactor: Implications for the branching ratio of the CH_3OH+OH reaction. *International Journal of Chemical Kinetics*, 40(7):423–441, 2008.

[43] P. Glarborg, M. U. Alzueta, K. Dam-Johansen, and J.A. Miller. Kinetic modeling of hydrocarbon/nitric oxide interactions in a flow reactor. *Combustion and Flame*, 115(1-2):1–27, 1998.

[44] C. L. Rasmussen, J. G. Jakobsen, and P. Glarborg. Experimental measurements and kinetic modeling of CH_4/O_2 and $CH_4/C_2H_6/O_2$ conversion at high sressure. *International Journal of Chemical Kinetics*, 40(12):778–807, 2008.

[45] J. G. Lopez, C. L. Rasmussen, M. U. Alzueta, Y. Gao, P. Marshall, and P. Glarborg. Experimental and kinetic modeling study of C_2H_4 oxidation at high pressure. *Proceedings of the Combustion Institute*, 32:367–375, 2009.

[46] C. L. Rasmussen, A. E. Rasmussen, and P. Glarborg. Sensitizing effects of NO_x on CH_4 oxidation at high pressure. *Combustion and Flame*, 154(3):529–545, 2008.

[47] A.M. Dean and J.W. Bozzelli. *Combustion chemistry of nitrogen*. Chapter 2, in: Gardiner, W.C. (Ed.), Gas Phase Combustion, Springer-Verlag, New York, 2000.

[48] E. G. Coda Zabetta and P. T. Kilpinen. Gas-phase conversion of NH_3 to N_2 in gasification part II: Testing the kinetic model. *IFRF Combustion Journal*, 2001.

[49] P. Glarborg, K. Dam-Johansen, J. A. Miller, R. J. Kee, and M. E. Coltrin. Modeling the thermal $DeNO_x$ process in flow reactors. Surface effects and nitrous-oxide formation. *International Journal of Chemical Kinetics*, 26(4):421–436, 1994.

[50] J. A. Miller and P. Glarborg. Modeling the thermal $DeNO_x$ process: Closing in on a final solution. *International Journal of Chemical Kinetics*, 31(11):757–765, 1999.

[51] T. Hasegawa and M. Sato. Study of ammonia removal from coal-gasified fuel. *Combustion and Flame*, 114(1-2):246–258, 1998.

[52] J. Gimenez-Lopez, C.T. Rasmussen, H. Hashemi, M. U. Alzueta, Y. Gao, Paul Marshall, C. F. Goldsmith, and P. Glarborg. Experimental and kinetic modeling study of C_2H_2 oxidation at high pressure. *International Journal of Chemical Kinetics*, 48(11):724–738, 2016.

[53] H. Hashemi, J.G. Jacobsen, C. T. Rasmussen, J.M. Christensen, P. Glarborg, S. Gersen, M. van Essen, H.B. Levinsky, and S. J. Klippenstein. High-pressure oxidation of ethane. *Combustion and Flame*, 182:150–166, 2017.

[54] S. J. Klippenstein, L. B. Harding, P. Glarborg, and J. A. Miller. The role of NNH in NO formation and control. *Combustion and Flame*, 158(4):774–789, 2011.

[55] T. Mendiara and P. Glarborg. Reburn chemistry in oxy-fuel combustion of methane. *Energy and Fuels*, 23(7):3565–3572, 2009.

[56] J. B. Homer and M. M. Sutton. Nitric oxide formation and radical overshoot in premixed hydrogen flames. *Combustion and Flame*, 20(1):71–76, 1973.

[57] N. Lamoureux, X. Mercier, C. Western, J. F. Pauwels, and P. Desgroux. NCN quantitative measurement in a laminar low pressure flame. *Proceedings of the Combustion Institute*, 32:937–944, 2009.

[58] N. Lamoureux, P. Desgroux, A. El Bakali, and J. F. Pauwels. Corrigendum to "Experimental and numerical study of the role of NCN in the prompt-NO formation in low pressure $CH_4/O_2/N_2$ and $C_2H_2/O_2/N_2$ flames" [Combust. Flame 157 (2010) 1929-1941]. *Combustion and Flame*, 160(3):745–746, 2013.

[59] N. Lamoureux, H. E. Merhubi, L. Pillier, S. de Persis, and P. Desgroux. Modeling of NO formation in low pressure premixed flames. *Combustion and Flame*, 163:557–575, 2016.

[60] P. A. Berg, D. A. Hill, A. R. Noble, G. P. Smith, J. B. Jeffries, and D. R. Crosley. Absolute CH concentration measurements in low-pressure methane flames: Comparisons with model results. *Combustion and Flame*, 121(1-2):223–235, 2000.

[61] L. S. Pedersen, P. Glarborg, and K. Dam-Johansen. A Reduced Reaction Scheme for Volatile Nitrogen Conversion in Coal Combustion. *Combustion Science and Technology*, 131(February 2015):193–223, 1998.

[62] E. Houshfar, Ø. Skreiberg, P. Glarborg, and T. Løvås. Mechanisms for NO_x emission prediction in biomass combustion. *International Journal of Chemical Kinetics*, 44(4):219–231, 2012.

[63] P. Glarborg, N. I. Lilleheie, S. Byggstoyl, B. F. Magnussen, P. Kilpinen, and M. Hupa. A reduced mechanism for nitrogen chemistry in methane combustion. *Twenty-Fourth Symposium (International) on Combustion/The Combustion Institute,*, pages 889–898, 1992.

[64] J. O. L. Wendt. Mechanisms governing the formation and destruction of NO_x and other nitrogenous species in low NO_x coal combustion systems. *Combustion Science and Technology*, 108(4-6):323–344, 1995.

[65] J. W. Mitchell and J. M. Tarbell. A kinetic model of nitric oxide formation during pulverized coal combustion. *AIChE Journal*, 28:302–311, 1982.

[66] N. Peters and B. Rogg. *Lecture Notes in Physics Monographs - Reduced Kinetic Mechanism for Applications in Combustions Systems*. Springer Link, 1993.

[67] G. Paczko, P. M. Lefdal, and N. Peters. Reduced reaction schemes for methane, methanol and propane flames. *Symposium (International) on Combustion*, 21:739–748, 1988.

[68] R. W. Bilger, S. H. Starner, and R. J. Kee. On reduced mechanisms for methane-air combustion in nonpremixed flames. *Combustion and Flame*, 80:135–149, 1990.

[69] A. Brink, P. Kilpinen, and M. Hupa. A simplified kinetic rate expression for describing the oxidation of volatile fuel-N in biomass combustion. *Energy and Fuels*, 15(4):1094–1099, 2001.

[70] C. Z. Zabetta, P. Kilpinen, M. Hupa, J. Leppalahti, M. Cannon, and J. Nieminen. Kinetic modeling study on the potential of staged combustion in gas turbines for the reduction of nitrogen oxide emissions from biomass IGCC Plants. *Energy and Fuels*, 14(4):751–761, 2000.

[71] J. A. Caton and D. L. Siebers. Comparison of nitric oxide removal by cyanuric acid and by ammonia. *Combustion Science and Technology*, 65(4-6):277–293, 1989.

[72] D. P. Teixeira, C. J. Lin, L. M. Muzio, D. G. Jones, and Okazaki. Joint epri/epa symposium on stationary no$_x$ control. 1993.

[73] R. Rota, D. Antos, É. F. Zanoelo, and M. Morbidelli. Experimental and modeling analysis of the NO$_x$OUT process. *Chemical Engineering Science*, 57:27–38, 2002.

[74] M. U. Alzueta, H. Rojel, P. G. Kristensen, P. Glarborg, and K. Dam-Johansen. Laboratory study of the CO/NH$_3$/NO/O$_2$ system implications for hybrid reburn/SNCR strategies. *Energy and Fuels*, 11(19):716–723, 1997.

[75] P. T. King, G. E. Andrews, M. M. Pourkashanian, and A. C. Mcintosh. Nitric oxide prediction for low NO$_x$ radial swirlers with central fuel injection using CFD. *Proceedings of ASME Turbo Expo 2012*, pages 1–9, 2012.

[76] M. Bugge, Ø. Skreiberg, N. E. L. Haugen, and M. Seljeskog. CFD modelling of NO$_x$ emissions from wood stoves. *Proceedings of the 1st International Workshop on CFD and Biomass Thermochemical Conversion*, pages 1–6, 2014.

[77] V. Fichet, M. Kanniche, P. Plion, and O. Gicquel. A reactor network model for predicting NO$_x$ emissions in gas turbines. *Fuel*, 89(9):2202–2210, 2010.

[78] M. Falcitelli, S. Pasini, N. Rossi, and L. Tognotti. CFD+reactor network analysis: An integrated methodology for the modeling and optimisation of industrial systems for energy saving and pollution reduction. *Applied Thermal Engineering*, 22:971–979, 2002.

[79] W. P. Adamczyk, S. Werle, and A. Ryfa. Application of the computational method for predicting NO$_x$ reduction within large scale coal-fired boiler. *Applied Thermal Engineering*, 73(1):343–350, 2014.

[80] M. Kanniche. Coupling CFD with chemical reactor network for advanced NO$_x$ prediction in gas turbine. *Clean Technologies and Environmental Policy*, 12:661–670, 2010.

[81] M. Bugge, N. E. L. Haugen, and O. Skreiberg. NO$_x$ emissions from wood stoves - A CFD modelling approach. *22nd European Biomass Conference and Exhibition*, pages 23–26, 2014.

[82] J. Andersen, P. A. Jensen, S. L. Hvid, and P. Glarborg. Experimental and numerical investigation of gas-phase freeboard combustion. Part 2: Fuel NO formation. *Energy and Fuels*, 23(5):5783–5791, 2009.

[83] G. P. Smith, D. M. Golden, M. Frenklach, N. W. Moriarty, B. Eiteneer, M. Goldenberg, C. T. Bowman, R. K. Hanson, S. Song, W. C. Gardiner, Lissianski J. V. V., and Z. Qin. GRI-Mech 3.0. *http://www.me.berkeley.edu/gri_mech/*.

[84] T. Løvås, E. Houshfar, M. Bugge, and Ø. Skreiberg. Automatic generation of kinetic skeletal mechanisms for biomass combustion. *Energy and Fuels*, 27:6979–6991, 2013.

[85] ANSYS FLUENT. User's Guide. 15317(February):2498, 2011.

[86] S. Werle. Impact of feedstock properties and operating conditions on sewage sludge gasification in a fixed bed gasifier. *Waste Management & Research*, 32:954–960, 2014.

[87] W.P. Jones and R.P. Lindstedt. Global reaction schemes for hydrocarbon combustion. *Combustion and Flame*, 73:233–249, 1988.

[88] B. Yang and S. B. Pope. An investigation of the accuracy of manifold methods and splitting schemes in the computational implementation of combustion chemistry. *Combustion and Flame*, 112:16–32, 1998.

[89] F. Battin-Leclerc, J. M. Simmie, and E. Blurock. *Cleaner Combustion - Developing Detailed Chemical Kinetic Models*. Springer, 2003.

[90] H. Wang and J. Jin. Reduced chemical kinetic mechanism for jet fuel combustion. *46th AIAA/ASME/SAE/ASEE Joint Propulsion Conference & Exhibit*, (July):1–10, 2010.

[91] T. Lu and C. K. Law. A directed relation graph method for mechanism reduction. *Proceedings of the Combustion Institute*, 30(1):1333–1341, 2005.

[92] L. Liang, J. G. Stevens, and J. T. Farrell. A dynamic adaptive chemistry scheme for reactive flow computations. *Proceedings of the Combustion Institute*, 32:527–534, 2009.

[93] S. B. Pope. Computationally efficient implementation of combustion chemistry using in situ adaptive tabulation. *Combustion Theory and Modelling*, 1:41–63, 1997.

[94] F. Contino, H. Jeanmart, To. Lucchini, and G. D'Errico. Coupling of in situ adaptive tabulation and dynamic adaptive chemistry: An effective method for solving combustion in engine simulations. *Proceedings of the Combustion Institute*, 33:3057–3064, 2011.

[95] T. Nagy and T. Turányi. Reduction of very large reaction mechanisms using methods based on simulation error minimization. *Combustion and Flame*, 156(2):417–428, 2009.

[96] T. Turányi. Reduction of Large Reaction-Mechanisms. *New Journal of Chemistry*, 14(11):795–803, 1990.

[97] W. Sun, Z. Chen, X. Gou, and Y. Ju. A path flux analysis method for the reduction of detailed chemical kinetic mechanisms. *Combustion and Flame*, 157(7):1298–1307, 2010.

[98] T. Nagy and T. Turányi. Reduction of very large reaction mechanisms using methods based on simulation error minimization. *Combustion and Flame*, 156(2):417–428, 2009.

[99] M. Østberg, P. Glarborg, A. D. Jensen, J. E. Johnsson, L. S. Pedersen, and K. Dam-Johansen. A model of the coal reburning process. *Symposium (International) on Combustion*, 27:3027–3035, 1998.

[100] R. Zanzi, K. Sjöström, and E. Björnbom. Rapid high-temperature pyrolysis of biomass in a free-fall reactor. *Fuel*, 75(5):545–550, 1996.

[101] R. Zanzi, K. Sjöström, and E. Björnbom. Rapid pyrolysis of agricultural residues at high temperature. *Biomass and Bioenergy*, 23(5):357–366, 2002.

[102] E. Vilas, U. Skifter, A. D. Jensen, C. López, J. Maier, and P. Glarborg. Experimental and modeling study of biomass reburning. *Energy and Fuels*, 18(11):1442–1450, 2004.

[103] L Fagbemi, L Khezami, and R Capart. Pyrolysis products from different biomasses. *Applied Energy*, 69(4):293–306, 2001.

[104] W. Kaminsky. Chemical recycling of mixed plastics by pyrolysis. *Advances in Polymer Technology*, 14(4):337–344, 1995.

[105] A. M Li, X. D Li, S. Q Li, Y. Ren, N. Shang, Y. Chi, J. H. Yan., and K. F. Cen. Experimental studies on municipal solid waste pyrolysis in a laboratory-scale rotary kiln. *Energy*, 24(3):209–218, 1999.

[106] W. Kaminsky and A. B. Kummer. Fluidized bed pyrolysis of digested sewage sludge. *Journal of Analytical and Applied Pyrolysis*, 16(1):27–35, 1989.

[107] M. R. Hajaligol, J. B. Howard, J. P. Longwell, and W. A. Peters. Product compositions and kinetics for rapid pyrolysis of cellulose. *Industrial and Engineering Chemistry Process Design and Development*, 21(3):457–465, 1982.

[108] D. Y C Leung, X. L. Yin, Z. L. Zhao, B. Y. Xu, and Y. Chen. Pyrolysis of tire powder: Influence of operation variables on the composition and yields of gaseous product. *Fuel Processing Technology*, 79(2):141–155, 2002.

[109] C. Ryu, Y. B. Yang, V. Nasserzadeh, and J. Swithenbank. Thermal reaction modeling of a large municipal solid waste incinerator. *Combustion Science and Technology*, 176:1891–1907, 2004.

[110] H. H. Frey, B. Peters, H. Hunsinger, and J. Vehlow. Characterization of municipal solid waste combustion in a grate furnace. *Waste Management*, 23:689–701, 2003.

[111] L. Sørum, Ø. Skreiberg, P. Glarborg, A. Jensen, and K. Dam-Johansen. Formation of NO from combustion of volatiles from municipal solid wastes. *Combustion and Flame*, 124:195–212, 2001.

[112] C. D. Goddard, Y. B. Yang, J. Goodfellow, V. N. Sharifi, J. Swithenbank, J. Chartier, D. Mouquet, R. Kirkman, D. Barlow, and S. Moseley. Optimisation study of a large waste-to-energy plant using computational modelling and experimental measurements. *Journal of the Energy Institute*, 78(3):106–116, 2005.

[113] H. Zhang and T. H. Fletcher. Nitrogen transformations during secondary coal pyrolysis. *Energy and Fuels*, 15(6):1512–1522, 2001.

[114] H. Baumann and P. Möller. Pyrolysis of hard coals under fluidised bed combustor conditions. *Science & Technology*, 44(1):29–33, 1991.

[115] Q. Ren, C. Zhao, X. Wu, C. Liang, X. Chen, J. Shen, and Z. Wang. Formation of NO_x precursors during wheat straw pyrolysis and gasification with. *Fuel*, 89:1064–1069, 2010.

[116] Q. Ren. NO_x and N_2O precursors from co-pyrolysis of biomass and sludge. *Journal of Thermal Analysis and Calorimetry*, 112:997–1002, 2013.

[117] Q. Ren, C. Zhao, X. Chen, L. Duan, Y. Li, and C. Ma. NO_x and N_2O precursors (NH_3 and HCN) from biomass pyrolysis: Co-pyrolysis of amino acids and cellulose , hemicellulose and lignin. *Proceedings of the Combustion Institute*, 33(2):1715–1722, 2011.

[118] F. Tian, B. Li, Y. Chen, and C. Li. Formation of NO_x precursors during the pyrolysis of coal and biomass. Part V. Pyrolysis of a sewage sludge. *Fuel*, 81:2203–2208, 2002.

[119] A Frassoldati, A Cuoci, and T Faravelli. Simplified kinetic schemes for oxy-fuel combustion. *1st International Conference on Sustainable Fossil Fuels for Future Energy*, pages 1–14, 2009.

[120] K. Speth, M. Murer, R. V. Raven, and H. Splietho. Influence of stoichiometry and mixing on NO_x reduction in Was-to-Energy plants. *Energy and Fuels*, 30(12):10893–10899, 2016.

[121] Affald+. http://www.affaldplus.dk/anlaeg/naestved-forbraendingsanlaeg.

[122] S. Clausen, A. Fateev, S. L. Hvid, J. B. Beutler, and V. Evsees. Combustion zone investigation in fuel flexible suspension fired boilers, Experimental. Technical report, Technical University of Denmark, 2011.

[123] S. Septien, S. Valin, C. Dupont, M. Peyrot, and S. Salvador. Effect of particle size and temperature on woody biomass fast pyrolysis at high temperature (1000-1400°C). *Fuel*, 97:202–210, 2012.

[124] M. Bøjer, P. A. Jensen, K. Dam-Johansen, O. H. Madsen, and K. Lundtorp. Release of corrosive species above the grate in a waste boiler and the implication for improved electrical efficiency. *Energy & Fuels*, 24(7):5696–5707, 2010.

[125] A. M. Eaton, L. D. Smoot, S. C. Hill, and C. N. Eatough. Components, formulations, solutions, evaluation, and application of comprehensive combustion models. *Progress in Energy and Combustion Science*, 25(4):387–436, 1999.

[126] R. Byron Bird, Warren E. Stewart, and Edwin N. Lightfoot. *Transport Phenomena*. John Wiley & Sons, second edition, 2009.

[127] M.J. Pilling and P. W. Seakins. *Reaction Kinetics*. Oxford Science Publications, 1st edition, 1999.

[128] B. F. Magnussen and B. H. Hjertager. On mathematical modeling of turbulent combustion with special emphasis on soot formation and combustion. *Symposium (International) on Combustion*, 16(1):719–729, 1977.

[129] D. B. Spalding. Mixing and chemical reaction in steady confined turbulent flames. *Symposium (International) on Combustion*, 13:649–657, 1971.

[130] Institut für technische Verbrennung. Lecture notes - Turbulent Combustion: The State of the Art.

[131] A. Brink, C. Mueller, P. Kilpinen, and M. Hupa. Possibilities and Limitations of the Eddy Break-Up Model. *Combustion and Flame*, 213(1-2):275–279, 2000.

[132] B. F. Magnussen. Modelling of NOx and Soot formation by the Eddy Dissipation Concept, 1989.

[133] B. F. Magnussen. On the structure of turbulence and a generalized eddy dissipation concept for chemical reaction in turbulent flow, 1981.

[134] E. I. Ertesvaag. *Turbulent strøymning og forbrenning*.

[135] W. Polifke, K. Dobbeling, T. Sattelmayer, D. G. Nicol, and P. C. Malte. A NOx Prediction Scheme for Lean-Premixed Gas Turbine Combustion Based on Detailed Chemical Kinetics. *Journal of Engineering for Gas Turbines and Power*, 118:765–772, 1996.

[136] A. Brink, P. Kilpinen, M. Hupa, and L. Kjäldman. Study of Alternative Descriptions of Methane Oxidation for CFD Modeling of Turbulent Combustors. *Combustion Science and Technology*, 141(February 2015):59–81, 1999.

[137] C. K. Westbrook and F. L. Dryer. Simplified Reaction Mechanism for the Oxidation of Hydrocarbon Fuels in Flames. *Combustion Science and Technology*, 27(1-2):31–43, 1981.

[138] D. F. Fletcher, B. S. Haynes, F. C. Christo, and S. D. Joseph. A CFD based combustion model of an entrained flow biomass gasifier. *Applied Mathematical Modelling*, 24:165–182, 2000.

[139] C. Yin, S. K. Kær, L. Rosendahl, and S. L. Hvid. Co-firing straw with coal in a swirl-stabilized dual-feed burner: Modelling and experimental validation. *Bioresource Technology*, 101(11):4169–4178, 2010.

[140] K. Jørgensen and D. Grévain. Bedmodel. *Internal report - B&W Vølund - Confidental*, pages 1–40, 2006.

[141] M. P. E. Dvirka. Practical application of incinerator burning rate equations.

[142] NEO monitors. NEO Lasergas II SP. *http://neomonitors.com/tdls-dust-and-gas-analyzers*, (Accessed on 11-01-2018).

[143] R. Kayser and H. S. Bennett. Evaporation of a liquid droplet. *Journal of Research of the National Bureau of Standards Section A: Physics and Chemistry*, 81A(2/3):257, 1977.

[144] W Duo. *Kinetic studies of the reactions involved in selective non-catalytic reduction of nitric oxide*. Technical University of Denmark, phd thesis edition, 1990.

[145] F. Kasuya, P. Glarborg, J. E. Johnsson, and K. Dam-johansen. The Thermal DeNOx Process: Influence of Partial Pressure and Temperature. *Chemical Engineering Science*, 50(9):1455–1466, 1995.

[146] Z. M. Lu and J. D. Lu. Influences of O_2 concentration on NO reduction and N_2O formation in thermal de-NO_x process. *Combustion and Flame*, 156(6):1303–1315, 2009.

[147] B&W Megtek. Turbotak Atomizing nozzle. *http://www.babcock.com/products/-/media/907e98a2e10740e49b48b48364fd3d6a.ashx*, (Accessed on 15-03-2017).

[148] European Environment Agency. Diverting waste from landfill: Effectiveness of waste management policies in the European Union. (7):1–68, 2009.

[149] E. Ranzi, S. Pierucci, P. C. Aliprandi, and S. Stringa. Comprehensive and detailed kinetic model of a traveling grate combustor of biomass. *Energy and Fuels*, 25(9):4195–4205, 2011.

[150] R. Bassilakis, R. M. Carangelo, and M. A. Wójtowicz. TG-FTIR analysis of biomass pyrolysis. *Fuel and Energy Abstracts*, 43(4):280, 2002.

[151] G. Stubenberger, R. Scharler, S. Zahirović, and I. Obernberger. Experimental investigation of nitrogen species release from different solid biomass fuels as a basis for release models. *Fuel*, 87(6):793–806, 2008.

[152] K. M. Hansson, J. Samuelsson, C. Tullin, and L. E. Åmand. Formation of HNCO, HCN, and NH3 from the pyrolysis of bark and nitrogen-containing model compounds. *Combustion and Flame*, 137(3):265–277, 2004.

Appendix A

Manuscript for publication

A.1 Measurements of the NOx Precursors and Major Species Concentrations above the Grate at a Waste-to-Energy plant

Morten Søe Jepsen[a,b], Peter Arendt Jensen[a], Sønnik Clausen[a], Alexander Fateev[a], Peter Glarborg[a] and Thomas Norman[b]

[a]Combustion and Harmful Emission Control (CHEC) Research Centre, Department of Chemical and Biochemical Engineering, Technical University of Denmark, Building 229, DK-2800 Kgs. Lyngby, Denmark, and [b]Babcock and Wilcox Vølund A/S, Odinsvej 19, DK-2600 Glostrup, Denmark

According to the European Landfill Directive the use of landfills has to be avoided whenever possible [148]. This has generated a shift in municipal solid waste handling, from disposal at landfills to extraction of energy through combustion. One of the main combustion technologies for solid waste is grate-firing [149]. By grate-firing of waste heat and power is produced and the volume of waste is greatly reduced. This technology enables the use of a wide range of fuels; both biomass and solid waste, with varying moisture content, and the fuel preparation and handling requirements are limited. Combustion of solid waste, similar to combustion of other solid fuels, emits nitrogen oxides (NOx). The emission of NOx continues to be a major environmental concern [1] as it is an acid rain precursor and participates in formation of photochemical smog, which is problematic in urban areas [1][2]. Nitrogen oxides are formed either from oxidation of the N_2 in the combustion air (thermal NO_x formation), promt NO formation, which is initiated by attack of CH radicals on the N_2 triple bond, the N_2O mechanism or from oxidation of organically bound nitrogen in the fuel (fuel-NO_x formation) [1]. For solid fuels such as waste, which has a significant content of organic nitrogen, the fuel-NO_x mechanism is the dominating source of NO_x [1] due to low combustion temperatures. The NO_x precursors, released during devolatilisation of the fuel in the fuel-bed, mostly consist of ammonia (NH_3) and hydrogen cyanide (HCN) [1]. It has been shown that the formation and partitioning of these NOx precursors depend strongly on fuel characteristics (i.e., biomass type, fuel nitrogen content, particle size, and moisture content [1][150][151]) and on process conditions (devolatilisation temperature and stoichiomet-

ric air ratio [1][152]). The reactive nitrogen species released from the fuel-bed are subsequently oxidized to either NO or N_2 in the freeboard. The selectivity for forming NO, rather than N_2, depends strongly on the reaction conditions in the freeboard, mainly temperature and stoichiometry [1].

Satisfactory results from modelling of NOx formation in CFD during combustion of Municipal Solid Waste (MSW) in grate-fired waste-to-energy plants is highly depended on accurate descriptions of the temperature field in the free-board above the waste bed. Accurate modelling of the temperature field relies on an accurate determination of the boundary conditions; the species concentration, gas temperature and gas velocity from the waste bed into the computational domain. In this study the gas temperature and the gas concentration profiles of O_2, H_2O, CO, CO_2, CH_4, C_2H_2, C_2H_4, NH_3 and HCN along the waste bed were measured. The measurements were performed on a 9 ton/h grate-fired waste-to-energy plant, Affald+ unit 4 in Denmark. The species concentration profiles were determined by gas extraction using a 6m water cooled probe and FTIR spectroscopy, while the gas temperatures were determined by suction pyrometer. The major combustible gasses were determined to be CO, CH_4 and C_2H_4, which are only found above the first half of the grate. Furthermore, it was determined that during grate-fired MSW combustion the majority of the NO_x precursors are released as NH3; more than 80%. The influence of NO_x precursor composition on the NOx formation was examined through CHEMKIN simulations. It was shown that for reliable modelling of the NO formation at high excess air ratios, $\lambda > 1.1$, it is important to determine the correct ratio between NH_3 and HCN. The importance of an accurate precursor determination increases considerably with decreasing temperatures.

A.1.1 Introduction

In order to achieve a satisfactory result from CFD modelling of NO_x formation during combustion of waste in grate-fired waste-to-energy plants an accurate description of the temperature field in the free-board is essential, due to the dependency of the temperature on the low temperature fuel NO_x chemistry [1][119]. Modelling of the temperature field in the free-board relies on an accurate determination of the boundary conditions, e.g., species concentrations, gas temperature and gas velocity from the bed into the computational domain. Most CFD models of grate-fired waste-to-energy (W-t-E) plants use a stand-alone model of the bed, describing the waste devolatilisation and the partial oxidation of volatiles. The volatile oxidation is strongly coupled to the combustion of gaseous species in the free-board due to the radiation onto the bed as indicated in figure A.1.

Figure A.1: Schematic overview of the procedure for CFD modeling of solid fuel combustion in grate-firing units

Coupling the devolatilisation of the fuel and partial oxidation of the volatiles in the bed with the combustion of gaseous species in the free-board has been applied with success in previous studies [5][109]. Recently the NO precursor concentrations were measured at a full-scale waste-to-energy plant [120]. However, the measurements were limited to two fixed positions above the grate. The objective of this study is to measure the gas temperature and species concentrations just above the fuel bed in a full-scale W-t-E plant. The gas species concentrations are measured by gas extraction and use of FTIR spectroscopy in four fixed positions above the bed. By suction pyrometer the gas temperatures were measured concurrently to the species concentrations. The results are useful for evaluation of bed models and will provide a more accurate description of the temperature field in the free-board. The species measurements include the NO_x precursors released from the bed. Based on the results, the importance of the partitioning of NO_x precursors on the formation of fuel NO_x in grate-fired W-t-E plants is discussed.

A.1.2 Plant and grate characteristics

Over a span of three days the gas composition and temperatures above the bed from combustion of municipal solid waste (MSW) were measured. All measurements were performed at Affald+, a W-t-E plant located in Næstved, Denmark. The W-t-E plant has a nominal waste capacity of 8.2t/h. During the days of measurements the plant was operated slightly below nominal capacity as seen in table 1. The plant uses the Dynagrate® grate technology. The grate is a single-lane grate, with dimensions 10.6x4m. The grate has been split into four zones with lengths of 2.8, 2.7, 2.7 and 1.8 meter, respectively. Predefined fractions of the primary air can be distributed to each zone.

Plant operation

During the three days of measurements, the waste-to-energy plant was running stable without any malfunctions or shut-downs. The plant was operated with an oxygen set point of 6 vol% (wet) and a steam production of 9.5 kg/s as shown in table 1. The steam pressure was kept at a constant value of 55.6±0.1bar with a steam production of

9.±0.1kg/s corresponding to full capacity. During the measurement campaign the plant was operated under two different settings, as seen in table A.1 and figure A.2, to evaluate the effect of primary air distribution on the concentration profile of combustibles, water, CO_2 and NO_x precursors. The tonnage was changed between the two plant settings to accommodate the changes in heating value of the fuel. The tonnage is lower that the yearly average of 9 ton/h [121] due to the high heating value of the waste, which in the period of measurements contained large quantities of dry waste wood.

Table 1. Specifications of Affald+ line 4 during the three days of measurements.

Table A.1: Specifications of Affald+ line 4 during the three days of measurements.

	Air dist. 1	Air dist. 2
Waste feed (tons/h)	7.2±1.6	7.3±0.9
Avg. heating value (MJ/kg)	13.5±1.2	13.8±0.5
Avg. primary air (Nm3/h)	17,454±1808	20,215±2017
Fraction on grate section 1	0.20	0.20
Fraction on grate section 2	0.35	0.27
Fraction on grate section 3	0.35	0.43
Fraction on grate section 4	0.10	0.10
Avg. secondary air (Nm3/h)	10,851±326	10,847±300
Temp. primary air (°C)	45.5±3.2	45.9±3.6
Temp. secondary air (°C)	41.9±0.6	40.6±0.6
Avg. O_2 (% wet)	6.3	6.2
Steam production (kg/s)	9.5	
Steam temperature (°C)	400	
Steam pressure (bar)	55.6	
Grate dimension	10m long, 6m wide	

The average waste feed and heating value of the fuel for the period of measurements provides data for an estimation of the waste composition. The waste composition was estimated based on correlations between waste feed and heating value established over a long period of time by B&W Vølund. In table A.2 the estimated waste composition has been shown.

Table A.2: Estimated waste composition based in the fuel input (tons/h) and the lower calorific value of the fuel (MJ/kg).

Component	wt %
C	0.311
H	0.044
O	0.184
N	0.011
S	0.002
Cl	0.007
Moisture	0.275
Ash	0.166

The primary and secondary air flows were obtained from the plant control system. The changes in primary air distribution involved only sections 2 and 3 on the grate. The

fractions of air on grate 1 and 4 were unchanged as grate 1 acts to dry the waste and grate 4 mainly serves as ash transport; full conversion of the waste has occurred on the previous 3 sections.

Figure A.2: The fraction of the total amount of primary air distributed under the grate for plant setting 1 and 2.

A.1.3   Gas phase composition and temperature measuring system

The flue gas composition was measured with a 6 meter water cooled probe. The temperature in the center of the probe and from end of the probe to the cooler was kept at 150°C to avoid water condensation. Prior to the O_2 analyzer the gas is cooled to 5°C to remove any water and aerosols. The system allows simultaneous IR, UV and O_2 measurements. Attached on the probe was a non-cooled suction pyrometer of equivalent length. This secured species concentration measurements and gas temperature measurements at equivalent locations at the same time. The concentrations of species CH_4, C_2H_2, C_2H_4, CO, CO_2, NH_3, HCN and H_2O were measured. The probe was inserted through an opening in the roof of the furnace in front of the fuel inlet. The probe was manually inserted into the furnace at a defined angle and distance. The species concentrations and gas temperature were measured at four predefined locations in the furnace close to the fuel bed. In figure A.3 the four points of measurement have been shown as circles. Furthermore the size of each grate-section and distance from the measuring point to the grate are indicated. Depending on the position on the grate the fuel bed can be as thick as 1m. The opening is shown in figure A.3 as a 45° cone in the front roof of the furnace. The insertion length and insertion angle of the water cooled probe is shown in table 2, corresponding to the measuring point shown in figure A.3. The point closest to the fuel inlet (left in figure A.3) is referred as measuring point 1, while the point closest to the ash pit (right in figure A.3) is referred to as measuring point 4.
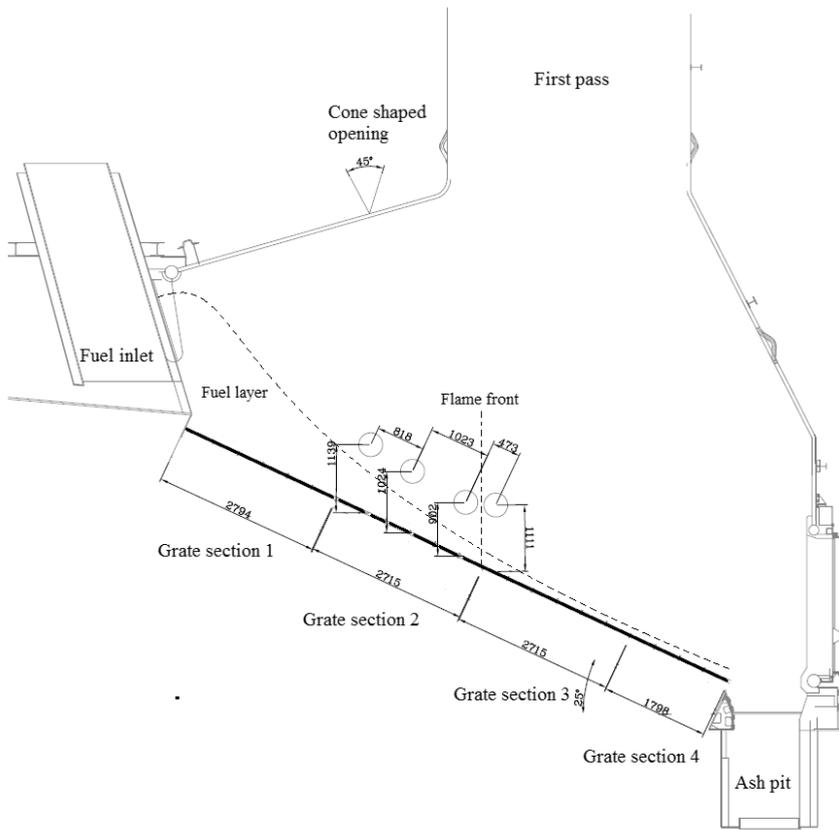
Figure A.3: Schematic drawing of the furnace. The measuring points are shown as circles. Measuring point 1 is closest to the fuel inlet, while measuring point 4 is closest to the ash pit. The dotted line shows the predicted height of the waste layer, the thick solid line shows the grate surface and the vertical dotted line shows the flame front during the experiments

Table A.3: The insertion length from the cone shape opening to the measuring point and insertion angle of the water cooled probe into the furnace. The points are shown in figure A.3 as well.

Measuring point	Distance (m)	Angle °
1	4.4	0
2	5.0	9
3	6.0	18
4	6.0	23

Concentrations of the above mentioned species have been determined from FTIR absorption measurements with use of Bomen MB100 FTIR spectrometer with built-in IR

light source and external DTGC detector. The gas sampling was performed at a constant
flow rate of 3 Nl/min controlled by an EL-Flow type Bronkhorst mass flow controller
with a response time from 0% to 98% signal level of the gas sampling system of about
50s. Concentrations of CO, CO_2, hydrocarbons, NH_3, HCN and water were determined
by FTIR measurements. The O_2 concentration was determined using a Siemens O_2
paramagnetic analyzer. The main sampling parameters were continuously logged by
an Agilent BenchLink Data Logger. The temperature of the gas in the sampling line
was kept constant at 150°C to avoid condensation of water and light tar products. To
avoid blockage of the system, two thimble filters were installed along the heated line to
remove particles, soot, heavy tars and aerosols. The system was leak tight and allowed
for operation between 1000mbar and 500mbar, limited by the lowest pressure of the
O_2 analyzer. After analysis of the flue gas by IR/UV absorption measurement the gas
was cooled for water removal for determination of the O_2 concentration. A schematic
overview of the measuring system is shown in figure A.4.

Figure A.4: Schematic overview of the gas phase composition and temperature measur-
ing system.

Analysis of the spectral data was performed with an in-house software at the Tech-
nical University of Denmark. The software uses the latest spectral databases HITRAN/HITEMP
for analysis of IR spectral data in the spectral range from 400 cm^{-1} to 6000cm^{-1}. The
pressure in the sampling system was determined and variations have been taken into
account in the data analysis. The uncertainties in the measurements are mainly defined
by the uncertainties in the spectral databases and by the S/N ratio in the measured
spectra. The uncertainties are shown in table 3.

A.1.4 Measurement results

The measurements are analyzed and discussed in this section. The gas temperature
profiles for both plant settings are shown in figure A.5. In figure 5 the profile of the
water vapor content in the flue gas for plant setting 2 is shown, while the species con-
centrations; CH_4, C_2H_2, C_2H_4, CO, CO_2, NH_3 and HCN are shown in figures A.8-A.10.
All measurements were performed at a distance approximately 50cm above the fuel bed
depending on bed thickness

Table A.4: The uncertainties in the extractive IR measurements. The uncertainty has been shown as relative %.

Species Relative uncertainty	
	Rel. %
H_2O	2
CO_2	3
CO	2
CH_4	3
C_2H_2	10
C_2H_4	7
HCN	8
NH3	5

Gas temperature profile

The gas temperature was measured continuously by a suction pyrometer attached on the side of the water cooled probe. The thermocouple was calibrated after the measurements at the thermometry facilities at DTU. The gas temperature profiles for both plant settings are seen in figure 5.5.
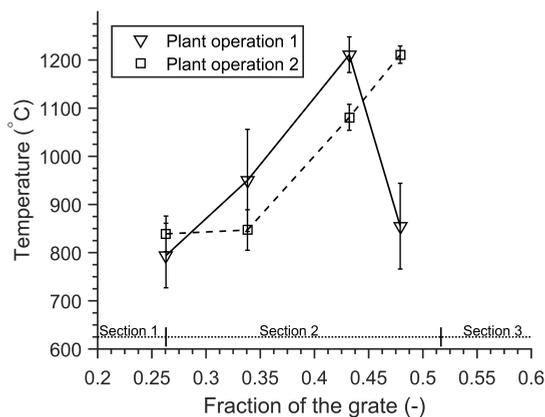
Figure A.5: The gas temperature profile for the two plant settings (shown in table 1) measured by suction pyrometer. The grate sections of the DynagrateÂ® have been shown in the figure 5.3 as well.

The temperature increases along the grate from measuring point 1 to 3. The low temperature at the initial part of the grate is a consequence of fuel drying, as seen from the large water content in the flue gas shown in figure A.7, and devolatilisation of the solid fuel. Lower gas temperatures are experienced in point 2 and 3 for the plant setting 2. This is attributed to a lower degree of oxidation in this region as a result of a lower fraction of the total primary air being provided on grate section 2 compared to that at plant setting 1, see figure 8 and 9. The maximum gas temperature for the two plant settings are in the same region; 1150-1250°C. The peak temperature is expected

to be a consequence of the char oxidation occurring in the region, this is supported by observations from the inspection window at the ash pit and figure A.6, showing the position of the probe at measuring point 4. The location of the tip of probe is outside of the flame region during plant setting 1. This indicates that devolatilisation has been completed and char oxidation is occurring. The tip of the probe was in the flame region during plant setting 2 indicating combustion of the volatiles; this is supported by the higher temperature at measuring point 4 during this plant setting.

Figure A.6: Picture of the combustion of waste on a grate at Affald+ during the measurements in this study. The probe is measuring in measuring point 4 during plant setting 2. The tip of the probe is outside of the flame region; the devolatilisation zone.

As a large fraction of the total primary air is provided under grate section 3 instead of grate section 2, during plant setting 2, the position of the peak gas temperature is moved towards the ash pit. The shift in gas temperature may cause a change in the release profile of species from the solid bed due to the dependency of temperature on the pyrolysis products formation [101][123] and on the position of the char oxidation on the grate.

Water concentration profile

Considerable water vapour concentrations in the flue gas will appear in regions where the fuel is dried. Drying of the fuel occurs initially in the combustion process for which reason the water content is expected to have a maximum above grate section 1.
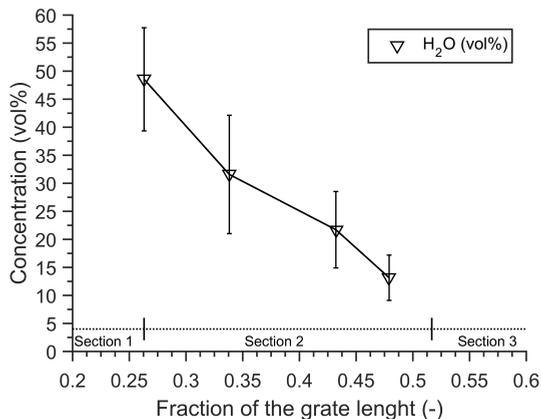
Figure A.7: The water concentration profile above the fuel bed.

The water concentration decreases linearly from the beginning of grate section 2 to the end of grate section 2. The level is highest at point 1 due to drying of the fuel. Downstream of section 1, water is mainly formed by oxidation of volatiles and the concentration approaches zero above the latter part of the grate where char oxidation has terminated.

Concentration profile of CO and CO_2 along the fuel bed

The most pronounced difference between the CO and CO_2 concentration profiles for the two plant settings are the shapes as seen in figure A.8. For plant setting 1 the concentration of CO gradually decreases, while the CO_2 concentration increases, from the initial part of grate section 2 to the latter part. For plant setting 2 the CO and CO_2 concentrations are somewhat constant along the grate section before the CO concentration drops to about 0% at measuring point 4; close to the intersection between grate section 2 and 3. Higher CO concentration at measuring point 3, the latter part of grate section 2, indicates a lower degree of oxidation due to the limited oxygen availability. This is a consequence of the lower amount of primary air supplied under grate section 2. The measurements indicate that the concentrations of CO and CO_2 at this point depend on the plant settings, i.e., the distribution of primary air on the second and third grate section.

(a) Plant operation 1 (b) Plant operation 2

Figure A.8: The concentration profiles of CO, CO_2 and O_2 along the grate during plant operation 1 and 2 (table 1).

The O_2 concentration is very low corresponding to a fuel rich zone at measuring point 1, 2 and 3 as a result of under-stoichiometric oxidation of the gas released from the bed. However, during plant setting 1 significant amounts of oxygen was measured at measuring point 1 and 2 along with larger amounts of CO and hydrocarbons. This may be a consequence of insufficient mixing of the combustible gasses and the oxidizer. This phenomenon is more pronounced during plant setting 1 where a larger fraction of the total combustion air was supplied in the region where measurements were done. From point 3 to point 4 a significant decrease in the CO concentration and an increase in the O_2 concentration were measured for both cases due to larger oxygen availability. It is expected that the devolatilisation process has been completed at this point. This is supported by hydrocarbon measurements, as discussed below.

From position 3 to 4 a more pronounced decrease in the CO concentration is experienced for plant setting 2 as the CO concentration is higher in the initial part of the grate due to limited oxygen availability caused by the primary air distribution. The results indicate that the release profile of gaseous products, CO, hydrocarbons and NO_x precursors, from the bed is unaltered as the primary air distribution changes; it is merely the degree of oxidation that changes.

Hydrocarbon concentration profile along the fuel bed

The major combustible released from the waste bed is CH_4. Also substantial amount of C_2H_4 is produced, along with small amounts of C_2H_2 as shown in figures A.9a and A.9b.

(a) Plant operation 1 (b) Plant operation 2
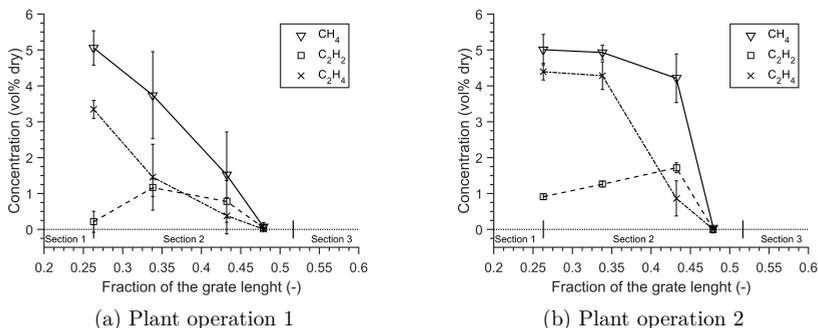
Figure A.9: The concentration profiles of the major hydrocarbon species during combustion of MSW along the grate during plant operation 1 and 2 (table 1).

It is evident that the concentrations of the major hydrocarbons are significantly lower at measuring point 2 and measuring point 3 under plant operation 1, presumably due to a larger supply of oxygen, promoting oxidation. The observations are supported by the CO and CO_2 measurements (figures A.8a and A.8b), which show a larger degree of oxidation for plant setting 1.

A roughly linearly decrease in the CH_4 and C_2H_4 concentrations from point 1 to point 4 was measured during plant setting 1, while the CH_4 concentration from point 1 to 3 was more or less constant during plant setting 2, presumably due to the lower oxygen availability. From point 3 to point 4, the CH_4, C_2H_4 and C_2H_2 concentrations decrease rapidly. At point 4 none of the major hydrocarbons were measured for any of the two plant settings, showing full oxidation of the combustible gasses from the bed. High CO_2 concentrations at this measuring point indicate that char oxidation is occurring. This is supported by figure A.6 where it is seen that the position of the probe tip is outside the flame region.

Smaller amounts of C_2H_2 were measured above the bed during both plant settings. Initially the concentration is negligible compared to the CH_4 and C_2H_4 concentration. However, at the end of grate section 2 (measuring point 3) the C_2H_2 concentration exceeds that of C_2H_4. The larger C_2H_2 concentration at the end of grate section 2 is expected since it is an intermediate product of oxidation of higher hydrocarbons.

The composition of the hydrocarbons measured in this study is in agreement with measurements reported in literature. The gas compositions from rapid pyrolysis of biomass in a drop-tube reactor [101][100] and of digested sewage sludge in a fluidized bed [106] show a similar partitioning of hydrocarbons.

Concentration profiles of HCN and NH3 pre-cursors from the solid fuel bed

Concentration profiles of NO_x precursors from the waste bed have, to the knowledge of the authors, not previously been reported in literature. From a NO_x modelling perspective the concentration profiles of these species are essential to effectively model the NO_x formation in CFD. Concurrent to the hydrocarbon, CO, CO_2 and H_2O concentrations, the NH_3 and HCN profiles were measured and are shown in A.10a and A.10a.

(a) Plant operation 1   (b) Plant operation 2
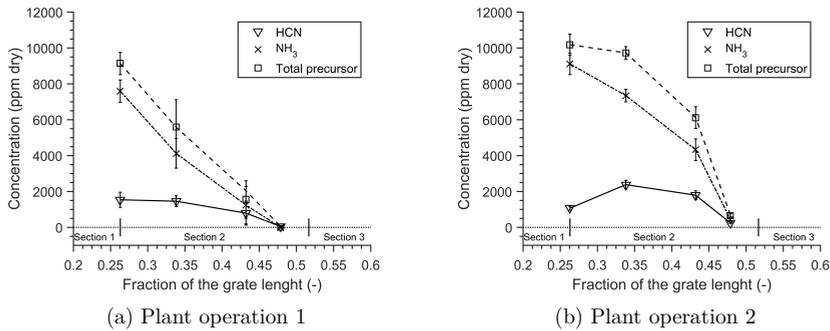
Figure A.10: The concentration profiles of the major NO_x precursors during combustion of MSW as a function of the grate length during plant operation 1 and 2 (table 1.

The profiles for NH_3 and HCN during plant setting 1 are similar to those of CH_4 and C_2H_4. The concentrations of NO precursors peak at a high level of approximately 10000ppm at point 1, after which they decrease to low levels at point 4, as seen in A.10a and A.10a

For plant setting 2 a constant total precursor concentration was measured from point 1 to point 2 after which the concentration drops to about 0 at point 4. The NH3 concentration drops linearly from point 1 to 3, whereas the HCN concentration initially increases from point 1 to 2. Again, the concentration profiles of the precursors during plant setting 2 follow a trend similar to CH_4.

According to literature the majority of the total NO_x precursors are released as NH3 during biomass and waste combustion [1]. The present measurements support this finding, as less than 1/5 of the total amount of precursor was identified as HCN. The error induced by modelling the fuel-NO_x formation using NH3 as the sole NO_x precursor is evaluated in section 5.

A.1.5 Comparison with previous measurements at W-t-E plants

The gas composition and gas temperature from drying, devolatilisation and char combustion of waste on a moving grate have previously been reported by Bøjer et al. [124] from Vestforbrændingen plant. These measurements were conducted at a waste-to-energy plant with a hydraulically forward-acting grate with a nominal waste capacity of 26t/h and a grate size of 13.1x9.75m. In the study the emphasis was put on measuring the release of alkali; besides alkali, only CO, CO_2 and NO concentrations were measured.
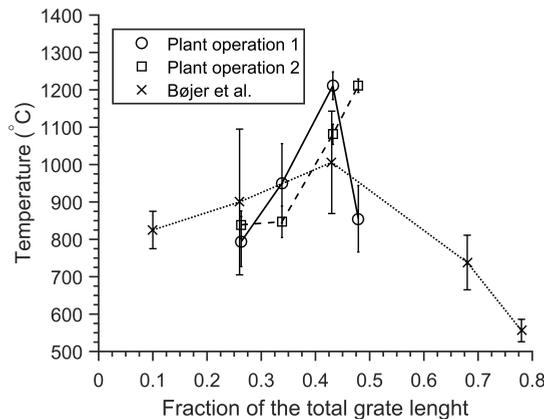
Figure A.11: The measured gas temperature at both plant operations compared with gas temperatures measured by Bøjer et al. at Vestforbrændingen [124].

Comparison between the gas temperatures measured in this study and measurements performed by Bœjer et al. is shown in figure A.11. Similar temperatures were found in both plants; Bøjer et al. measured the temperatures at a W-t-E plant with a different grate technology and a nominal capacity approximately 3 times larger than Affald+. At both plants the highest gas temperature was obtained at a location approximately 45% down the grate. However, the gas temperature is significantly higher in the present study. The higher gas temperature is suspected to be due to a number of differences between the two studies. The heating value of the fuel was higher by approximately 3MJ/kg in this study. During the measurements dry waste wood was mixed with the MSW increasing the homogeneity of the fuel, as a consequence lower fluctuations in the position of the flame front occurs. Bøjer at al. measured the gas temperatures close to the side walls; the cooling effect of walls may affect the gas temperature. Also differences in the primary air distribution might affect the gas temperatures. Lastly, in this study the reaction zone was very narrow, for this reason a sharp increase in the gas temperature is seen. This was supported by IR-camera inspections. A broad reaction zone was experienced by Bøjer et al. [124], corresponding to a flat gas temperature curve as seen in figure A.11. It is suspected that the homogeneity of the fuel and differences in the control strategy can explain the low fluctuation in the position of the flame front during measurements at Affald+.
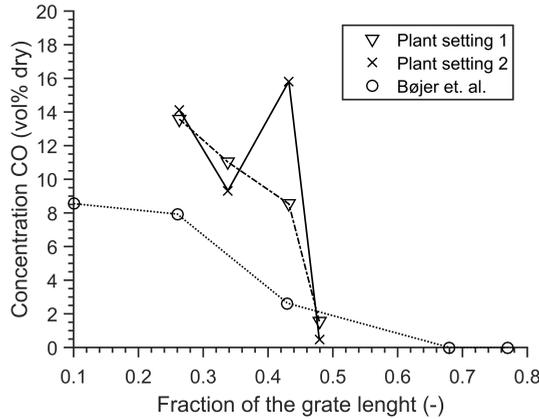
Figure A.12: The CO concentration for both plant settings obtained in this study. These have been compared with measurements obtained by Bøjer et al. at Vestforbrændingen [124].

In figure A.12 the CO concentration as a function of the grate length found in this study has been compared with results found by Bøjer et al. [124]. They reported peak CO and CO_2 concentrations of approximately 8 and 15 vol % dry, respectively. The results indicate that the release of volatiles and oxidation of these species occur over a larger part of the grate for the measurements during operation at Vestforbrændingen as CO was depleted after approximately 70% of the total grate length, while CO concentrations reach about 0% after approximately 50% of the grate length at Affald+. The differences might be due partly to differences in primary air distribution under the grate. Due to differences in the primary air distribution, heating value of the fuel, lower gas temperatures and large fluctuations in the position of the flame front, large standard deviations in the CO concentrations were experienced by Bøjer et al [124].
The total hydrocarbon peak concentration was estimated by Bøjer et al. on the basis of measurements of the CO and CO_2 concentration profiles to be approximately 10 vol% dry [124]; this is similar to the measured levels in this study. In both studies the hydrocarbons are depleted after the initial half of the grate.

Despite the differences (size, grate technology) between the W-t-E plants, the measured species concentrations in the two test campaigns show significant similarities. Devolatilisation of the fuel occurs on the first half of the grate and gas temperatures peak after approximately half of the total grate length. These similarities indicate robustness in gas temperatures as well as composition and concentrations of gasses released from the waste bed in grate fired W-t-E plants.

A.1.6 The influence of precursor speciation on the NO_x formation

A robust bed model is essential for a correct prediction of the NO_x formation in CFD. In particular the composition of gasses released from the fuel bed is an input parameter to a CFD model. In this section the influence of the choice of precursor on the NO_x formation is evaluated. The evaluation is done through Perfectly Stirred Reactor (PSR)

simulations in CHEMKIN 10131, using reactor conditions as shown in table 5.5. The combustion is simulated using the detailed chemical kinetic model (DCKM) developed by Mendiara and Glarborg [36]. Included in this mechanism is high temperature NH_3 and HCN oxidation.

Table A.5: The inlet gas composition used in PSR simulations in CHEMKIN 10131. The gas composition was determined based on the extractive IR measurements.

Species Vol	Concentration %
CO	13.6
CO_2	11.6
CH_4	5.1
C_2H_4	3.3
NH_3	0.8
HCN	0.2
N_2	65.4

The composition of the inlet gas for the PSR simulations, shown in table 4, was determined based on the extractive IR measurements conducted on Affald+; these are shown in figure A.8 to figure A.10. The composition was found at normal primary air configuration (plant setting 1) at measuring point 1. Even though it has been shown in previous measurements that the gas above the bed contains a significant amount of H_2 [105], this species could not be quantified in the present work and was neglected in the simulations. N_2 account for the majority of the devolatilisation gas due to supply of atmospheric air under the grate; NO formed in the bed is not included in the inlet gas. These assumptions might alter the NO_x concentration after oxidation in the PSR reactor slightly but is not expected to influence the analysis of the precursor influence.

Figure A.13:   The influence of the precursor on the NO_x formation at T=800, 1000 and 1200°C for increasing λ.   The pressure is 1 atm and the nominal residence time is 1s.   The total precursor concentration was 10000ppm for all simulations. - NH3=9000ppm and HCN=1000ppm, — NH3=10000ppm and HCN=0ppm, — NH3=0ppm and HCN=10000ppm.

The calculations were performed at 800, 1000 and 1200°C, covering the expected range above the grate (figure A.5). The simulations were done using three different inlet gas compositions; the composition shown in table 4, i.e., 80% NH_3 and 20% HCN, and compositions where all reactive N was NH_3 and HCN, respectively. The predicted formation of NO_x is shown in figure A.13. As expected the NO concentration increases with increasing excess air ratio (λ) until a certain point where no more NO is generated and the gas is merely diluted by additional air. At values of λ below 1.1, the choice of precursor does not influence the final NO concentration in the temperature interval investigated. At high excess air ratios, the choice of precursor has a large impact on the predicted NO formation, with HCN oxidation yielding significantly higher levels of NO. At λ=1.5 the NO_x concentrations found from the PSR simulation are 128, 71 and 54% higher when HCN is used as precursor, compare to NH_3, for temperatures of 800, 1000 and 1200°C, respectively. Ammonia consumption yields NH_2 radicals, which can subsequently react with NO to form atmospheric nitrogen and water through reaction:

$$NH_3 + OH \leftrightarrow NH_2 + H_2O \tag{A.1}$$

$$NH_3 + O \leftrightarrow NH_2 + OH \tag{A.2}$$

$$NO + NH_2 \leftrightarrow N_2 + H_2O \tag{A.3}$$

Hydrogen cyanide is oxidized through a different sequence of reactions which has a higher selectivity for forming NO [1]. For modelling reliably the NO formation at high

excess air ratios it is thus important to determine the correct ratio between NH_3 and HCN. With decreasing temperatures the importance of an accurate precursor determination increases considerably.

A.1.7 Summary

The gas temperatures and concentration profiles of the major species above the fuel bed in combustion of waste at a grate-fired W-t-E plant were measured for two different plant operations. The gas temperature increased from 800°C at the initial part of the grate to a maximum value of 1200°C about halfway down the grate, with the position depending slightly on the primary air distribution. The gas released from the fuel bed consisted primarily of water, CO, CO_2, CH_4 and C_2H_4, with significant amounts of C_2H_2 detected downstream. The concentration profiles depended on the distribution of the primary air under the grate. A larger supply of combustion air in the early grate sections (section 2) enhanced oxidation, leading to lower levels of combustible gasses.

The measurements show that volatile nitrogen from the bed is mostly released as NH_3, with minor amounts of HCN. The concentration of the precursors was measured to about 1%vol above the initial part of the grate (section 2). Chemical kinetic modelling of NO formation at representative temperatures shows that at excess air ratios below 1.1 the NO yield is roughly independent of the choice of precursor. However, at higher values of λ the N-speciation influences the formation of NO significantly because HCN has a higher selectivity for forming NO. For this reason reliable determination of the partitioning of NO-precursors is important for predicting NO in grate-fired systems.

A.1.8 Acknowledgement

Appendix B

Comments from reviewer and editor

Reviewer/Editor comments:

Reviewer #1: The manuscript reports on in-furnace measurements taken in a municipal waste incinerator; temperature and concentration of the main combustion species as well as NO_x precursors have been measured along four traverses.
There exists a proliferation of mathematical models for performance predictions of grate furnaces while in-furnace data is scarce. The manuscript provides very important information for both the development and validation of such models. The manuscript also contains some predictions of the NOx emissions, however this is not the key part. I strongly recommend publication. In my opinion the manuscript is simple and informative.

Perhaps the authors could include an extra paragraph on the waste burned (chemical analysis, type, description of different fractions and so on)?

Fuel Ref: JFUE-D-17-01213R1 Title: Measurements of the NOx Precursors and Major Species Concentrations above the Grate at a Waste-to-Energy plant

Dear Mr. Morten Søe Jepsen,

A final disposition of "Accept" has been registered for the above-mentioned manuscript.

Kind regards,

John William Patrick, B,Sc., Ph.D, Principal Editor

Appendix C

Predictions from the bed model

C.1   Inlet gas composition and temperature from the bed for determination of NO$_x$ formation using CFD

General Comments on Calculations:

——————————————————-

Setup:

Amount of waste 2.028 [kg/s]
7300.000 [kg/h]

Waste composition:

Carbon 0.305254 [kg/kg]
Hydrogen 0.0410491 [kg/kg]
Oxygen 0.176452 [kg/kg]
Nitrogen 0.0131346 [kg/kg]
Water 0.290479 [kg/kg]
Ash 0.173632 [kg/kg]
LCV 13500 [kJ/kg]
Combustion Air 12.3 [kg/s]

Gasification Rate 0.3500 [-]

——————————————————-

Grate 1 = grate 1 1

Ratio of primary air 5.000000e-002
Ratio of heat release 1.280469e-002
Ratio of heat release as pyrolysis gas 1.055578e-003
Ratio of waste water evaporation 1.778647e-001
Ratio of total particle release 1.280469e-002
CO/CH4 ratio 5.000000e-002
Qpyro 3.041509e+001
Mass fraction flue gas
ch4 1.088994e-003
o2 1.412112e-001
co2 4.625387e-002
co 9.690367e-005
h2o 2.152795e-001
n2 5.960695e-001
sum species 1.000000e+000
Error mass balance 0.000000e+000
Total mass flow of gas 5.486156e-001 [kg/s]
Mass flow of C particles 7.071567e-004 [kg/s]
Number of particles 2.701815e+006 at diameter 1.000000e-004 [m]
Temperature of gas 3.393126e+002 [K]
Temperature of solid 3.393126e+002 [K]
Mass flow of solid of grate 1.908955e+000 [kg/s]

Grate 2 = grate 1 2
Ratio of primary air 5.000000e-002
Ratio of heat release 3.829673e-002
Ratio of heat release as pyrolysis gas 8.032712e-003
Ratio of waste water evaporation 2.005284e-001
Ratio of total particle release 3.829673e-002
CO/CH4 ratio 1.500000e-001
Qpyro 2.314521e+002
Mass fraction flue gas
ch4 7.469349e-003
o2 7.962824e-002
co2 1.141492e-001
co 1.952094e-003
h2o 2.400133e-001
n2 5.567878e-001
sum species 1.000000e+000
Error mass balance 0.000000e+000
Total mass flow of gas 5.885402e-001 [kg/s]
Mass flow of C particles 2.114990e-003 [kg/s]
Number of particles 8.080688e+006 at diameter 1.000000e-004 [m]
Temperature of gas 5.572269e+002 [K]
Temperature of solid 5.572269e+002 [K]
Mass flow of solid of grate 1.748800e+000 [kg/s]

Grate 3 = grate 1 3
Ratio of primary air 5.000000e-002
Ratio of heat release 5.745909e-002
Ratio of heat release as pyrolysis gas 1.888912e-002
Ratio of waste water evaporation 1.659910e-001
Ratio of total particle release 5.745909e-002
CO/CH4 ratio 2.500000e-001
Qpyro 5.442653e+002
Mass fraction flue gas
ch4 1.700442e-002
o2 6.153669e-002
co2 1.484348e-001
co 7.419163e-003
h2o 2.076019e-001
n2 5.580029e-001
sum species 1.000000e+000
Error mass balance 0.000000e+000
Total mass flow of gas 5.881732e-001 [kg/s]
Mass flow of C particles 3.173258e-003 [kg/s]
Number of particles 1.212398e+007 at diameter 1.000000e-004 [m]
Temperature of gas 8.398676e+002 [K]
Temperature of solid 8.398676e+002 [K]
Mass flow of solid of grate 1.587953e+000 [kg/s]

Grate 4 = grate 1 4
Ratio of primary air 5.000000e-002
Ratio of heat release 6.985743e-002
Ratio of heat release as pyrolysis gas 2.881563e-002
Ratio of waste water evaporation 1.275958e-001
Ratio of total particle release 6.985743e-002
CO/CH4 ratio 3.500000e-001
Qpyro 8.302848e+002
Mass fraction flue gas
ch4 2.554669e-002
o2 6.111540e-002
co2 1.609551e-001
co 1.560800e-002
h2o 1.688534e-001
n2 5.679214e-001
sum species 1.000000e+000
Error mass balance 0.000000e+000
Total mass flow of gas 5.784825e-001 [kg/s]
Mass flow of C particles 3.857973e-003 [kg/s]
Number of particles 1.474006e+007 at diameter 1.000000e-004 [m]
Temperature of gas 1.106078e+003 [K]
Temperature of solid 1.106078e+003 [K]
Mass flow of solid of grate 1.436113e+000 [kg/s]

Grate 5 = grate 2 1
Ratio of primary air 8.750000e-002
Ratio of heat release 1.359101e-001
Ratio of heat release as pyrolysis gas 6.378326e-002
Ratio of waste water evaporation 1.483607e-001
Ratio of total particle release 1.359101e-001
CO/CH4 ratio 4.875000e-001
Qpyro 1.837831e+003
Mass fraction flue gas
ch4 3.191838e-002
o2 6.632117e-002
co2 1.625221e-001
co 2.716264e-002
h2o 1.265014e-001
n2 5.855743e-001
sum species 1.000000e+000
Error mass balance 2.220446e-016
Total mass flow of gas 9.824473e-001 [kg/s]
Mass flow of C particles 7.505822e-003 [kg/s]
Number of particles 2.867730e+007 at diameter 1.000000e-004 [m]
Temperature of gas 1.426360e+003 [K]
Temperature of solid 1.426360e+003 [K]
Mass flow of solid of grate 1.199535e+000 [kg/s]

Grate 6 = grate 2 2
Ratio of primary air 8.750000e-002
Ratio of heat release 1.363845e-001
Ratio of heat release as pyrolysis gas 6.480492e-002
Ratio of waste water evaporation 8.352779e-002
Ratio of total particle release 1.363845e-001
CO/CH4 ratio 6.625000e-001
Qpyro 1.867269e+003
Mass fraction flue gas
ch4 3.203557e-002
o2 6.847191e-002
co2 1.594024e-001
co 3.705413e-002
h2o 9.408518e-002
n2 6.089509e-001
sum species 1.000000e+000
Error mass balance 0.000000e+000
Total mass flow of gas 9.447536e-001 [kg/s]
Mass flow of C particles 7.532021e-003 [kg/s]
Number of particles 2.877739e+007 at diameter 1.000000e-004 [m]
Temperature of gas 1.666601e+003 [K]
Temperature of solid 1.666601e+003 [K]
Mass flow of solid of grate 1.000624e+000 [kg/s]

Grate 7 = grate 2 3
Ratio of primary air 8.750000e-002
Ratio of heat release 1.253404e-001
Ratio of heat release as pyrolysis gas 5.450070e-002
Ratio of waste water evaporation 4.562698e-002
Ratio of total particle release 1.253404e-001
CO/CH4 ratio 8.375000e-001
Qpyro 1.570367e+003
Mass fraction flue gas
ch4 2.661176e-002
o2 6.696554e-002
co2 1.570596e-001
co 3.890767e-002
h2o 7.920675e-002
n2 6.312487e-001
sum species 1.000000e+000
Error mass balance 2.220446e-016
Total mass flow of gas 9.109157e-001 [kg/s]
Mass flow of C particles 6.922096e-003 [kg/s]
Number of particles 2.644707e+007 at diameter 1.000000e-004 [m]
Temperature of gas 1.846235e+003 [K]
Temperature of solid 1.846235e+003 [K]
Mass flow of solid of grate 8.361614e-001 [kg/s]

Grate 8 = grate 2 4
Ratio of primary air 8.750000e-002
Ratio of heat release 1.091184e-001
Ratio of heat release as pyrolysis gas 4.076631e-002
Ratio of waste water evaporation 2.446847e-002
Ratio of total particle release 1.091184e-001
CO/CH4 ratio 1.012500e+000
Qpyro 1.174628e+003
Mass fraction flue gas
ch4 1.963328e-002
o2 6.816318e-002
co2 1.535694e-001
co 3.470316e-002
h2o 7.213851e-002
n2 6.517925e-001
sum species 1.000000e+000
Error mass balance 2.220446e-016
Total mass flow of gas 8.815417e-001 [kg/s]
Mass flow of C particles 6.026218e-003 [kg/s]
Number of particles 2.302421e+007 at diameter 1.000000e-004 [m]
Temperature of gas 1.957746e+003 [K]
Temperature of solid 1.957746e+003 [K]

Mass flow of solid of grate 7.019684e-001 [kg/s]

Grate 9 = grate 3 1
Ratio of primary air 8.750000e-002
Ratio of heat release 9.157002e-002
Ratio of heat release as pyrolysis gas 2.815717e-002
Ratio of waste water evaporation 1.295955e-002
Ratio of total particle release 9.157002e-002
CO/CH4 ratio 1.187500e+000
Qpyro 8.113122e+002
Mass fraction flue gas
ch4 1.335013e-002
o2 7.549083e-002
co2 1.461511e-001
co 2.767821e-002
h2o 6.700178e-002
n2 6.703279e-001
sum species 1.000000e+000
Error mass balance 0.000000e+000
Total mass flow of gas 8.564687e-001 [kg/s]
Mass flow of C particles 5.057081e-003 [kg/s]
Number of particles 1.932146e+007 at diameter 1.000000e-004 [m]
Temperature of gas 1.985521e+003 [K]
Temperature of solid 1.985521e+003 [K]
Mass flow of solid of grate 5.938176e-001 [kg/s]

Grate 10 = grate 3 2
Ratio of primary air 8.750000e-002
Ratio of heat release 7.482962e-002
Ratio of heat release as pyrolysis gas 1.835774e-002
Ratio of waste water evaporation 6.802670e-003
Ratio of total particle release 7.482962e-002
CO/CH4 ratio 1.362500e+000
Qpyro 5.289544e+002
Mass fraction flue gas
ch4 8.551752e-003
o2 8.878360e-002
co2 1.341433e-001
co 2.034117e-002
h2o 6.147260e-002
n2 6.867076e-001
sum species 1.000000e+000
Error mass balance 2.220446e-016
Total mass flow of gas 8.353906e-001 [kg/s]
Mass flow of C particles 4.132570e-003 [kg/s]
Number of particles 1.578920e+007 at diameter 1.000000e-004 [m]
Temperature of gas 1.927844e+003 [K]

Temperature of solid 1.927844e+003 [K]
Mass flow of solid of grate 5.076695e-001 [kg/s]

   Grate 11 = grate 3 3
Ratio of primary air 8.750000e-002
Ratio of heat release 5.993257e-002
Ratio of heat release as pyrolysis gas 1.145705e-002
Ratio of waste water evaporation 3.546729e-003
Ratio of total particle release 5.993257e-002
CO/CH4 ratio 1.537500e+000
Qpyro 3.301200e+002
Mass fraction flue gas
ch4 5.232703e-003
o2 1.060061e-001
co2 1.186394e-001
co 1.404622e-002
h2o 5.520476e-002
n2 7.008708e-001
sum species 1.000000e+000
Error mass balance 0.000000e+000
Total mass flow of gas 8.179428e-001 [kg/s]
Mass flow of C particles 3.309860e-003 [kg/s]
Number of particles 1.264589e+007 at diameter 1.000000e-004 [m]
Temperature of gas 1.801079e+003 [K]
Temperature of solid 1.801079e+003 [K]
Mass flow of solid of grate 4.397918e-001 [kg/s]

   Grate 12 = grate 3 4
Ratio of primary air 8.750000e-002
Ratio of heat release 4.725124e-002
Ratio of heat release as pyrolysis gas 6.909681e-003
Ratio of waste water evaporation 1.839401e-003
Ratio of total particle release 4.725124e-002
CO/CH4 ratio 1.712500e+000
Qpyro 1.990935e+002
Mass fraction flue gas
ch4 3.087111e-003
o2 1.247754e-001
co2 1.014339e-001
co 9.237699e-003
h2o 4.860989e-002
n2 7.128560e-001
sum species 1.000000e+000
Error mass balance 2.220446e-016
Total mass flow of gas 8.037171e-001 [kg/s]
Mass flow of C particles 2.609515e-003 [kg/s]
Number of particles 9.970107e+006 at diameter 1.000000e-004 [m]

Temperature of gas 1.631505e+003 [K]
Temperature of solid 1.631505e+003 [K]
Mass flow of solid of grate 3.868402e-001 [kg/s]

Grate 13 = grate 4 1
Ratio of primary air 2.500000e-002
Ratio of heat release 1.148479e-002
Ratio of heat release as pyrolysis gas 1.391062e-003
Ratio of waste water evaporation 3.381524e-004
Ratio of total particle release 1.148479e-002
CO/CH4 ratio 1.825000e+000
Qpyro 4.008164e+001
Mass fraction flue gas
ch4 2.143755e-003
o2 1.368075e-001
co2 9.025417e-002
co 6.832989e-003
h2o 4.440947e-002
n2 7.195521e-001
sum species 1.000000e+000
Error mass balance 0.000000e+000
Total mass flow of gas 2.274219e-001 [kg/s]
Mass flow of C particles 6.342632e-004 [kg/s]
Number of particles 2.423313e+006 at diameter 1.000000e-004 [m]
Temperature of gas 1.549139e+003 [K]
Temperature of solid 1.549139e+003 [K]
Mass flow of solid of grate 3.740341e-001 [kg/s]

Grate 14 = grate 4 2
Ratio of primary air 2.500000e-002
Ratio of heat release 1.068098e-002
Ratio of heat release as pyrolysis gas 1.191688e-003
Ratio of waste water evaporation 2.798667e-004
Ratio of total particle release 1.068098e-002
CO/CH4 ratio 1.875000e+000
Qpyro 3.433694e+001
Mass fraction flue gas
ch4 1.824626e-003
o2 1.419763e-001
co2 8.538853e-002
co 5.969971e-003
h2o 4.261252e-002
n2 7.222281e-001
sum species 1.000000e+000
Error mass balance 0.000000e+000
Total mass flow of gas 2.265496e-001 [kg/s]
Mass flow of C particles 5.898721e-004 [kg/s]

Number of particles 2.253709e+006 at diameter 1.000000e-004 [m]
Temperature of gas 1.478341e+003 [K]
Temperature of solid 1.478341e+003 [K]
Mass flow of solid of grate 3.621446e-001 [kg/s]

    Grate 15 = grate 4 3
Ratio of primary air 2.500000e-002
Ratio of heat release 9.924957e-003
Ratio of heat release as pyrolysis gas 1.019002e-003
Ratio of waste water evaporation 2.315614e-004
Ratio of total particle release 9.924957e-003
CO/CH4 ratio 1.925000e+000
Qpyro 2.936120e+001
Mass fraction flue gas
ch4 1.548192e-003
o2 1.470090e-001
co2 8.061278e-002
co 5.210819e-003
h2o 4.086761e-002
n2 7.247516e-001
sum species 1.000000e+000
Error mass balance 0.000000e+000
Total mass flow of gas 2.257330e-001 [kg/s]
Mass flow of C particles 5.481196e-004 [kg/s]
Number of particles 2.094186e+006 at diameter 1.000000e-004 [m]
Temperature of gas 1.414796e+003 [K]
Temperature of solid 1.414796e+003 [K]
Mass flow of solid of grate 3.511135e-001 [kg/s]

    Grate 16 = grate 4 4
Ratio of primary air 2.500000e-002
Ratio of heat release 9.214976e-003
Ratio of heat release as pyrolysis gas 8.698103e-004
Ratio of waste water evaporation 1.915420e-004
Ratio of total particle release 9.214976e-003
CO/CH4 ratio 1.975000e+000
Qpyro 2.506245e+001
Mass fraction flue gas
ch4 1.312621e-003
o2 1.518904e-001
co2 7.596701e-002
co 4.529274e-003
h2o 3.917277e-002
n2 7.271279e-001
sum species 1.000000e+000
Error mass balance 2.220446e-016
Total mass flow of gas 2.249693e-001 [kg/s]

Mass flow of C particles 5.089099e-004 [kg/s]
Number of particles 1.944379e+006 at diameter 1.000000e-004 [m]
Temperature of gas 1.356018e+003 [K]
Temperature of solid 1.356018e+003 [K]
Mass flow of solid of grate 3.408853e-001 [kg/s]

C.2 Inlet gas composition and temperature from the bed for determination of NO$_x$ reduction using CFD

General Comments on Calculations:

—————————————————-

Setup:

Amount of waste 2.194 [kg/s]
7900.000 [kg/h]

Waste composition:

Carbon 0.305254 [kg/kg]
Hydrogen 0.0410491 [kg/kg]
Oxygen 0.176452 [kg/kg]
Nitrogen 0.0131346 [kg/kg]
Water 0.290479 [kg/kg]
Ash 0.173632 [kg/kg]
LCV 13300 [kJ/kg]
Combustion Air 12.3 [kg/s]

Gasification Rate 0.3500 [-]

—————————————————-

Grate 1 = grate 1 1
Ratio of primary air 5.000000e-002
Ratio of heat release 1.280469e-002
Ratio of heat release as pyrolysis gas 1.055578e-003
Ratio of waste water evaporation 1.778647e-001
Ratio of total particle release 1.280469e-002
CO/CH4 ratio 5.000000e-002

Qpyro 3.245168e+001
Mass fraction flue gas
ch4 1.141217e-003
o2 1.353543e-001
co2 4.951213e-002
co 1.035539e-004
h2o 2.281823e-001
n2 5.857065e-001
sum species 1.000000e+000
Error mass balance 2.220446e-016
Total mass flow of gas 5.583703e-001 [kg/s]
Mass flow of C particles 7.071567e-004 [kg/s]
Number of particles 2.701815e+006 at diameter 1.000000e-004 [m]
Temperature of gas 3.246361e+002 [K]
Temperature of solid 3.246361e+002 [K]
Mass flow of solid of grate 2.065867e+000 [kg/s]

   Grate 2 = grate 1 2
Ratio of primary air 5.000000e-002
Ratio of heat release 3.829673e-002
Ratio of heat release as pyrolysis gas 8.032712e-003
Ratio of waste water evaporation 2.005284e-001
Ratio of total particle release 3.829673e-002
CO/CH4 ratio 1.500000e-001
Qpyro 2.469501e+002
Mass fraction flue gas
ch4 7.794100e-003
o2 6.970236e-002
co2 1.219732e-001
co 2.044769e-003
h2o 2.537077e-001
n2 5.447778e-001
sum species 1.000000e+000
Error mass balance -2.220446e-016
Total mass flow of gas 6.016689e-001 [kg/s]
Mass flow of C particles 2.114990e-003 [kg/s]
Number of particles 8.080688e+006 at diameter 1.000000e-004 [m]
Temperature of gas 5.321408e+002 [K]
Temperature of solid 5.321408e+002 [K]
Mass flow of solid of grate 1.892583e+000 [kg/s]

   Grate 3 = grate 1 3
Ratio of primary air 5.000000e-002
Ratio of heat release 5.745909e-002
Ratio of heat release as pyrolysis gas 1.888912e-002
Ratio of waste water evaporation 1.659910e-001
Ratio of total particle release 5.745909e-002

CO/CH4 ratio 2.500000e-001
Qpyro 5.807092e+002
Mass fraction flue gas
ch4 1.774494e-002
o2 4.957943e-002
co2 1.591739e-001
co 7.746558e-003
h2o 2.197621e-001
n2 5.459930e-001
sum species 1.000000e+000
Error mass balance 0.000000e+000
Total mass flow of gas 6.013413e-001 [kg/s]
Mass flow of C particles 3.173258e-003 [kg/s]
Number of particles 1.212398e+007 at diameter 1.000000e-004 [m]
Temperature of gas 8.110346e+002 [K]
Temperature of solid 8.110346e+002 [K]
Mass flow of solid of grate 1.718569e+000 [kg/s]

Grate 4 = grate 1 4
Ratio of primary air 5.000000e-002
Ratio of heat release 6.985743e-002
Ratio of heat release as pyrolysis gas 2.881563e-002
Ratio of waste water evaporation 1.275958e-001
Ratio of total particle release 6.985743e-002
CO/CH4 ratio 3.500000e-001
Qpyro 8.858805e+002
Mass fraction flue gas
ch4 2.668387e-002
o2 4.812928e-002
co2 1.734062e-001
co 1.630648e-002
h2o 1.792277e-001
n2 5.562464e-001
sum species 1.000000e+000
Error mass balance 0.000000e+000
Total mass flow of gas 5.908991e-001 [kg/s]
Mass flow of C particles 3.857973e-003 [kg/s]
Number of particles 1.474006e+007 at diameter 1.000000e-004 [m]
Temperature of gas 1.079559e+003 [K]
Temperature of solid 1.079559e+003 [K]
Mass flow of solid of grate 1.554312e+000 [kg/s]

Grate 5 = grate 2 1
Ratio of primary air 8.750000e-002
Ratio of heat release 1.359101e-001
Ratio of heat release as pyrolysis gas 6.378326e-002
Ratio of waste water evaporation 1.483607e-001

Ratio of total particle release 1.359101e-001
CO/CH4 ratio 4.875000e-001
Qpyro 1.960892e+003
Mass fraction flue gas
ch4 3.339883e-002
o2 5.265718e-002
co2 1.761259e-001
co 2.842230e-002
h2o 1.348187e-001
n2 5.745771e-001
sum species 1.000000e+000
Error mass balance 0.000000e+000
Total mass flow of gas 1.001769e+000 [kg/s]
Mass flow of C particles 7.505822e-003 [kg/s]
Number of particles 2.867730e+007 at diameter 1.000000e-004 [m]
Temperature of gas 1.411525e+003 [K]
Temperature of solid 1.411525e+003 [K]
Mass flow of solid of grate 1.298412e+000 [kg/s]

    Grate 6 = grate 2 2
Ratio of primary air 8.750000e-002
Ratio of heat release 1.363845e-001
Ratio of heat release as pyrolysis gas 6.480492e-002
Ratio of waste water evaporation 8.352779e-002
Ratio of total particle release 1.363845e-001
CO/CH4 ratio 6.625000e-001
Qpyro 1.992301e+003
Mass fraction flue gas
ch4 3.360261e-002
o2 5.435252e-002
co2 1.735448e-001
co 3.887246e-002
h2o 1.006475e-001
n2 5.989801e-001
sum species 1.000000e+000
Error mass balance 0.000000e+000
Total mass flow of gas 9.609786e-001 [kg/s]
Mass flow of C particles 7.532021e-003 [kg/s]
Number of particles 2.877739e+007 at diameter 1.000000e-004 [m]
Temperature of gas 1.665831e+003 [K]
Temperature of solid 1.665831e+003 [K]
Mass flow of solid of grate 1.083276e+000 [kg/s]

    Grate 7 = grate 2 3
Ratio of primary air 8.750000e-002
Ratio of heat release 1.253404e-001
Ratio of heat release as pyrolysis gas 5.450070e-002

Ratio of waste water evaporation 4.562698e-002
Ratio of total particle release 1.253404e-001
CO/CH4 ratio 8.375000e-001
Qpyro 1.675518e+003
Mass fraction flue gas
ch4 2.798122e-002
o2 5.271111e-002
co2 1.712053e-001
co 4.091448e-002
h2o 8.479625e-002
n2 6.223917e-001
sum species 1.000000e+000
Error mass balance 2.220446e-016
Total mass flow of gas 9.243194e-001 [kg/s]
Mass flow of C particles 6.922096e-003 [kg/s]
Number of particles 2.644707e+007 at diameter 1.000000e-004 [m]
Temperature of gas 1.858758e+003 [K]
Temperature of solid 1.858758e+003 [K]
Mass flow of solid of grate 9.054099e-001 [kg/s]

Grate 8 = grate 2 4
Ratio of primary air 8.750000e-002
Ratio of heat release 1.091184e-001
Ratio of heat release as pyrolysis gas 4.076631e-002
Ratio of waste water evaporation 2.446847e-002
Ratio of total particle release 1.091184e-001
CO/CH4 ratio 1.012500e+000
Qpyro 1.253281e+003
Mass fraction flue gas
ch4 2.069106e-002
o2 5.420450e-002
co2 1.673104e-001
co 3.657489e-002
h2o 7.714181e-002
n2 6.440774e-001
sum species 1.000000e+000
Error mass balance 2.220446e-016
Total mass flow of gas 8.924722e-001 [kg/s]
Mass flow of C particles 6.026218e-003 [kg/s]
Number of particles 2.302421e+007 at diameter 1.000000e-004 [m]
Temperature of gas 1.981033e+003 [K]
Temperature of solid 1.981033e+003 [K]
Mass flow of solid of grate 7.602865e-001 [kg/s]

Grate 9 = grate 3 1
Ratio of primary air 8.750000e-002
Ratio of heat release 9.157002e-002

Ratio of heat release as pyrolysis gas 2.815717e-002
Ratio of waste water evaporation 1.295955e-002
Ratio of total particle release 9.157002e-002
CO/CH4 ratio 1.187500e+000
Qpyro 8.656376e+002
Mass fraction flue gas
ch4 1.409905e-002
o2 6.232249e-002
co2 1.590816e-001
co 2.923118e-002
h2o 7.152806e-002
n2 6.637376e-001
sum species 1.000000e+000
Error mass balance 2.220446e-016
Total mass flow of gas 8.652747e-001 [kg/s]
Mass flow of C particles 5.057081e-003 [kg/s]
Number of particles 1.932146e+007 at diameter 1.000000e-004 [m]
Temperature of gas 2.015553e+003 [K]
Temperature of solid 2.015553e+003 [K]
Mass flow of solid of grate 6.433297e-001 [kg/s]

    Grate 10 = grate 3 2
Ratio of primary air 8.750000e-002
Ratio of heat release 7.482962e-002
Ratio of heat release as pyrolysis gas 1.835774e-002
Ratio of waste water evaporation 6.802670e-003
Ratio of total particle release 7.482962e-002
CO/CH4 ratio 1.362500e+000
Qpyro 5.643731e+002
Mass fraction flue gas
ch4 9.049058e-003
o2 7.683155e-002
co2 1.459087e-001
co 2.151937e-002
h2o 6.550592e-002
n2 6.811854e-001
sum species 1.000000e+000
Error mass balance 2.220446e-016
Total mass flow of gas 8.424033e-001 [kg/s]
Mass flow of C particles 4.132570e-003 [kg/s]
Number of particles 1.578920e+007 at diameter 1.000000e-004 [m]
Temperature of gas 1.959499e+003 [K]
Temperature of solid 1.959499e+003 [K]
Mass flow of solid of grate 5.501688e-001 [kg/s]

    Grate 11 = grate 3 3
Ratio of primary air 8.750000e-002

Ratio of heat release 5.993257e-002
Ratio of heat release as pyrolysis gas 1.145705e-002
Ratio of waste water evaporation 3.546729e-003
Ratio of total particle release 5.993257e-002
CO/CH4 ratio 1.537500e+000
Qpyro 3.522248e+002
Mass fraction flue gas
ch4 5.544626e-003
o2 9.553975e-002
co2 1.289831e-001
co 1.489117e-002
h2o 5.871326e-002
n2 6.963281e-001
sum species 1.000000e+000
Error mass balance 2.220446e-016
Total mass flow of gas 8.234674e-001 [kg/s]
Mass flow of C particles 3.309860e-003 [kg/s]
Number of particles 1.264589e+007 at diameter 1.000000e-004 [m]
Temperature of gas 1.829077e+003 [K]
Temperature of solid 1.829077e+003 [K]
Mass flow of solid of grate 4.767666e-001 [kg/s]

Grate 12 = grate 3 4
Ratio of primary air 8.750000e-002
Ratio of heat release 4.725124e-002
Ratio of heat release as pyrolysis gas 6.909681e-003
Ratio of waste water evaporation 1.839401e-003
Ratio of total particle release 4.725124e-002
CO/CH4 ratio 1.712500e+000
Qpyro 2.124247e+002
Mass fraction flue gas
ch4 3.277104e-003
o2 1.159013e-001
co2 1.102674e-001
co 9.799497e-003
h2o 5.157242e-002
n2 7.091822e-001
sum species 1.000000e+000
Error mass balance 2.220446e-016
Total mass flow of gas 8.080264e-001 [kg/s]
Mass flow of C particles 2.609515e-003 [kg/s]
Number of particles 9.970107e+006 at diameter 1.000000e-004 [m]
Temperature of gas 1.651459e+003 [K]
Temperature of solid 1.651459e+003 [K]
Mass flow of solid of grate 4.195057e-001 [kg/s]

Grate 13 = grate 4 1

Ratio of primary air 2.500000e-002
Ratio of heat release 1.148479e-002
Ratio of heat release as pyrolysis gas 1.391062e-003
Ratio of waste water evaporation 3.381524e-004
Ratio of total particle release 1.148479e-002
CO/CH4 ratio 1.825000e+000
Qpyro 4.276550e+001
Mass fraction flue gas
ch4 2.276863e-003
o2 1.289491e-001
co2 9.810578e-002
co 7.257287e-003
h2o 4.703107e-002
n2 7.163799e-001
sum species 1.000000e+000
Error mass balance 2.220446e-016
Total mass flow of gas 2.284640e-001 [kg/s]
Mass flow of C particles 6.342632e-004 [kg/s]
Number of particles 2.423313e+006 at diameter 1.000000e-004 [m]
Temperature of gas 1.565708e+003 [K]
Temperature of solid 1.565708e+003 [K]
Mass flow of solid of grate 4.056574e-001 [kg/s]

Grate 14 = grate 4 2
Ratio of primary air 2.500000e-002
Ratio of heat release 1.068098e-002
Ratio of heat release as pyrolysis gas 1.191688e-003
Ratio of waste water evaporation 2.798667e-004
Ratio of total particle release 1.068098e-002
CO/CH4 ratio 1.875000e+000
Qpyro 3.663613e+001
Mass fraction flue gas
ch4 1.938564e-003
o2 1.345539e-001
co2 9.281779e-002
co 6.342437e-003
h2o 4.508776e-002
n2 7.192596e-001
sum species 1.000000e+000
Error mass balance 0.000000e+000
Total mass flow of gas 2.275171e-001 [kg/s]
Mass flow of C particles 5.898721e-004 [kg/s]
Number of particles 2.253709e+006 at diameter 1.000000e-004 [m]
Temperature of gas 1.490909e+003 [K]
Temperature of solid 1.490909e+003 [K]
Mass flow of solid of grate 3.928004e-001 [kg/s]

Grate 15 = grate 4 3
Ratio of primary air 2.500000e-002
Ratio of heat release 9.924957e-003
Ratio of heat release as pyrolysis gas 1.019002e-003
Ratio of waste water evaporation 2.315614e-004
Ratio of total particle release 9.924957e-003
CO/CH4 ratio 1.925000e+000
Qpyro 3.132722e+001
Mass fraction flue gas
ch4 1.646597e-003
o2 1.400130e-001
co2 8.763433e-002
co 5.531368e-003
h2o 4.319791e-002
n2 7.219768e-001
sum species 1.000000e+000
Error mass balance 2.220446e-016
Total mass flow of gas 2.266307e-001 [kg/s]
Mass flow of C particles 5.481196e-004 [kg/s]
Number of particles 2.094186e+006 at diameter 1.000000e-004 [m]
Temperature of gas 1.423190e+003 [K]
Temperature of solid 1.423190e+003 [K]
Mass flow of solid of grate 3.808716e-001 [kg/s]

Grate 16 = grate 4 4
Ratio of primary air 2.500000e-002
Ratio of heat release 9.214976e-003
Ratio of heat release as pyrolysis gas 8.698103e-004
Ratio of waste water evaporation 1.915420e-004
Ratio of total particle release 9.214976e-003
CO/CH4 ratio 1.975000e+000
Qpyro 2.674063e+001
Mass fraction flue gas
ch4 1.396137e-003
o2 1.453064e-001
co2 8.258350e-002
co 4.810854e-003
h2o 4.136609e-002
n2 7.245370e-001
sum species 1.000000e+000
Error mass balance 0.000000e+000
Total mass flow of gas 2.258016e-001 [kg/s]
Mass flow of C particles 5.089099e-004 [kg/s]
Number of particles 1.944379e+006 at diameter 1.000000e-004 [m]
Temperature of gas 1.360261e+003 [K]
Temperature of solid 1.360261e+003 [K]
Mass flow of solid of grate 3.698112e-001 [kg/s]

Appendix D

Nozzle characteristics

D.1 Data sheet provided from Megtek
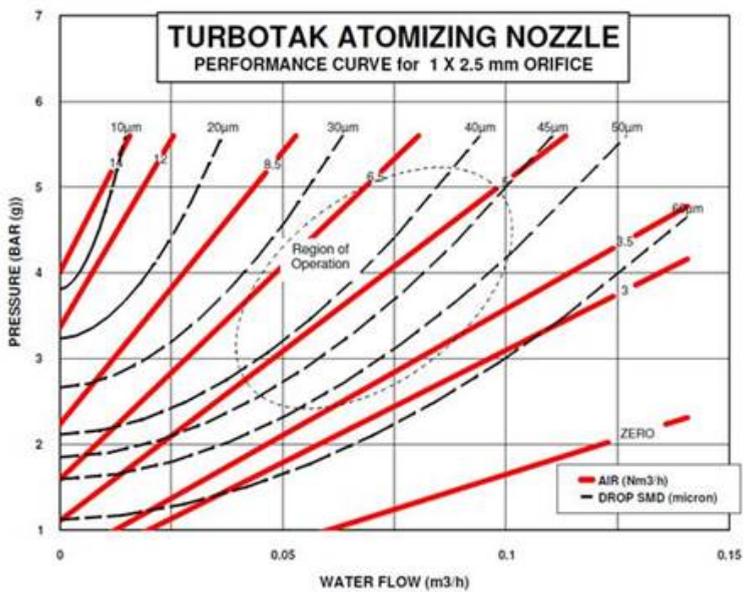
Figure D.1: Nozzle characteristic for the Turbotak^{TM} nozzle used in at Affald+ for NO$_x$ reduction i the SNCR system